MLS Multipath Studies, Phase 3 Volume II: Development and Validation of Model for MLS Techniques

J. E. Evans
S. J. Dolinar
D. A. Shnidman
R. C. Burchsted

Lincoln Laboratory

MASSACHUSETTS INSTITUTE OF TECHNOLOGY

LEXINGTON, MASSACHUSETTS

1. Report No. FAA-RD-79-21	2. Government Accession No.	3. Recipient's Catalog No.

4. Title and Subtitle	5. Report Date
MLS Multipath Studies, Phase 3. Final Report, Vol. II: Development and Validation of Model for MLS Techniques	7 February 1980
	6. Performing Organization Code

7. Author(s) J.E. Evans D.A. Shnidman S.J. Dolinar R.C. Burchsted	8. Performing Organization Report No. ATC-88, Volume II

9. Performing Organization Name and Address	10. Work Unit No. (TRAIS)
Massachusetts Institute of Technology Lincoln Laboratory P.O. Box 73 Lexington, MA 02173	
	11. Contract or Grant No. DOT-FA74-WAI-461
	13. Type of Report and Period Covered

12. Sponsoring Agency Name and Address	13. Type of Report and Period Covered
Department of Transportation Federal Aviation Administration System Research and Development Service Washington, DC 20591	Project Report
	14. Sponsoring Agency Code

15. Supplementary Notes

16. Abstract

This report presents work done during phase 3 of the US national Microwave Landing System (MLS) program toward the developing of a computer simulation mode of MLS multipath effects, the experimental validation of the model, and the application of the model to investigate multipath performance of ICAO proposals for the new approach and landing guidance system.

The second volume of the report presents the mathematical models and validation data for the MLS techniques which were assessed in detail by the All Weather Operations Panel of the International Civil Aviation Organization. The specific techniques modeled are:

1. The Time Reference Scanning Beam (TRSB) system proposed by the United States (US) and Australia, with prime emphasis on the US equipment implementation and field test data,

2. the Doppler scan (DMLS) proposed by the United Kingdom,

and

3. the DME Based Landing System (DLS) proposed by the Federal Republic of Germany.

17. Key Words	18. Distribution Statement
Microwave Landing System (MLS) DME Based Landing System (DLS) Doppler MLS (DMLS) Time Reference Scanning Beam (TRSB)	Document is available to the public through the National Technical Information Service, Springfield, VA 22151.

19. Security Classif. (of this report)	20. Security Classif. (of this page)	21. No. of Pages	
Unclassified	Unclassified	332	

ABSTRACT

This report presents work done during phase 3 of the US national Microwave Landing Systems (MLS) program toward developing a computer simulation model of MLS multipath effects, the experimental validation of the model, and the application of the model to investigate the multipath performance of proposals for the new approach and landing guidance system. The model was developed by separately considering the characteristics of the four basic elements affecting system operation in a multipath environment, i.e., airport, flight profile, propagation, and system elements. This modeling approach permits the examination of the effect on system performance of individual multipath performance factors such as: (a) reflections from terrain, aircraft, buildings with differing orientations, (b) shadowing by aircraft, building, and convex runways, (c) aircraft flight profiles and approach speeds, and (d) system design features to combat multipath.

The first volume of the report presented an overview of the overall simulation as well as a description of the refined mathematical models and validation of the propagation portion of the simulation. In this volume, we present the mathematical models and validation data for the three MLS techniques which were assessed in detail by the All Weather Operations Panel (AWOP) of the International Civil Aviation Organization (ICAO).

The first two chapters consider the Time Reference Scanning Beam (TRSB) system proposed by Australia and the United States. Both theoretical models and field data were utilized in arriving at the final TRSB simulation model, with particular emphasis being placed on emulating the dynamic characteristics of the antenna patterns as the beam is electronically scanned. The validation of the TRSB model was principally accomplished by comparing the simulation model with bench simulator data and with field data from a variety of sites inside and outside the US.

The next two chapters are concerned with the Doppler scan (DMLS) systems proposed by the United Kingdom. Theoretical models and the results of bench

simulations were utilized in arriving at the final DMLS model. Of particular concern in the DMLS modeling was the representation of various dynamic effects associated with the receiver electronics (e.g, AGC) and/or receiver motion. Validation was principally accomplished by analytical calculations and by comparison of the simulation model with results from the UK hybrid bench simulator.

The final two chapters are concerned with the DME Based Landing System (DLS) proposed by the Federal Republic of Germany (FRG). Theoretical models and close collaboration with the FRG were the principal means of modeling the DLS system since the DLS technique relied heavily on digital signal processing in a ground based computer. Validation of the DLS model also had to rely heavily on analytical calculations since very limited multipath field test data was reported by the FRG. However, by supplementing the FRG data with bench simulation tests at Lincoln Laboratory on a related interferometer system, it was possible to obtain a satisfactory validation of the DLS model.

ACKNOWLEDGMENTS

CONTENTS

CONTENTS (cont'd)

CONTENTS (cont'd)

LIST OF ILLUSTRATIONS

I. TRSB MODEL

A. Introduction

The Time Reference Scanning Beam System (TRSB) was proposed to ICAO by Australia [16] and the United States [65] and subsequently adopted as the new international standard MLS by the ICAO All Weather Operations Division [94]. This chapter describes version 2.0 of the TRSB system model, which is a combination of:

(1) the version 1.0 model utilized for the ICAO All Weather Operations Panel (AWOP) assessment activity, which considered the signal processing and antenna patterns for the proposed azimuth and elevation functions. This model was based on the TRSB system as described in various papers presented by the U.S. to AWOP [65, 66, 69].

(2) additional functions [e.g., flare and out-of-coverage/sidelobe suppression (OCI/SLS)] and antenna models (e.g., the phase III Basic Narrow and small community antennas which are currently in use). The receiver flare processor model is based on recent studies at the Calspan Corporation [92], while the OCI/SLS models are based on the U.S. data provided to AWOP [65, 95] and discussions with the Bendix designers of the TRSB phase III receivers. The new antenna pattern models are based on data from the respective manufacturers [93, 97, 99].

The TRSB concept was discussed in chapter I, Volume I of this report; Fig. 1-1 summarizes the essential ideas in the TRSB concept. Figure 1-2 provides a more detailed description of the relationship between the various ground antenna patterns and the received signal format for the azimuth and elevation functions.

Figure 1-3 shows a flowchart of the Bendix phase III TRSB receiver, which was modeled for the AWOP assessment. During the first received signal frame, the receiver searches the data for the peak signal and takes it as the candidate to acquire. In the second and subsequent frames, it builds up confidence that it is tracking the correct target. In doing so, it checks that the tracked component exceeds anything out of beam at least 50% of the time, determines dwell gates, and validates them, but does not output an error value, analogous to the cockpit situation in which the flag is down.

ANGLE MEASUREMENT TECHNIQUE
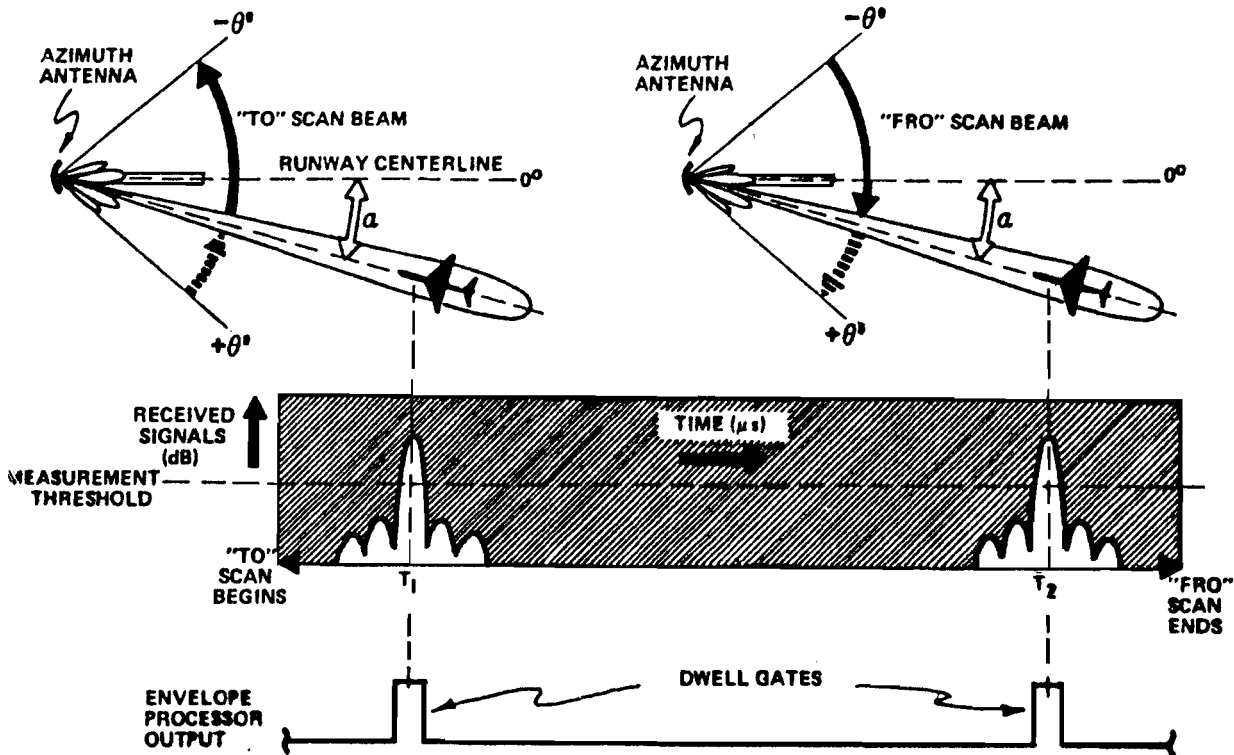
- TIME DIFFERENCE $T_2 - T_1$ RELATES DIRECTLY TO MEASURED ANGLE α
  - MICROPROCESSOR CALCULATES ANGLE

- GATES PROVIDE FOR MULTIPATH/INTERFERENCE DISCRIMINATION
  - COMPARE RECEIVED POWER INSIDE GATES/OUTSIDE GATES FOR CONFIDENCE
  - TRANSIENTS OCCURRING OUTSIDE GATES ARE REJECTED TO PRESERVE CONFIDENCE

- SAME TECHNIQUE APPLIES TO ALL ANGLE FUNCTIONS, INCLUDING 360° AZIMUTH

- THRESHOLD SETTING/ANGLE MEASUREMENT IS INSENSITIVE TO RECEIVED SIGNAL LEVEL

Fig. 1-1 TRSB angle measurement techniques.
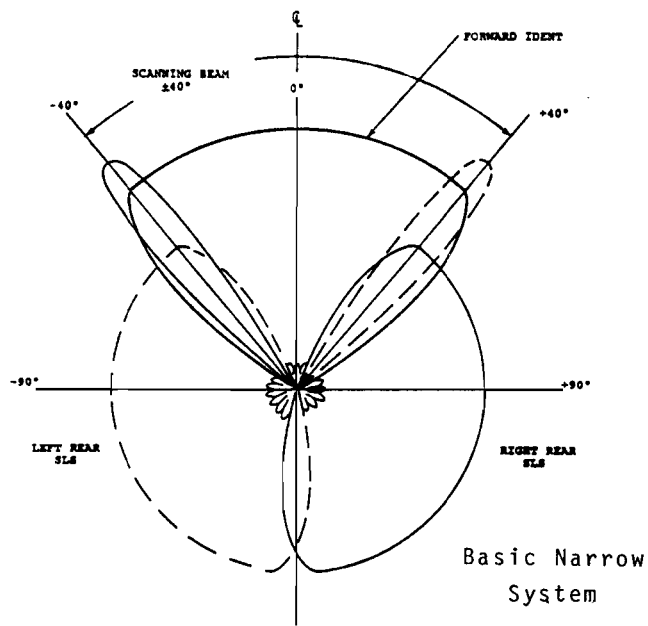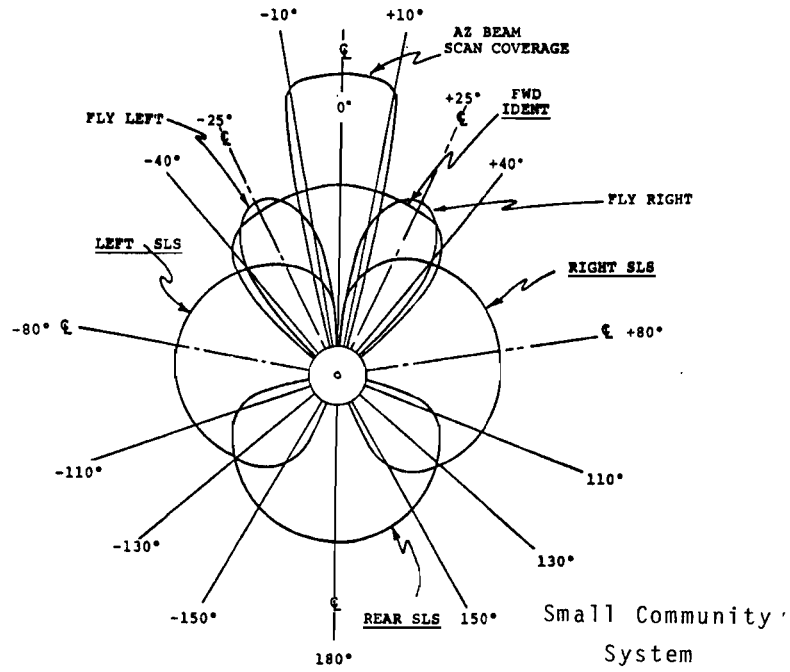
Fig. 1-2a Coverage of TRSB azimuth system.

* Basic Narrow scan limits illustrated; small community limits are ±12° while expanded limits are ±62°

Fly Rt, Fly Left pulses present only with small community system
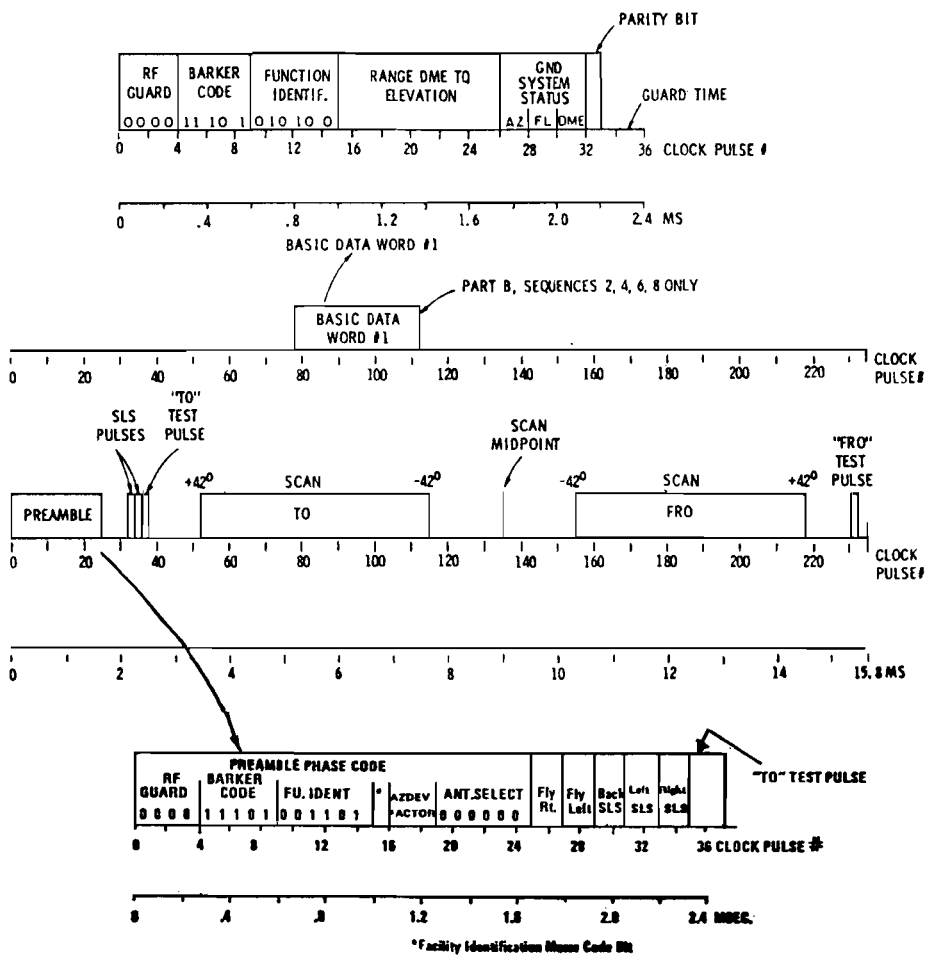
Fig. 1-2b Azimuth signal format.

Elevation Angle (Degrees)

ELEVATION COVERAGE

Signal Format

* EL GROUND SYSTEM STATUS
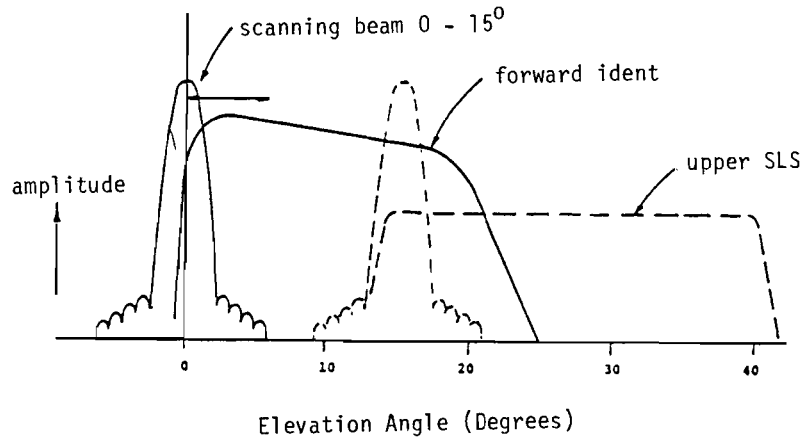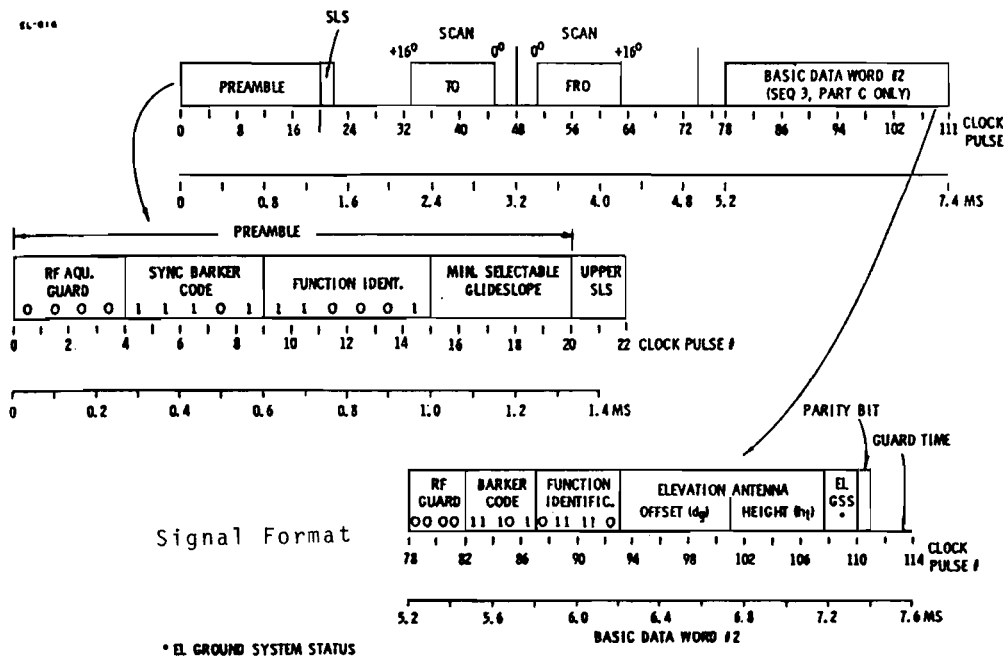
Fig. 1-2c Elevation function coverage and format.
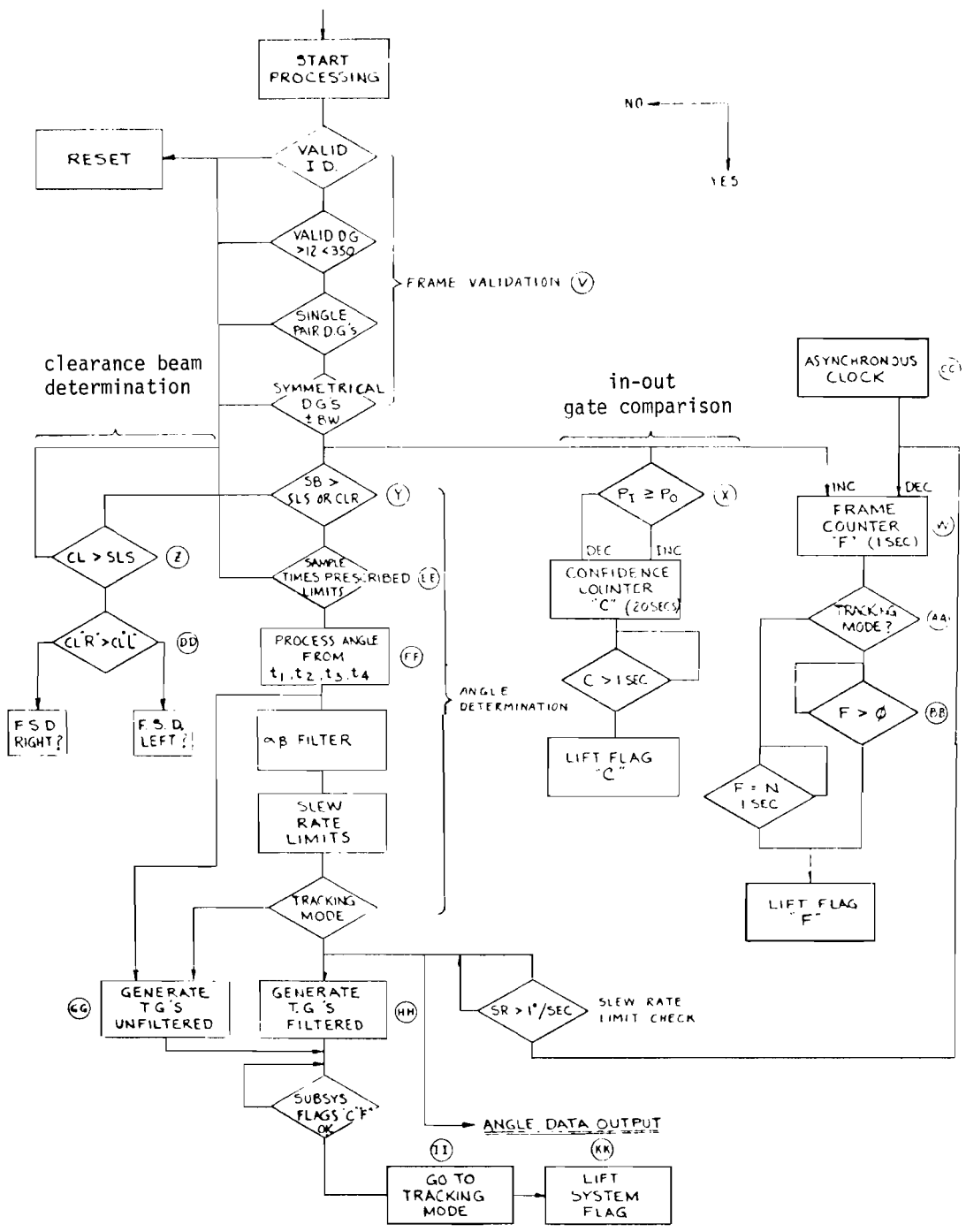
Fig. 1-3 MLS Phase III receiver-processing flow chart (from [69]).

Upon satisfying all acquisition criteria, the system enters track mode by raising system flags. In tracking mode, the validation tests are performed, and when the scan is validated, the raw angle error is computed by numerical simulation of the TO-FRO dwell gate processor. The raw error sequence is input to the filter/slew rate limiter combination from which emerges a smooth angle estimate stream at the raw data rate. A coast mode is also provided to maintain track during short periods (less than 1 sec) of invalid data.

The single edge processor (SEP) used for flare is based on the Calspan Corp. LSI-11 digital receiver [92]. Figure 1-4 shows the technique used to perform SEP angle estimation. The processing shown in Fig. 1-3 is used in parallel with the SEP algorithm so as to determine dwell gates, flags, etc.

The remainder of the model description has been organized to roughly parallel the signal flow in Fig. 1-1. Section B derives the basic received signal model used for scanning beam and OCI/SLS envelopes. Section C describes the antenna models, including experimental and analytical data used to develop the models. Section D presents the receiver processor models. The validation of the receiver model and end-to-end validation of the entire model is describes in the next chapter. Section E discusses some insights gained during the modeling process.

B. Received Signal Model

In this section we describe how the multipath characteristics obtained by the simulation propagation model (e.g., amplitude, rf phase, azimuth and elevation angles, etc. for each component) are utilized to obtain the received envelope as a function of time. For purposes of discussion, we consider here principally the scanning beam envelope since the clearance and OCI envelopes are a special case of the scanning beam envelope calculation.

The transmitter excitation is a sine wave burst which is spatially modulated by the scanning antenna pattern. This antenna pattern is represented as the product of a scanned pattern (e.g., the azimuth pattern in the AZ function) and an element pattern (e.g., the elevation pattern of the azimuth antenna elements), denoted respectively by $P_a(\cdot)$ and $P_b(\cdot)$. The arguments of

a **Dwell Gate Processor**

t_1 and t_2 found by interpolation between sampling points (dashed lines)

Dwell Gate Width = $t_2 - t_1$

Beam Center Time = $\dfrac{t_1 + t_2}{2}$

3 dB

t_1 t_2

t_n t_{n+1} PEAK DIGITZED VALUE t_m t_{m+1}
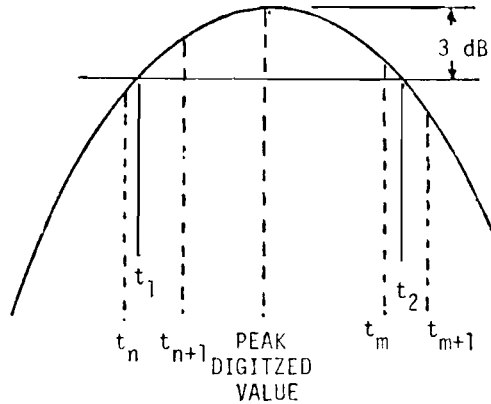
b **Single Edge Processor**

Time of 9 dB in 16 microseconds slope found by interpolation between times of greater and less slope

(Equivalent to analog delay and compare thresholding.)

9 dB

9 dB

16 μseconds

t_n t_{n+3}
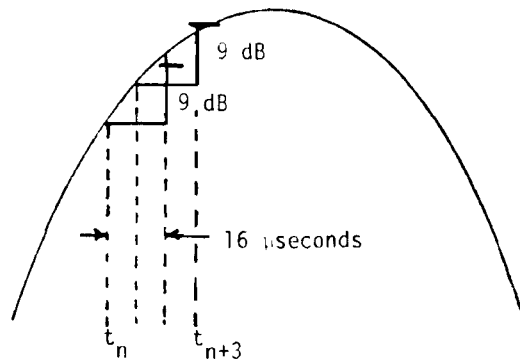
Split Gate Processor

Difference of sums of four amplitudes on either side of peak $(\Sigma_1^+ - \Sigma_1^-)$ is interpolated with shifted difference $(\Sigma_2^+ - \Sigma_2^-)$ to determine beam centroid.

Σ_1^- PEAK VALUE Σ_1^+

Σ_2^- Σ_2^+
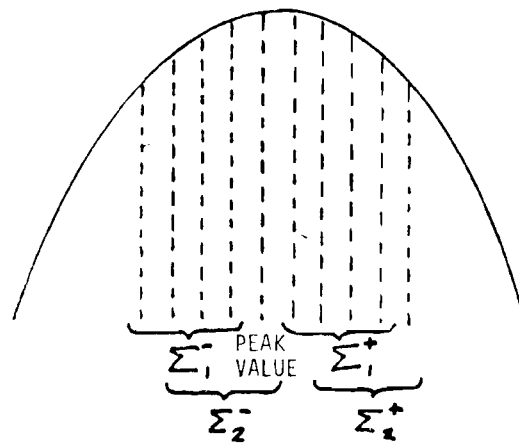
Fig. 1-4   Angle processing techniques studies by Calspan [92].

$P_a(\cdot)$ are in sine-angle coordinates. The transmitting antennas are electronically scanned line arrays which are phase programmed to scan the beam direction linearly in time. Thus, a stationary receiver located at (θ_0, Φ_0) = (scan plane coordinate, orthogonal coordinate) receives a pulse proportional to $P_a(\sin \dot{\theta}t - \sin \theta_0)\ P_b(\theta_0, \Phi_0)$, where $\dot{\theta}$ is the scan rate. This expression establishes our convention that t = 0 corresponds to beam passage through 0° as observed at the receiver. The rate $\dot{\theta}$ is assumed positive, so that the argument given $P_a(\cdot)$ above corresponds to a positive-directed scan (FRO-scan); on the TO scan replace $\dot{\theta}$ by $-\dot{\theta}$.[*] Multiply by $e^{j\omega t}$, where ω = carrier frequency (rad/sec) to get the received complex envelope.

For a moving receiver, the time varying delay $\tau_0(t)$, defined below, must be introduced:

$$\tau_0(t) = - \frac{V_a \cos \beta_0}{c}\ t \qquad (1-1)$$

where

V_a = A/C speed

β_0 = conical angle between A/C velocity vector and LOS to transmitter antenna phase center

c = speed of light in air

Introduction of the delay merely replaces the carrier ω by a Doppler shifted frequency ω_0:

$$\omega_0 = \omega \left[1 + \frac{V_a \cos \beta_0}{c} \right] \qquad (1-2)$$

The effect upon the low bandwidth envelope is small enough to neglect. Thus, the received direct signal model (FRO-scan) is

---

[*]The scan format described here corresponds to the format used in the original US ICAO submission; more recent changes in the scan format can be incorporated in the model by a change in the sign of $\dot{\theta}$.

$$r_0(t) = P_a(\sin \dot{\theta}t - \sin \theta_0)P_b(\theta_0,\Phi_0)\, e^{j\omega_0 t} \tag{1-3}$$

Each multipath component has a relative amplitude ρ_i, a nominal differential delay τ_i, phase ϕ_i and arrival angle β_i, defined as

$$\beta_i = \text{conical angle between A/C velocity vector and LOS to i-th image transmitter}$$

and its own arrival direction (θ_i, Φ_i). The corresponding time varying delay is:

$$\tau_i(t) = \tau_i - \frac{V_a \cos \beta_i}{c}\, t \tag{1-4}$$

Only the nominal delay is included in the envelope term. Thus, the multipath representation is

$$r_i(t) = \rho_i P_a[\sin \dot{\theta}(t-\tau_i) - \sin \theta_i]P_b(\theta_i,\Phi_i)e^{j[(\omega_i-\omega_0)t - \omega\tau_i + \phi_i]} \tag{1-5}$$

The composite TO-scan received envelope is the magnitude of the sum of all the components:

$$e_{TO}(t) = \left| \sum_{i=0}^{M} \rho_i P_a[-\sin \dot{\theta}(t-\tau_i) - \sin \theta_i]P_b(\theta_i,\Phi_i)e^{j[(\omega_i-\omega_0)t-\omega\tau_i+\phi_i]} \right| \tag{1-6}$$

In the above equation the frequencies are all referenced to the received direct component frequency as the result of premultiplying by $e^{-j\omega_0 t}$.

For the FRO-scan, Eq. (1-6) is altered only by replacing $\dot{\theta}$ with $-\dot{\theta}$ and replacing the nominal delay τ_i by $\tau_i + T_z$, where T_z is the time between the two 0° passages of the beam.

Multiple scan processing is also taken into account in the receiver routine. Ordinarily, newly computed multipath parameters are supplied to the receiver at the desired MLS output data rate, although this is not a requirement of the program. When the raw data frame rate exceeds the output rate (as is now the case for all TRSB functions), the scan-to-scan multipath update is

done within the receiver program. Over the frame duration (200 msec for a 5 Hz output data rate), it is assumed that the multipath is stationary with respect to amplitude ρ_i, nominal delay τ_i, nominal coordinates of the specular point as seen by the transmitter (θ_i, Φ_i), and angle of arrival β_i. Only the differential phase is updated for each scan. The update is accomplished by adding a scan-dependent delay to $\tau_i(t)$, viz.,

$$\tau_{ik}(t) = \tau_i - \frac{V_a \cos \beta_i}{c} \left(t + T_k\right) \tag{1-7}$$

where T_k is time of the k-th scan midpoint relative to the 1st. The method by which T_k is determined is discussed in Appendix C. Although the $\{T_k\}$ are sufficiently long to influence the envelope, the time scale is rearranged so that each scan passes through $0°$ at t=0, thus putting the effect of T_k into the phase term. Thus, we arrive at the final expressions for the received envelopes on the k-th TO and FRO scans:

$$e_{TOk}(t) = \left| \sum_{i=0}^{M} \rho_i P_a [-\sin \dot{\theta}(t-\tau_i) - \sin \theta_i] P_b(\theta_i, \Phi_i) \right.$$

$$\left. \cdot \exp j \left\{ (\omega_i - \omega_0)t - \omega \tau_i - \frac{V_a \cos \beta_i}{c} T_k + \phi_i \right\} \right| \tag{1-8}$$

$$e_{FROk}(t) = \left| \sum_{i=0}^{M} \rho_i P_a [\sin \dot{\theta}(t-\tau_i) - \sin \theta_i] P_b(\theta_i, \Phi_i) \right.$$

$$\left. \cdot \exp j \left\{ (\omega_i - \omega_0)t - \omega \tau_i - \frac{V_a \cos \beta_i}{c} (T_k + T_z) + \phi_i \right\} \right| \tag{1-9}$$

Figure 1-5 shows the TRSB signal format used in the Phase II and III receivers. The format uses time division multiplex within a full cycle of 592 msec. The computer model assumes a data output every 200 msec for a 5 Hz data rate. Since the smoothed data rate equals the raw data rate, smoothed values are sampled at a 5 Hz average rate to yield the guidance signal: in the com-
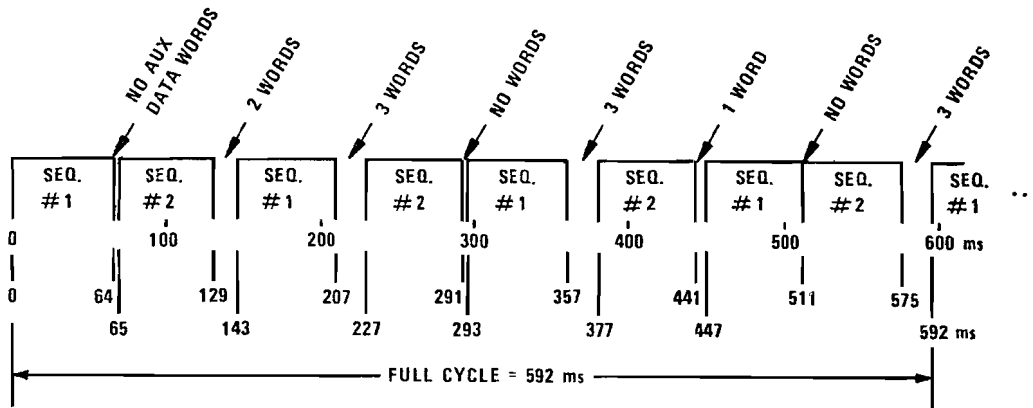
(a) Full Cycle of Functions
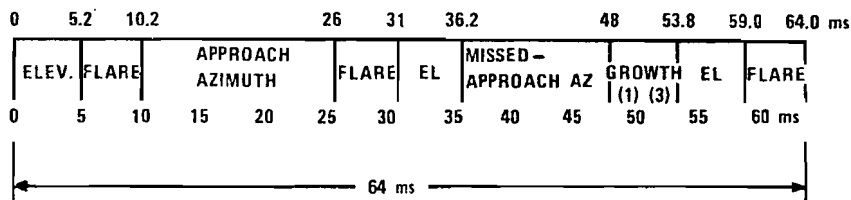
(b) Subsequence #1
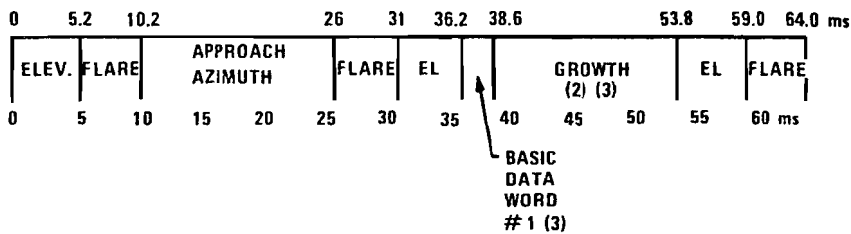
(c) Subsequence #2

NOTES: (1) AUXILIARY DATA (1 WORD) OR MISSED APPROACH ELEVATION
       (2) 360° AZIMUTH OR AUXILIARY DATA (2 WORDS)
       (3) BASIC DATA WORD #2 TRANSMITTED EITHER IN GROWTH
            OR BETWEEN SEQUENCES

Fig. 1-5 TRSB signal format (TDM).

puter model, every eighth EL point and every third AZ point is taken. The timing for adjacent TO-FRO scan pairs is determined from the timing sequences in Fig. 1-5. Appendix C details the actual implementation of the timing for adjacent TO-FRO scan pairs.

One potential problem which can arise with the multiple scan averaging is the effect of staircase steps in the direct signal angle every frame on the $\alpha - \beta$ tracking filter. To reduce these effects (which are an artifact of the multipath/system error computation procedure), an option exists whereby the estimated angle (and the direct signal value used in the error computation) are modified by an angle velocity/acceleration correction term before the $\alpha-\beta$ filter output and angle error are computed.[+] The implicit assumption here is that the small change in direct signal angle which occurs over a 0.2 sec time period would also result in offsetting multipath angle changes such that the multipath errors would not be changed significantly.

The transmitted OCI and clearance signals are not modulated in time by the transmitter and, the ground antennas are fixed radiators. Additionally, the duration of the signals is quite small ($\sim$ 130 μsec) relative to the peak scalloping rates* encountered in practice. Therefore, the magnitude of these OCI/SLS signals are determined by evaluating eq. (1-8) at a single instant of time with P_a = 1 and P_b an appropriate antenna pattern.

C.   Antenna Pattern Models

This section describes the methods by which the various antenna patterns were generated for the TRSB simulation. In many of the cases the array pattern was first calculated from the appropriate aperture distribution over a grid of points in the sine space coordinate. In other cases the pattern data is taken directly from field measurements. Where required, subsequent modifications are made to account for effects such as phase-shifter quantization in dynamic patterns. A signed table of values is stored and coupled with an

---

*i.e., $V_a (\cos \beta_i - \cos \beta_0)/c$

[+]Appendix D discusses this option in detail,

interpolation algorithm to reconstruct the pattern without having to recompute the full array function each time the beam pattern routine is called.

Section 1 reviews the general methodology of array pattern representation. Following that, descriptions are given of the fully filled AZ array (2), the thinned AZ 1^O array (3), a Basic Narrow 2^O azimuth array (4), a Small Community 3° azimuth array (5), the COMPACT 1^O EL, (6) a filled 1^O elevation array, (7) a 1.5^O Basic Narrow elevation array (8) a 2^O Small Community elevation array (9), a 0.5^O flare array (10), and a 1^O bench simulator pattern (11).

1. Linear Array Patterns

Assume an M-element linear array with uniform element spacing $d = s\lambda$ in which the m-th element has complex excitation $a_m e^{j\phi m}$. An observer stationed at angle θ_R (relative to the array normal) in the far field will sense a phase differential $-2\pi s \sin \theta_R$ between the signals from adjacent elements due to the differential path length ($d \sin \theta_R$), resulting in a net reception

$$P(\theta_R) = \sum_{m=1}^{M} a_m e^{j(\phi_m - 2\pi ms \sin \theta_R)} \tag{1-10}$$

If the intent is to point the mainlobe of the antenna pattern at boresight angle θ_B, the appropriate phase excitation at the aperture is

$$\phi_m = 2\pi ms \sin \theta_B \tag{1-11}$$

and now the signal received at θ_R is

$$P(\theta_R, \theta_B) = \sum_{m=1}^{M} a_m e^{j2\pi ms(\sin \theta_B - \sin \theta_R)} \tag{1-12}$$

Because of the resulting sinusoidal dependence on θ_R and θ_B shown in eq. (1-12) it is convenient to express the received pattern in the coordinates u_R and u_B,

$$u_R = \sin \theta_R \tag{1-13}$$

$$u_B = \sin \theta_B \tag{1-14}$$

which allows patterns having uniform phase characteristics to be represented in terms of the difference variable $u = u_B - u_R$ in sine angle space. For example, the normalized* pattern of a full, uniformly illuminated array, $\{a_m = 1\}$, $1 < m < M$, is

$$P(u) = \frac{\sin M\pi su}{M \sin \pi su} \tag{1-15}$$

2. Expanded Fully Filled 1° AZ Array

Two versions of a fully filled AZ array providing $\pm 60^o$ of proportional coverage have been prepared for the simulation. The first is the exact theoretical design. The second is based on field measurements of the Bendix array at NAFEC and is modified for phase shifter quantization. The latter model is incorporated in the computer programs.

a. Theoretical Model

The fully filled AZ array has 117 uniformly spaced elements at almost half-wave spacing ($s = d/\lambda = 0.514$) with a Taylor weighted amplitude distribution having -27 dB sidelobes and $\overline{n} = 8$. The coefficients are symmetric about the center element (#59), i.e..

$$a_m = a_{118-m} \quad ; \quad 59 \leq m \leq 117 \tag{1-16}$$

allowing the pattern to be written

$$P(u) = \sum_{m=1}^{117} a_m e^{j2\pi msu}$$

$$= \sum_{m=1}^{58} a_m \left[e^{j2\pi msu} + e^{j2\pi(118-m)su} \right] + a_{59} e^{j2\pi(59)su}$$

---

*The normalization simply consists of dividing the sum in eq. (1-9) by $P(0,0)$ so that the normalized single variable pattern satisfies $P(0) = 1$.

$$= e^{j2\pi(59)su} \ 2 \sum_{m=1}^{58} \cos 2\pi(59-m)su + a_{59} \qquad (1\text{-}17)$$

Equation (1-17) shows that the linear pattern is a superposition of harmonically related sinusoids having u-space frequencies f_m:

$$f_m = (59-m)s \quad : \quad 1 \leq m \leq 58 \qquad (1\text{-}18)$$

All components have the same period as the fundamental, i.e., 1/s, and since they are cosinusoids, they have even symmetry about the half period point $u = 1/2s$. The stored values cover only the region $0 \leq u \leq 1/2s$, and for values outside that range the extrapolation rule

$$f(u) = f(\frac{1}{s} - u) \quad ; \frac{1}{2s} < u < \frac{1}{s} \qquad (1\text{-}19)$$

is used once enough multiples of 1/s have been added or subtracted to put u into the desired range. Values of the normalized pattern

$$P(u) = \frac{2 \sum\limits_{m=1}^{58} a_m \cos 2\pi(59-m) \ su + a_{59}}{\left(2 \sum\limits_{m=1}^{58} a_m\right) + a_{59}} \qquad (1\text{-}20)$$

are stored over a grid from u=0 to u=1/2s (=0.09728) with increment Δu = 0.005, supplemented by a fine grid (spacing 0.001) between 0.0 and 0.005 to more accurately represented the mainlobe region.

Figure 1-6 shows static patterns so computed by both Bendix and Lincoln Laboratory. In both cases analog phase shifter characteristics were assumed. Although it would be possible to incorporate the phase shift quantization (4 bits) and the scan program into the Lincoln simulation (this would amount to a replication of work done by Bendix), it would be computationally pro- hibitive to run such a model in typical scenarios. The model discussed below takes these factors into account.

BW = 1.0135°

117 ELEMENTS
-27.00 DB SIDELOBES
SCAN ANGLE = 0.00000
COSINE ELEMENT PATTERN
SPACING = 0.514
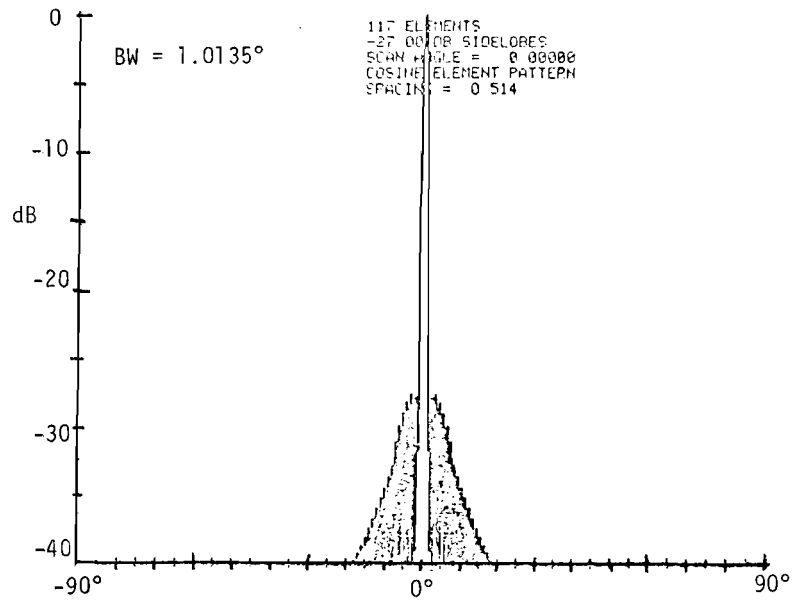
(a) Bendix calculation

(b) Lincoln calculation

Azimuth Angle (deg)
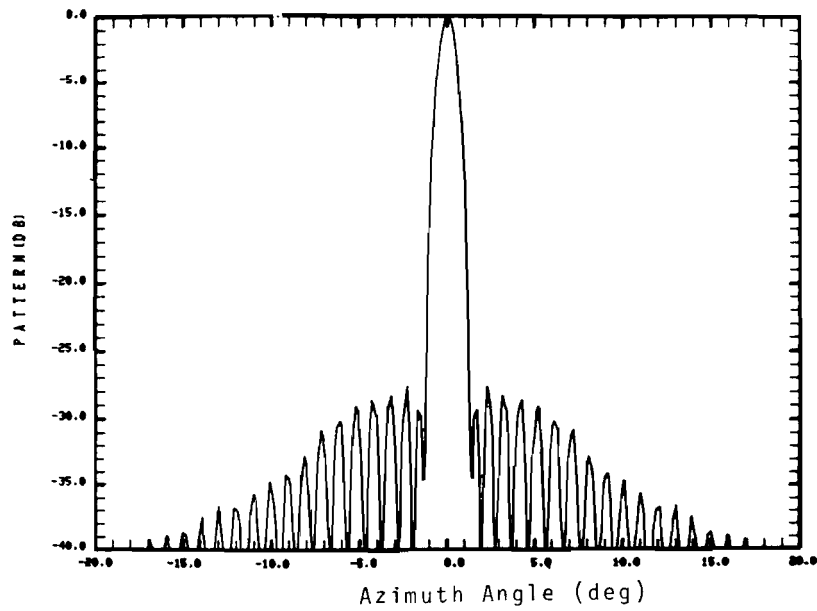
Fig. 1-6 Fully filled Taylor weighted AZ array.

b. Experimental Data Based Model

The Bendix AZ array designed for the FRSB[*] field trials equipment was
modified for TRSB use during Phases II and III of the U.S. MLS program, and
its measured pattern was used as the basis for the computer simulation model.
Figure 1-7 (a) illustrates the measured pattern. Samples were taken from
this pattern over two grids. Within 1.5° of boresight, the pattern was sam-
pled every 1/6°; between 1.5° and 15°, the grid increment is 0.5°. Outside
15°, the measured data was erratic, and not well matched to the static design
theory or measurements described above.

In addition to the field measurements, we have had available the results
of antenna simulations performed by the AZ array designers, Bendix Communica-
tions Division. In these simulations, the beam steering unit (BSU) logic
and the IF and video filters are modeled in great detail.

Figure 1-8 shows two plots taken from these simulations. Figure 1-8 (a)
shows raw (unfiltered) beam data as it would appear at the aircraft antenna.
Sidelobe levels above -20 dB are evident. The second figure illustrates the
beam as it would appear at the output of the 25 KHz 4-pole envelope filter.
There is evident both a considerable smoothing of the rapid beam oscillations
and general decrease in sidelobe level as well. The filtered beam appears to
meet the desired -27 dB sidelobe level.

Figures 1-9 through 1-12 show beam envelope recordings made at NAFEC
(14 June, 1976) during an orbital flight at 2,000 ft altitude. In those tests,
the effects of any ground reflection components should be minimal. Envelopes
along centerline (0°), 30° and ±60° are shown. Note that the general charac-
ter of the sidelobe structure is largely independent of the beam pointing
angle. The recording bandwidth is similar to that used in the MLS receiver
(26 KHz), but there is the difference that in the receiver, the log envelope
is filtered, whereas the recorded sample has a single pole filter operating on
the linear envelope. The results of these two processes are somewhat different,

---

[*] Frequency Reference Scanning Beam.

1-18

Phased Array
Performance

dB

−10

−20

MEASURED AZ-1
STATIC PATTERN

THEORETICAL

−12   −8   −4   0   4   8   12
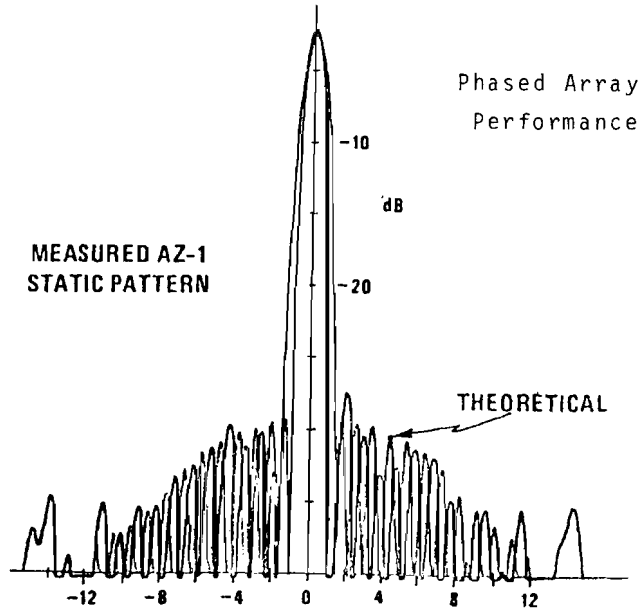
(a) Measured pattern of AZ array.

FORWARD IDENT
AZIMUTH PATTERN
5050.7 MHz

— 2
— 4
— 6
— 8
— 10
— 12
— 14
— 16
— 18
— 20

dB Below Peak

−72°   −36°   0°   36°   72°
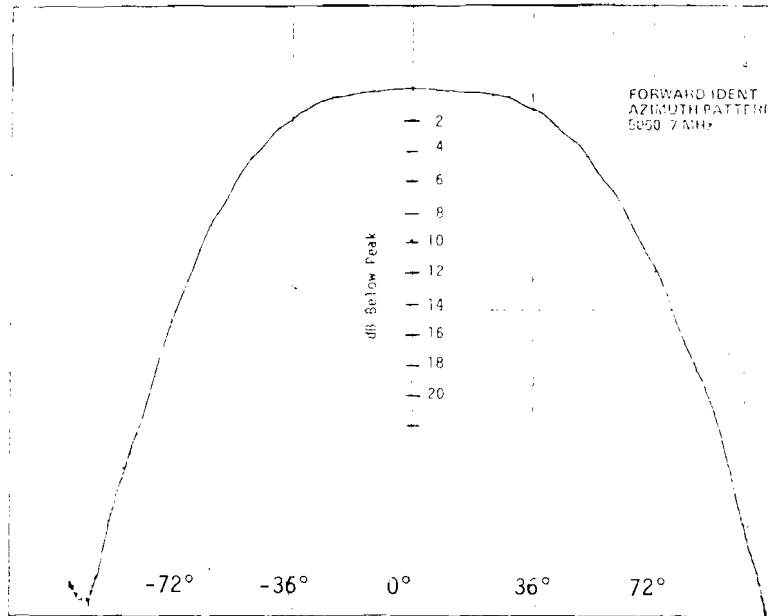
(b) Measured pattern of forward ident element
    (identical to AZ element)

Fig. 1-7 Bendix data used in modeling AZ array.

KHZ IN CHANNEL

(a) Raw beam data

26 KHZ IN CHANNEL
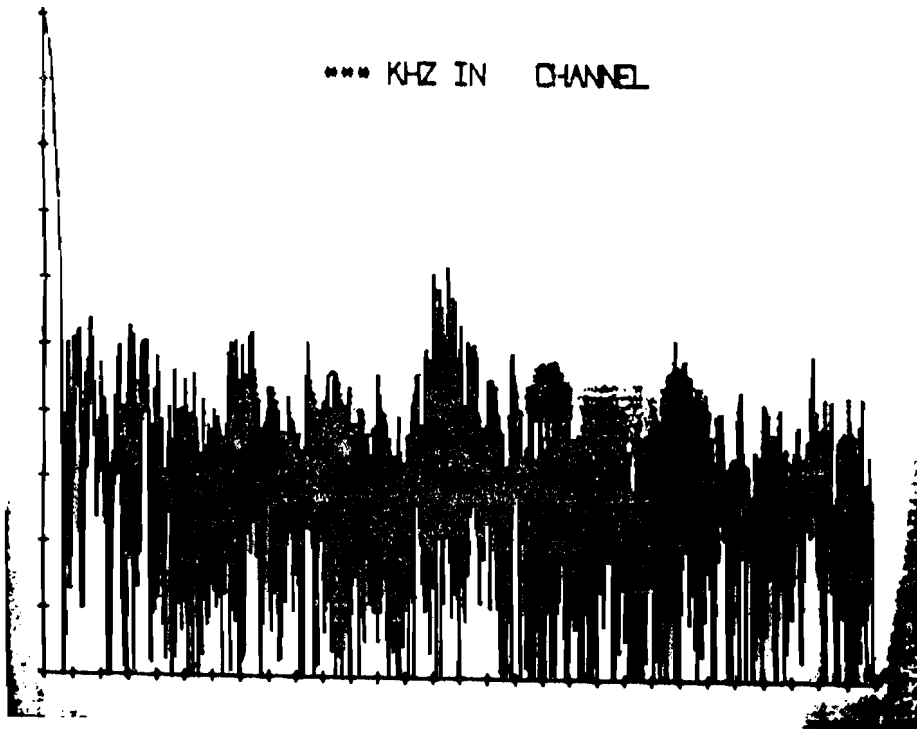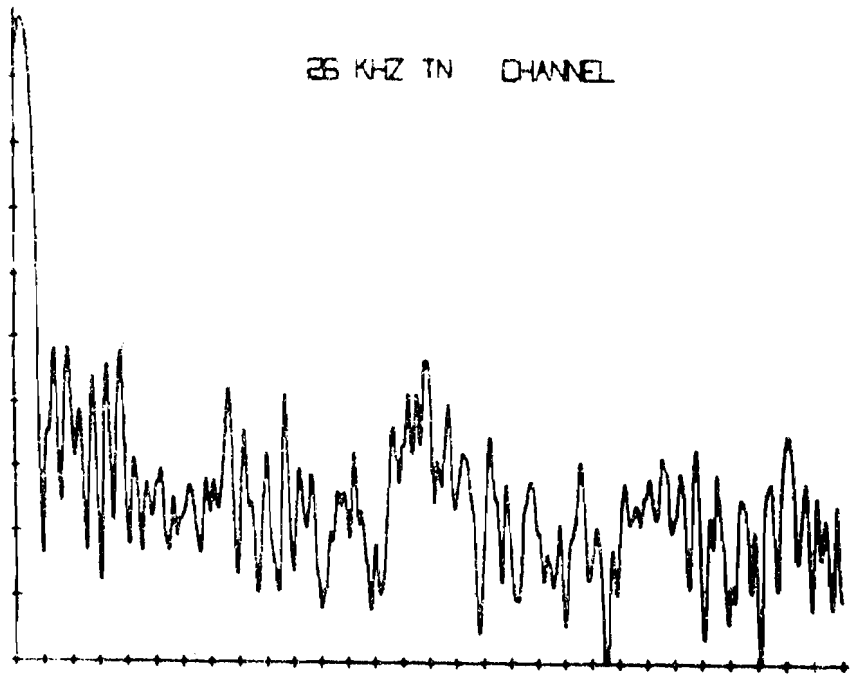
(b) Output of 26 KHz envelope filter

Fig.1-8   Bendix simulation of fully filled AZ array patterns.
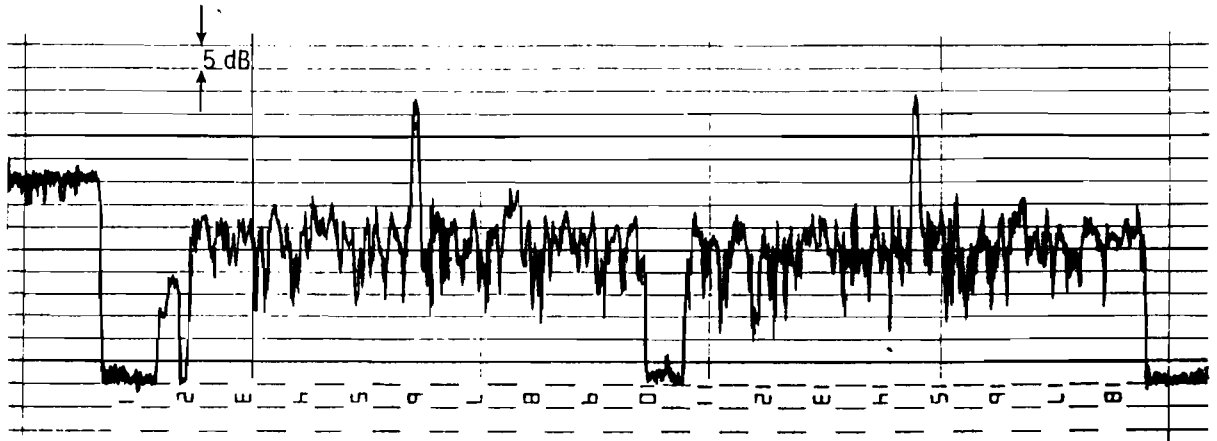
Fig. 1-9   Measured beam envelope at -0.17° (C_L).
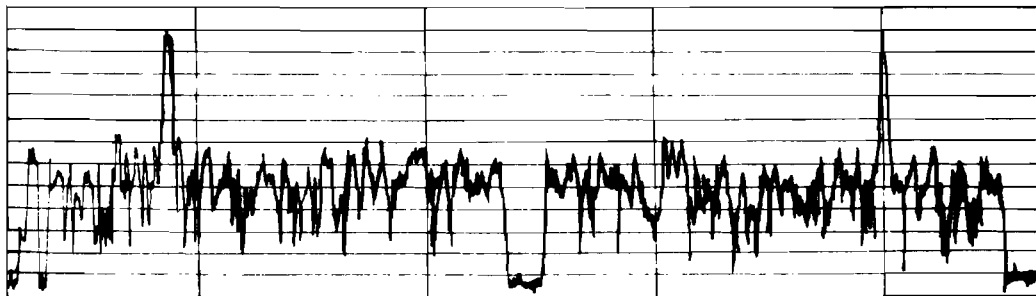
Fig. 1-10   Measured beam envelope at 30° azimuth.
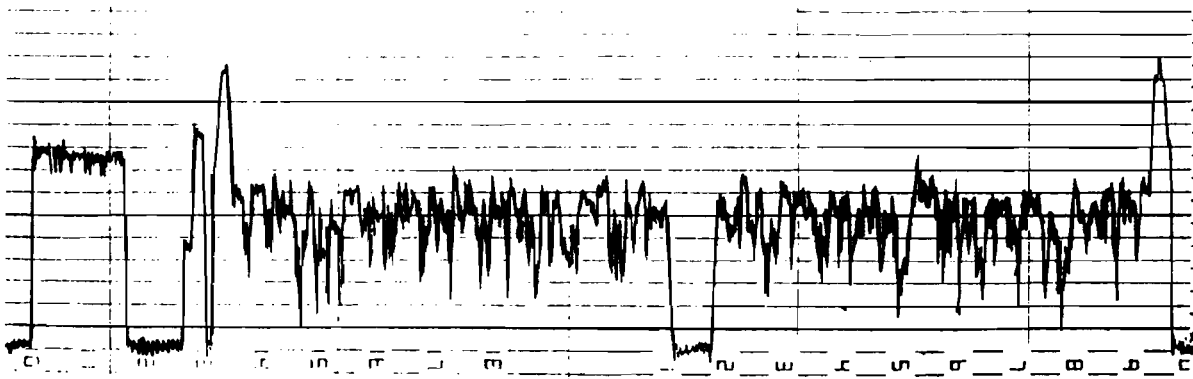
Fig. 1-11 Measured beam envelope at 59.5° azimuth.
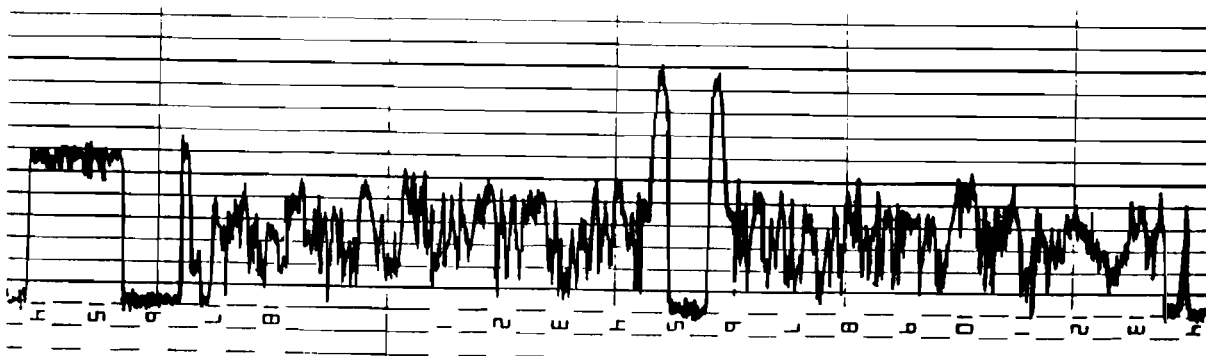
Fig. 1-12 Measured beam envelope at -60.2° azimuth.

but because of the similar bandwidths the comparison is meaningful. Occasional sidelobes near -20 dB occur, but over the majority of angular locations, the level is below -25 dB.

Both the Bendix simulations and the NAFEC data show that the dynamic side-lobe level at angles greater than 15° boresight are significantly higher than the static patterns. These further out sidelobes have a complicated structure that changes from scan to scan (due to certain phase cycling algorithms used in the digital phase shifter driver program); however, the overall level is roughly constant. We chose to represent the array factor sidelobe structure in this region by a constant amplitude sineusoid with sine space frequency of half the beamwidth and an amplitude of -26 dB. This sine space frequency choice was based on two considerations:

1) correspondence to the frequency of the far out sidelobes for

and   a uniformly weighted array

2) near "worst case" spatial frequency for TRSB dwell gate pro-cessor errors due to sidelobe multipath.

Similarly, the amplitude choice roughly represents the worst case peaks in the simulation and field test data.

In addition to the above array-related features, element factors are super-imposed to account for the pattern of the individual radiators. The measured pattern of the testbed azimuth antenna (Fig. 1-7(a)) is used. The element fac-tor model is shown in Fig. 1-13. The composite simulation static pattern is shown in Fig. 1-14.

Figure 1-15 shows field measurements of the elevation pattern of the Bendix azimuth column radiators. This pattern is approximated by interpolation from a look-up table of values taken from Fig. 1-15 with the result being the pattern shown in Fig. 1-16.
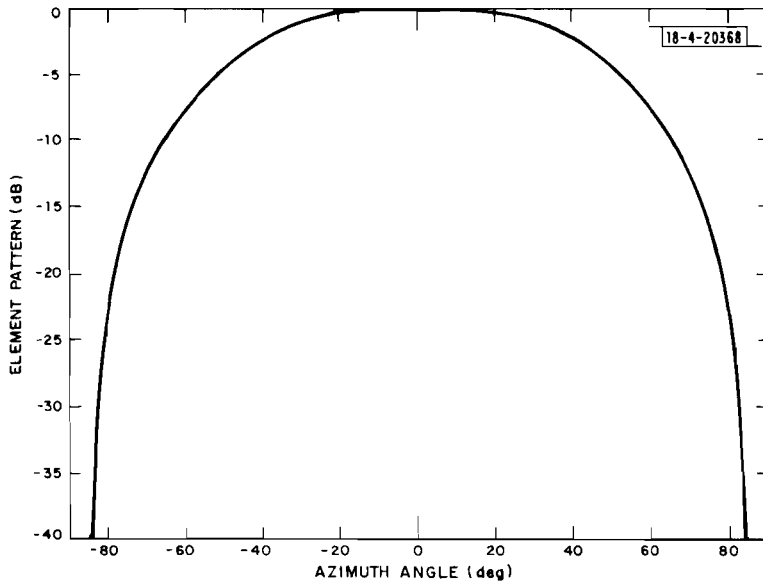
Fig. 1-13   Model for TRSB azimuth array element
pattern in azimuth plane.
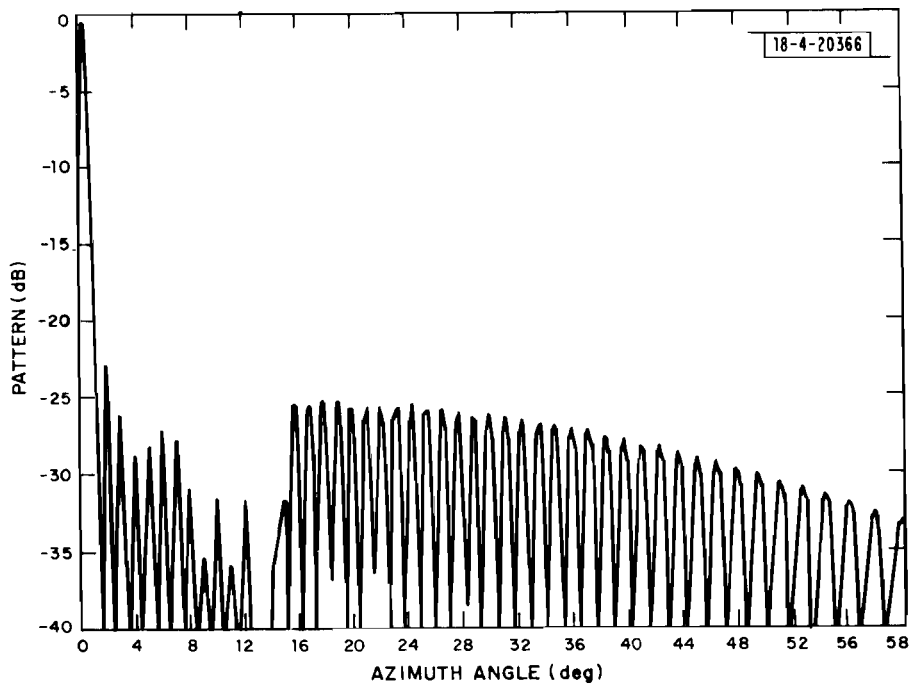
Fig. 1-14   Simulation model of fully filled AZ
array static pattern based on field measurements.
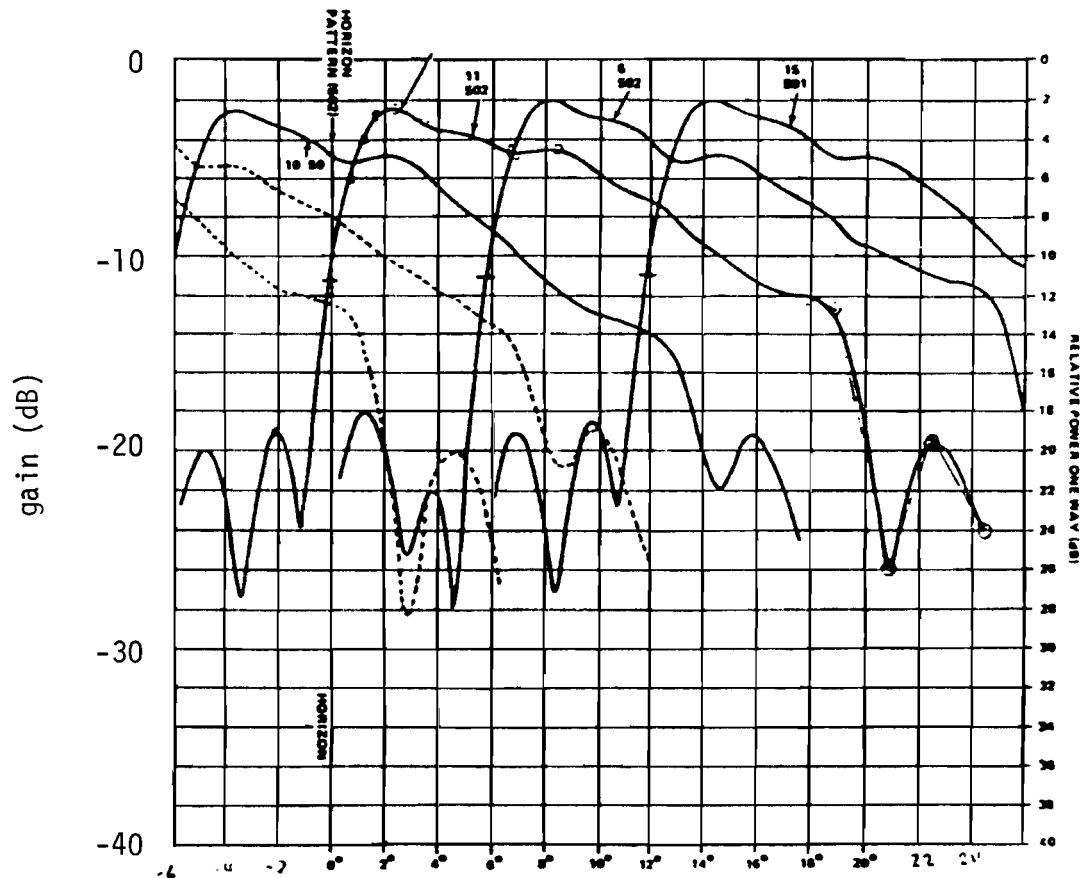
Fig. 1-15   Azimuth angle and DPSK antenna pattern, vertical cut [65]
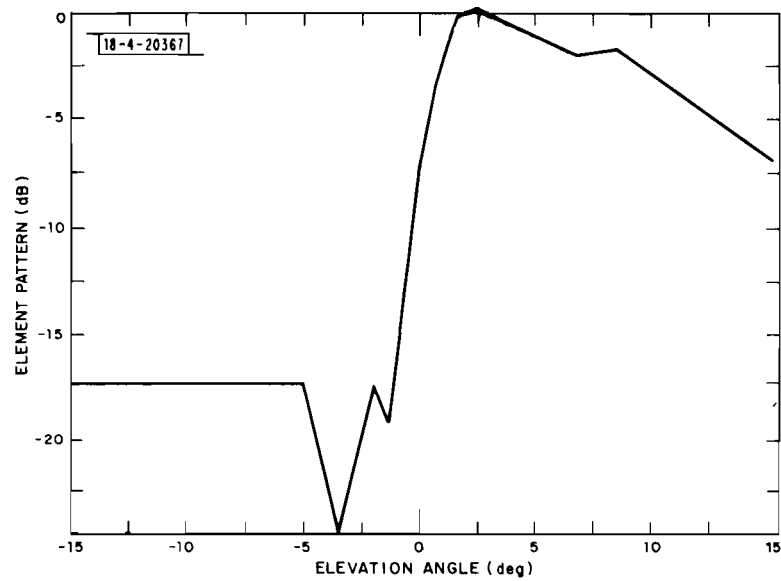
Fig. 1-16   Model of azimuth array elevation pattern.

3. Thinned AZ 1° Array

The proposed thinned AZ implementation is designed so as to be testable by modifying the Bendix filled array at NAFEC. The number of elements (117) and their spacing (0.514λ) coincide for the two. In the thinned array only 35 of the 117 elements are active (the selection of which elements are to be active was made according to a density taper analogous to a Taylor amplitude weighting) and the illumination of the active elements is uniform, that is, the coefficients a_m take on only values of 0 or 1. The elements that are "on" (numbered from the end of the array) correspond to m = 3, 9, 15, 20, 24, 28, 31, 34, 37, 40, 42, 45, 47, 50, 52, 54, 57, 59.

Figure 1-17 shows the idealized pattern in dB as calculated by Bendix and as replicated, using eq. (1-17), by Lincoln Laboratory. The grid points and symmetry rules used in the full array theory (Section 1) are retained here.

In Fig. 1-18 the theoretical pattern is compared to two other pieces of data. The first is a simulation of the thinned array pattern performed at Plessey Industries, U.K. [91]. In this simulation the phase shifter quantization (4 bits) is taken into account, although the BSU logic assumed there is no longer current in the Bendix implementation. The second curve is a receiver log video trace from the NAFEC flight tests of the thinned array (July 1976). Although the specific locations and values of the various sidelobes differ among these, the general shape of the envelope is in good mutual agreement, especially for angles more than 15° away from the mainlobe. Within the $\pm15^O$ region, both the field data and the U.K. simulation show sidelobes at the -20 to -25 dB level, which is roughly 5 dB above theoretical. Thus for simulation the sidelobes have been raised 5 dB in the region between the mainlobe edge (1.35^O) and 15°.

The final simulation model is shown in Fig. 1-19. It incorporates both the sidelobe boost and the element factor shown in Fig. 1-7. It is important to note that the inclusion of the element factor in Fig. 1-19 is not inconsistent with the data shown in the preceding figure. In Fig. 1-19 the antenna is pointed at 0° azimuth and the pattern shows what is simultaneously

(a) Bendix pattern   u = sin α

(b) Lincoln pattern   u = sin θ
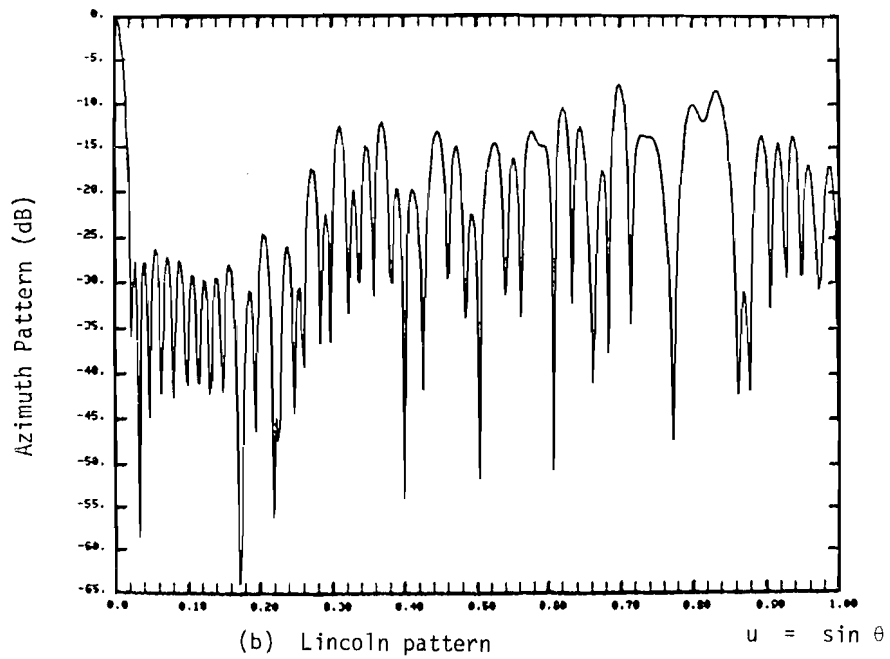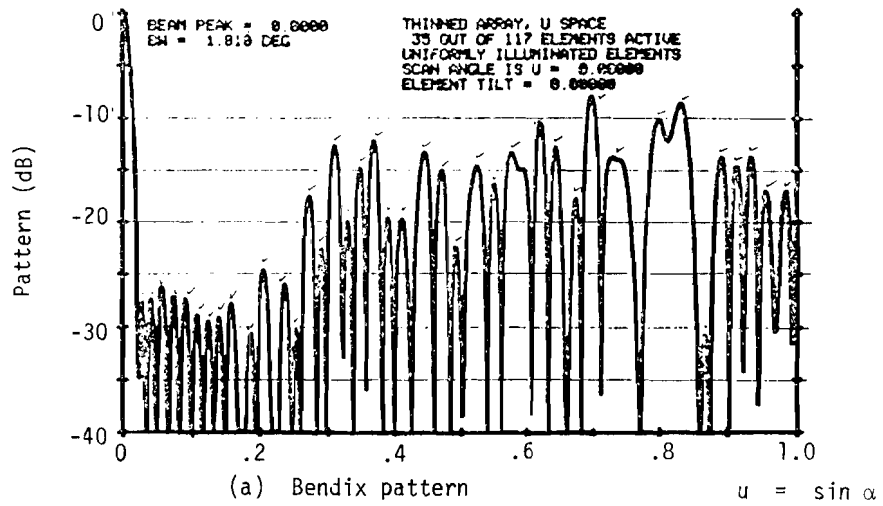
Fig. 1-17   Thinned AZ array pattern: 35/117 elements active.

U.K. Thinned
TRSB AZ Array
Simulation [91]

U.S. Thinned
TRSB AZ Array
Field Data
(150 kHz
bandwidth IF)
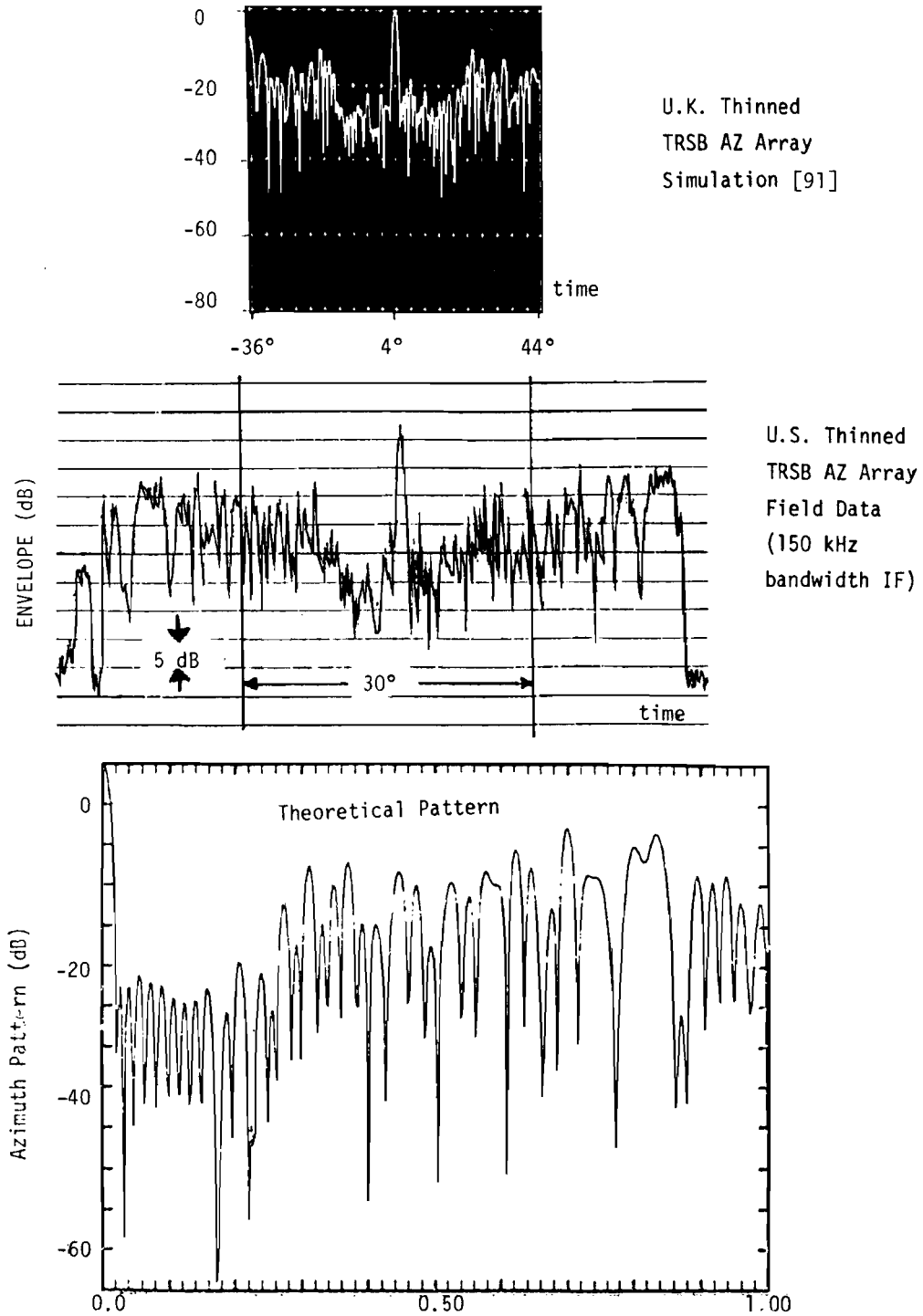
Fig. 1-18   Various simulations of the thinned AZ array pattern.
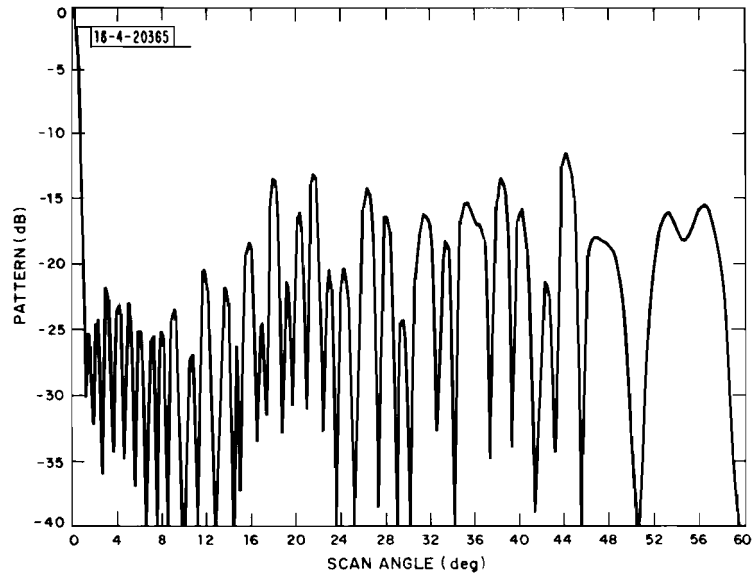
Fig. 1-19 Simulation model of thinned AZ
array factor.

radiated at all angles within ±60. The earlier figures are in terms of a
fixed receiver location and they show the pattern as the beam scans by. Natu-
rally the latter would not show a dependence upon the individual element
patterns.

The vertical pattern used for the thinned azimuth array elements was
that used for the filled azimuth array.

4. Basic Narrow Filled 2° Azimuth Array

The Bendix phase III Basic Narrow (BN) azimuth array utilizes a Rotman
lens (see figure 1-20) to give the required phase excitation at the aperture
over a proportional coverage region of ±40. The details of the scanning
mechanism are discussed in the Bendix reports [93]. Although this scan
mechanism is different from that of the phased array antennas discussed in
sections 2 and 3, the theory of section 1 and dynamic scan issues of section
2 are applicable to antenna modeling for this array.

In the nomenclature of Section 1, the BN array has the following parameters:

$$M = 64$$
$$s = 0.5$$
$$a_i = \cos [2\pi \ i/(M+1)] \quad 32 \leq i \leq + 32$$

The corresponding theoretical pattern has a first sidelobe level of -23 dB with
the outer sidelobes decreasing at a rate of -18 dB/octave [54]. Measured static
patterns (see Fig. 1-21) show a first sidelobe level at $\approx$ - 26 dB and further
out sidelobes which are substantially higher than the theoretical pattern (due
to scan mechanization effects). Dynamic patterns (see Fig. 1-21) also show a
mainlobe/first sidelobe similar to the theoretical pattern, but higher outer
sidelobes.

As in the case of the 1° filled array, this outer sidelobe structure was
modeled as a sineusoid of (sine space) period $1/32\pi$ and a level of -26 dB.
Fig. 1-22 shows the final model pattern at 0° on a logarithmic and linear scales

48 ACTIVE
INPUTS

64
ELEMENTS

$\dfrac{d}{\lambda} = 0.54$

F

R

α_o

G
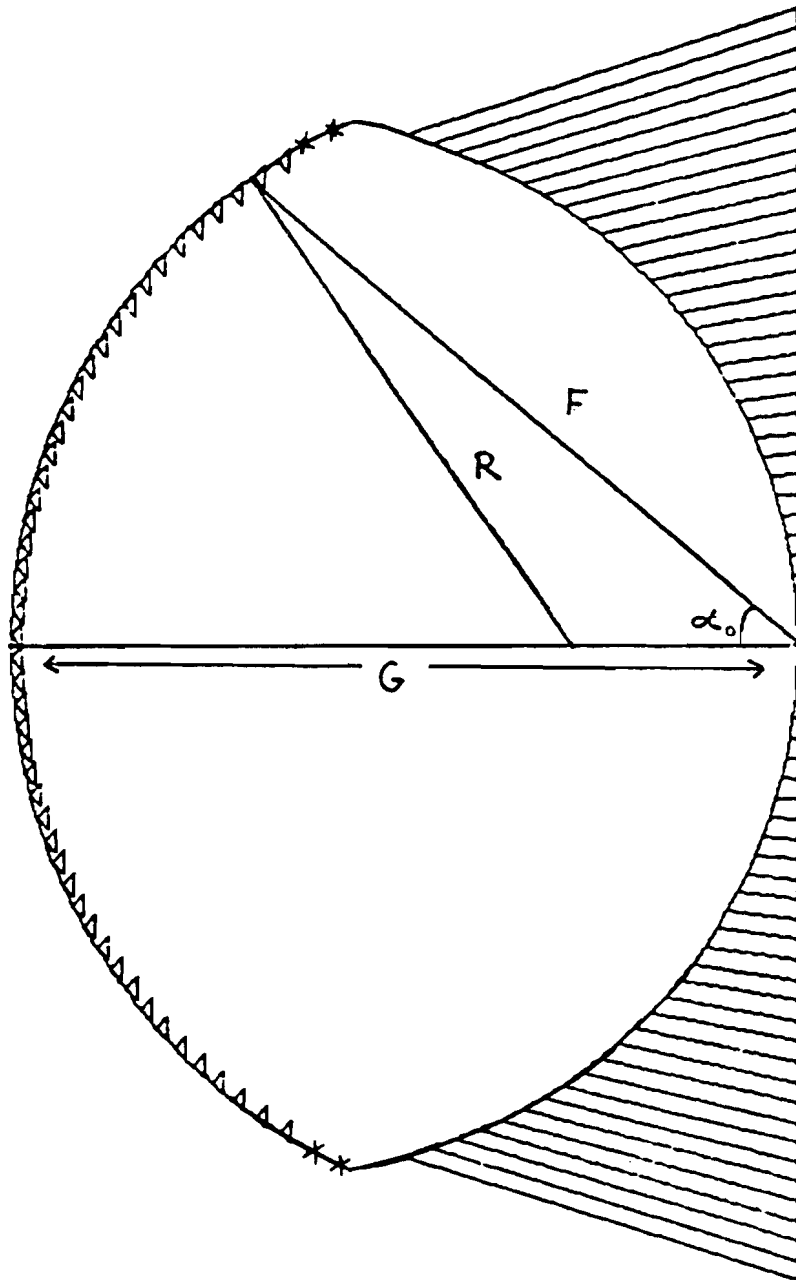
F = 1.140m
G = 1.254m
R = 0.896m
α_o = 40°

Fig. 1-20   Bendix BN azimuth Rotman lens.

18-4-20412
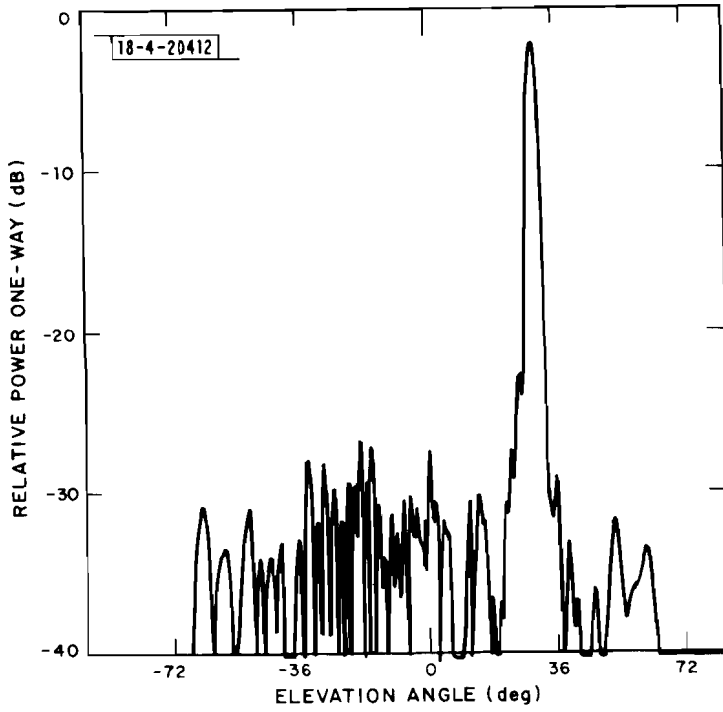
Fig. 1-21a   Static azimuth pattern, BN AZ,
0 degree.

ANTENNA: BN AZ,   AZ ANGLE: 0°,   22 JUL 1977   -4-20395

├←─2 msec

├←─0.2 msec
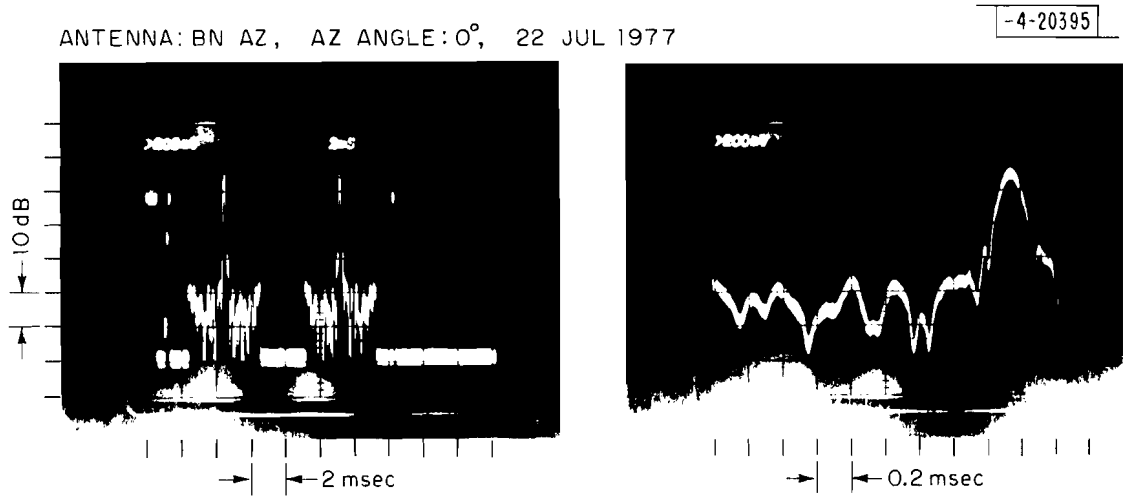
Fig. 1-21b   Dynamic pattern of Bendix basic narrow azimuth array.
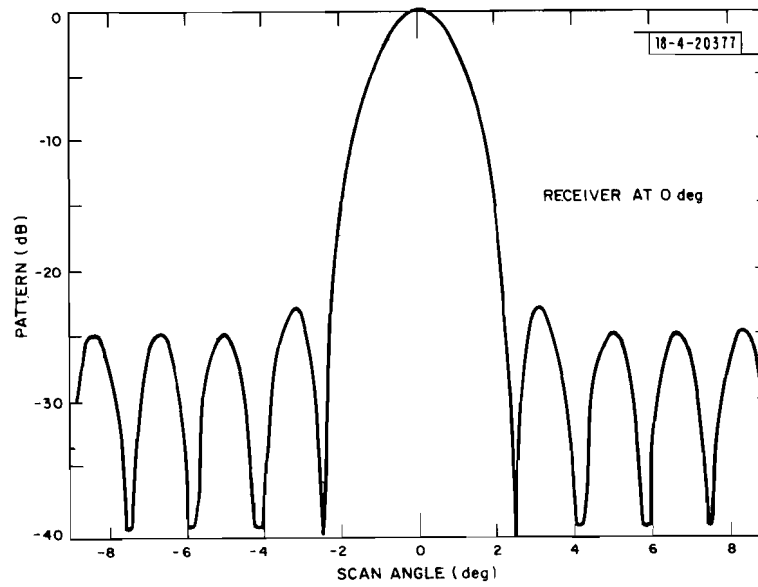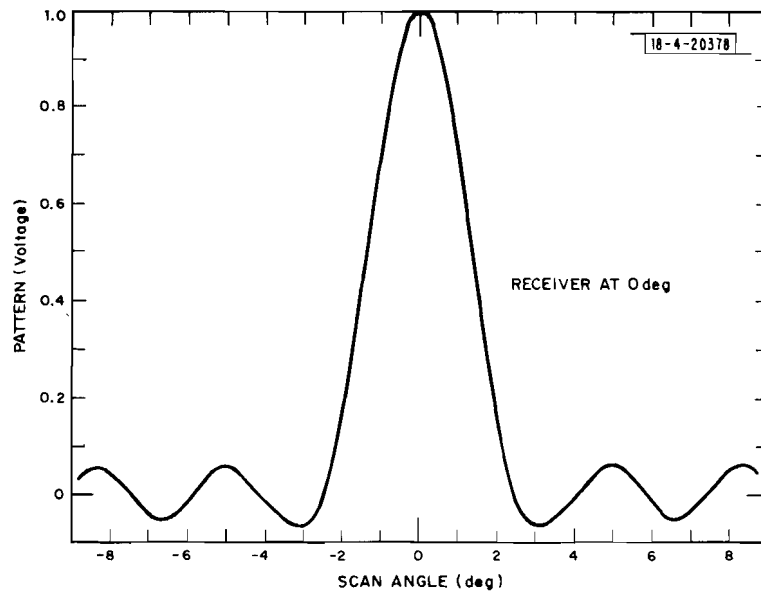
Fig. 1-22 Array factor for model of
Basic Narrow 2° azimuth array.

to illustrate the alternation in sign between successive sidelobes. Fig. 1-23 shows the measured elevation pattern of the elements while Fig. 1-24 shows the model element elevation pattern. The model element azimuth pattern is shown in Fig. 1-13.

One feature of the Basic Narrow system model which was not considered in the preceding system models is the SLS antennas. Fig. 1-25 shows the measured azimuth pattern of the azimuth SLS antenna, while Fig. 1-26 shows the model approximation. The elevation pattern of the azimuth SLS antennas was assumed to be identical to that of the main azimuth array.

5. Small Community 3° Filled Azimuth Array

The Bendix phase III small community (SC) azimuth array is a Rotman lens essentially identical to the BN array except that now M = 46 so as to yield a 3° beamwidth and, the proportional coverage region is ±10. Figs. 1-27 and 1-28 show representative measured static and dynamic patterns. The dynamic data does not show the magnitude of the outer sidelobes;* however, due to the similarity to the BN, it is anticipated that they would be similar to those of the BN. Therefore, the SC model is based on using the theoretical pattern for the mainlobe and first sidelobe with the outer sidelobes represented by a sineusoid of amplitude 0.05 (-26 dB) and sine space period $1/23\pi$. Fig. 1-29 shows the final model array factor pattern. The element pattern (azimuth and elevation planes) is identical to that of the BN.

The SC SLS antennas and their model are identical to those for the BN SLS antenna. However, in addition, the SC has two clearance antennas which radiate signals in the regions from $+10^{\circ}$ to $+40^{\circ}$ and -10° to -40° to furnish "fly left" and "fly right" guidance respectively. Fig. 1-30 shows the measured clearance antenna patterns while Fig. 1-31 shows the model antenna pattern. The elevation pattern of the clearance antenna was assumed identical to that for the SLS antennas.

---

*To measure these, the receiver would have to be positioned outside the SC $\pm 10^{\circ}$ coverage volume.

0°   6°   12°   18°   24°
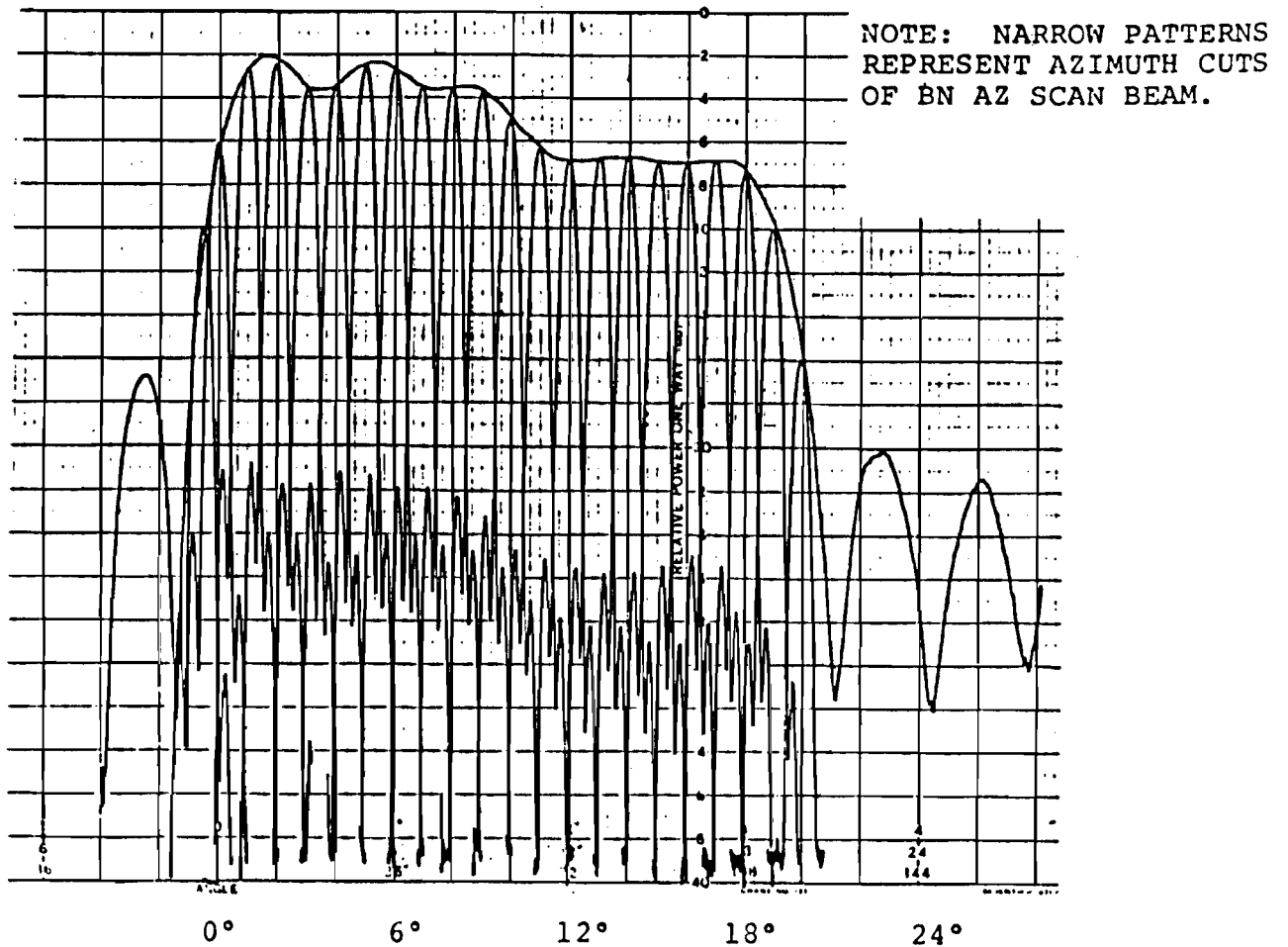
ELEVATION PATTERN OF:

Basic Narrow AZ Scanning Beam
            Right and Left SLS
            Forward Ident
Small Community AZ Scanning Beam
            Right/Left/Rear SLS
            Forward Ident
            Left/Right Clearance
            Beams

Fig. 1-23a Measured elevation pattern of Bendix
Phase III arrays.

1-35
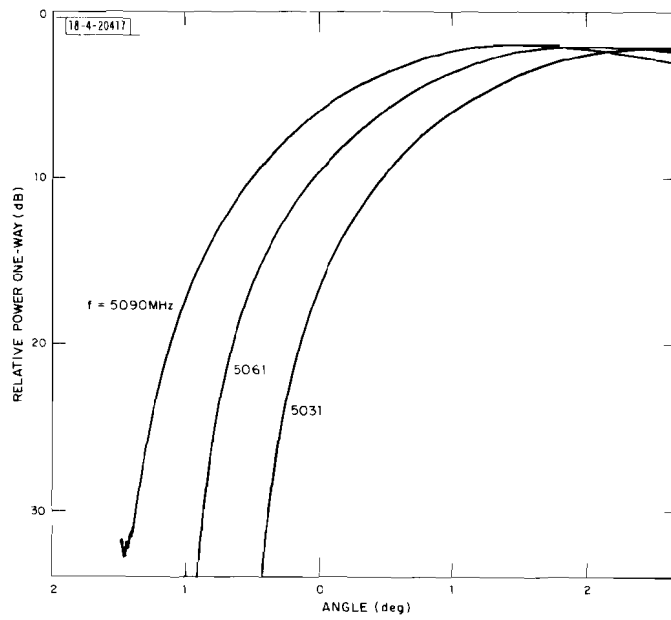
Fig. 1-23b Expanded view of basic narrow
azimuth array elevation pattern.
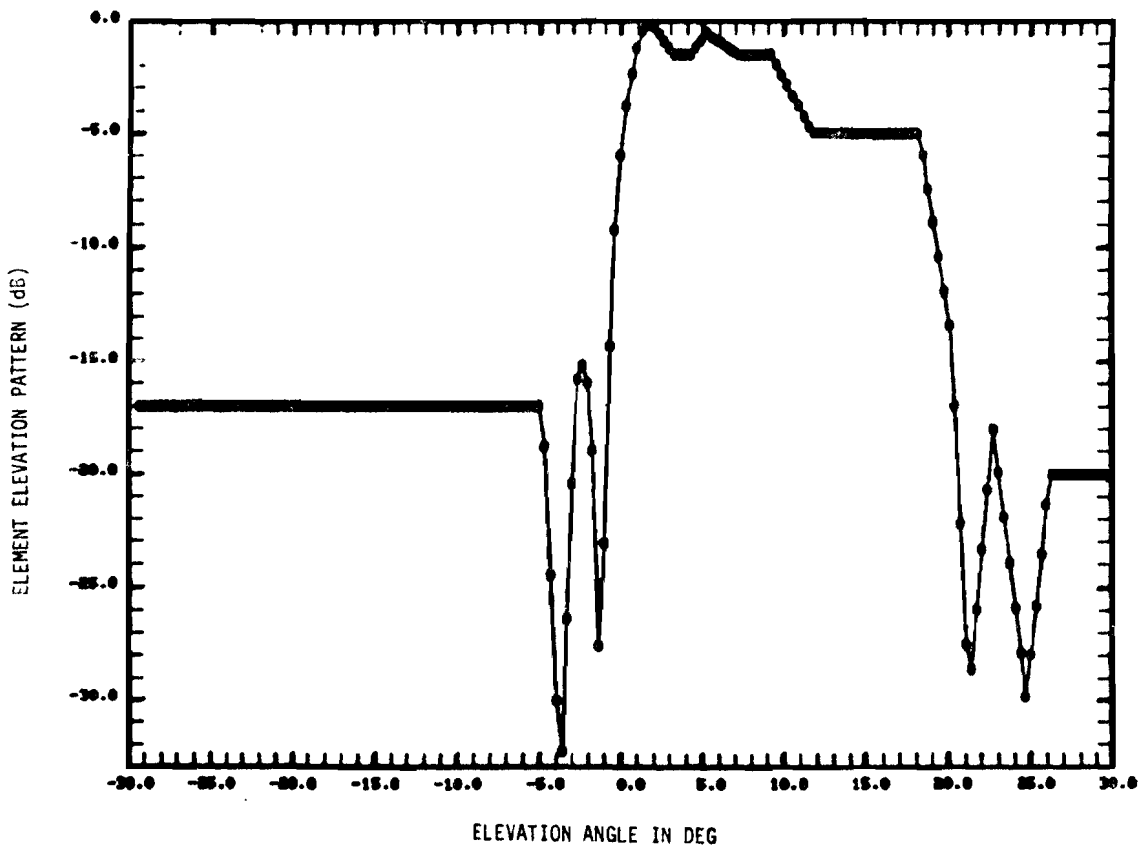
Fig. 1-24 Elevation pattern for basic narrow azimuth array.
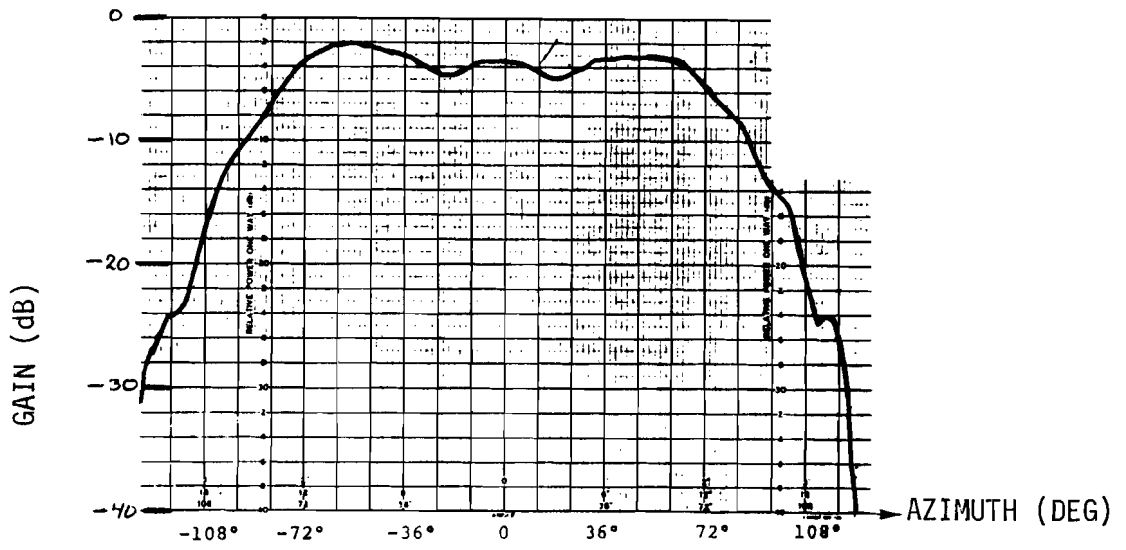
Fig. 1-25 Measured SLS azimuth patterns for Bendix basic narrow and small community arrays.
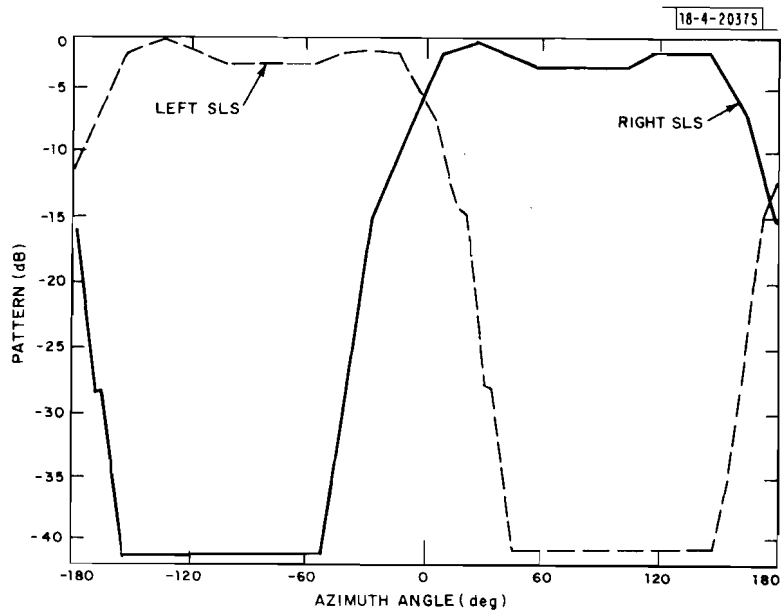
Fig. 1-26 Model of TRSB OCI (SLS) antennas.
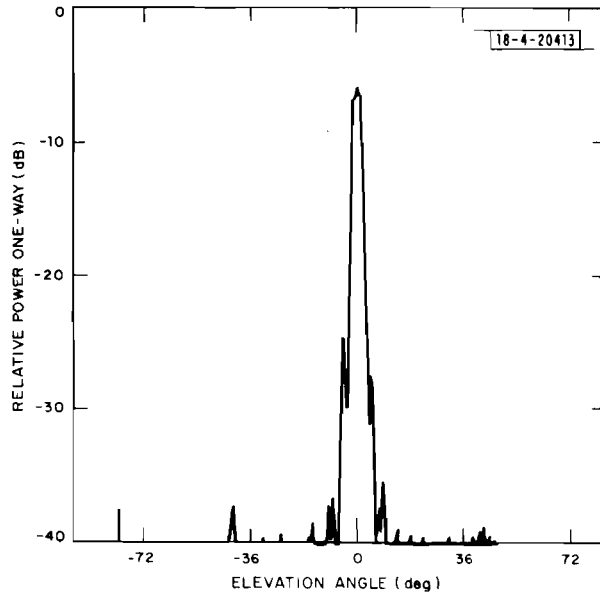
Fig. 1-27 Measured static pattern of Bendix small community azimuth array.

ANTENNA:SC AZ, AZ ANGLE:0°, 22 JUL 1977
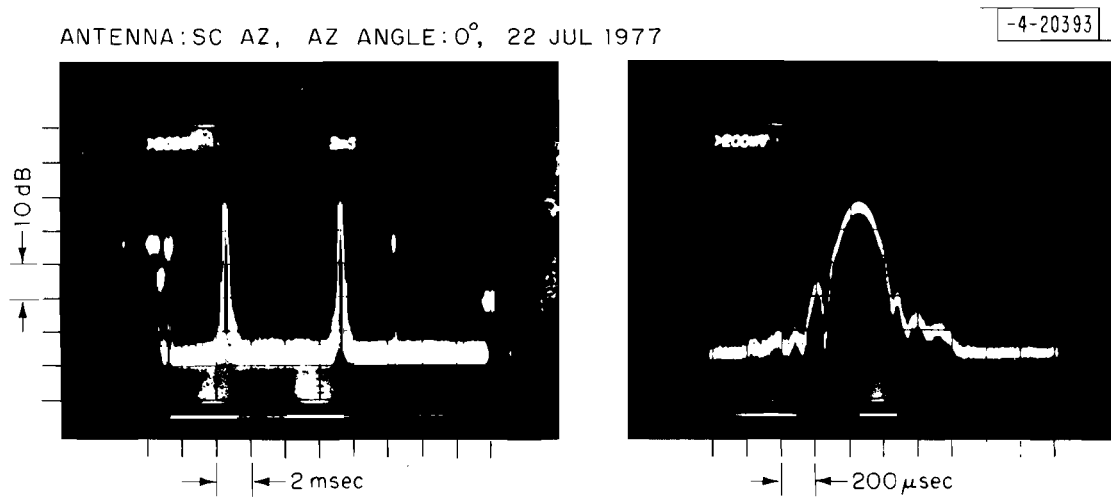
Fig. 1-28 Measured dynamic pattern of Bendix small community azimuth array.
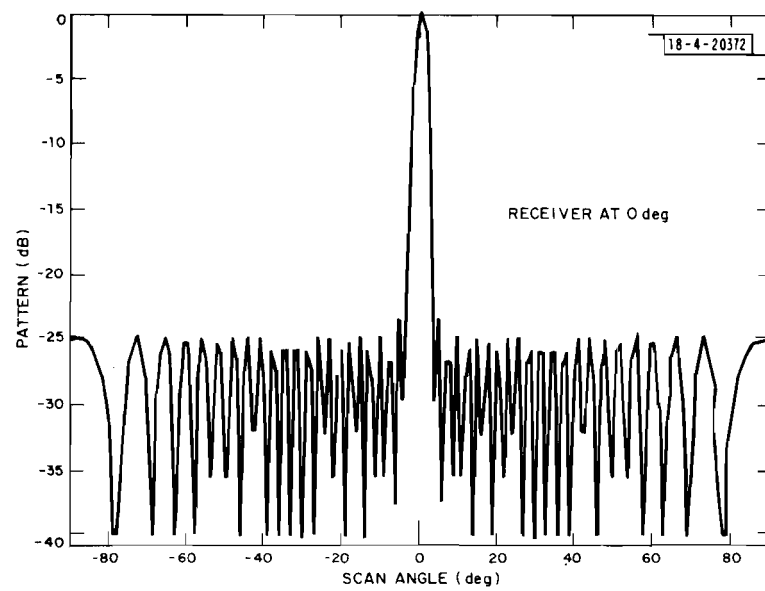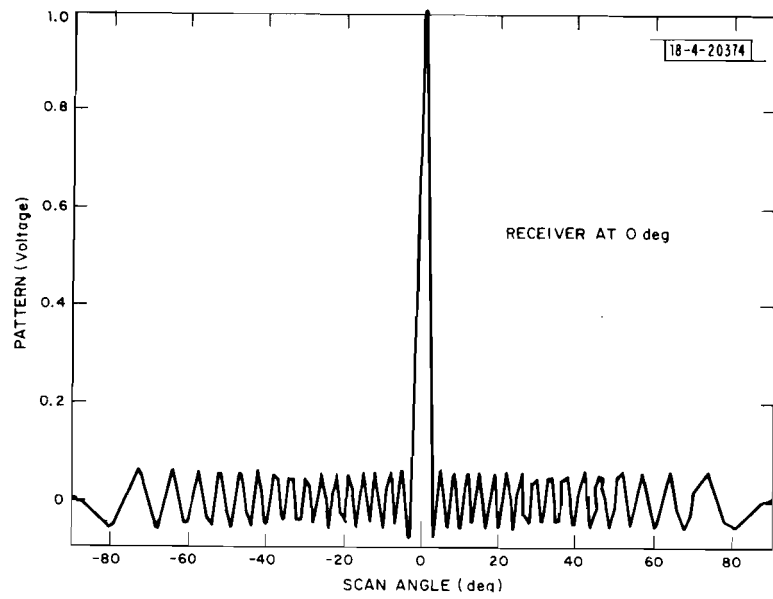
Fig. 1-29 Array factor of small community azimuth model.
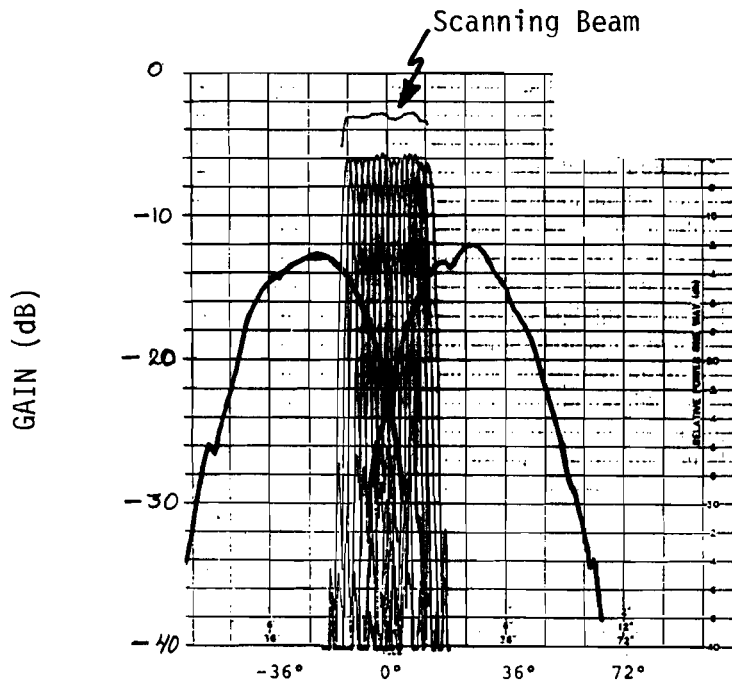
Fig. 1-30 Measured pattern of every 10th beam of small community azimuth with overlay right and left clearance beams.
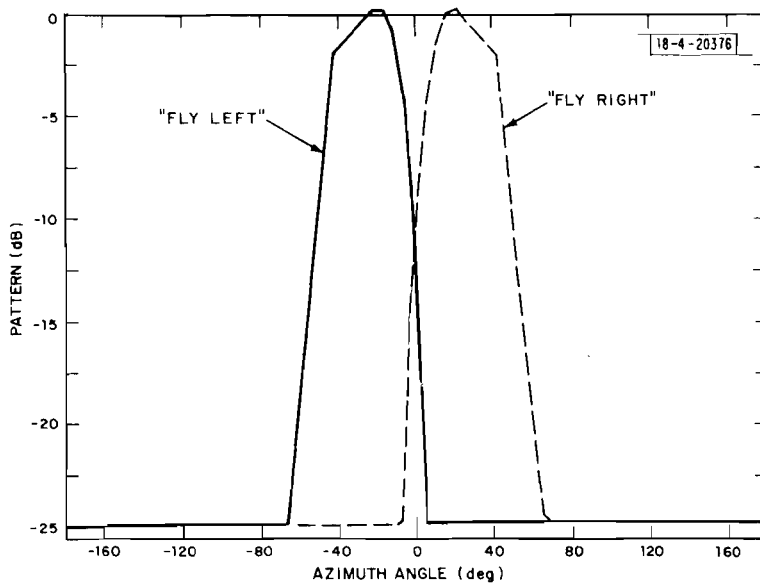
Fig. 1-31 Model of small community clearance patterns.

6.   COMPACT EL 1° Array

The design of the EL array modeled for the AWOP assessment incorporates some additional principles. A description of the array hardware design is given in [65, 96]. For the purpose of analytic description, the array functions can be thought of as follows: the entire array is used to form a roughly rectangular synthetic element pattern of 20° width (the coverage zone) in elevation by means of a sin x/x type aperture excitation applied to element pairs. A phase gradient across the array orients the element pattern into the coverage zone (0°- 20°). A scanned array factor with 1° BW is superimposed on the element pattern by applying linear phase shifts to groups of four adjacent elements. Thus with respect to phase shifters the array is thinned by 75% (24 phase shifters, 96 elements) although the aperture is filled. In hardware this is accomplished by a hybrid coupling network between the phase shifters and the radiating elements which distributes the phase shifts across the array. The resulting pattern consists of the array factor of a uniform array which translates linearly through u-space as the array scans multiplied by the element pattern and an element pair factor.

a.   Synthetic Element Pattern

The element pattern excitation is sketched in Fig. 1-32. Each given value is applied to a pair of adjacent elements. The amplitudes of the "on" pairs decrease by 7.15 dB (0.439) progressing outward from the array center. In addition to the 180° phase reversals, there is a linear phase taper of $2\pi s u_{o}$ rad/element across the array which centers the element pattern at 11.3^{o}; thus u_{o} = sin 11.3^{o} = 0.19515. The dipole spacing is s = 0.6. Let $b_{n}e^{j\delta}n$ represent the element pattern excitation. Then the element pattern formula can be developed as follows:
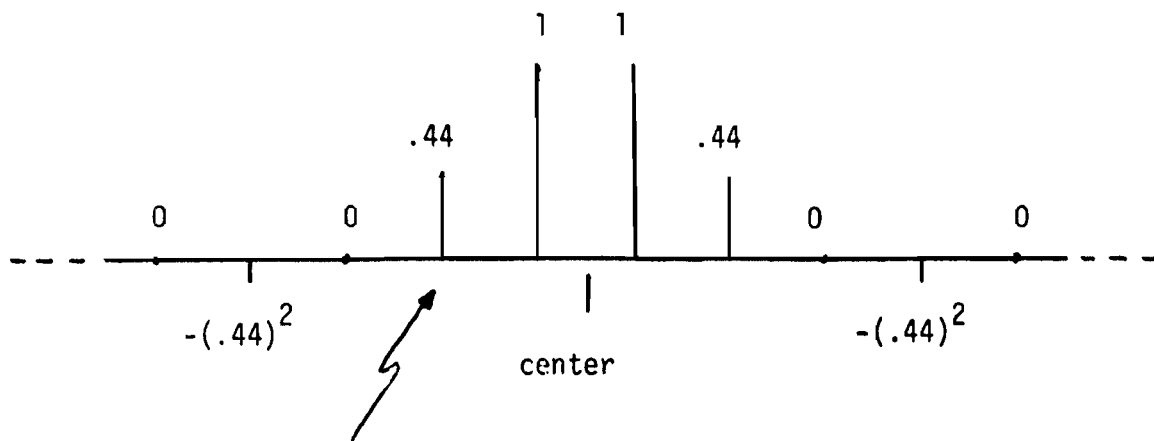
$$E(u) = \sum_{n=1}^{96} b_{n}e^{j(2\pi nsu + \delta_{n})}$$

Fig. 1-32 COMPACT EL array synthetic element pattern excitation.

$$= \left(\underbrace{\sum_{\text{odd } n}}_{n=2\ell-1} + \underbrace{\sum_{\text{even } n}}_{n=2\ell} \right)_{,} b_n e^{j(2\pi nsu + \delta_n)}$$

$$= \sum_{\ell=1}^{48} b_{2\ell-1} e^{j[2\pi(2\ell-1)\,su + \delta_{2\ell-1}]}$$

$$+ \sum_{\ell=1}^{48} b_{2\ell} e^{j[2\pi(2\ell)\,su + \delta_{2\ell}]} \tag{1-21}$$

Because elements are illuminated pairwise, the coefficients satisfy

$$b_{2\ell-1} = b_{2\ell} \stackrel{\Delta}{=} a_\ell : \quad 1 \le \ell \le 48 \tag{1-22}$$

The phase angles include both the contributions to the synthetic element pattern $\{\phi_n\}$ and the pointing gradient:

$$\delta_{2\ell-1} \stackrel{\Delta}{=} \phi_\ell - 4\pi\ell\,su_0 \tag{1-23}$$

$$\delta_\ell \stackrel{\Delta}{=} \phi_\ell - 2\pi(2\ell+1)\,su_0 \tag{1-24}$$

which allows (1-21) to be written as

$$E(u) = \underbrace{\cos\pi s(u-u_0)}_{\text{pair factor}} \sum_{\ell=1}^{48} a_\ell \underbrace{e^{j[4\pi\ell(u-u_0)s + \phi_\ell]}}_{\text{synthetic element pattern}} \tag{1-25}$$

The above product is shown in Fig. 1-33 along with the element pattern as computed by the designers, Hazeltine Corp. Figure 1-34 is a close-up showing the pattern near the horizon. The null is at -1.5° and at 0° the

COVERAGE SECTOR   GROUND

0 dB

−5 dB

−10 dB

−15 dB

−20 dB

−25 dB

CALCULATED
MEASURED

20°   10°   0°   −10°   −20°
ELEVATION ANGLE

(a) Hazeltine calculation [96]

PATTERN(DB)

elevation angle (deg)
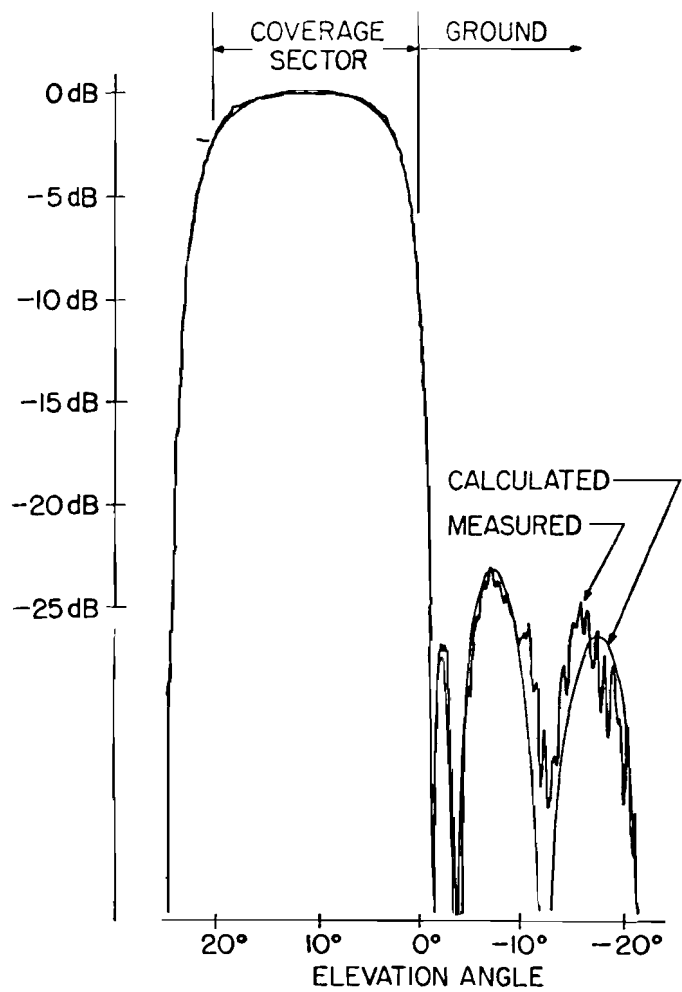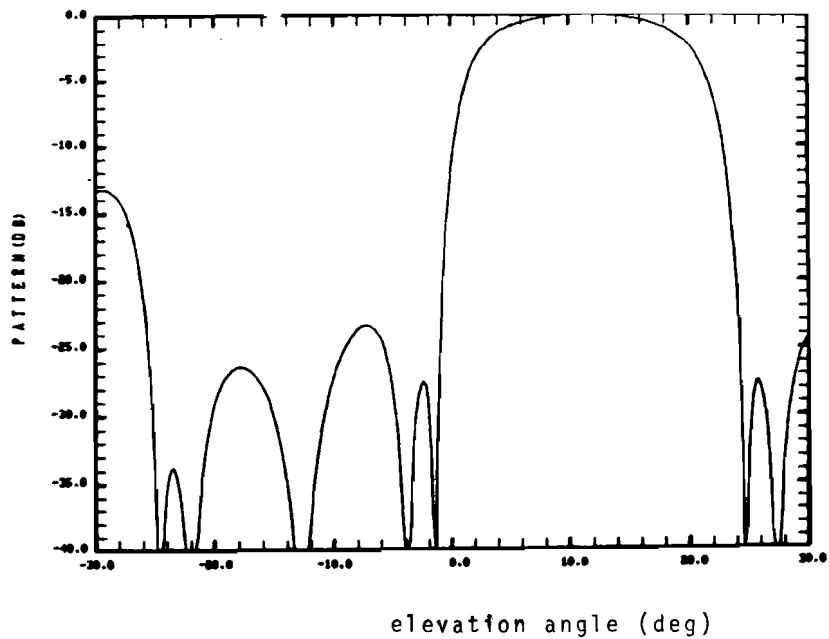
(b) Lincoln calculation

Fig. 1-33 COMPACT EL antenna synthetic element pattern.
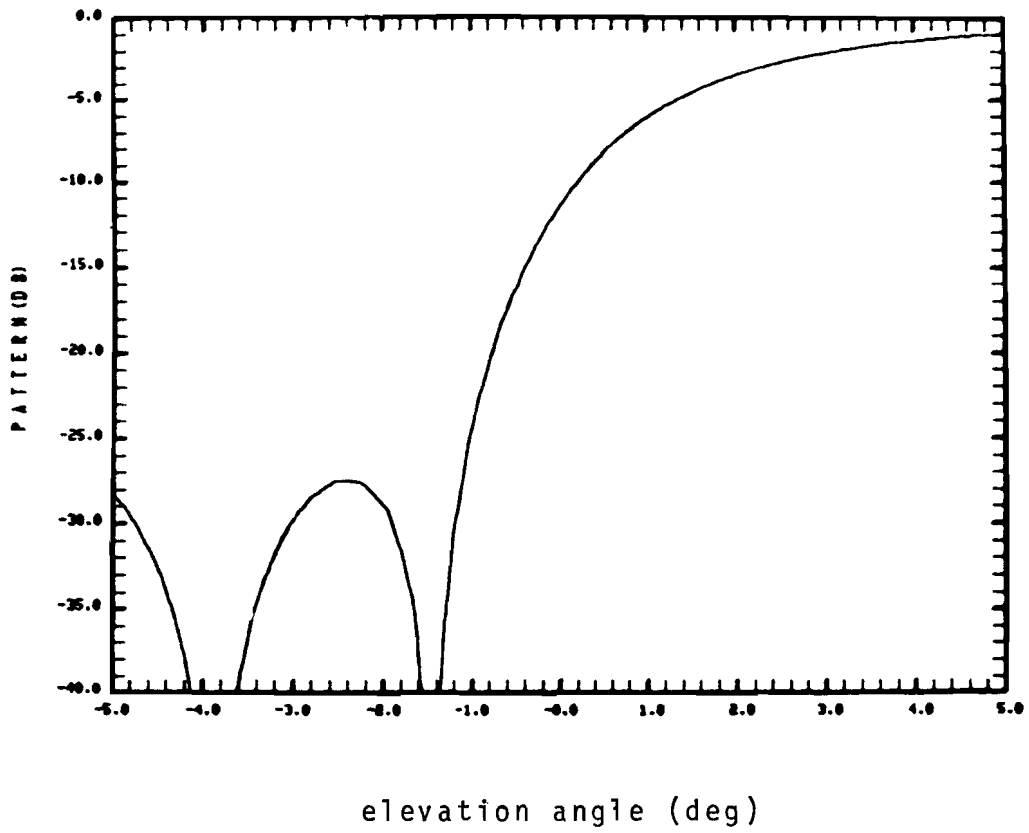
Fig. 1-34 COMPACT EL antenna synthetic element pattern near 0° elevation.

pattern is about -11 dB relative to the peak at the center of coverage.

7.   Full Array Pattern

As discussed earlier, the full pattern is the product of the element pattern and an array factor, $A(\cdot)$:

$$P(u_R, u_B) = E(u_R) \; A(u_B - u_R) \tag{1-26}$$

where $A(\cdot)$ is the pattern of a 24 element uniformly illuminated array with effective spacing $4s = 2.4$, i.e.,

$$A(u) = \frac{\sin 96 \, \pi s u}{24 \sin 4 \pi s u} \tag{1-27}$$

The array factor is shown in Fig. 1-35.

The composite pattern is shown in Fig. 1-36 along with comparable Hazeltine data. The boresight angle is 2^O in each case. The curves differ at some points, primarily high elevation angles, for two reasons: (i) the Hazeltine data incorporates only 19, not 24, phase shifters, and (ii) the high sidelobes which occur every 8° on the positive side of the mainlobe in the Hazeltine pattern do not show up in the simulation computed according to eq. (1-27). These lobes are primarily due to phase shifter quantization (4 bits). It has been decided not to replicate these in the simulation since elevation multipath with $+8^O$ or greater separation angle in elevation is unlikely to occur; certainly it did not in the ICAO scenarios.

The measured azimuth pattern of the Bendix elevation array is shown in Fig. 1-37. This pattern is approximated by linear interpolation between various points taken from Fig. 1-35 with the result being the pattern shown in Fig. 1-38.
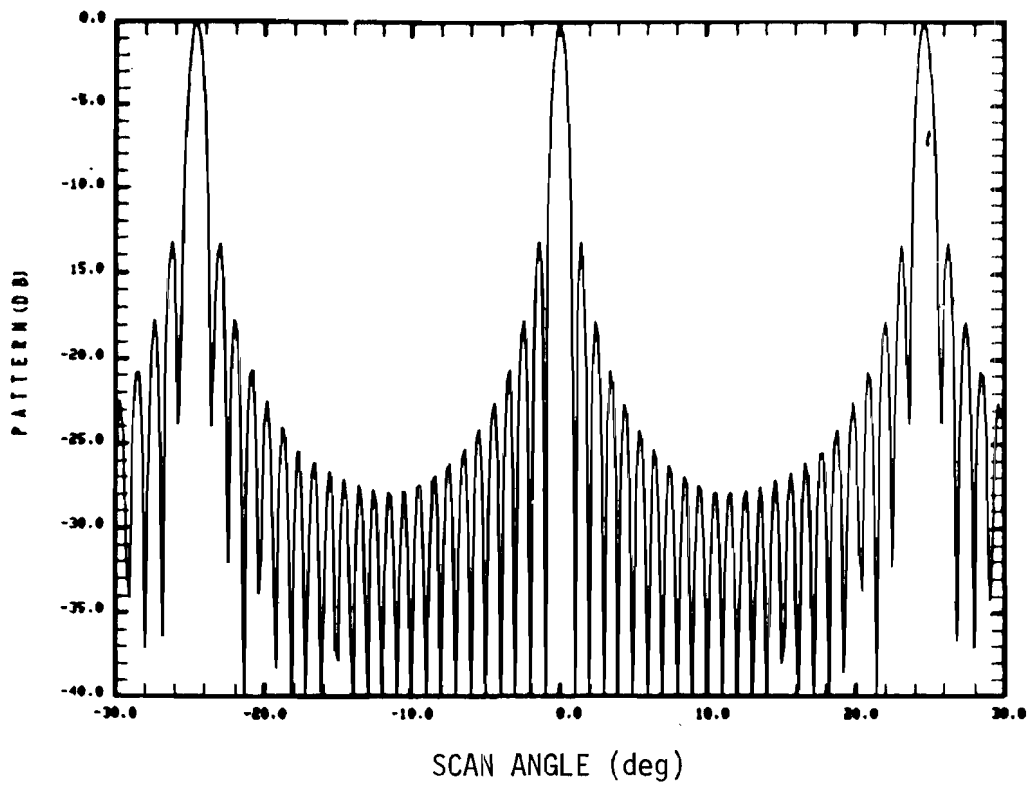
Fig. 1-35   COMPACT EL antenna array factor.
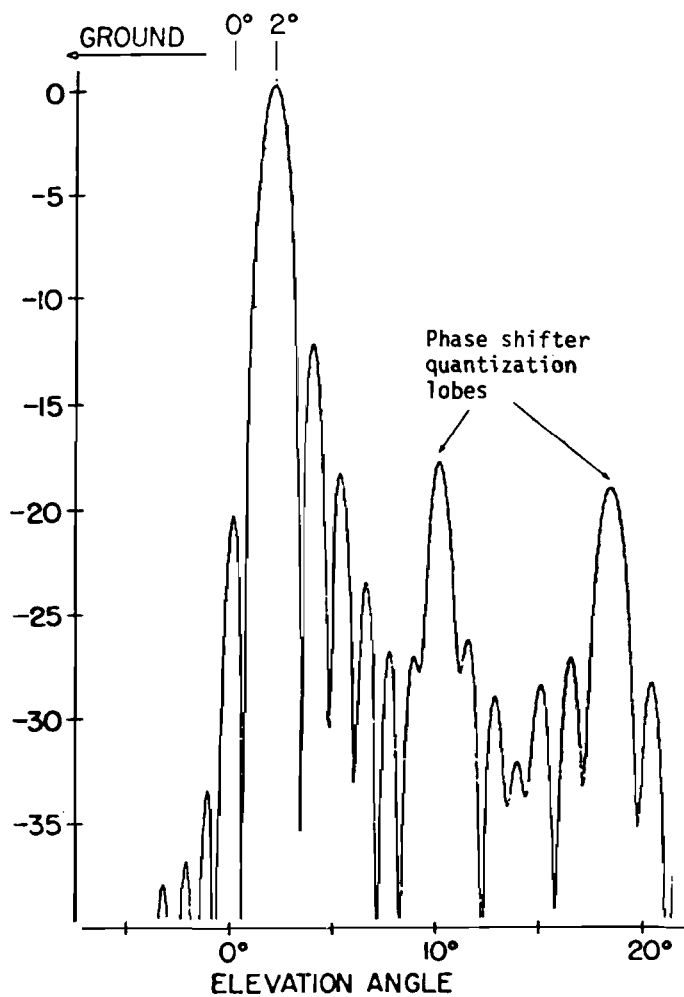
(a) Hazeltine calculation
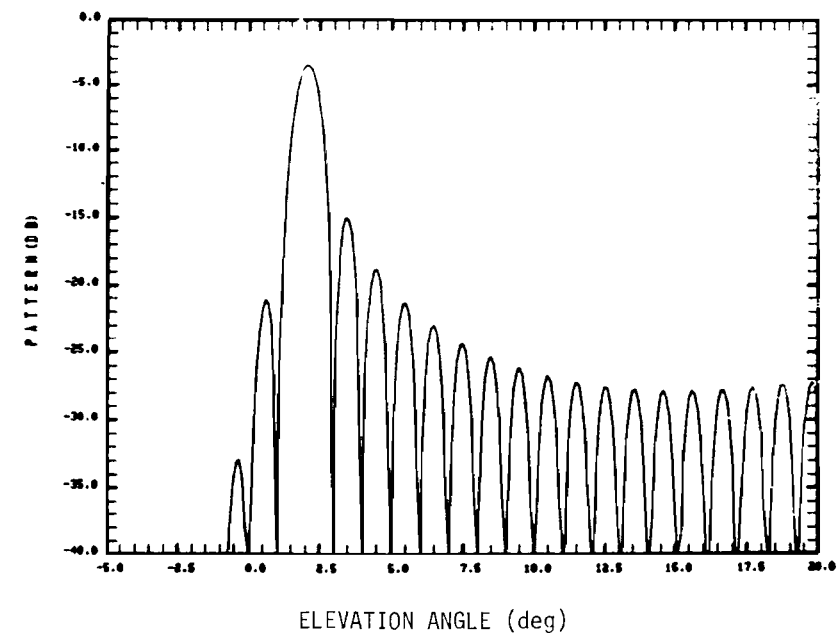
(b) Lincoln calculation

Fig. 1-36 COMPACT EL antenna pattern: 2° boresight.
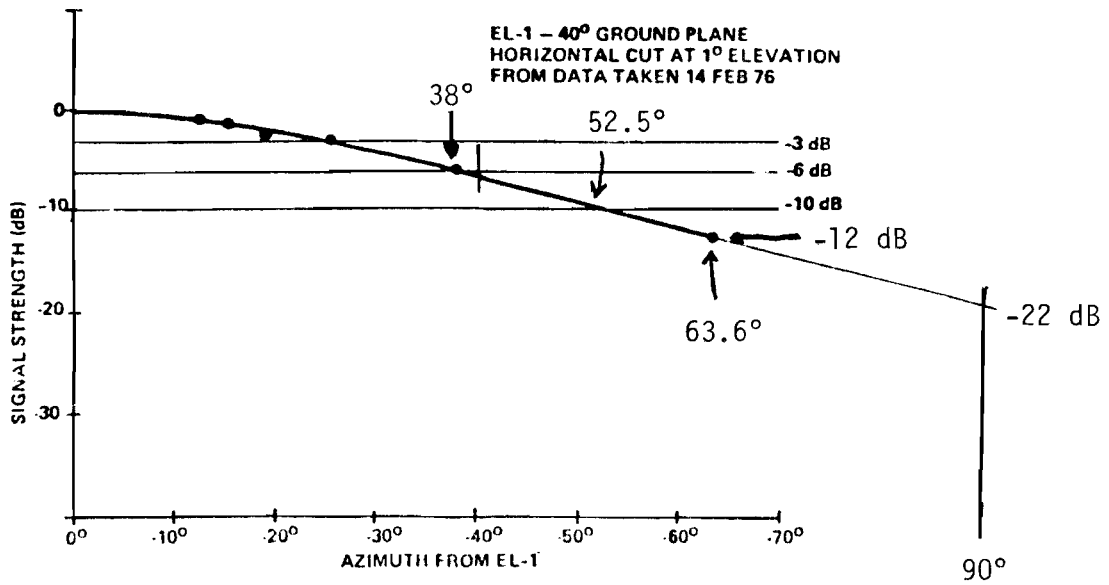
Fig. 1-37   Elevation antenna pattern, horizontal cut
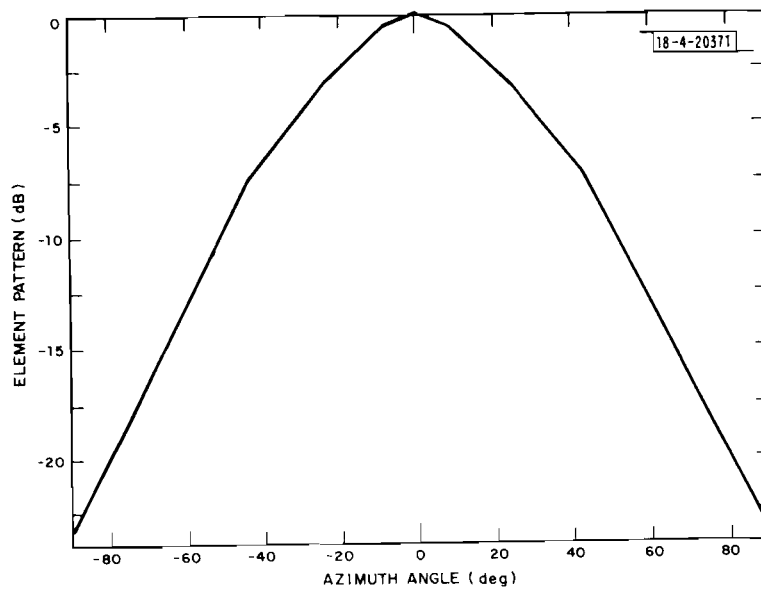
Fig. 1-38   Model for azimuth pattern of elevation array.

8. Testbed 1° Filled EL Array

The bulk of the US TRSB elevation field tests were accomplisned using a Bendix fully filled phased array. This array has 94 uniformly spaced elements with s = 0.75 and a Taylor weighted distribution. The close similarity of this array to the azimuth 1° filled array permitted a virtually identical modeling approach whereby

a) based on experimental dynamic and static patterns, the theoretical array factor as computed from Eq. (1-9) is used to represent the main lobe and first few sidelobes while the outer sidelobes are represented by a sinusoid of amplitude 0.05 and (sine space) period 1/64π.

b) the element pattern model is taken from measured patterns

Figures 1-39 and 1-40 show static and dynamic measured patterns, while Fig. 1-41 shows the model array factor. The model element pattern in the azimuth plane is as shown in Fig. 1-38 and flat in the elevation plane.

9. Basic Narrow 1.5° EL Array.

The Bendix Phase III Basic Narrow (BN) 1.5° beamwidth elevation antenna is a Rotman lens array which is virtually identical to the previously described BN azimuth array except for a larger spacing between elements (s = 0.75). Thus, the modeling approach was essentially identical:

a) based on the measured static patterns (Fig. 1-42) and dynamic scan envelopes (Fig. 1-43), the array factor was modeled by the theoretical array factor [Eq. (1-9)] for the mainlobe and first two sidelobes, and a sinusoid of amplitude 0.05 and (sine space period 1/50π.

b) the element pattern model consists of a piecewise linear fit to the measured array pattern as shown in Fig. 1-44.

Figure 1-45 shows the resulting model array factor. The elements are assumed to be omni-directional in the elevation plane. Figure 1-46 shows the BN upper SLS measured pattern while Fig. 1-47 shows the model SLS pattern.

Elevation Angle (Deg.)

Static
Patterns

RELATIVE POWER ONE WAY (←dB)
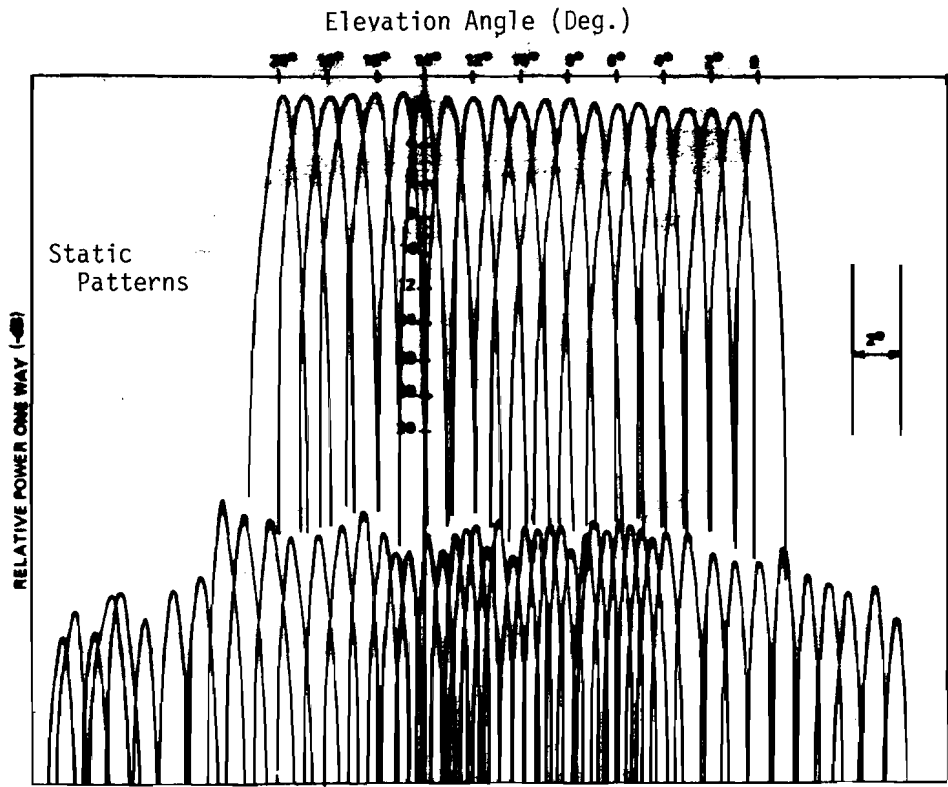
Fig. 1-39 Measured elevation pattern and peak elevation gain
as a function of elevation angle.

5 dB

ENVELOPE (dB)

FUNCTION I-D

"TO" scan

"FRO" scan

time →
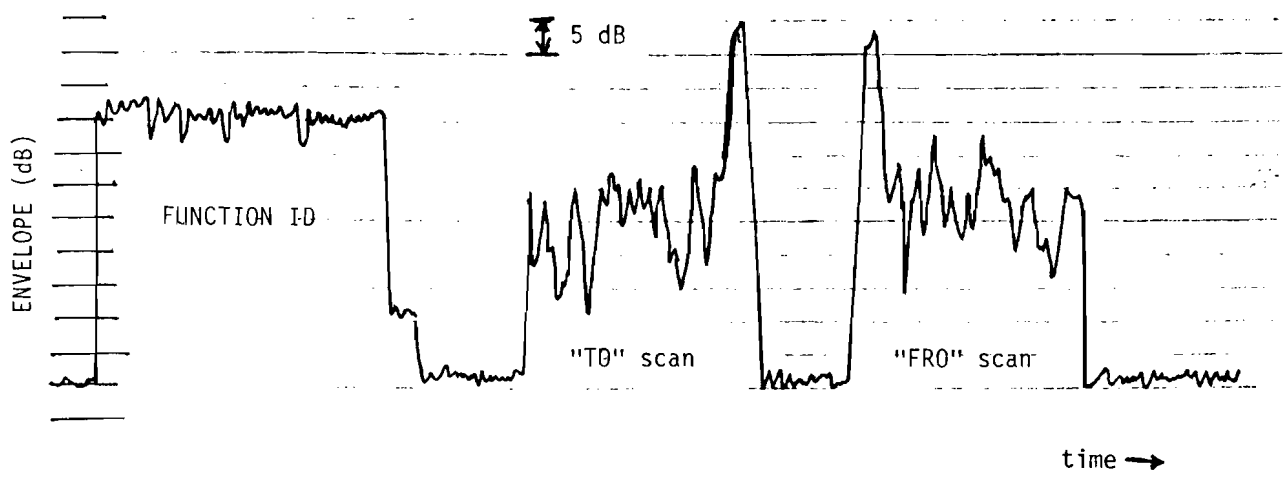
Fig. 1-40 TRSB testbed elevation array envelope.
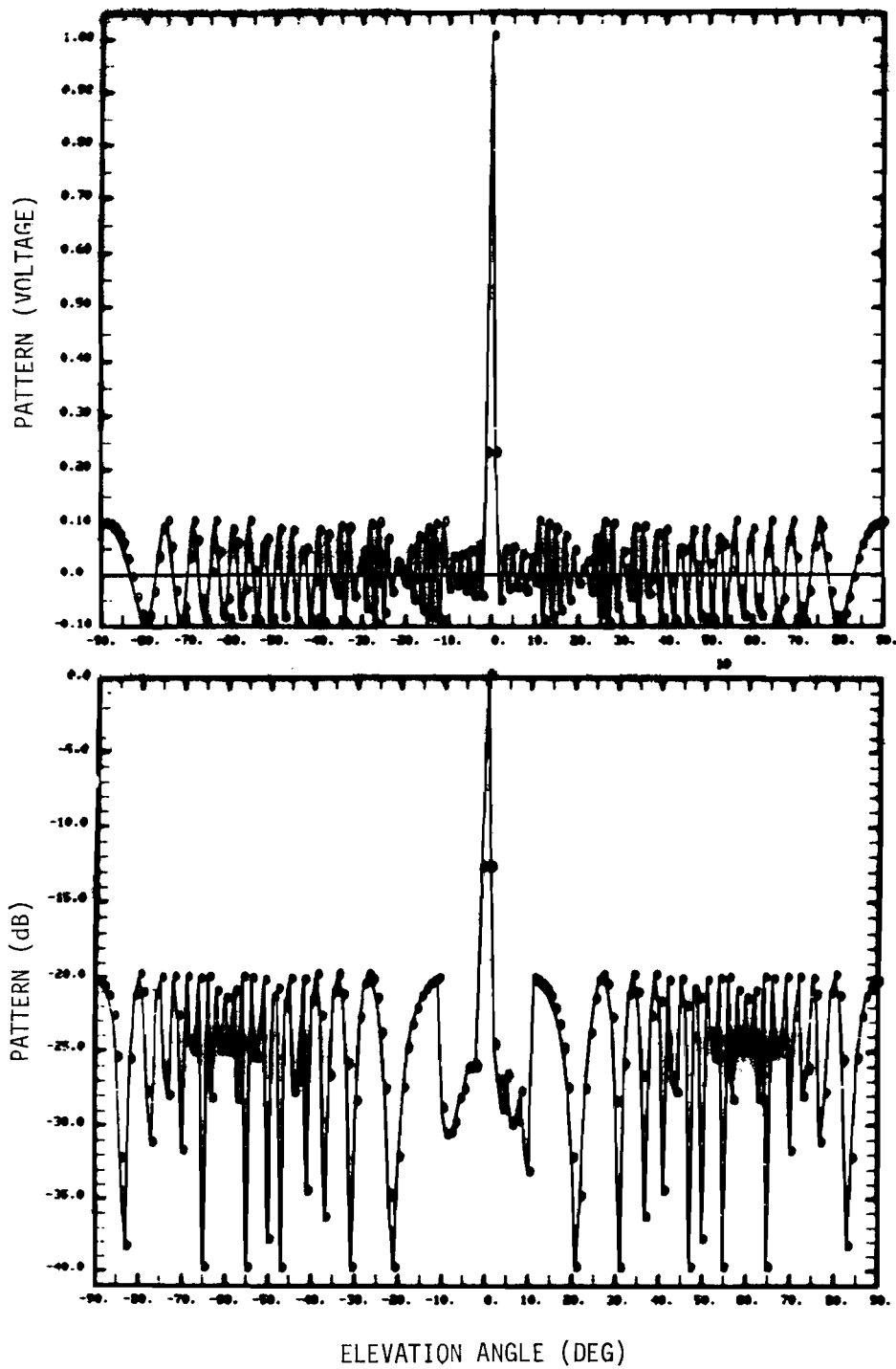
Fig. 1-41   Model array factor for testbed elevation array.
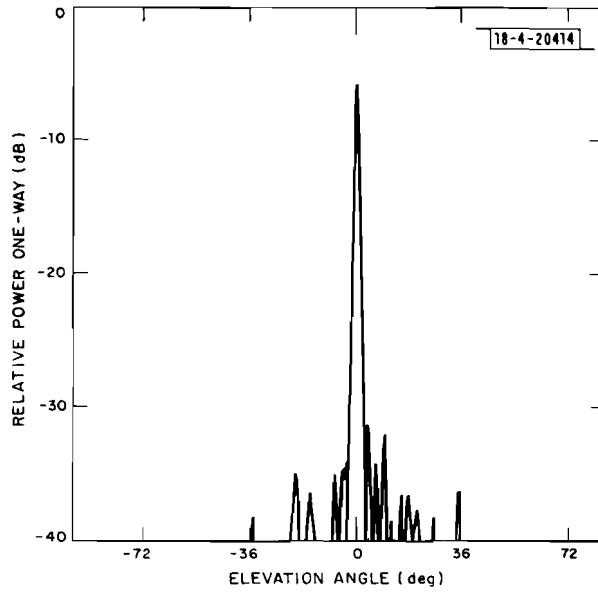
Fig. 1-42 Measured static pattern of Bendix basic
narrow elevation array.

ANTENNA:BN EL, EL ANGLE:30°, 22 JUL 1977 |-4-20392|
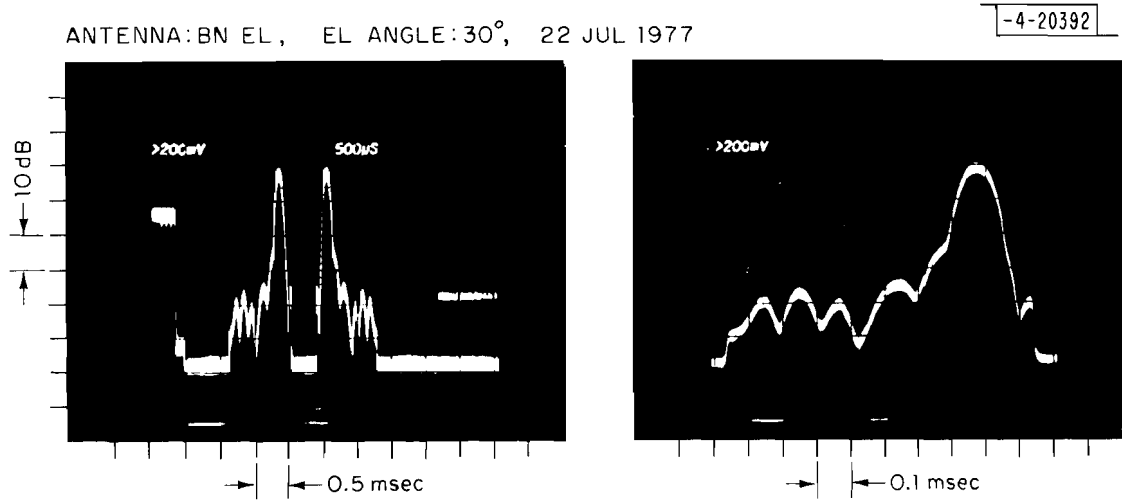
Fig. 1-43 Measured dynamic pattern of Bendix basic
narrow elevation array.
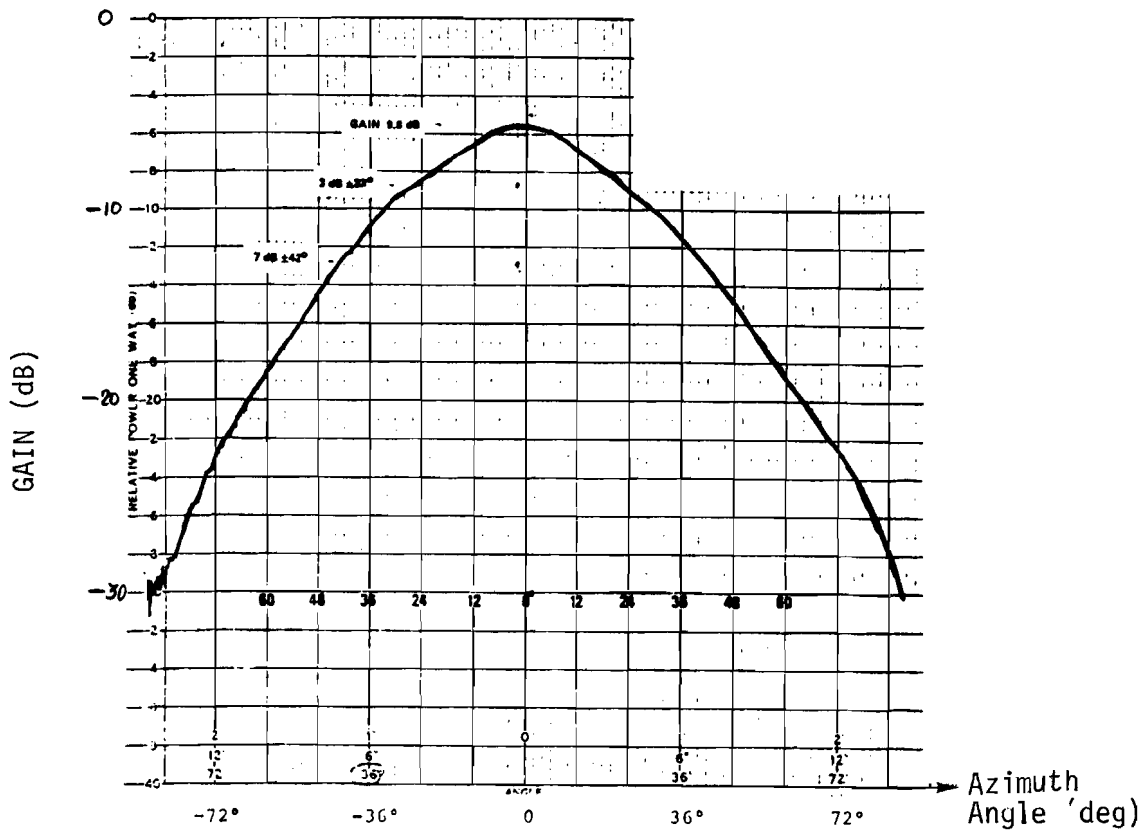
Fig. 1-44a Measured pattern of Bendix Phase III elevation arrays.
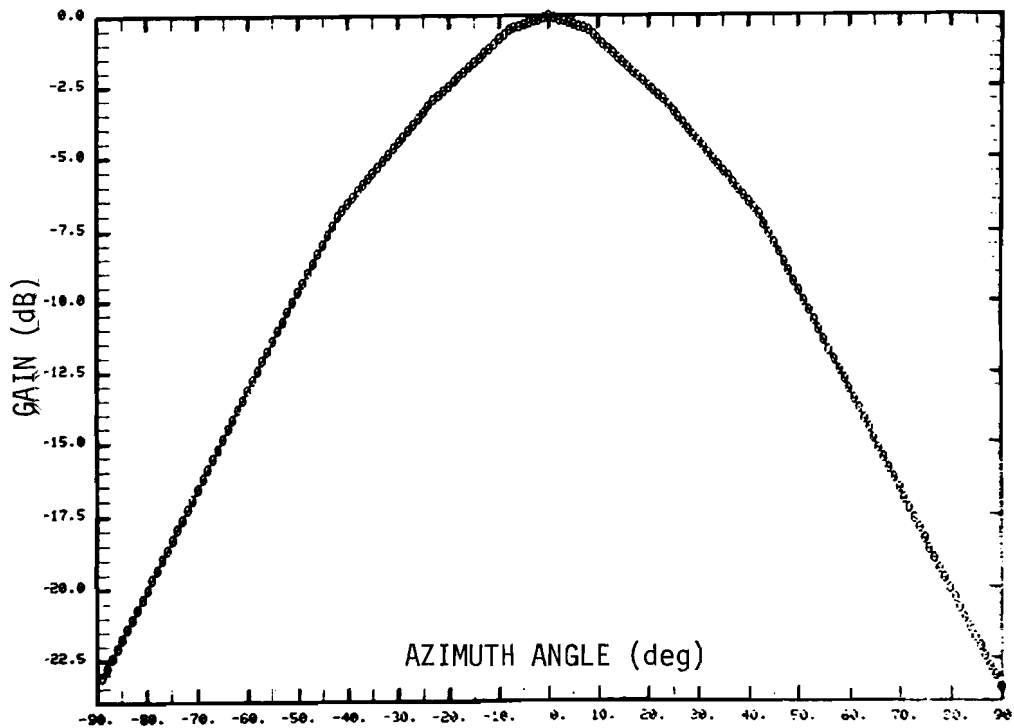
Fig. 1-44b Model pattern for phase III elevation arrays.

1-54
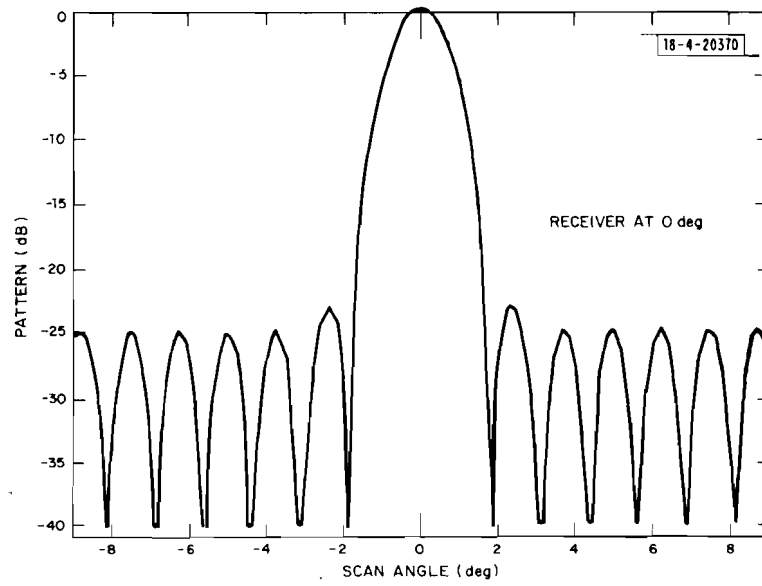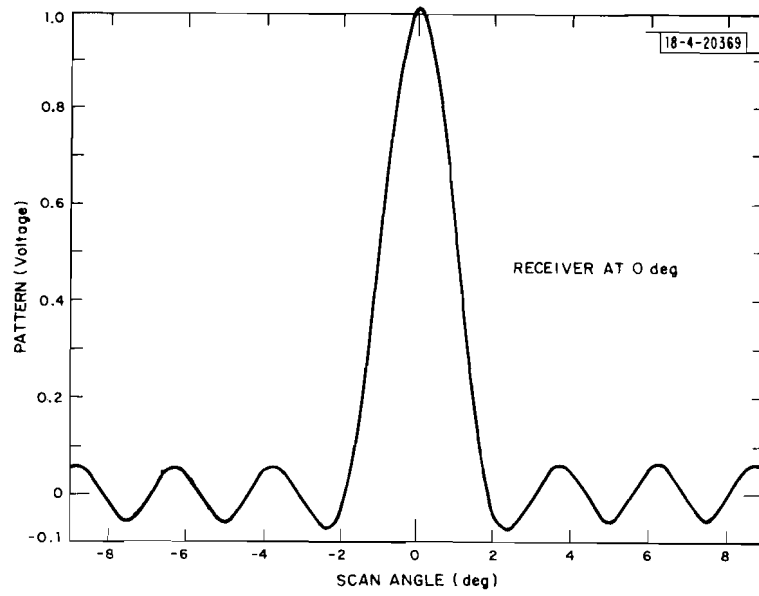
Fig. 1-45 Array factor of basic narrow elevation array model.
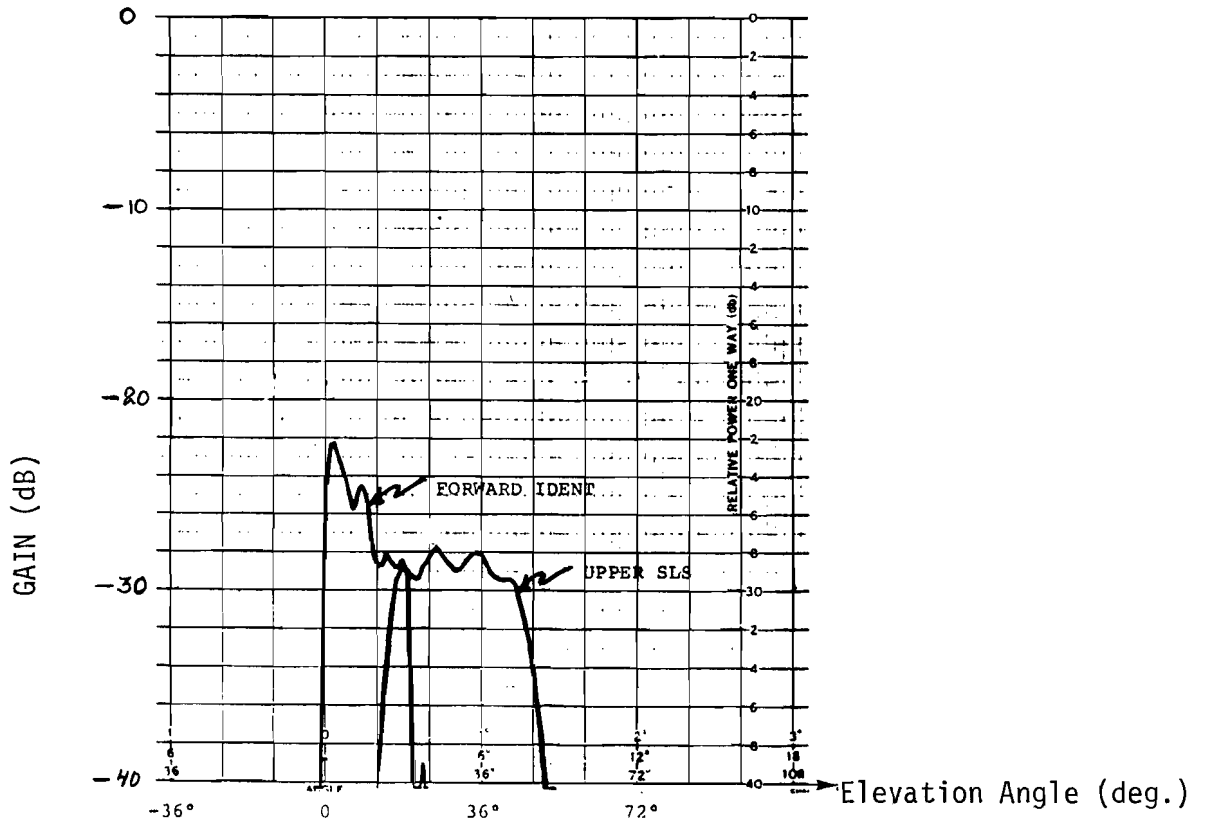
Fig. 1-46 Measured elevation patterns of ident and upper SLS
antennas for Bendix basic narrow and small community elevation arrays.
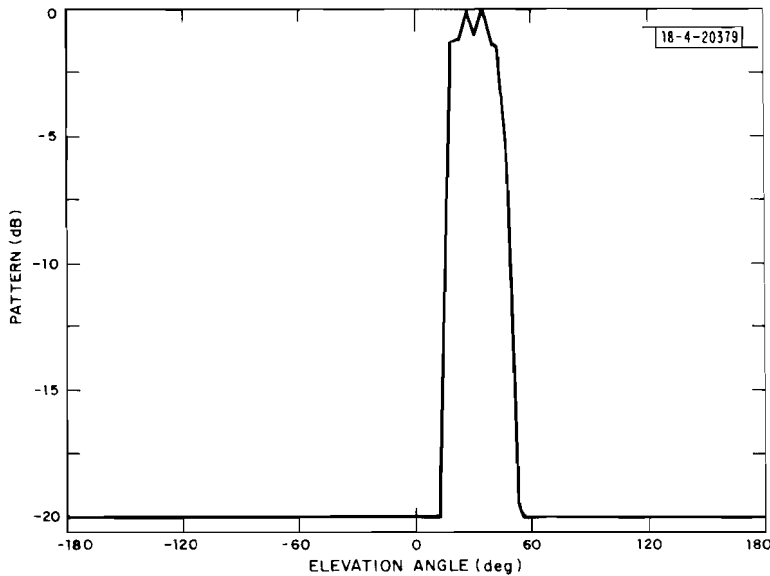
Fig. 1-47 Elevation pattern of elevation SLS model for basic
narrow and small community elevation arrays.

9. Small Community 2° EL Array

The Bendix phase III small community (SC) 2.0° elevation antenna is a Rotman lens array which differs from the BN EL array only by virtue of the smaller number of elements (M = 46). The modeling approach and resulting model was identical to that of the BN array except that the (sinespace) frequency of the outer sidelobes is $1/27\pi$. Figures 1-48 and 1-49 show measured static and dynamic patterns while Fig. 1-50 shows the model array factor. The element pattern of this array is identical to that of the BN EL array.

10. COMPACT 0.5° Flare Antenna

The modeled TRSB flare (EL 2) antenna implementation is a COMPACT array similar to that described earlier except that there are twice as many elements. This yields the same element pattern as described earlier, and an array factor which is essentially a 2:1 scaled version of Fig. 1-35. The other difference between the flare and EL antennas lies in the azimuth pattern of the elements. Figure 1-51a shows the proposed azimuth pattern (based on a Ku band flare antenna built by Bendix) while Fig. 1-51b shows the model pattern.

11. Calspan Bench Test Pattern

For their hybrid multipath tests, Calspan developed an antenna pattern designed to exhibit worst case sidelobes (-20 dB). The pattern was derived from a cosine aperture excitation pattern

$$P(\theta) = \frac{\pi^2}{4} \frac{\cos 69\pi \sin\theta}{\frac{\pi^2}{4} - (69\pi \sin\theta)^2} \qquad (1-28)$$

whose first two sidelobes are raised to -20 dB level by a multiplicative constant. The unmodified sidelobes are -23 and -31 dB, respectively. Only the first two sidelobes are retained in the model. Figure 1-52 shows the Lincoln Lab simulation and the Calspan pattern.

In their simulation, Calspan used the sidelobes only on the multipath beam and not on the direct. For the Lincoln simulations, the pattern as shown is used for all components. This descrepancy should cause no appreciable difference in the results since the direct sidelobes will not influence the dwell gate crossings.

0

RELATIVE POWER ONE-WAY (dB)

-10

-20

-30

-40

18-4-20415

-72   -36   0   36   72

ELEVATION ANGLE (deg)
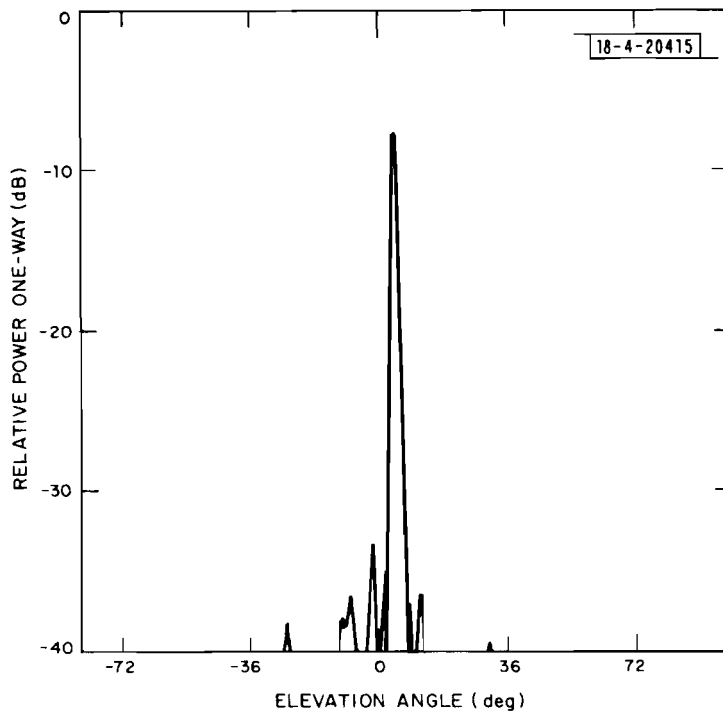
Fig. 1-48   Measured Bendix small community
elevation array static pattern.

-4-20394

ANTENNA: SC EL,   EL ANGLE: 2.5°,   22 JUL 1977

>200mV   500µS

10 dB

|← 500 µsec

>200mV

|← 100 µsec
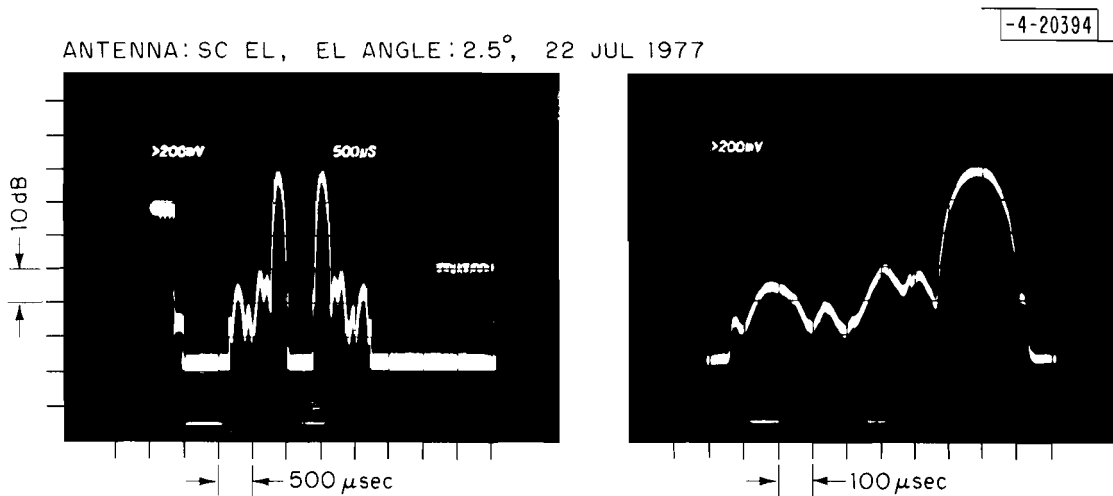
Fig. 1-49   Measured Bendix small community
elevation array dynamic patterns.

1-58
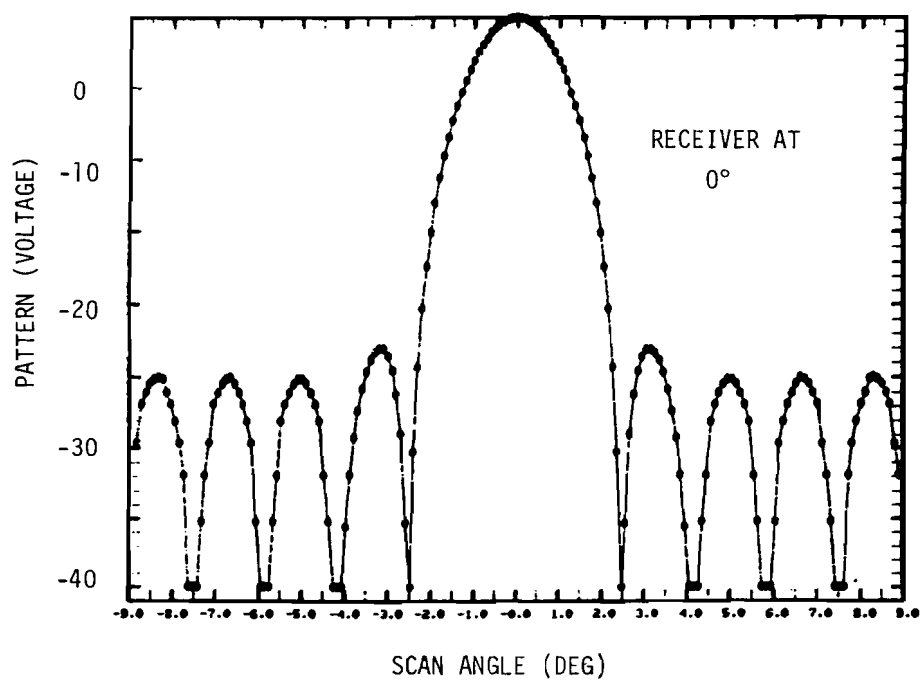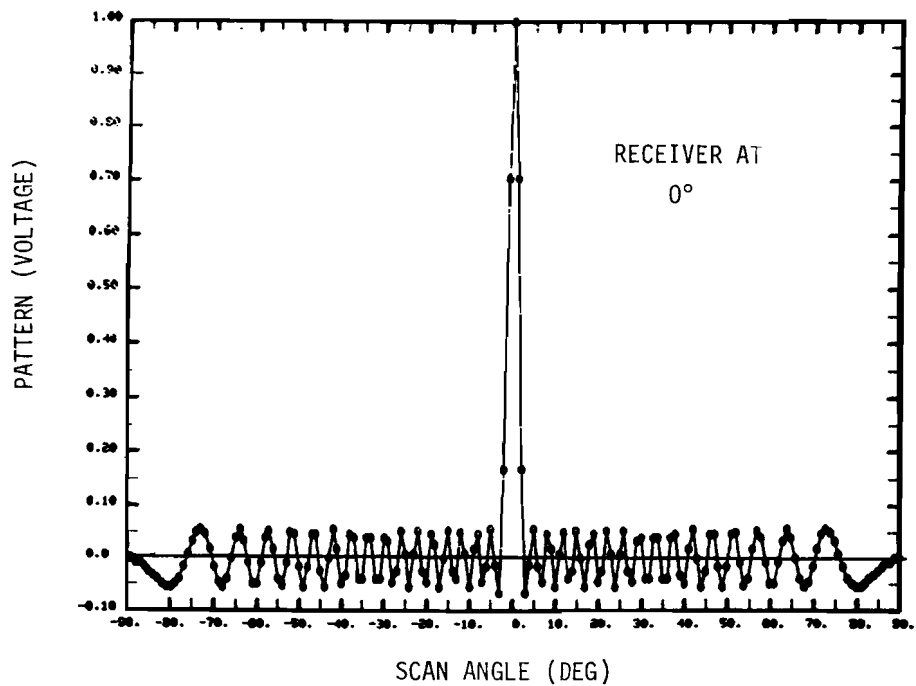
Fig. 1-50 Array factor model for small community elevation array.
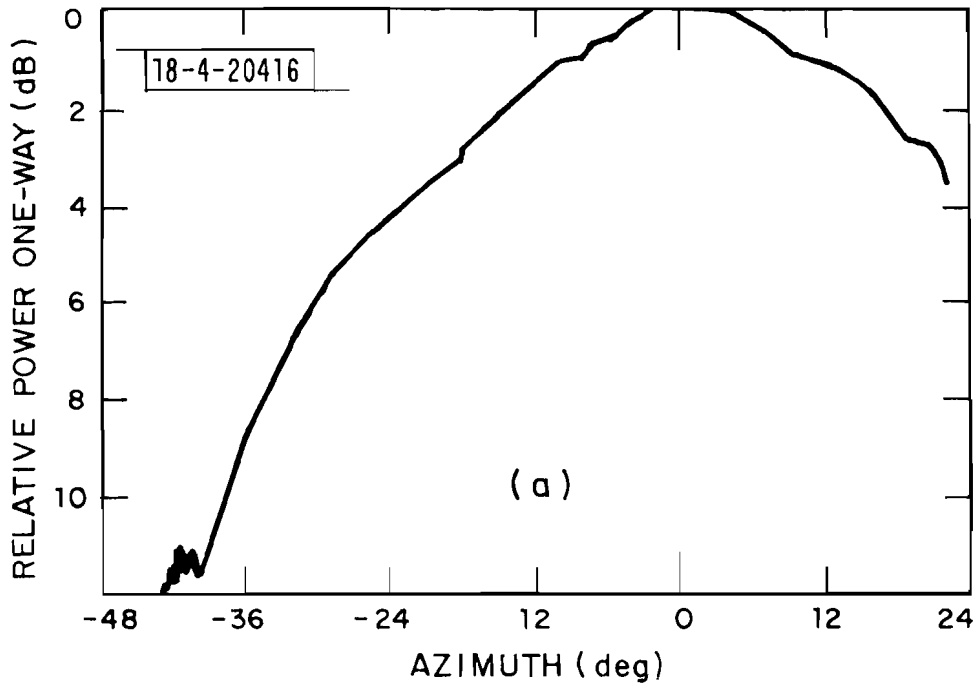
Fig. 1-51a   Measured flare antenna azimuth pattern.
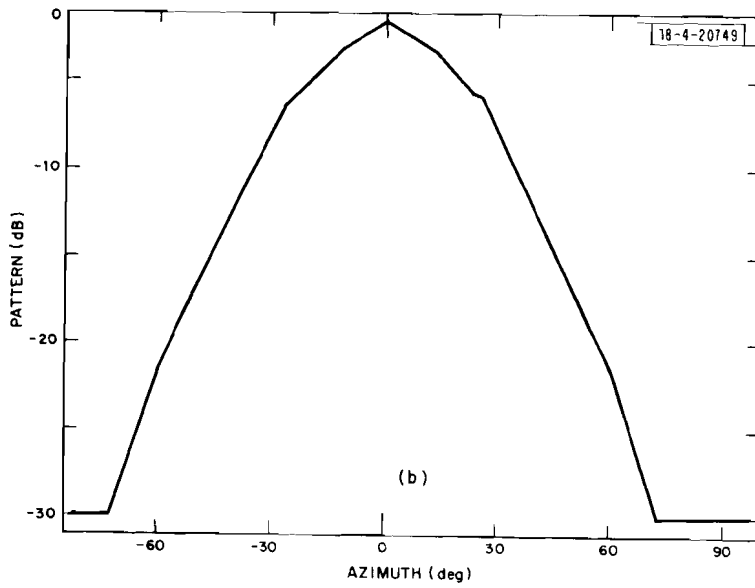
Fig. 1-51b   Model flare antenna azimuth pattern.

MODIFIED COSINE ANTENNA ILLUMINATION

(plot: Beam Envelope Amplitude (dB) vs Angle off Boresight (deg))

(a) Calspan pattern

(plot: PATTERN(DB) vs Angle off boresight (deg))
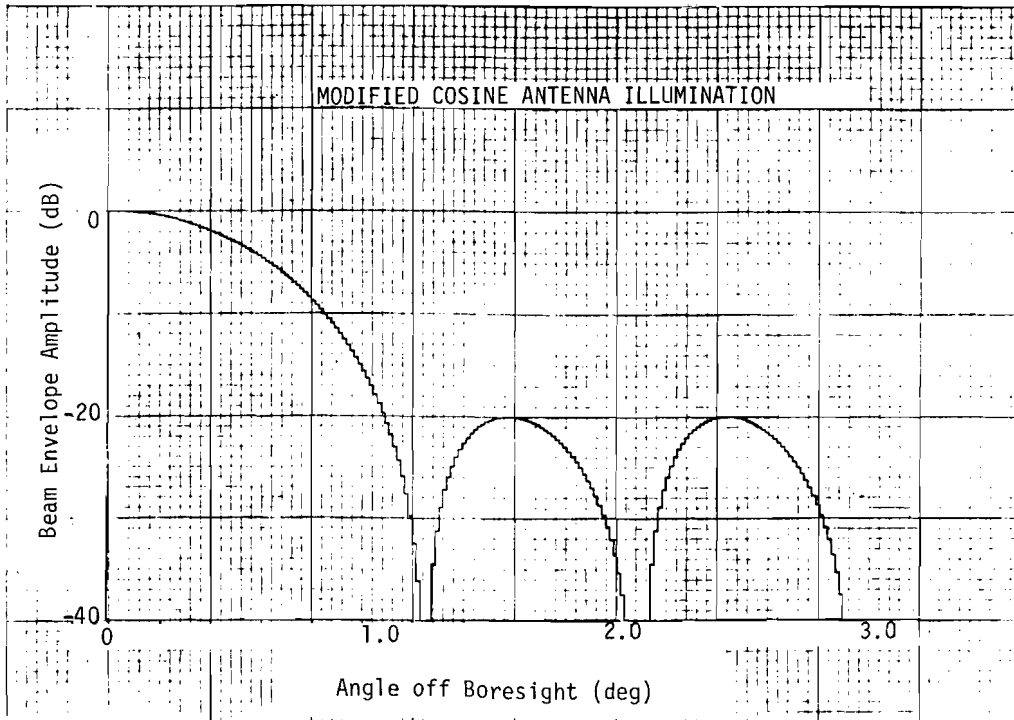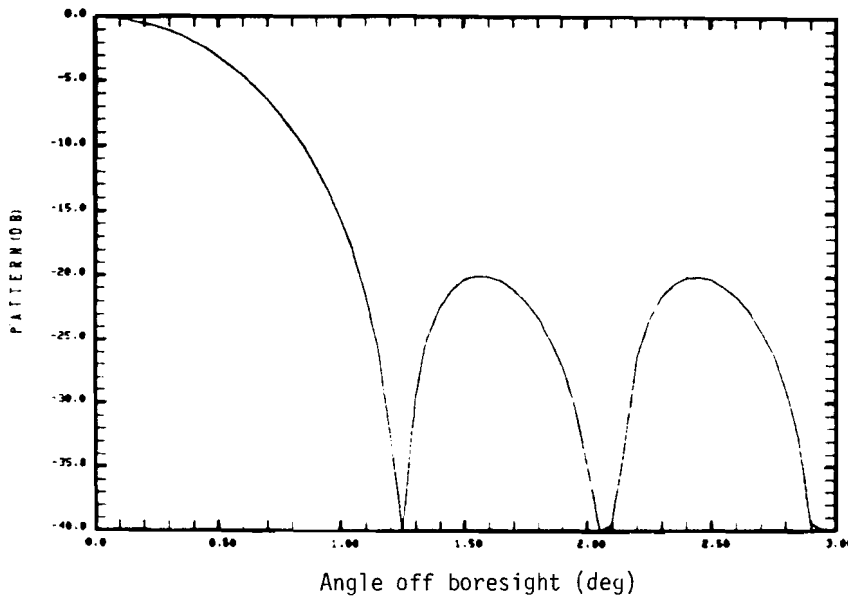
(b) Lincoln simulation

Fig. 1-52 Calspan bench simulator antenna patterns.

D. Receiver Processing Model

In this section we discuss how the receiver processing of the received envelopes (see Section B) is modeled. First we consider the processing of the scanning beam envelopes with emphasis on <u>acquiring</u> a track on a given envelope peak and then determining its centroid using a dwell gate processor. Next, we describe the single edge processor (SEP) algorithm which is an alternative means of determining the beam centroid. Finally, the model for OCI (SLS) and clearance beam processing is discussed.

1. Acquisition

Acquisition is the process by which a track is established. It has two steps, which are (1) determination of a likely candidate to be tracked, and (2) accumulation of enough data to give reasonable assurance that the candidate to be tracked is a valid signal and is, on the average, the largest component and thus is presumably the direct component. Should invalid data be received during track mode, a coast mode is provided to maintain track for 1 second. If the receiver drops out of track at some point, reacquisition is initiated. Reacquisition is identical to the initial acquisition process described below and is the same for all angle functions.

a. Determining a Candidate to Acquire

At the beginning of acquisition the receiver tracking gate is wide open. On the first TO-scan, the receiver finds the largest peak and stores its time location (T_{to}) relative to the scan midpoint (determined from the data preceding the scan). The same is done for the FRO-scan (T_{fro}). At the conclusion of the bidirectional scan pair, the two arrival time estimates* are subjected to a symmetry test:

$$\left| \, \left| T_{to} \right| - \left| T_{fro} \right| \, \right| \begin{array}{c} \text{fail} \\ > \\ < \\ \text{pass} \end{array} \quad 50 \text{ } \mu\text{sec} \text{ } (= 1 \text{ BW for } 1° \text{ beams}) \qquad (1\text{-}29)$$

If the peaks are within 50 μsec, it is assumed that they correspond to the same signal, and tracking gates are set up centered on the peaks and the second

---

* for the purpose of this test, the time of the peak is taken to be the arrival time.

phase of acquisition is entered. If the symmetry test is failed, the above procedure is continually repeated until symmetric peaks are found.

In the TRSB simulation, evaluation of the received envelope, as determined by Eq. (1-6), is one of the most time-consuming processes. It is obviously impractical to compute closely spaced envelope samples across each entire scan and to search for a peak. For the simulation, a simple algorithm to find the local maxima has been implemented that takes advantage of the internal knowledge concerning angular locations of the multipath components. This algorithm is used not only for the present function, but for other aspects of acquisition and tracking as well. Basically, it evaluates the envelope at the location of each multipath component. The details of this procedure and a justification of it are found in Appendix A.

b) Acquisition Algorithm

Once a pair of TO-FRO peaks has been found which passes the symmetry test, a track on that component is initiated, but no output data is provided (i.e., the system does not enter tracking mode) until sufficient confidence in the track is built up. For this purpose, the receiver contains two counters which we designate as the frame counter and the confidence counter. Each accepts one of three inputs: increment (+1), decrement (-1), or reset (to zero). Their various functions will be described subsequently.

On the scan-pair that passes the symmetry test, the frame counter is incremented from its initial state of zero. Then, the incoming data is processed in much the same way as it is when in track. There are tests for in and out-of-gate peaks and dwell gate validation whose outcomes influence the confidence and frame counts, respectively. Each test is described below.

c) Confidence Count (In and Out-of-Gate Test)

On each scan pair, a test is made to determine if the peak signal level is within the tracking gate. The peaks are found by the evaluation procedure described in Appendix A.

The test that is performed is

$$\text{if } (t_{to-} \leq T_{to} \leq t_{to+}) \text{ and } (t_{fro-} \leq T_{fro} \leq t_{fro+}) \qquad (1-30)$$
$$\text{increment confidence counter}$$

otherwise, decrement confidence counter

where

t_{to+}, t_{to-} are the leading and trailing to scan gate times.

t_{fro-}, t_{fro+} are the leading and trailing fro scan gate times

T_{to}, T_{fro} are the times of the peak of the to and fro scan, respectively.

Thus a positive confidence count indicates at least 50% of the time the tracked peak exceeds anything out of beam. If at any time the confidence count reaches zero, the frame counter is reset and the entire acquisition procedure procedure must be restarted.

The confidence counter is governed solely by the out-of-beam multipath test outcome. It will saturate at some count level (at present corresponding to 20 sec of consecutive increments), and in between will increment and decrement as described above. The remaining acquisition/validation tests influence the acquisition counter.

d) Acquisition (Frame) Count

Four validation checks are performed on each received data frame. All four tests must be passed to validate the frame and enable the angle processing. The checks are: (i) function ID decode, (ii) acceptable dwell gate width, (iii) single pair of dwell gates, and (iv) dwell gate symmetry. In the simulation model, the function ID test is not included because it is not as fundamentally related to the angle system multipath performance as are the other three.

If all the tests succeed, the frame counter is incremented by one. Otherwise, the validation tests do not influence the frame count. However, there is an asynchronous clock driving the decrement input to the frame counter (review

1-64

Fig. 1-3) which runs at half the frame rate. Thus, for every two validated frames there are two increment and one decrement inputs, resulting in a net +1 count. Thus, for example, in EL, the count corresponding to one second's worth of data is 20.

(i) Dwell Gate Width and Number

The dwell gate circuitry output goes into a PWD (pulse width detector) which checks that the width lies within a specific range of values. The lower and upper limits can be varied with ease: for Phase III, they are T_{min} = 12 µsec < dwell gate < T_{max} = 350 µsec. Following the PWD, there should be only one valid dwell gate within the tracking window (for a detailed discussion of how dwell gates are computed, see Appendix B) and if there are none[*], or more than one, the remaining tests are not performed and the system essentially ignores the scan.

On the scan which initiates a track, the TRSB receiver used the threshold crossing pair which brackets the peak signals as no tracking gate has been accepted. This process is approximated in this version of the simulation by setting up a pseudo tracking gate which is 2 beamwidths wide (using a user specified value for the beamwidth) and then performing the dwell gate tests that are used for the subsequent scan processing. If a single dwell gate is not found within the pseudo tracking gate, the program prints an error message and ignores the scan. To date, this approximation has proved satisfactory.

(ii) TO-FRO Symmetry

In the hardware receiver, this test is exactly the same as the symmetry test used to initiate acquisition. In our implementation of the latter, beam peak locations, rather than dwell gate centroids, were used as arrival times for simplicity. For the validation test, the centroids are used. The difference in centroid times must be less than 50 µsec.

---

[*]On the basis of July 1976 data from Bendix engineers, the model used for the simulations reported here ignores a scan where no dwell gate was found within the tracking gate. The most recent data from Bendix Avionics indicates that when no dwell gate is found, the receiver will set the dwell gate times equal to the tracking gate times and continue processing as if a valid dwell gate were encountered.

e) Slew Rate Limiting and Tracking

Upon passage of the validation tests, angle processing follows. When the frame angle estimate is obtained, it is input to the tracking filter and the output subjected to slew rate limiting. Tracking gates are generated from (i) the raw angle data if the system is not in track mode, or (ii) the slew limiter output if in track mode.

The receiver utilizes slew limiting whenever an output angle estimate shows too great a deviation from the previous slew limited ouput. The slew rate limit is 1.0°/sec for both AZ and EL, but the test is implemented on a per scan basis using limits of 0.025° for EL and 0.07° for AZ. Whenever there is a slew violation, the output value is reset at the previous smoothed value ± the per scan slew limit, the sign being chosen in accordance with the algebraic sign of the initial deviation.

In determining whether to decrement the frame count on a slew failure, polarity of the slew must be taken into account.[*] When the first slew violation occurs, its polarity is noted and the count decremented. Subsequent slews in the same direction also generate a decrement input. A slew in the opposite direction is not counted as a failure. If a scan with no or, an opposite sense slew violation occurs, the polarity indicator is zeroed. The polarity indication will then be reset when the next slew violation occures. Thus, if successive slew violations alternate +-+-, the frame counter is decremented twice by the slew test.

The Phase III receiver uses an $\alpha-\beta$ tracker, which is a second order linear filter. The recursion formula relating the input and output sequences $\{x_n\}$ and $\{y_n\}$

$$y_n = (2-\alpha-\beta) y_{n-1} - (1-\alpha) y_{n-2} + (\alpha+\beta) x_{n-1} - \alpha x_{n-2} \qquad (1-31)$$

is more simply expressed in terms of the prediction error

$$e_n = x_n - y_n$$

---

[*] The description of slew limiter polarity here is based on Bendix data furnished in 1976. It is our understanding that the current (1980) phase III receiver μP program does not consider polarity in determining whether the counter should be decremented.

as follows:

$$y_n = y_{n-1} + \alpha e_{n-1} + \beta \sum_{j=0}^{n-1} e_j \qquad (1\text{-}32)$$

The parameter values (α,β) are (0.25, 0.031) for AZ and (0.125, 0.00781) for EL.

The slew rate limiter operates on the filter outputs and has no feedback into the filter, i.e., the slewed output y_n' is

$$y_n' = \begin{cases} y_n & ; \quad |y_n - y_{n-1}'| < \varepsilon & (1\text{-}33) \\ y_n' + \varepsilon \, \mathrm{sgn}(y_n - y_{n-1}') & ; \text{ otherwise} & (1\text{-}34) \end{cases}$$

Until the system flag has been lifted, neither the α-β filter recursion above nor the slew rate limiter tests are applied since the validity of the tentative track has not been established. The α,β filter values are, however, set as follows:

$$y_n = x_n$$
$$e_n = 0$$
$$\Sigma e_j = 0$$

This results in the predicted angle estimate at the beginning of track having the value of the preceding raw angle estimate for that function and a zero initial angle velocity estimate.

f) Coast Mode

In the event that the angle measurement for a given scan is invalidated (e.g., by the failure to find one of the dwell gate), the tracker goes into coast mode for that scan. The coast consists of projecting the angular coordinate linearly at the most recent velocity estimate. This is readily accomplished in the receiver as follows. If there is no valid input data (x_n) at time n=N, the predicted output value is used in place of x_N, i.e.,

$$x_N \equiv y_N = > e_N \equiv 0 \qquad (1\text{-}35)$$

Substituting this into Eq. (1-32) at time n = N+1 yields

$$y_{N+1} = y_N + \beta \sum_{j=0}^{n-1} e_j \qquad (1-36)$$

i.e., the "coasted" value y_{N+1} is just the previous output plus the velocity correction.

In the Phase II receiver, the output was held constant during coast. This procedure can also be explained as a feedback of output to input, the difference being that there is no velocity estimate inherently available in the first-order tracker. Thus, the Phase III coast mode is the second-order equivalent of the Phase II coast mode.

2. Angle Processing

Tracking mode is entered from acquisition when the frame counter reaches saturation (20 counts for EL and FLARE, 8[*] for AZ). During tracking, the validation tests (out-of-beam multipath, PWD, symmetry, etc.) initiated during acquisition continue and their outputs are processed in exactly the same way relative to the counters, that is, whenever data failures decrement either the confidence counter or the frame counter to zero, reacquistion begins. In this section the data processing for angle output and the operation of the tracker which both drives the tracking gates and smoothes the angle data is described.

a) Single Scan Angle Estimate (Dwell Gate Processing)

Following passage of all the validation tests on a given scan pair, there exists a single dwell gate $(\hat{t}_1, \hat{t}_2)$ on each scan (see Appendix B for detailed algorithm). Its centroid $\hat{t}$ is calculated:

$$\hat{t} = \frac{\hat{t}_1 + \hat{t}_2}{2} \qquad (1-37)$$

For each scan pair the two time centroids are related to the angle estimate $\hat{\theta}$ through the scan rate:

---
[*] The TRSB data rate for AZ is 13 1/3 Hz, but in the simulation, AZ measurements are taken at the rate of three per output interval, i.e., 15 Hz. Recall that the frame counter has one net increment per two valid frames.

1-68

$$-\dot{\theta}\hat{t}_{TO} = \hat{\theta}_{TO} \tag{1-38}$$

$$\dot{\theta}\hat{t}_{FRO} = \hat{\theta}_{FRO} \tag{1-39}$$

which gives us the net angle estimate as the average of $\hat{\theta}_{TO}$ and $\hat{\theta}_{FRO}$:

$$\hat{\theta} = \dot{\theta} \left(\frac{\hat{t}_{FRO} - \hat{t}_{TO}}{2} \right) \tag{1-40}$$

from which the true angle θ_o is subtracted to yield the "single scan" error

$$\varepsilon = \hat{\theta} - \theta_o \tag{1-41}$$

If the scan pair has been invalidated in the earlier tests, the "single scan" estimate is set equal to the previous "dynamic" angle estimate and the output angle estimate; the errors are found by subtracting the direct component angle. During tracking mode the tracking gate for the subsequent scan is centered on the smoothed estimate. During acquisition, the gate is centered on the raw data. In both cases, the gate width for a given scan is $\pm$ one dwell gate width, as determined from the preceding scan pair for the opposite direction scan (i.e., dwell gate on current "FRO" scan generates tracking gate width for "TO" portion of next TO-FRO pair and vice versa).

b)   Single Scan Angle Estimate (Single Edge Processing)

The single edge processor (SEP) model is a straight forward extrapolation from Fig. 1-4. When the SEP mode is invoked (for elevation and/or flare), three changes are made to the normal dwell gate processing:

1.   the tracking gate time interval over which envelope values are computed is increased from ± 1 beamwidth to ± 2.5 beamwidths

2.   the search for -3 dB threshold crossings works downward on either side of the largest peak within the dwell gate until the -3 dB points are encountered

and 3.   multiple valid dwell gates within the tracking gate are ignored.

At the start of a new track, the SEP counter is zeroed. If there was not a valid dwell gate, the model does no SEP processing and the counters remain zeroed.

1-69

If a valid dwell gate was found, envelope sample pairs separated by approximately 16 μsec are compared until the ratios satisfy the relationship indicated in Fig. 1-4:

$$\frac{V(T_i)}{V(T_i + \Delta T)} \leq R < V(T_i)/V(T_i + \Delta T) \tag{1-42}$$

where $V(t)$ = (linear) envelope value at time t

$$\Delta T \approx + 16 \text{ μsec if } T_i > T_{peak}$$
$$- 16 \text{ μsec otherwise}$$

$$20 \log_{10} R = (9/16) \Delta T \text{ where } \Delta T \text{ is in μsec}$$

When (1-42) is satisfied, a refined SEP crossing estimate is obtained by linear interpolation between the pair centroid times $(T_i + \Delta T/2)$ and $(T_j + \Delta T/2)$. The SEP crossing times for the to and fro scans are combined to yield the SEP angle estimate

$$\hat{\theta}_{sep} = \dot{\theta} (t_{to} - t_{fro})/2 \tag{1-43}$$

The SEP angle estimate is biased by approximately the antenna beamwidth. To correct this bias, a correction factor must be applied. For each valid SEP estimate, the difference

$$\Delta \theta = \hat{\theta}_{sep} - \hat{\theta}_{dwell} \tag{1-44}$$

is computed. If the difference between $\Delta \theta$ and the time smoothed difference, $\Delta \theta_{av}$, is within a certain limit (currently 4 μsec), $\Delta \theta_{av}$ is updated by the equation

$$\Delta \theta_{av} = \alpha \Delta \theta_{av} + (1 - \alpha) \Delta \theta \tag{1-45}$$

where α = exp(- 1/800) corresponding to a 20 second time average. Equation (1-45) is initialized with the value of $\Delta \theta$ obtained on the first SEP estimate. The returned angle estimate is

$$\hat{\theta} = \hat{\theta}_{sep} - \hat{\theta}_{av} \tag{1-46}$$

Analogous to the dwell gate frame counter, the SEP algorithm has a SEP counter which is incremented if a valid SEP estimate is obtained [per eq. (1-40)] and $\Delta\theta$ is sufficiently close to $\Delta\theta_{av}$. Otherwise, the SEP counter is decremented. The SEP counter has a saturation limit corresponding to 20 seconds of data.

3. SLS/OCI and Clearance Signal Processing

The sidelobe suppression (SLS)/out of coverage indication (OCI) and clearance signal model processing model follows directly from Fig. 1-3. When the OCI/SLS or clearance beam peak is greater than the largest scanning beam peak, then no dwell date processing occurs and the frame and acquisition counters will be decremented by the synchronous counter. If:

1. the clearance signal is greater than the SLS/OCI signals, then the clearance counter (CC) will be incremented until it reaches a saturation value corresponding to 1 second of data. When the CC saturates, the clearance flag is lifted and a "fly right" or "fly left" indication made (manifested in the model by an error of $\pm 1000°$). The indication of "right" or "left" is determined by which clearance signal dominated on the given scan (i.e., there were not separate fly right/fly left clearance counters in the phase III receivers). The clearance flag remains lifted until the clearance counter becomes less than or equal to zero (due to decrements by the asynchronous clock).

(2) the SLS/OCI signals are greater than the clearance signal, then no further processing of the clearance or scanning beam signals will occur. In such a case, the asynchronous clock will decrement the frame, acquisition and clearance counters.

E. Comments on TRSB Modeling

During the TRSB model development and refinement, considerable insight
was gained into the various model tradeoffs as well as utility of various
types of experimental data. Since new TRSB hardware mechanizations will be
arising as implementation proceeds, it seems worthwhile to make a few com-
ments here which may be of aid in development of the models for such equipment.

In the case of the receivers, the modeling process to date was straight-
forward, since the bulk of the processing is digital in nature. This trend
towards all digital implementation seems likely to continue [92], thus sim-
plifying future receiver modeling development. In validating such models,
hybrid simulator data such as obtained at CALSPAN is invaluable and should
be a routine part of the evaluation/acceptance procedure for new receiver
implementations.

Similarly, models for non-scanning antennas and elements are quite
straightforward, given static range measurements. In the case of torus azi-
muth antennas (e.g., as used for the Australian TRSB arrays), there are prac-
tical problems in:

1. measuring the elevation pattern of the array in the
    absence of the ground.

2. extrapolating measurements with one type (e.g., flat, grassy)
    ground present to other situations (e.g., snow cover).

Some theoretical work, coupled with experimental data (full scale or scale
model), would be of use here. Another (lesser) problem encountered in many
cases was an insufficient range of measured pattern data, e.g.:

1. Azimuth patterns (of all arrays) are typically shown only for
    the front sector ($|\theta_{az}| < 90°$), whereas SLS/OCI modeling re-
    quires consideration of the patterns over the full range of
    azimuth angles.

2.   Elevation patterns are generally not shown for large negative
     elevation angles (e.g., -15°), thus making it difficult to
     model the sidelobe characteristics in that region. Also, in
     many cases, the azimuth array elevation pattern near the horizon
     is not displayed with a fine grain scale to permit estimating the
     (rather important) slope at the horizon.

These problems could be reduced by appropriate changes in the requirements
for data to be delivered.

The area requiring the greatest amount of study and additional experi-
mental data is the sidelobes of the scanning beam dynamic pattern. Refining
the estimate of the effective level of these sidelobes is an important area
in TRSB system specification/procurement, as well as modeling. We have found
that the dynamic pattern sidelobes at angles well removed from the main beam:

1.   are considerably higher than the theoretical array factor side-
     lobes and the measured static patterns.[*]

2.   show an apparent level which is a strong function of receiver
     filtering (and thus must be assessed at the output of a rep-
     resentative receiver).

3.   have complicated spatial variation, which is quite important
     in determing the resulting angle errors due to multipath.

4.   can have multipath error characteristics which are significantly
     smaller (e.g., 3-5 dB) than would be estimated from the measured
     dynamic sidelobe magnitude (e.g., see the testbed 1° azimuth data
     discussion in Chapter II of this volume). Appendix F discusses
     some of the issues involved here in greater detail.

----

[*]"dynamic pattern" here refers to the pattern as a function of time at a
given receiver angle, whereas "static pattern" is the pattern as a function
of angle at a fixed point in scan time.

However, the test range/field measurement data to date has not generally been fully adequate for addressing these issues in many cases:

(a) dynamic patterns are typically obtained only for receiver positions within the scan coverage, however, the sidelobes outside that region can be important in many cases (especially for small community type azimuth arrays and elevation arrays).

(b) dynamic patterns at a given receiver angle are not normalized to the peak gain at a reference receiver angle (e.g., 0° for azimuth arrays), even though it is ratios such as the (sidelobe level at angle B)/(main beam level at angle A), which are of greatest importance.

(c) the available dynamic pattern data in many cases is obtained at field sites which have significant environmental effects (e.g., shadowing or ground reflection) on the observed pattern.

(d) experiments to yield effective multipath sidelobe levels (e.g., by using a repeater in the antenna far field), have not been performed on most arrays in use today.

Items (a) - (c) could be alleviated to a significant degree by more extensive dynamic testing at an antenna test range prior to equipment deployment. In the case of elevation arrays, it probably would be necessary to lay the array on its side (thus yielding a horizontally polarized azimuth array) to obtain the desired data over the full range of angles (in particular, negative elevation angles). For phased array implementations, the ICAO tests using a screen as the multipath source were quite helpful in determining the effective sidelobe level*. However, it is not clear that those results can be extrapolated to other (e.g., Rotman lens type) implementations.

_____

*Fortuitously, the ICAO test plan located the screen at the azimuth angle corresponding the the largest dynamic sidelobe of the Bendix 1° testbed azimuth array. Such a "worst case" location should be utilized for testing of other array types.

The receiver model could be extended in two directions. The first of these concerns situations where the multipath level is low and acquisition/validation (including OCI/SLS signals) are not of concern*. In such cases, use of a closed form error approximation such as was utilized in the critical areas studies [28] can provide a significant computation time reduction. However, in doing this, one must be particularly careful in the azimuth case to utilize the "effective" M/D levels in the formulas rather than the "raw" multipath levels supplied by the propagation model (see section 8.1 of [28] for more details). However, these approximations are generally not valid for shadowing multipath where blockage by large obstacles (e.g., a taxiing aircraft) is involved. To date, the TRSB model has not been "adaptive" in the sense of recognizing when the closed form error expression could be used as opposed to the detailed model.

Another area of possible extention would be to incorporate the envelope filter in the simulation. To date, this has not been deemed necessary since there was good agreement with CALSPAN bench simulator test data for the dwell gate processor. The SEP processor operates further down on the received envelope skirts and hence may be more sensitive to filtering effects. There does seem to be slightly larger differences between our simulation results and CALSPAN data in the case of SEP (see chapter II of this report); however, the agreement still should suffice for most purposes.

The one situation in which the envelope filter could produce quite significant results is when a high elevation beam stop angle is used (e.g., as in the Texas Instruments Phase III Crows Landing Tests [109]). In a small number of those tests, the beam was shut off at an angle well within the normal dwell gate period for the given glideslope. In such a case, the computer simulation would yield an infinitely sharp trailing (or, leading) edge in the processed envelope data, whereas the filtered envelope would decrease (or, increase) much more slowly. Although incorporating an appropriate filter into the simulation would be straightforward, it was not viewed as necessary at this point since such abnormal beam stop angles (e.g., 1.75°) should not be necessary for normal operation.

---

*Examples of this include inbeam elevation multipath from vertical surfaces and sidelobe azimuth multipath effects.

II. TRSB MODEL VALIDATION

Model validation is a process by which one gains sufficient confidence in the operation of the simulation model to rely upon its predictions for previously untested situations. The primary validation tool is the comparison of model outputs to other data calculated for or experimentally measured in corresponding situations and to explain both the similarities and discrepancies which are evident. For each of the Lincoln Laboratory MLS system models, and for the TRSB model in particular, theoretical calculations, bench test experiments, and field tests have all been used as data inputs to the validation process illustrated in Fig. 2-1. This section traces the path by which the conclusions of the individual tests culminated in validation and tolerancing of the TRSB simulation for the purpose of the ICAO multipath assessment.

The validation process is most usefully viewed within the context of its primary modeling objectives, which are:

(i)   Representative received signal-in-space model in the presence of multipath sources.

(ii) Receiver modeling at the functional signal processing level,

(iii) Emphasis upon multipath-induced effects, and not elements of clean accuracy such as front end noise, beam stepping quantization, receiver time and amplitude quantization, etc.

The analytical work was oriented toward deriving formulas for the errors as a function of the input parameters. Comparison of these formulas with computer simulation results served as a check on the validity of the computer code. The CALSPAN bench simulator could inject into an actual TRSB receiver an idealized if waveform corresponding to the reception of a direct signal and a single multipath signal. Comparisons of the bench simulator test results with the simulation results provided confirmation of the receiver

COMPARISON

HYBRID BENCH
TESTS BY CALSPAN

FIELD
DATA

RECEIVER
SIMULATION

THEORY

CALSPAN*
RECEIVERS

PHASE III
RECEIVERS

RECEIVER
TEST
PROGRAM

PROPAGATION
MODEL

DWELL GATE
LINEARIZED MODEL

PEAK LOCATION,
IDEAL SPLIT GATE

TIMING JITTER,
BOUND ON MOTION
AVERAGE FACTOR
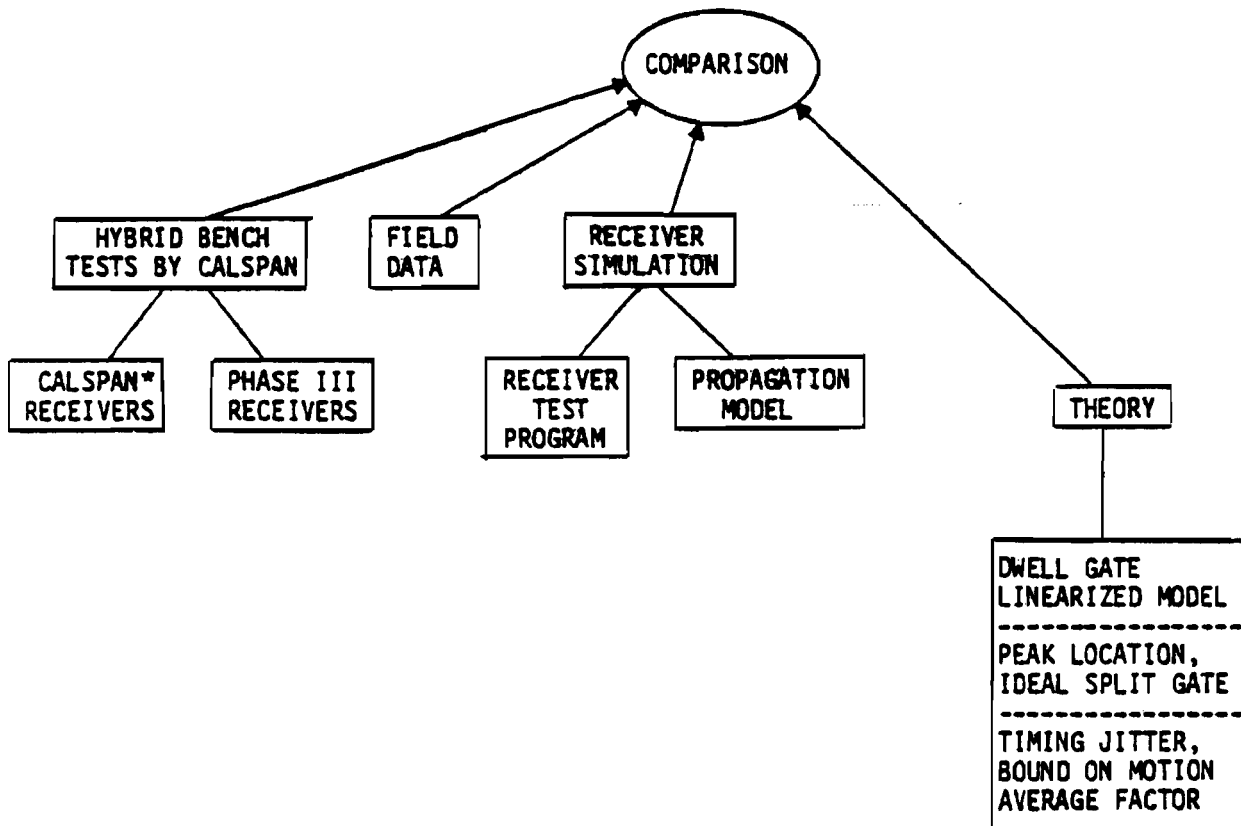
*Formerly Cornell Aeronautical Laboratory

Fig. 2-1   Elements of TRSB angle receiver model validation process.

functional modelling approach (including justification for ignoring various non-multipath related error sources). Finally, the comparison with field test data provided confirmation for the signal-in-space models.

A. Theoretical (Analytical) Results

In an earlier report [78], we presented first order results for single scan TRSB static errors as well as a detailed analysis of motion averaging benefits. In this section, we present more refined results for the standard dwell gate processor response to in-beam (i.e., mainlobe) multipath. A detailed derivation of these results is given in appendix E.

For the purpose of studying in-beam multipath error, it is adequate to model the scanning beam antenna pattern as having Gaussian shape, i.e.:

$$P(x) = e^{-kx^2} \quad ; \quad k = 2 \ln 2 = 1.386 \qquad (2-1)$$

where x is angular displacement in beamwidths. Expression for mean, rms, and peak-to-peak errors are presented below, where the averaging is over rf phase from 0 to 2π. These are given as functions of relative multipath amplitude ρ, separation angle θ (BW), and nominal threshold crossing points $\pm v$ (BW)*
The derivations, given in the appendix E, take into account terms through squared order in the variable $\eta = \rho \exp(-k\theta^2)$. Previous results of this type [28] only retained terms through first order in η and consequently were incapable of obtaining the bias result:

$$\text{(bias): } e = \frac{1}{2} k \rho^2 \theta^3 e^{-2k\theta^2} \left[\frac{\sinh 2kv\theta}{kv\theta}\right]^2 \left[2 \cosh 2kv\theta + 1 - \frac{\sinh 2kv\theta}{2kv\theta}\right] \qquad (2-2)$$

$$\text{(rms) } \sigma_e = \frac{1}{\sqrt{2}} \rho |\theta| e^{-k\theta^2} \frac{\sinh 2kv\theta}{2kv\theta} \qquad (2-3)$$

---

*Beamwidths (BW) are measured at the -3 dB points on the waveform. Typical values in the MLS application range from 0.5° to 3.0°.

$$\text{(Peak-peak)} \quad e_{pp} = 2\rho \, |\theta| \, e^{-k\theta^2} \, \frac{\sinh 2kv\theta}{2kv\theta} \tag{2-4}$$

For small separation angles the bias term is:

$$\bar{e} \simeq 1.39 \, \rho^2 \, \theta^3 \, e^{-2k\theta^2} \tag{2-5}$$

We note in particular the θ^3 dependence of bias on angle. The rms error formula is identical to the one obtained from the first order analysis; no new terms appear in the extension. The same is true of the peak-to-peak error, although with the aid of the higher order error vs. phase formula, more accurate expressions for the positive and negative peak errors have been obtained [see Eqs. (E-15) and (E-16) in appendix E].

B.   Bench Tests

Throughout Lincoln Laboratory's participation in the MLS program, bench test data has been used to validate the MLS system models. The most valuable source of such data is the CALSPAN Corporation bench test facility [71]. The main objective of the bench simulator work was to characterize the TRSB receiver response to multipath which had an angle code very close to the direct signal (i.e., in-beam multipath) since theory and field tests data have shown that this "in-beam" multipath is the principal threat to a low sidelobe TRSB antenna.*

The bench test comparisons are shown in Figs. 2-2 to 2-7. There are three tests each for AZ and EL, one at essentially no scalloping rate (the scalloping rates used by CALSPAN were chosen so the the α-β filter had unity gain), and two at frequencies where motion averaging should be evident. The match in the static cases is good. In the dynamic cases, there is some mismatch resulting from the fact that the computer program which drives the TRSB simulation in the bench test mode does not cycle it through all possible phases

---

*Multipath which is well separated (e.g., more than two ground antenna beamwidths) from the direct signal (i.e., "out-of-beam") yields errors through sidelobe leakage.
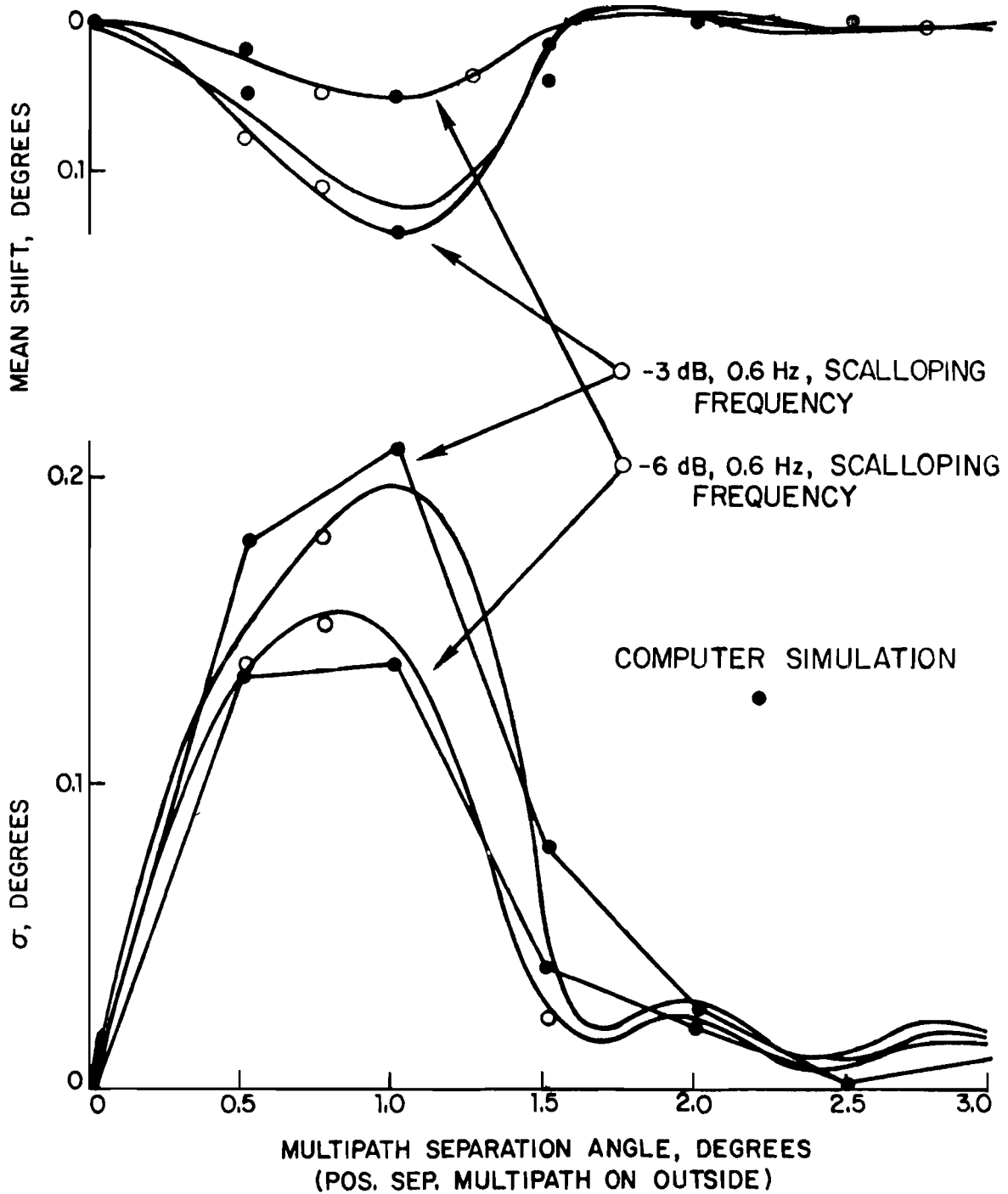
Fig. 2-2 Comparison of CALSPAN simulation azimuth data with simulation
at 0.6 Hz scalloping frequency.

MEAN SHIFT, DEGREES

0

-0.1

— — — — -3 dB MULTIPATH

———— -6 dB MULTIPATH

— — — — -10 dB MULTIPATH

Lincoln Laboratory data - large dots

σ, DEGREES

0.1

0

0   0.5   1   1.5   2   2.5   3

Multipath Separation Angle, Degrees
Multipath on Negative Side (Inside)
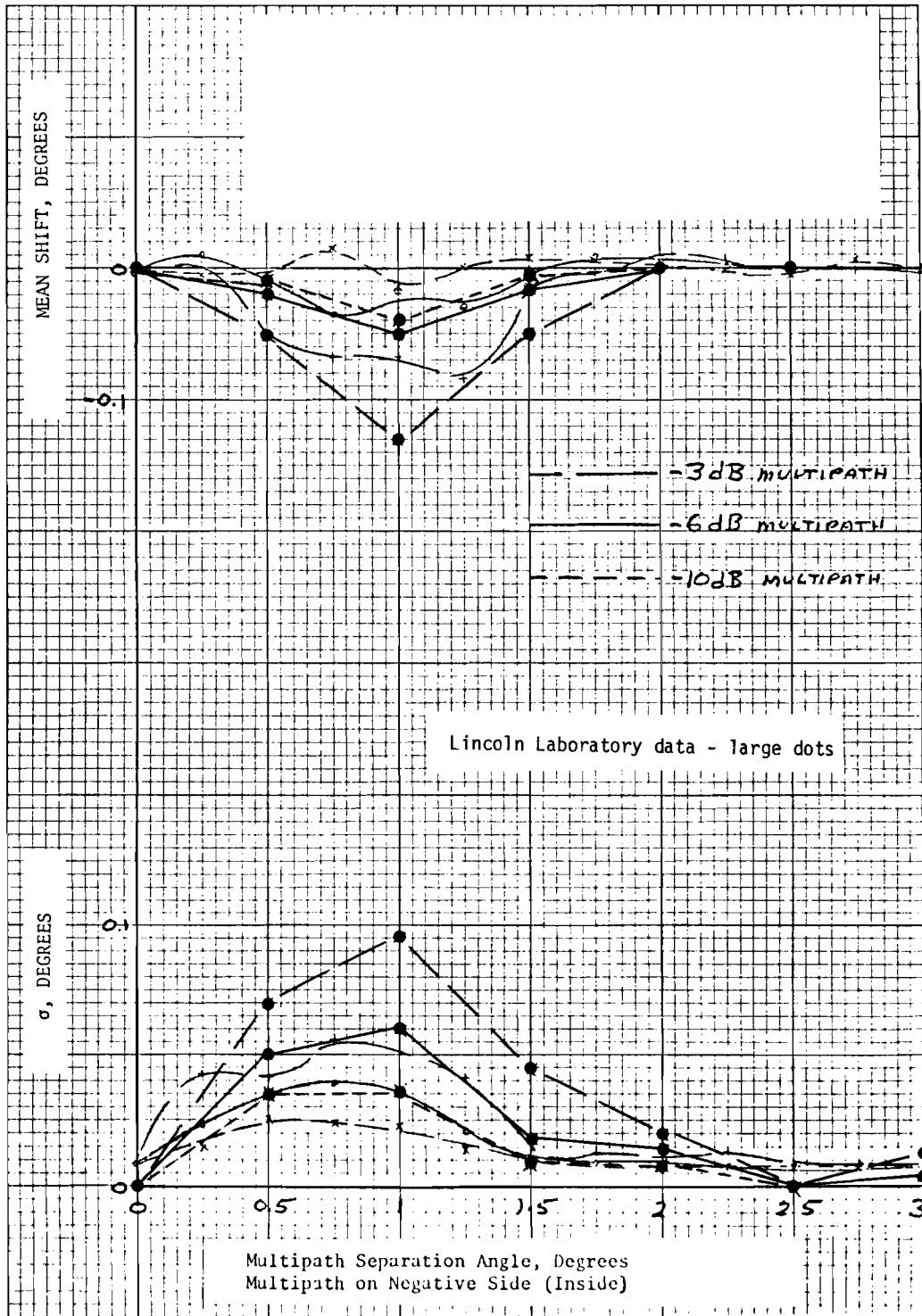
Fig. 2-3 Azimuth baseline tests; Bendix receiver P101, 20.32 Hz
scalloping frequency, -20 dB sidelobes.

2-6
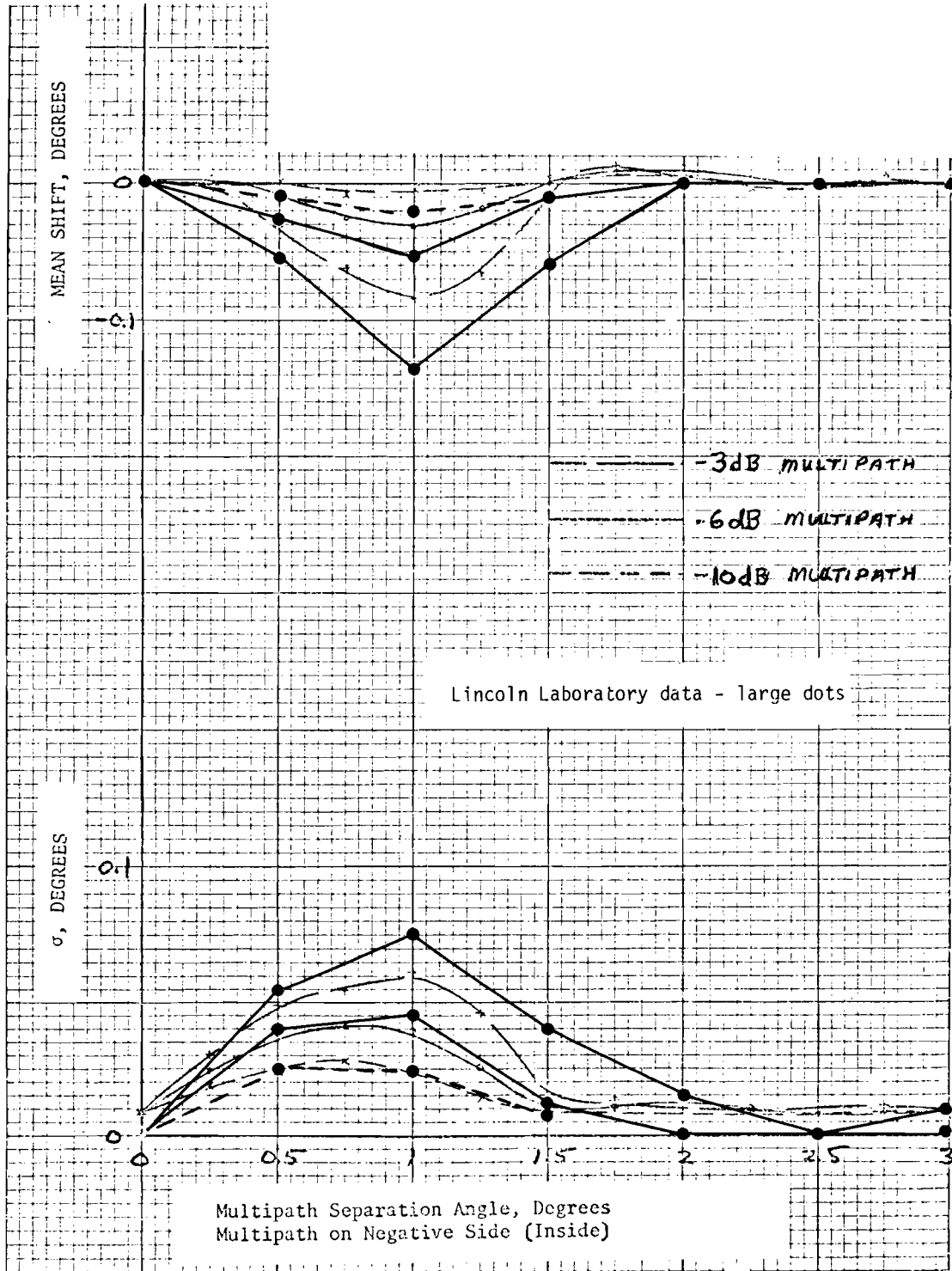
Fig. 2-4 Azimuth baseline tests; Bendix receiver P101, 40.32 Hz
scalloping frequency, -20 dB sidelobes.
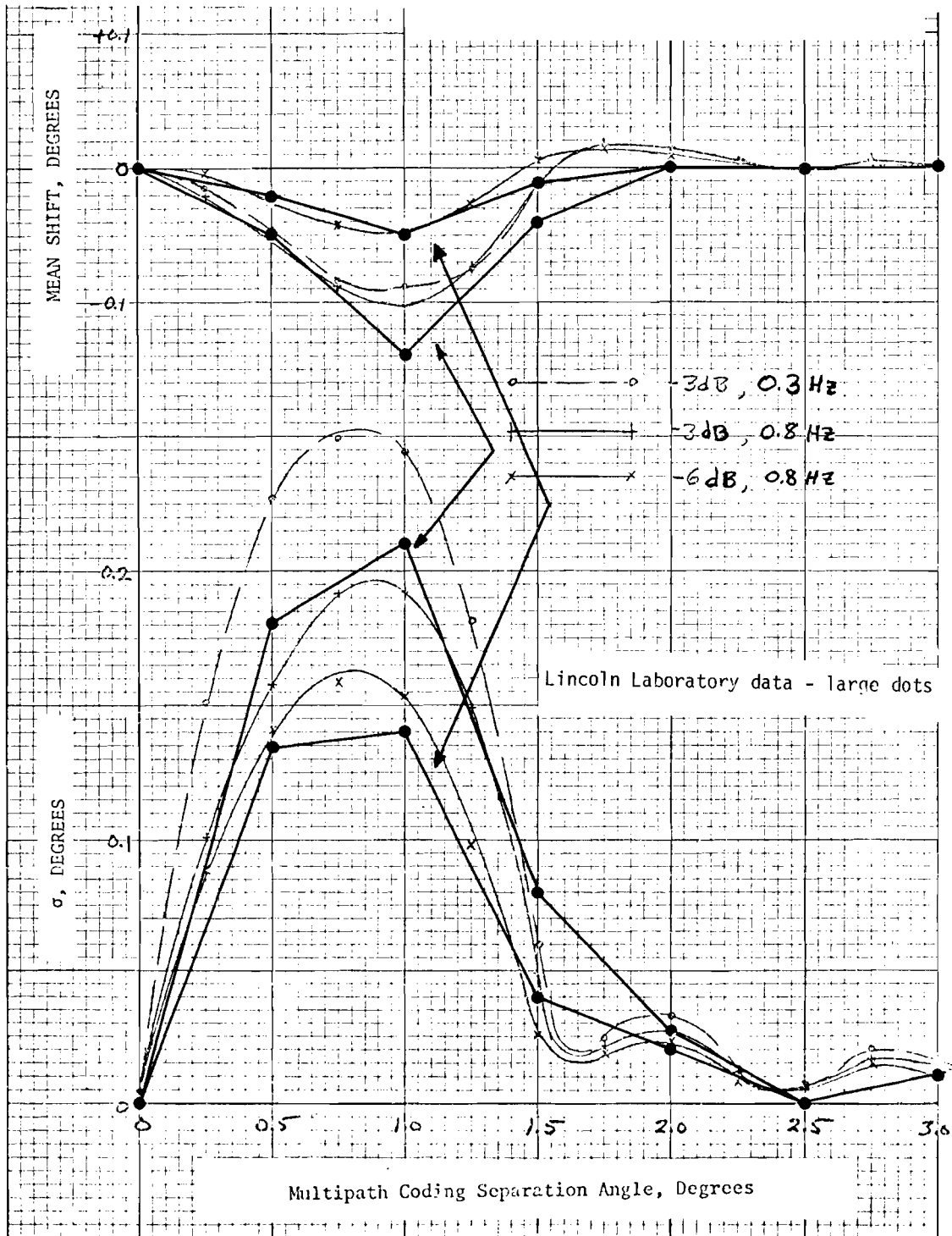
Fig. 2-5 Elevation baseline tests; Bendix receiver P101, -25 dB sidelobes.
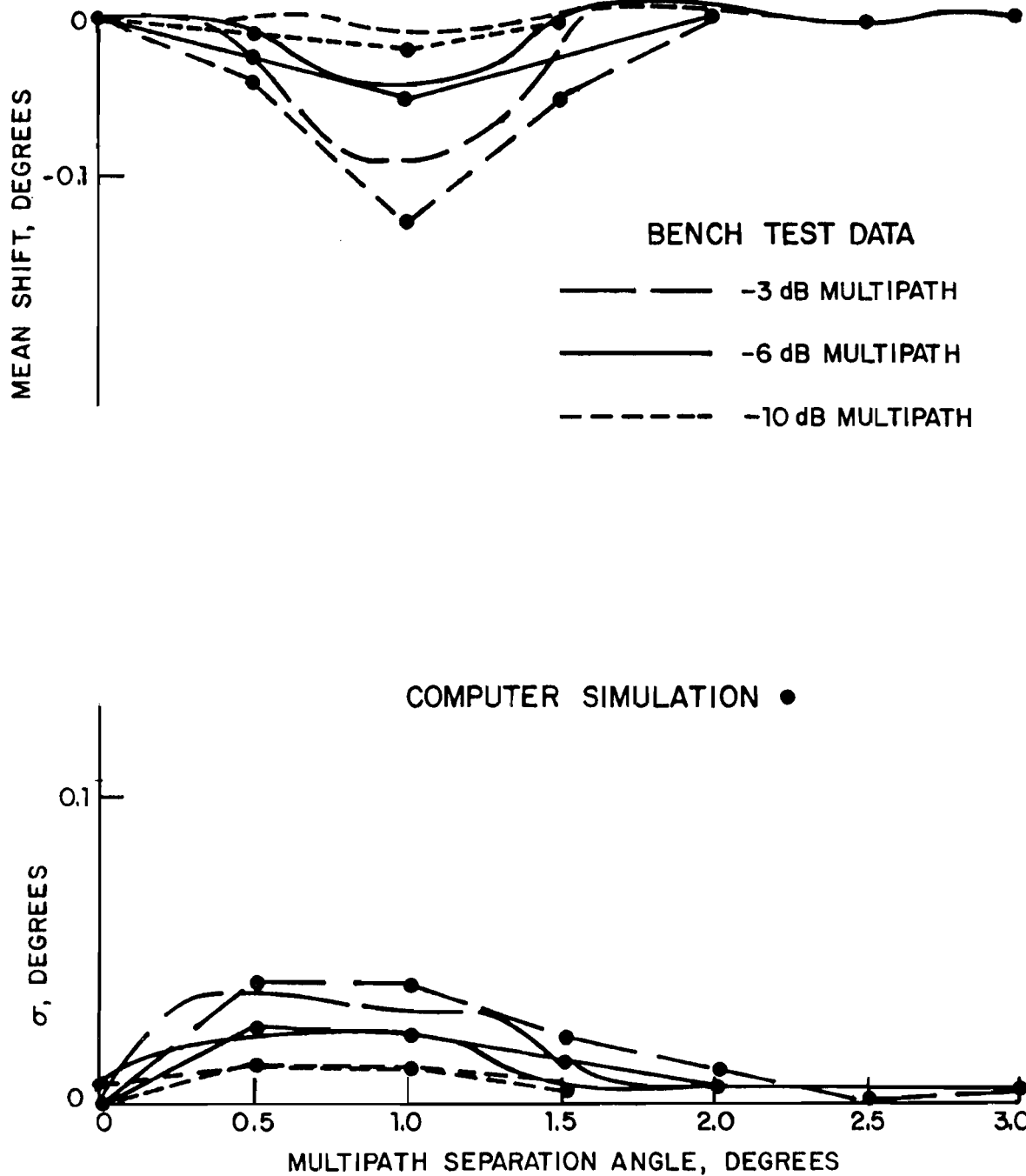
Fig. 2-6 Comparison on CALSPAN simulator elevation data with simulation model at 20 Hz scalloping frequency.
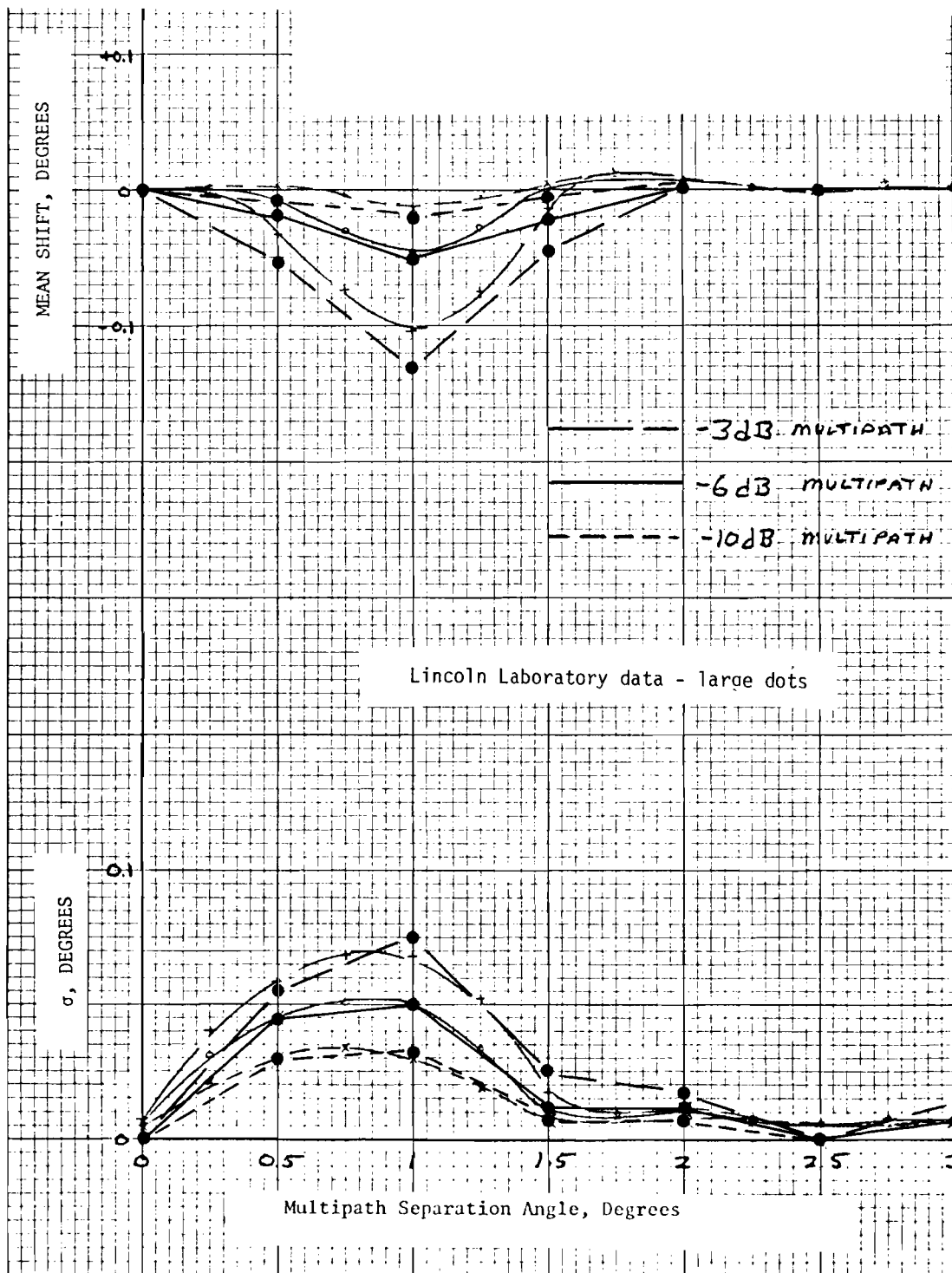
Fig. 2-7 Elevation baseline tests; Bendix receiver P101, 40.32 Hz
scalloping frequency, -20 dB sidelobes.

of the signal format jitter sequence. Thus, the averaging characteristics are not the same as for the CALSPAN data.

Comparison of the static bench test and simulation data (Figs. 2-2 and 2-5) for the Phase III receiver shows discrepancies between the two which do not exceed ± 0.02° (bias) and ± 0.015 (rms) with high confidence. These figures are consistent with ± 0.5 dB tolerance on M/D ratio obtainable in the CALSPAN analog multipath simulator.

CALSPAN tests also confirmed that the DPSK waveform used in the TRSB signal format to transmit function identity, system status, auxiliary data, etc., is quite immune to multipath. As field test data [66] in a severe multipath environment gave similar results, the computer modelling was restricted to considering angle data effects.

C. Field Tests

Model validation based upon full scale scenario simulations and corresponding field trial records has been accomplished to the extent possible. The field data has been particularly valuable for validation of the antenna models and thus the received signal model, as demonstrated below.

1. Azimuth Tests

a. Out-of-Beam Multipath

The AZ array used in both Phase II and Phase III is the Bendix phased array at NAFEC, so in this case the Phase II and Phase III antenna patterns in the simulation coincide. Differences in the two receivers, primarily the filter and slew rate limiter, should be negligible for the AZ multipath at rollout tests in which the scalloping rates are low.

In the simulation of the AZ array, a sidelobe model has been adopted which, if anything, overestimates the amplitude of the sidelobe oscillations. This assessment is based on examination of appropriately filtered dynamic beam simulations (Bendix), field recordings of beam envelopes, and the "azimuth multipath at rollout" field tests results. In this section, we consider the azimuth multipath tests using the screen shown in Fig. 2-8 to generate out-of-beam multipath signals.
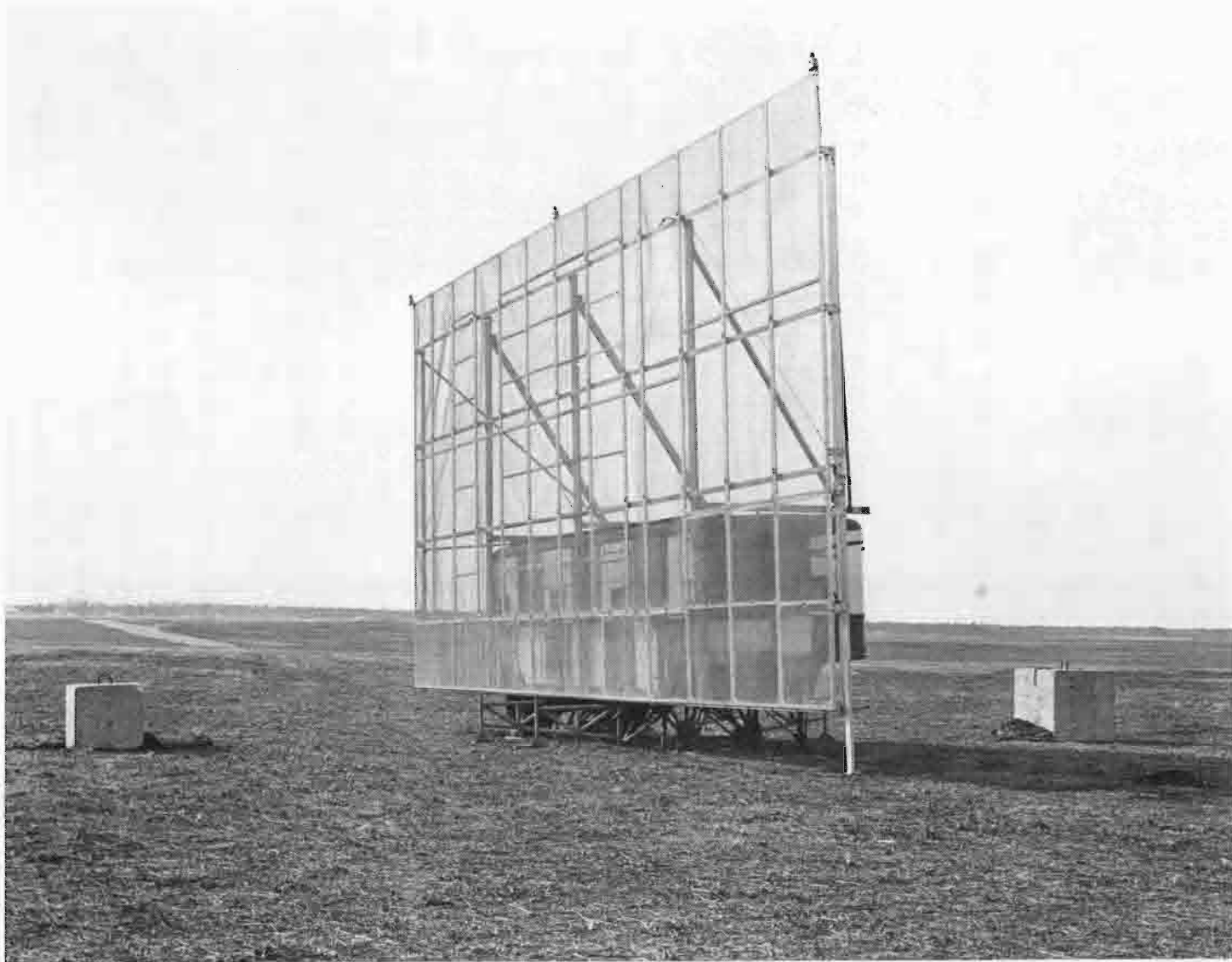
Fig. 2-8 Vertical screen used to provide TRSB reflection multipath.

Figure 2-9 shows the position of the reflecting screen used for the "multipath at rollout" test. This particular position and screen rotation (13.79°) yields a primary multipath region from 0.7 nmi prior to threshold (multipath azimuth = 29.2°) to 0.14 nmi past threshold (multipath azimuth = 30.8°). The M/D levels with such a geometry are quite sensitive to the unmeasured screen tilt from the vertical; thus, it was not feasible to compare the measured M/D levels with the propagation model results. However, it is quite easy with the TRSB system to determine out-of-beam multipath levels from received envelope traces and then compare the expected errors for that M/D with the actual errors.

Figure 2-10 shows envelope traces from two of the AZ multipath at rollout tests. The multipath is the larger of the two spikes by about 3-5 dB. Table 2-1 summarizes the M/D levels encountered. The peak control motion error observed in the multipath region (Figs. 2-11 and 2-12) is about 0.04°, which, using the result that peak sidelobe errors are about equal to $\rho \times$ SL*, indicates about a -31 dB sidelobe level. This implies that the computer model overestimates the sidelobe level by up to as much as 5 dB.

Then, a fair tolerancing of the "worst case"** simulation error overestimate for sidelobe multipath is (1.77-1.0) $\times \rho \times$ SL = 77% $\times$ (computed error). Inbeam discrepancies are considered negligible since the actual mainlobe pattern is used and it shows very little variation from static to dynamic conditions.

The low frequency error component in both the raw and control motion traces in Fig. 2-11 and 2-12 is not due to the screen, but rather a combination of the theodolite error and ground reflection effects. Both effects show up in the corresponding clean accuracy plot (Fig. 2-13). The ground reflection effect remains after film correction (Fig. 2-14). Unfortunately, the multipath data cannot be film-corrected due to tracking equipment failures during the test.

*Multipath amplitude $\times$ sidelobe level.

**We use the term "worst case" here because the TRSB testbed dynamic sidelobes were largest in the angular region corresponding to screen multipath.

2-13

$\gamma = 13.59^{\circ}$

NOT TO SCALE
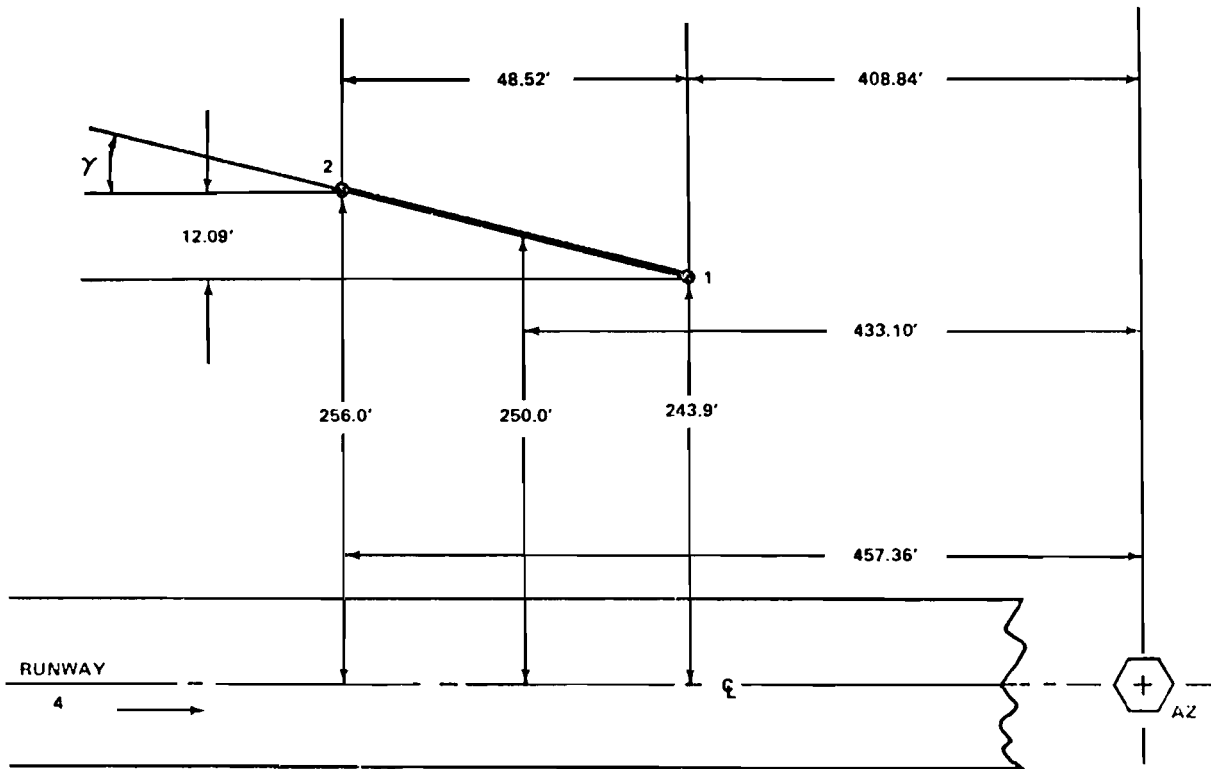
Fig. 2-9 Screen position of multipath at rollout test.

2-14

MULTIPATH

DIRECT

5 DB

1-23-76 RUN 5 1112

6 dB

MULTIPATH TO 1408:50.6

x = 10,124'

z = 153'

OMNI
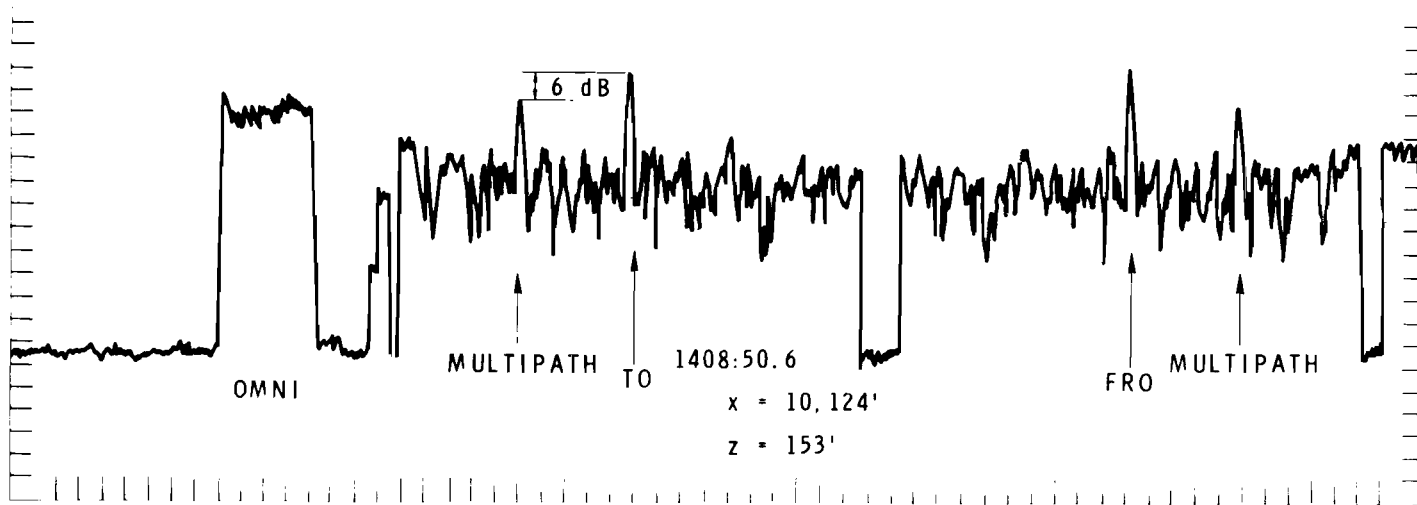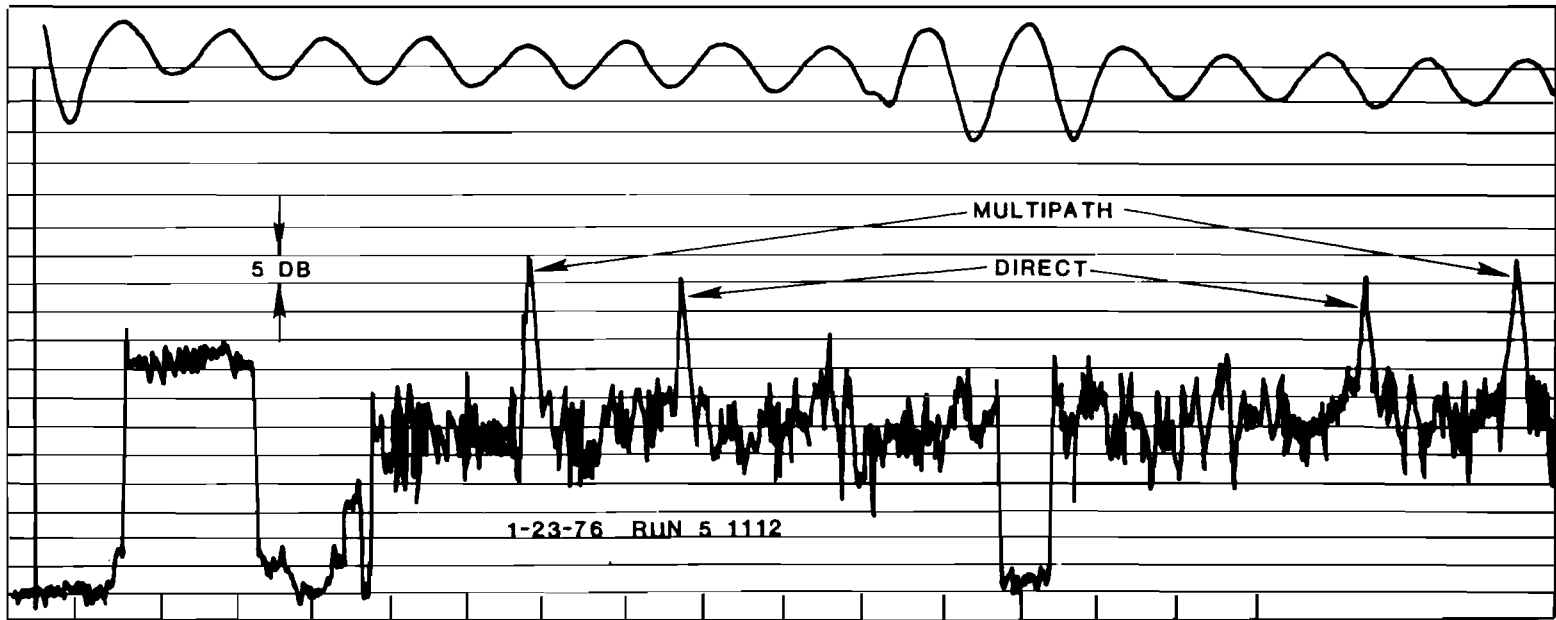
FRO MULTIPATH

AZ MULTIPATH AT THRESHOLD

Fig. 2-10 Received envelope on TRSB "multipath at threshold" test.

TABLE 2-1

MEASURED MULTIPATH LEVELS VS. RECEIVER LOCATION FOR

NAFEC "AZIMUTH MULTIPATH AT ROLLOUT" TESTS

Run #	Range (nmi)*	Relative Multipath Amplitude (dB)
5	(+) 0.01	(-) 3.5
5	(-) 0.18	(+) 2.5
5	(-) 0.41	(+) 5.0
5	(-) 0.52	(-) 3.0
6	(+) 0.01	(-) 1.0
6	(-) 0.19	(+) 1.0
6	(-) 0.30	(+) 2.5
6	(-) 0.41	(+) 5.0
6	(-) 0.52	(+) 3.0
6	(-) 0.58	(-) 3.5

*From runway threshold
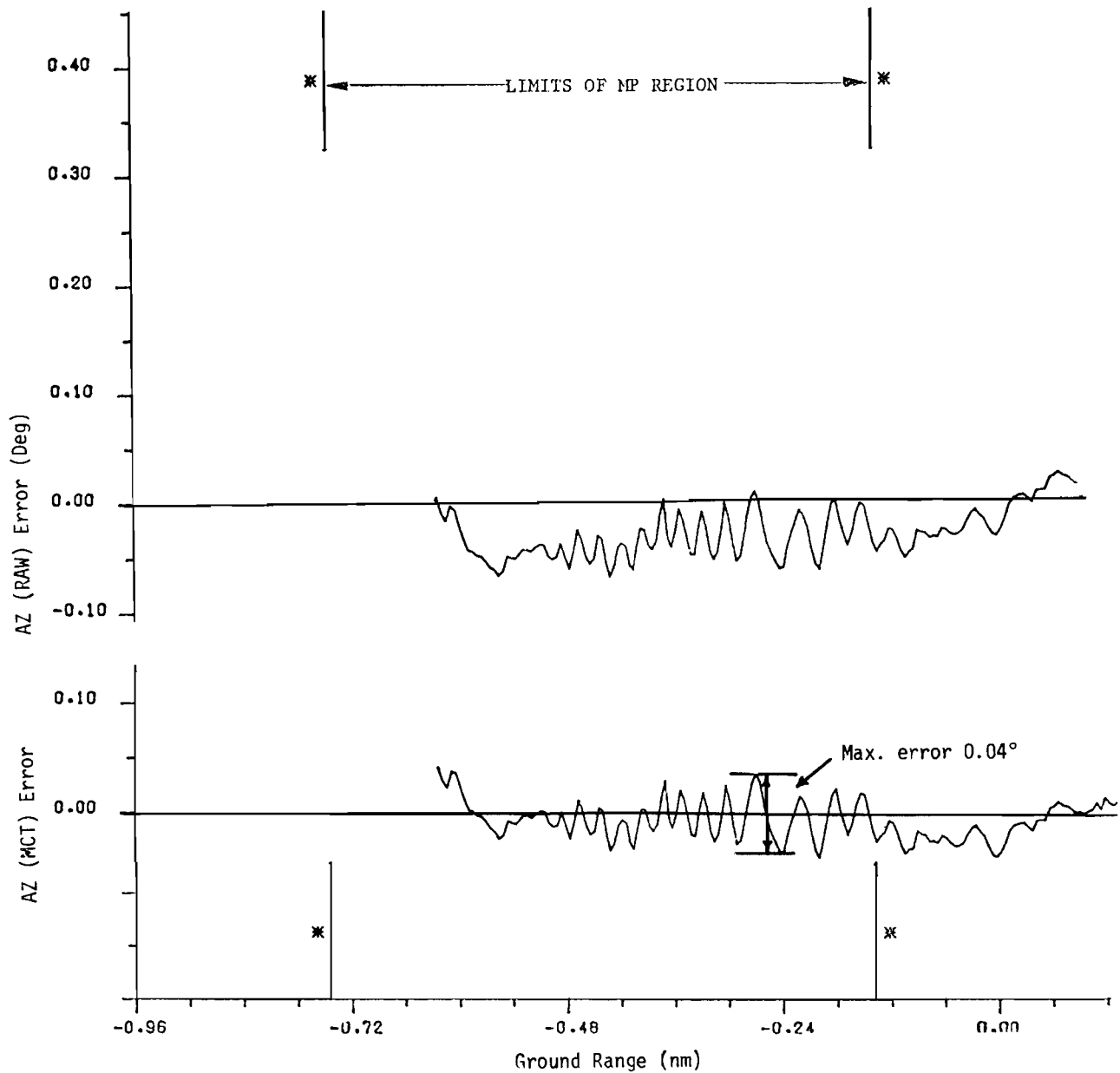
Fig. 2-11   Raw and control motion errors for "AZ multipath
at rollout" test.
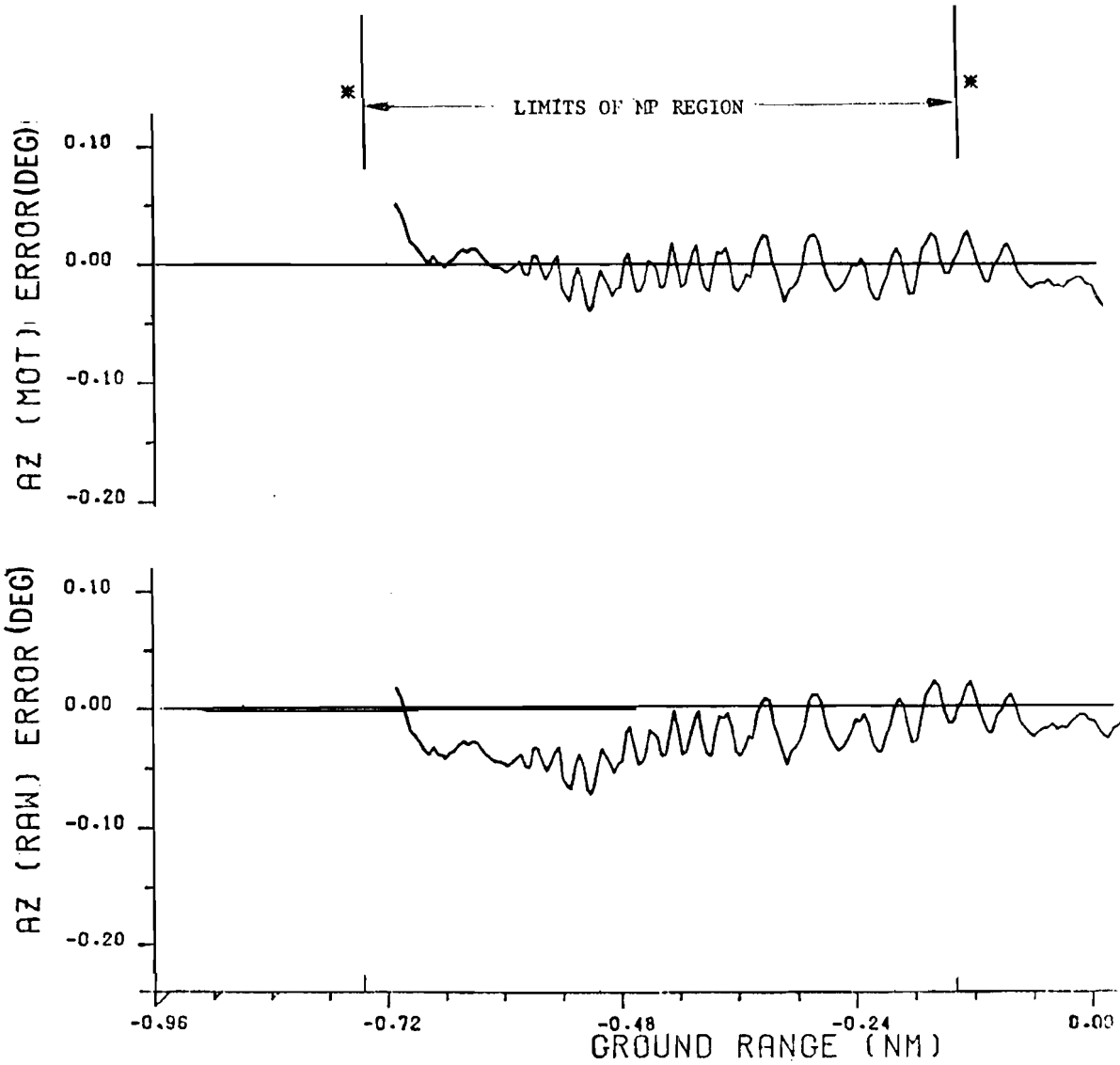
Fig. 2-12   Raw and control motion errors for "AZ multipath at threshold" test.

TIME REFERENCED SCANNING BEAM
MICROWAVE LANDING SYSTEM

DATE	28AUG75	TRACKING	THEODOLITE
A/C	DC-6	TEST	13/1-1
PATTERN	3 DEGREE CENTERLINE. LOW APPROACH

CENSORED PTS.   0

1-B.2.AZ.AP.1.6   APP AZIMUTH   ACCURACY   3 DEG APPROACH

TIME REFERENCED SCANNING BEAM
MICROWAVE LANDING SYSTEM

DATE	28AUG75	TRACKING	THEODOLITE
A/C	DC-6	TEST	13/1-1
PATTERN	3 DEGREE CENTERLINE. LOW APPROACH

CENSORED PTS.   0

FILM CORRECTED

1-B.2.AZ.AP.1.4   APP AZIMUTH   ACCURACY   3 DEG APPROACH

Fig. 2-13 Clean accuracy error plot for
AZ rollout (without film correction).
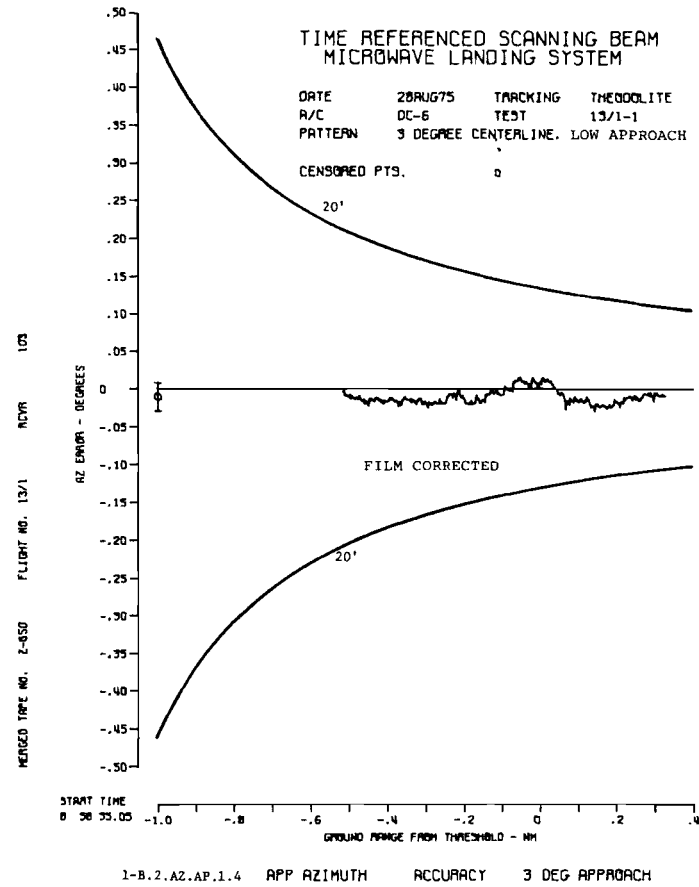
Fig. 2-14 Clean accuracy error plot for
AZ rollout (with film correction).

b.   Inbeam Multipath

Inbeam azimuth reflections from buildings or aircraft is quite unlikely due to the geometry required; however, inbeam diffraction (shadowing) multipath was encountered in several of the shadowing tests carried out at NAFEC. Tests were carried out with the shadowing aircraft over flying the azimuth ground station (e.g., as by an aircraft taking off in front of the landing aircraft) and with the shadowing aircraft turning off the runway (as after rollout).

Figure 2-15 shows the precision tracker angular positions of the shadowing CV880 and test aircraft for an overflight test conducted in November, 1976. Figure 2-16 compares the measured overflight azimuth error with the computed error using the tracker data to generate simulation flight profiles. Both the error magnitude and waveform are seen to be in good agreement.

Another set of tests were carried out with the CV880 taxiing down the runway and turning off the runway as the aircraft, with a TRSB receiver, neared the runway threshold. In this case, the location of the landing aircraft at the time of turnoff commencement was noted; however, there was not precise tracking of the CV880 during turnoff. The actual turnoff manuver is a somewhat complicated combination of rotation on centerline followed by a slightly curved forward trajectory. This was (crudely) approximated in the simulation by having the aircraft taxiing at 5 m.p.h. in a straight line which was at an angle of 60° with respect to runway centerline (see figure 2-17). Figure 2-18 compares the simulation result with the measured errors on two of the flights. We see that the initial negative going portion of the error is emulated fairly well; however, the final positive error spike is smaller in the simulation than was the case in the field test. This difference is felt to arise from the differences between the actual CV880 tail fin profile and that assumed in the simulation model (see Fig. 2-19). Given the fairly crude profile and taxiing aircraft path approximations, the overall agreement between simulation and field test here is regarded as quite good.

It should also be noted that studies of inbeam azimuth diffraction errors
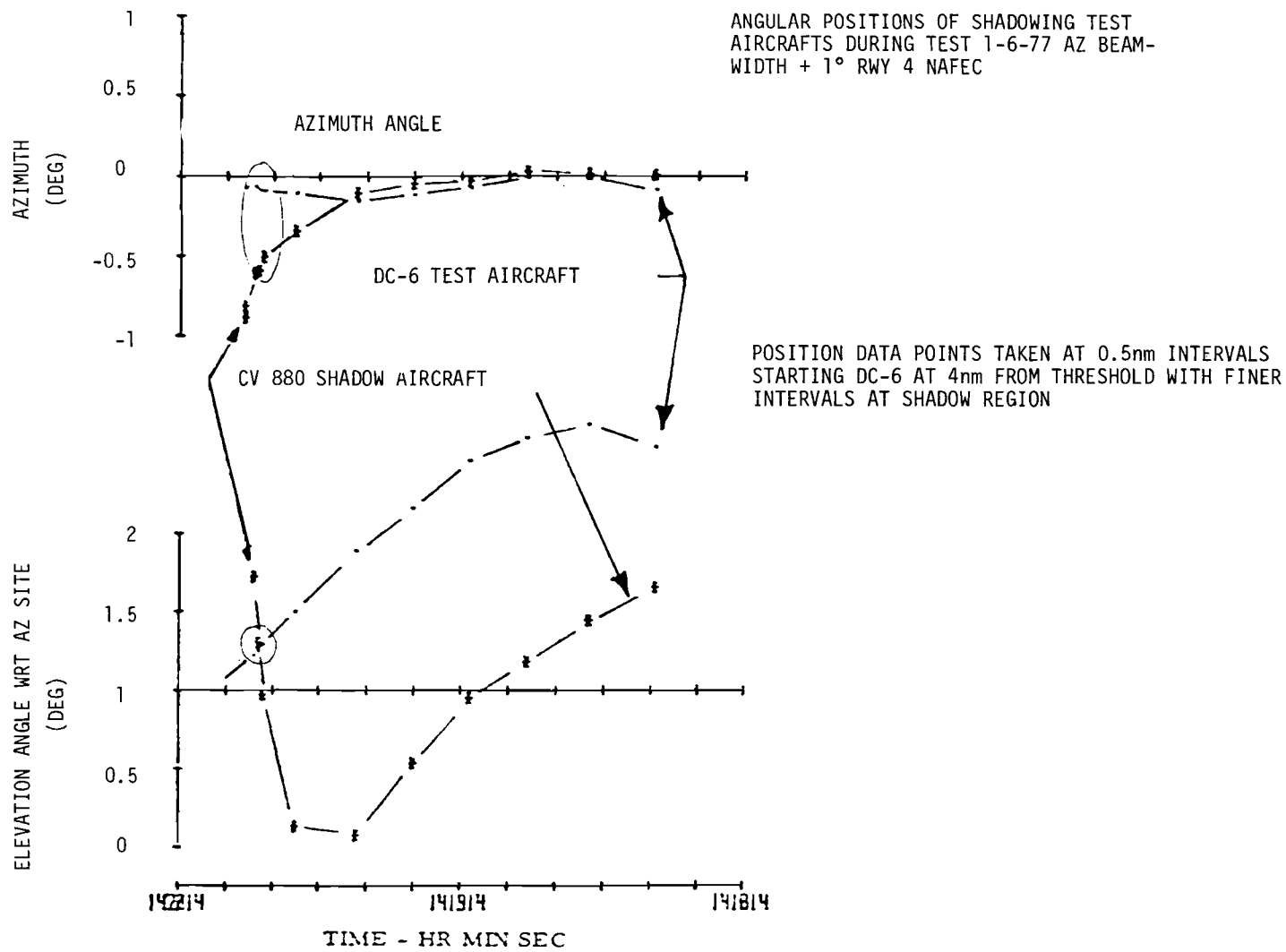
Fig. 2-15 DC-6 and CV 880 tracked AZ and EL (re AZ site) on Run #4.
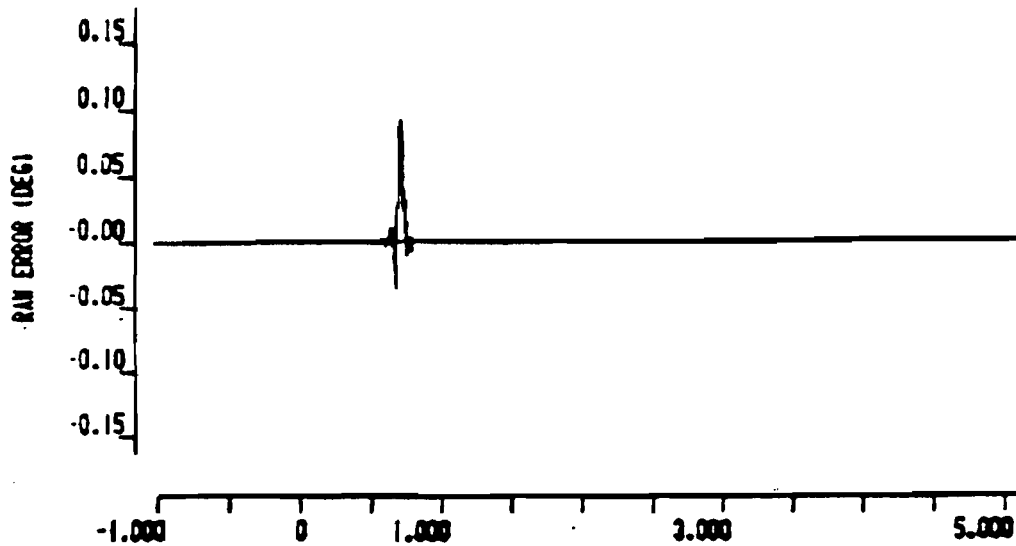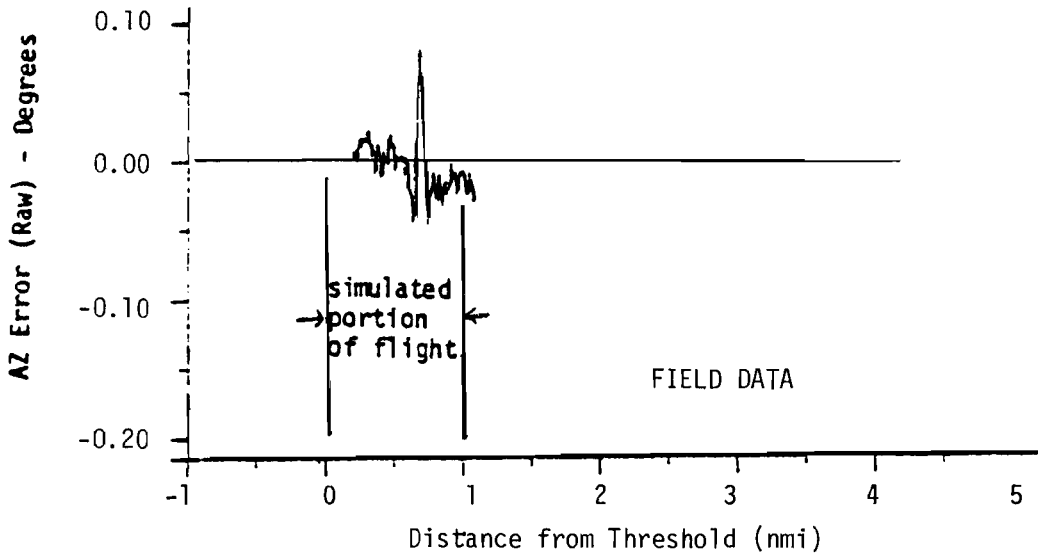
Fig. 2-16   Comparison of simulation and field data for TRSB overflight test.

Y POS FT

2000.

1000.

0.

-1000.

Az   SA1

ℓ_{L2} ℓ_{L1}

C1
RUNWAY

Path followed by taxiing aircraft

0.   1000.   2000.   3000.   4000.   5000.   6000.   7000.   8000.   9000.   10000.

X POS FT
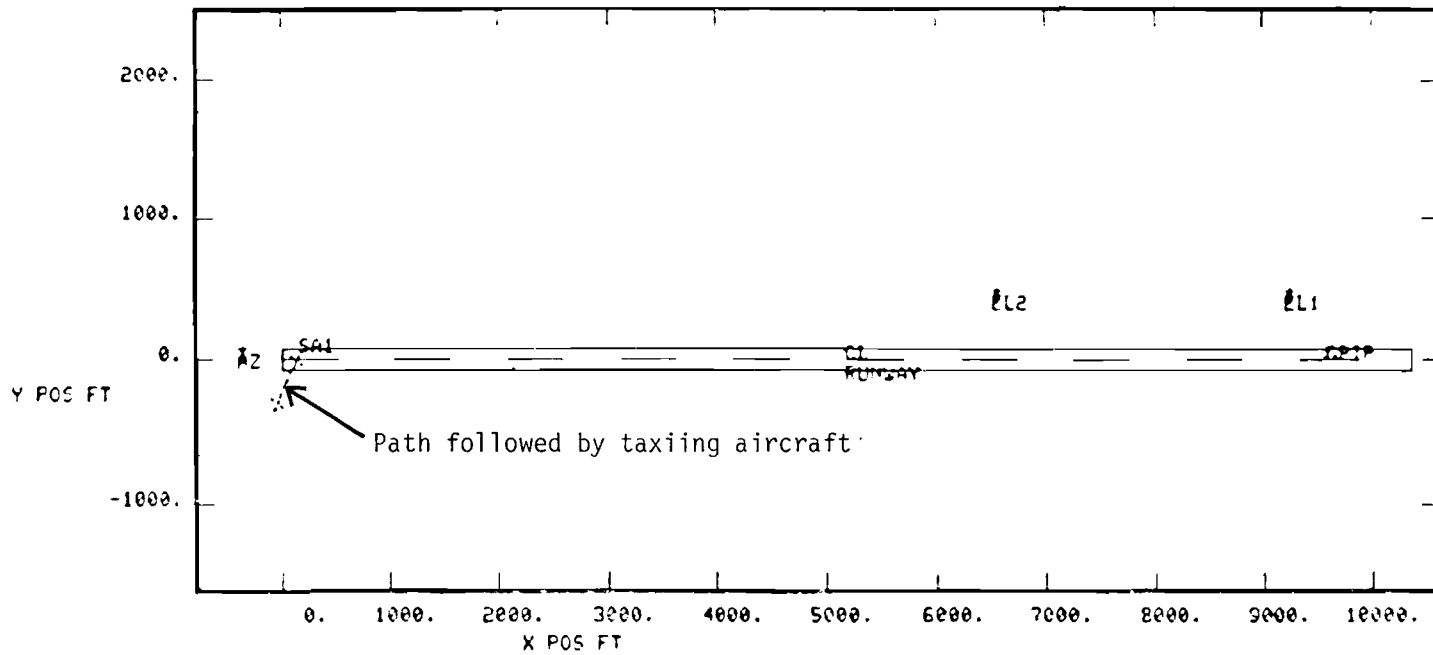
Fig. 2-17   Assumed geometry for simulation of shadowing by taxiing aircraft.
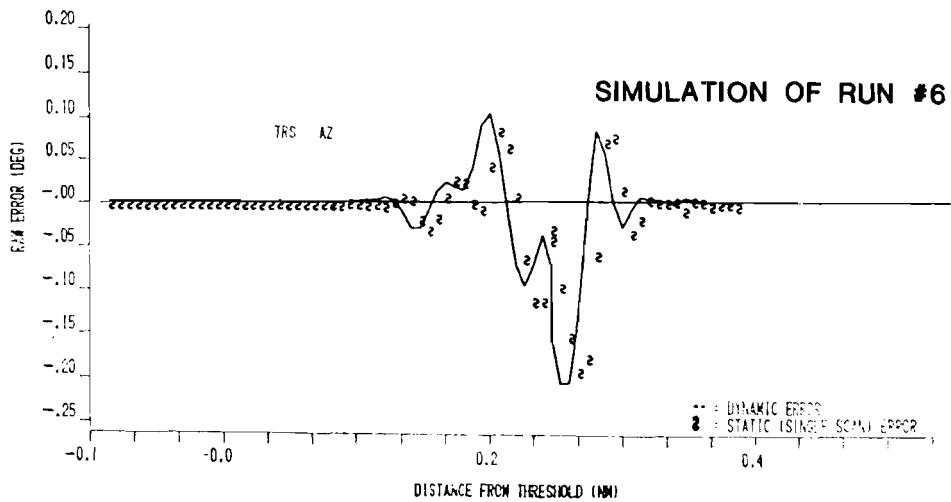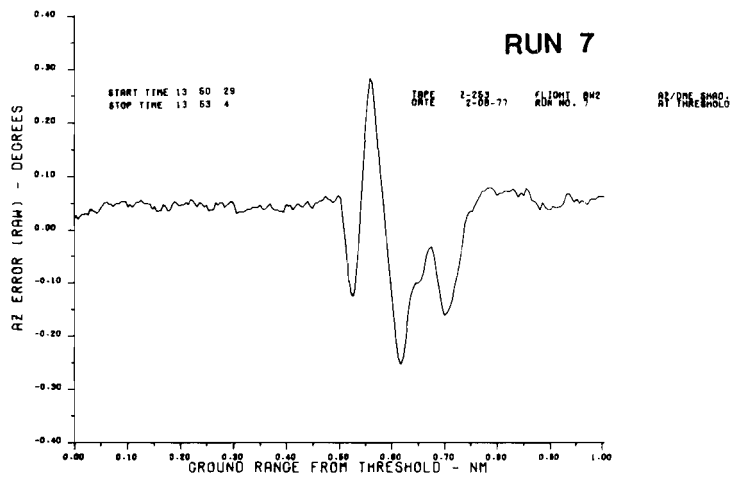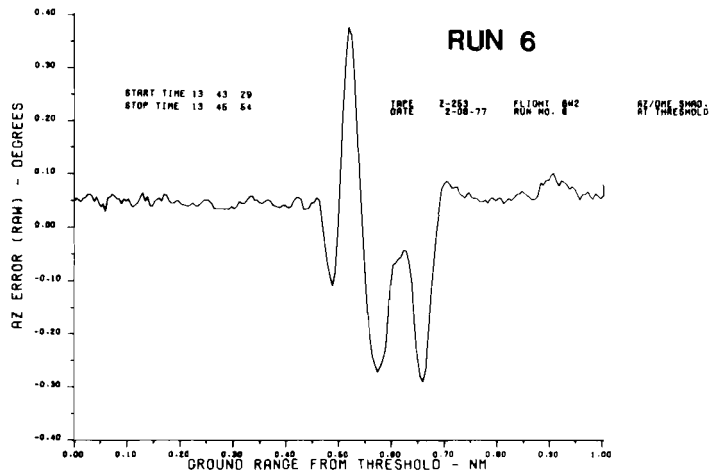
Fig. 2-18 Comparison of simulation with TRSB taxiing aircraft shadowing test data.

(a) side view of CV 880 aircraft

—— = aircraft side profile

--- = approximating profile with two rectangular plates
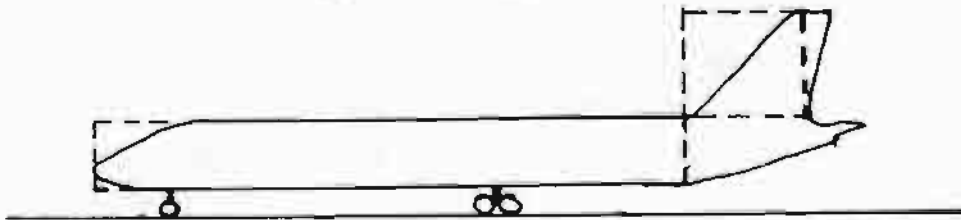
(b) shadowing profiles

Fig. 2-19 Comparison of actual CV-880 profile with simulation model profile.

due to a MLS monitor structure were reported in Chapter IV of volume I of this report. However, in that case, the shadowing object was in the very near field of the ground antenna and hence of lesser interest for validation of the far field antenna/received signal models.

2. Elevation

a. Out-of-Beam Multipath

The principal source of out of beam elevation multipath for the TRSB system is specular reflections from the ground. It was not possible to ascertain the level of these reflections from the received envelope traces since the elevation scanning beam does not scan down into the ground. Therefore, a simulation was made for the testbed 1° elevation array over flat terrain $(\varepsilon/\varepsilon_0 = 6)$ for an aircraft flying along a 0° azimuth radial at a height of 2,000 feet. This particular profile gives rise to a sizable range of separation angles and relative rf phases such that sidelobe errors should be evident Figure 2-20 shows the computed multipath characteristics, while Figure 2-21 compares the simulation errors with the flight test results for one such radial at NAFEC. We see that the flight test error at the multipath frequency (1 cycle per 0.4° in elevation angle) is slightly smaller than the simulation error, again suggesting that the sineusoid sidelobe model is probably conservative.

b. Inbeam Multipath

In-beam reflection elevation multipath from structures or aircraft is more common with the elevation system than the azimuth system, since the elevation fan beam has a wide azimuth extent, which can illuminate vertical surfaces while it is illuminating the aircraft. One source of such multipath was the ICAO multipath tests using a screen in the near field of the elevation antenna.

(i.) Screen Multipath Tests at NAFEC

The "EL multipath at threshold" test is shown in Fig. 2-22, taken from the U.S. TRSB submission [65]. In this test, the results might have been somewhat different had a TRSB phase III receiver been used instead of a TRSB

X = G
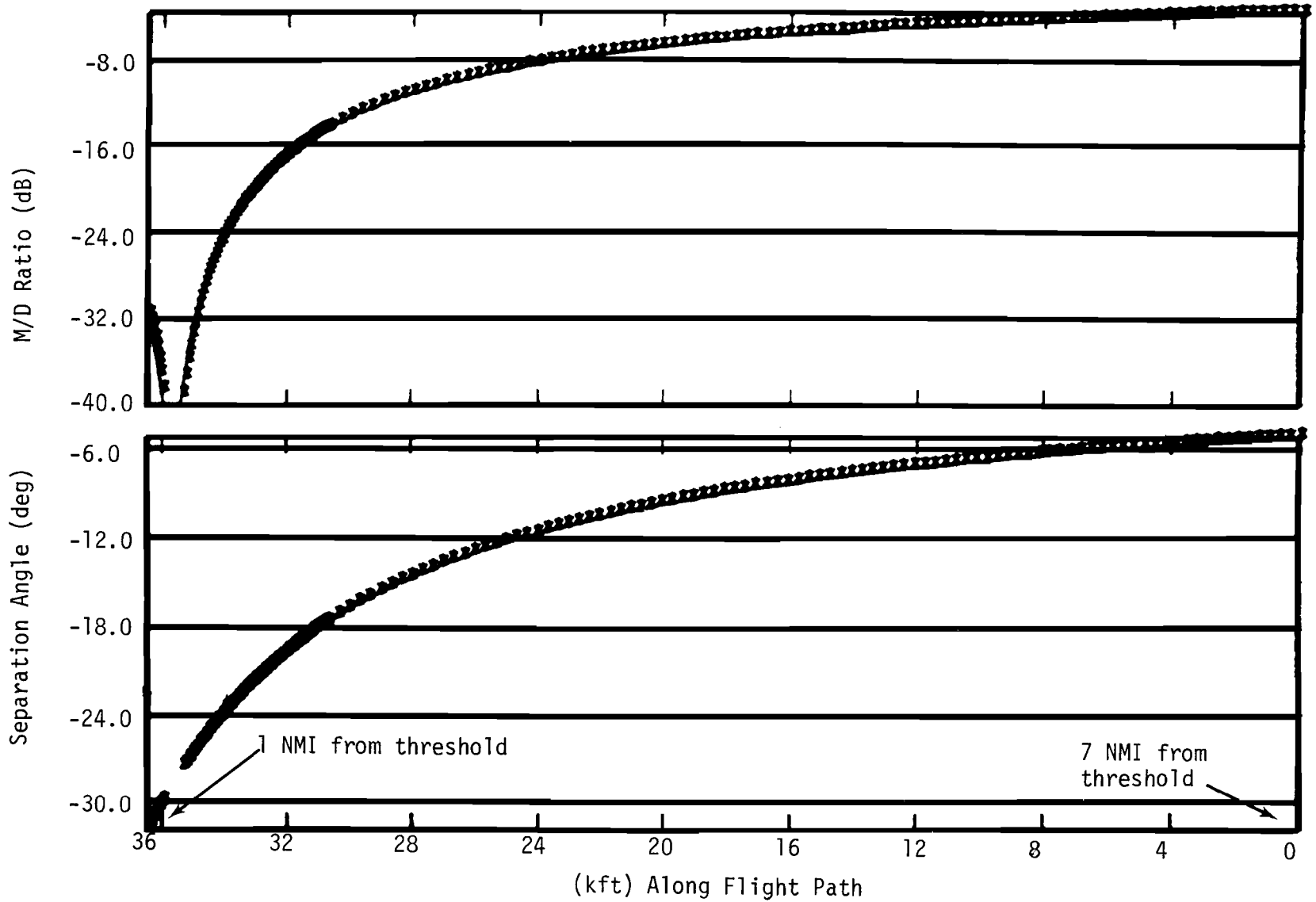
Fig. 2-20 Computed ground reflection multipath characteristics for 0° azimuth radial flight at 2000 ft.
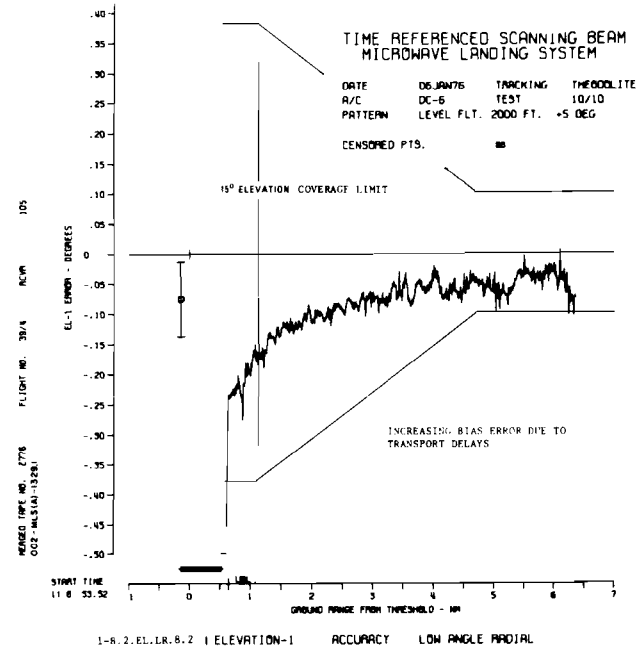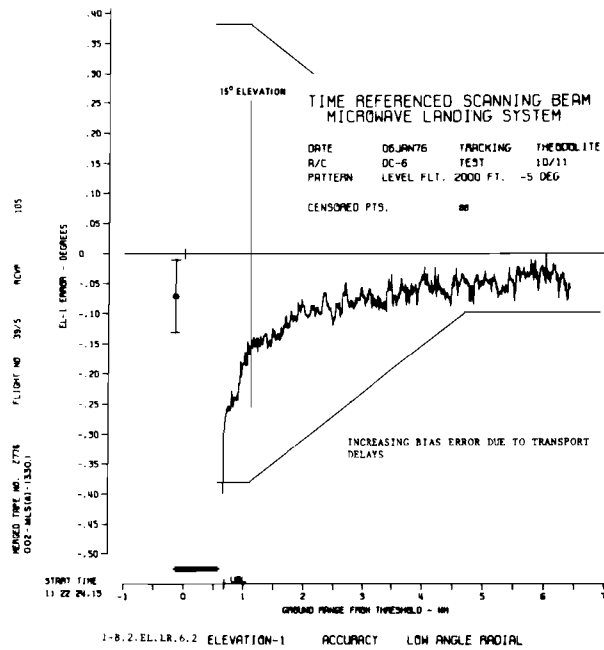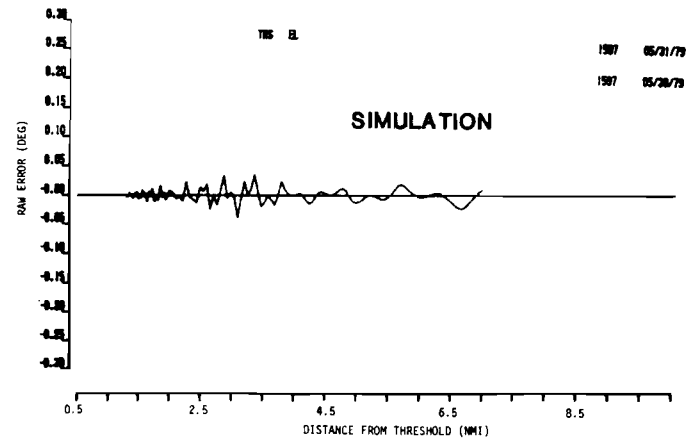
Fig. 2-21   Simulation of elevation error due to ground reflections along CL radial at 2000 ft. altitude.
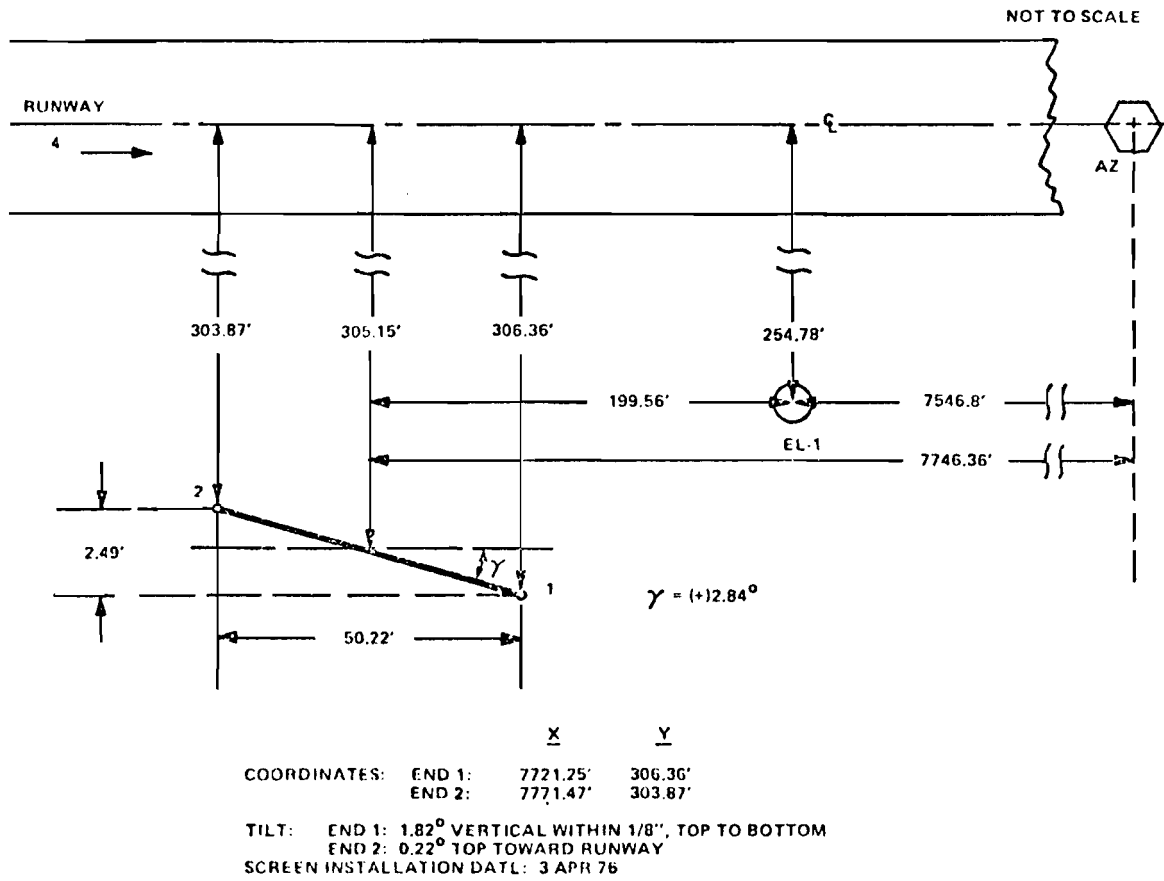
Fig. 2-22 EL "multipath at threshold" test.

Phase II receiver. The Phase II slew limiter, which was placed ahead of the smoothing filter, introduces a bias component into the errors. This topic has been studied extensively, and summary results are provided in Volume III.

To simulate this test, a warped/tilted screen model consisting of five separate 10 foot wide vertical plates with linearly increasing tilts are used. The computed multipath characteristics are shown in Fig. 2-23. The simulation output and the film-corrected error traces are shown in Fig. 2-24. These match quite well, except for an offset of 0.05° in the test data. There is no known reason (e.g., the slew limiter) to expect a bias such as that in the test, and it does not appear in the simulation. The most likely explanation is that there is still an uncorrected error in the tracker.

Figure 2-25 illustrates the test geometry for the "EL multipath on glide slope" ICAO test. This test provided a better validation of the Phase III receiver model since the processor characteristics are virtually identical at the low scalloping rates. Both 2° and 3° approaches were flown. Two separate sets of simulations were performed. In the first simulations, the aircraft was assumed to fly on the nominal glidepath without any vertical or horizontal excursions and a 5 plate model utilized for the screen. Figures 2-26 and 2-27 show the computed multipath characteristics for the 2° and 3° nominal glideslopes.

The results of three runs on the 2° approach are shown in Fig. 2-28 along with the simulation output. Although the three experimental traces differ somewhat in detail, there is reasonable similarity among them, especially with regard to the observed scalloping rates and general level of error magnitudes. The error plot generated by the simulation exhibits similar characteristics. Fig. 2-29 contains comparative results for the 3° approach. Again, the error magnitudes, scalloping rates, and general time history of the traces show good similarity.

To better understand the role of the deviations of the actual flight profile from the nominal flight path in generating differences between the

Bi = multipath for ith screen segment

1 • B1   X • B3   + • B4   Y • B2   0 • B5
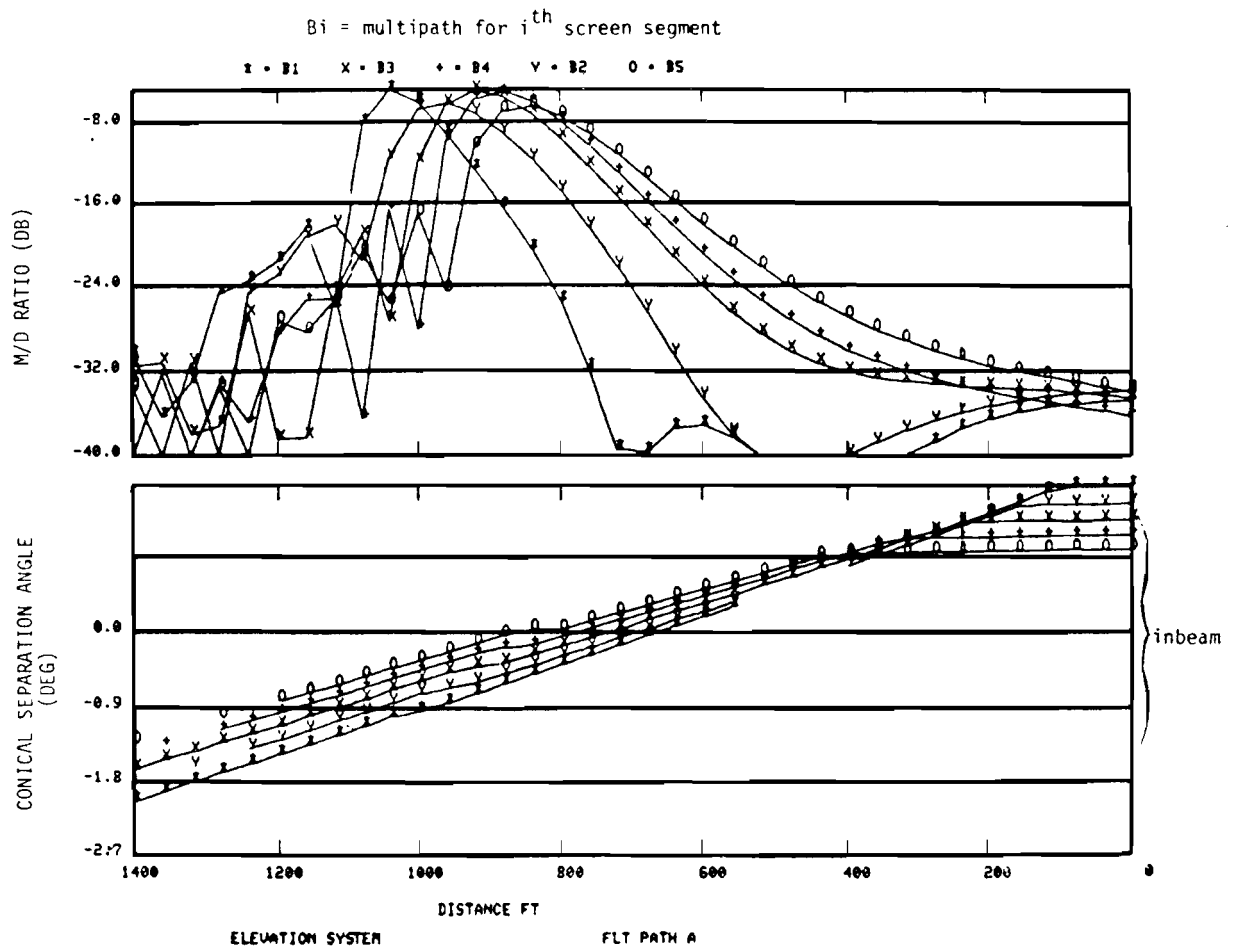
Fig. 2-23 Elevation multipath characteristics for tilted/warped screen used for "multipath at threshold" test.

2-31
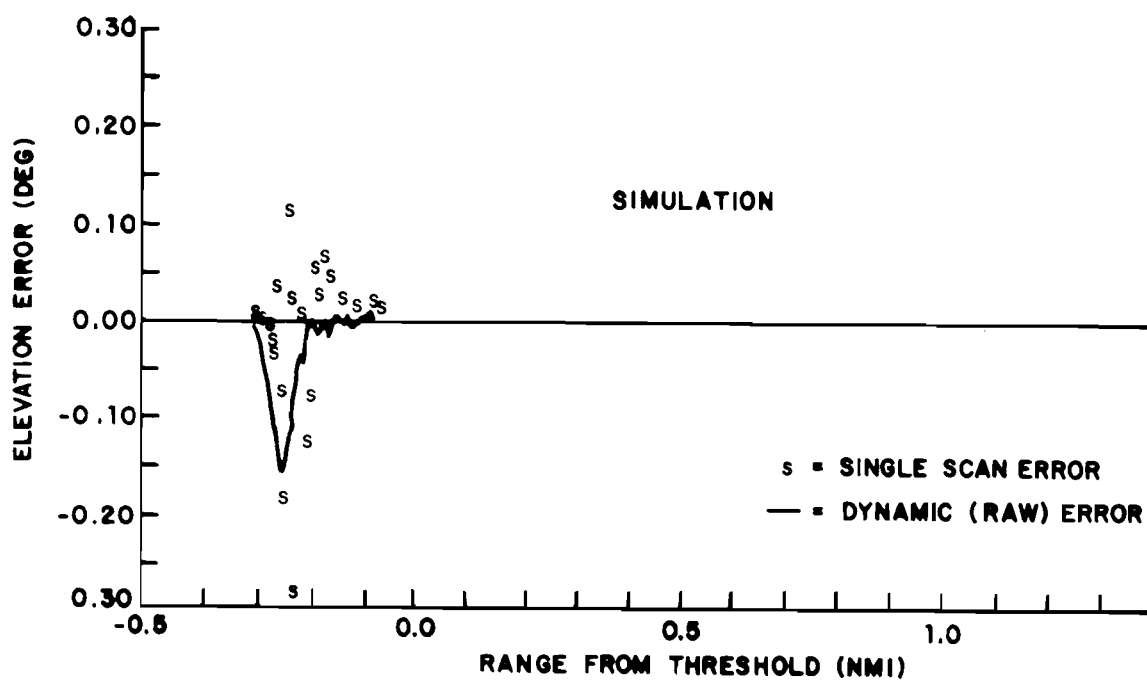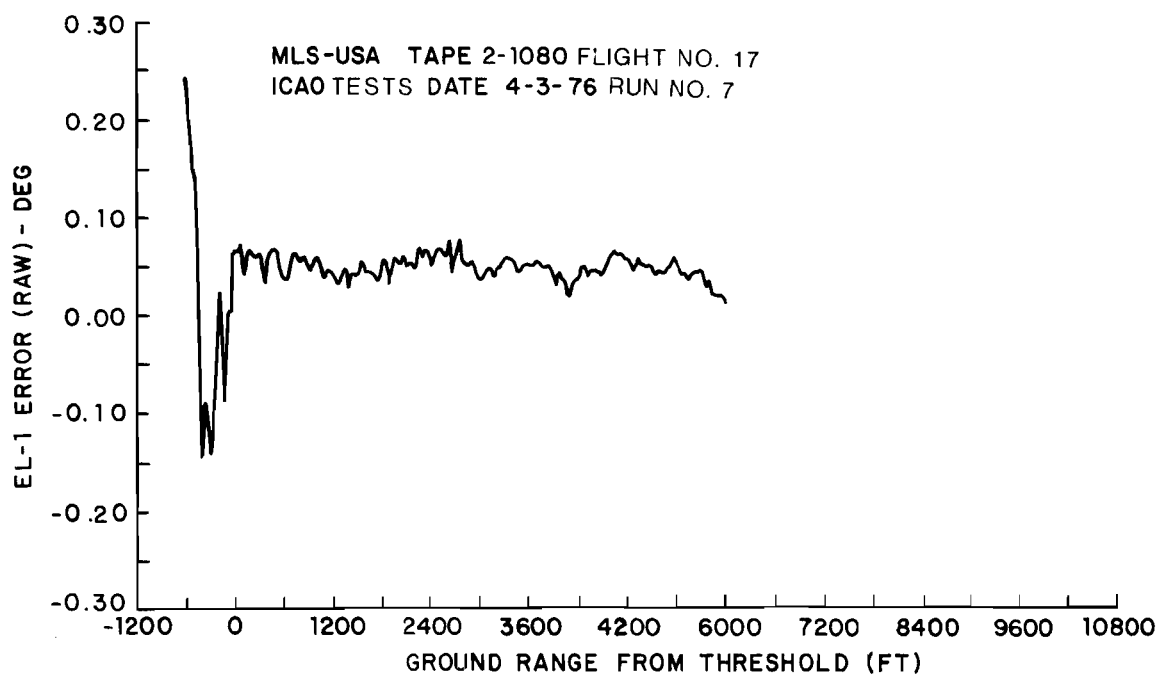
Fig. 2-24 Comparison of simulation with "EL multipath at threshold" field test.

RUNWAY

⊄

AZ

309.75'   306.94'   304.13'

254.78'

199.61'

EL-1

7546.8'

7746.41'

1

γ

5.62'

2

49.86'

γ = (–)6.43°
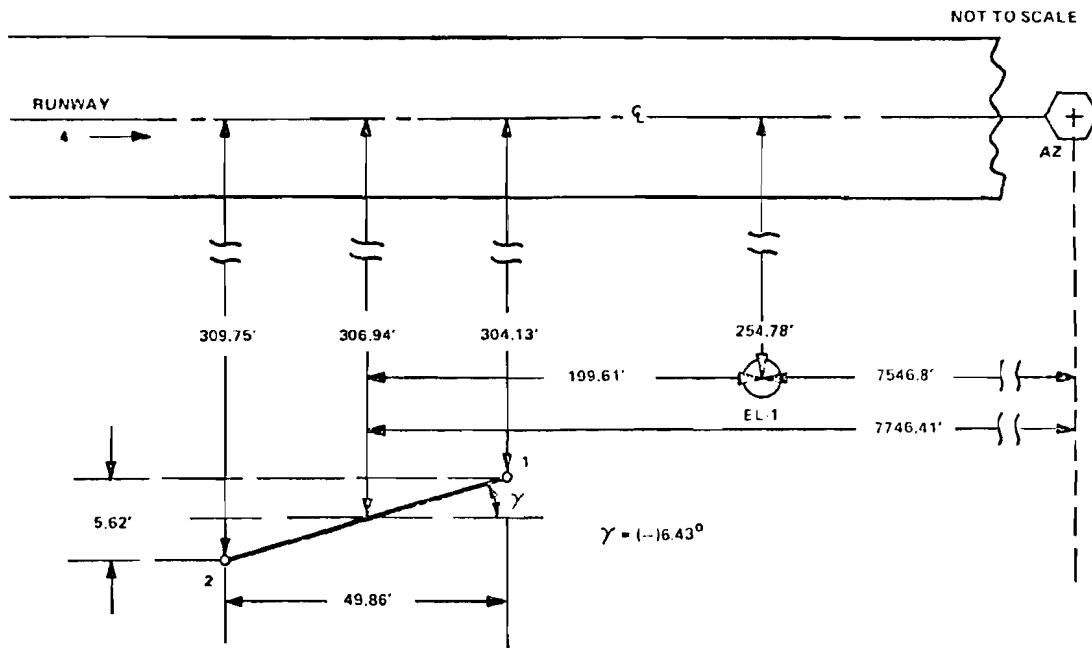
		X	Y
COORDINATES:	END 1:	7721.48'	304.13'
	END 2:	7771.34'	309.75'

TILT: END 1: 0.00° VERTICAL WITHIN 1/8", TOP TO BOTTOM
         END 2: 1.63° TOP TOWARD RUNWAY
SCREEN INSTALLATION DATE: 4 APR 76

Fig. 2-25 EL "multipath on glide slope" test setup.
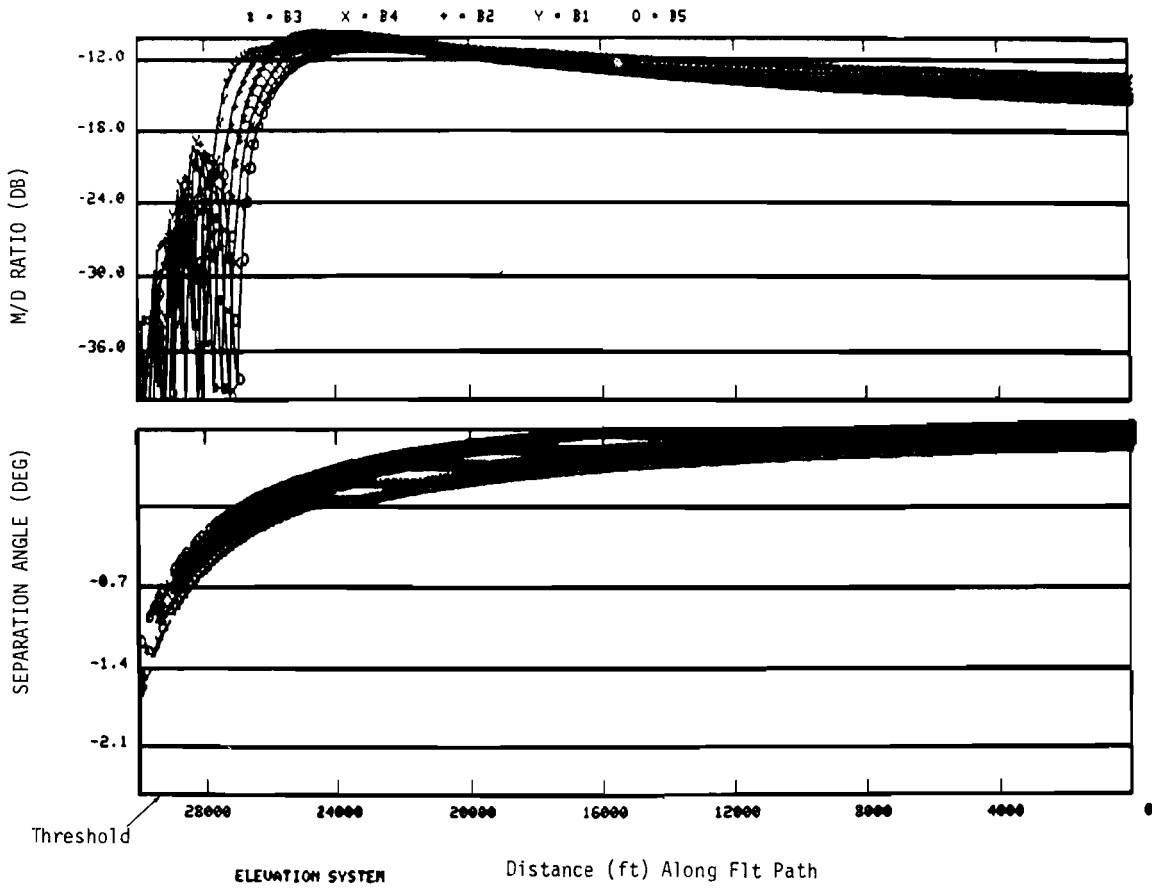
Fig. 2-26 Multipath characteristics for warped/tilted screen used at NAFEC for "elevation multipath on glide slope" test (2° approach).
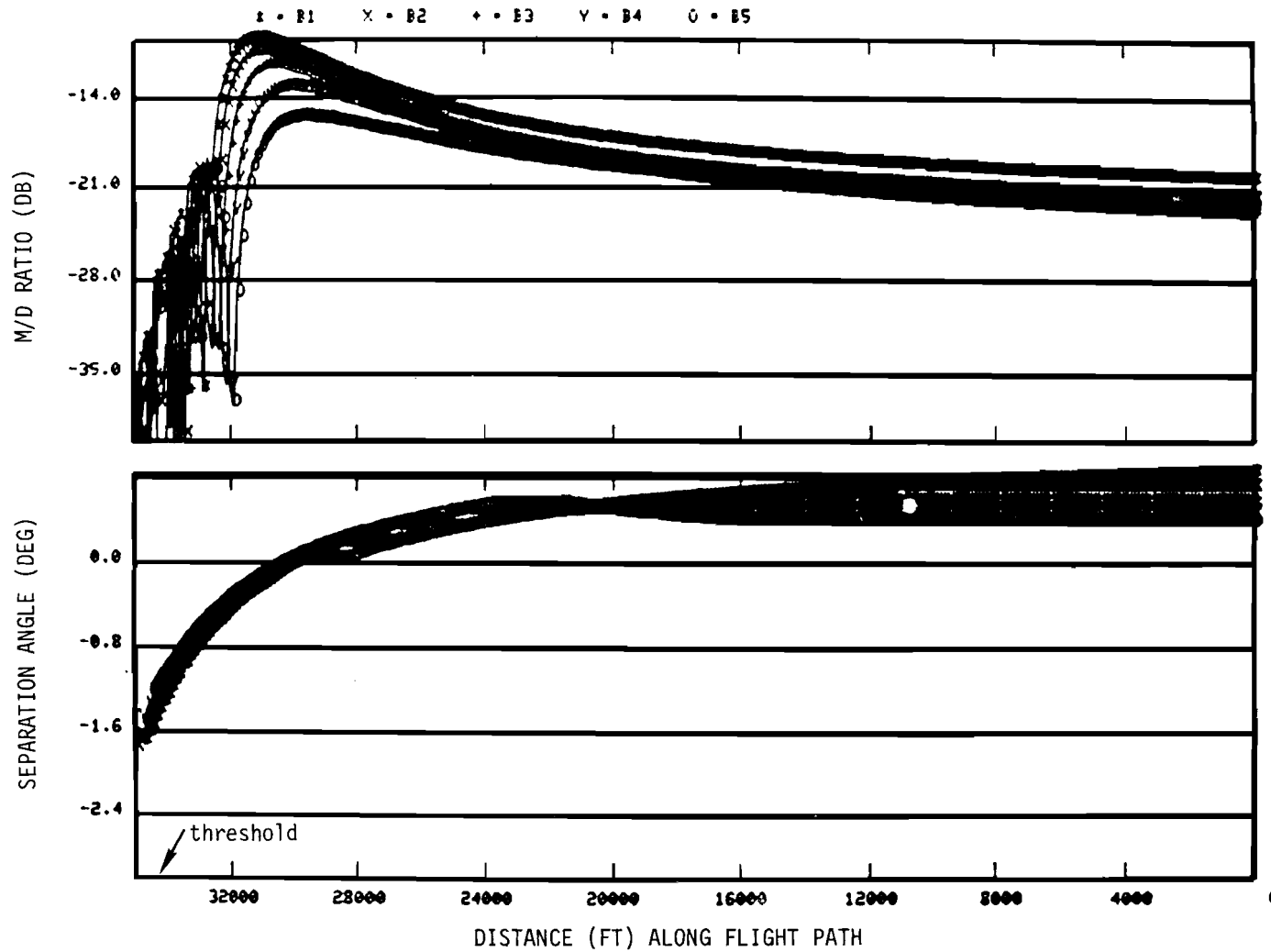
Fig. 2-27 Multipath characteristics for warped/tilted screen used at NAFEC for "elevation multipath on glide slope" test (3° approach).
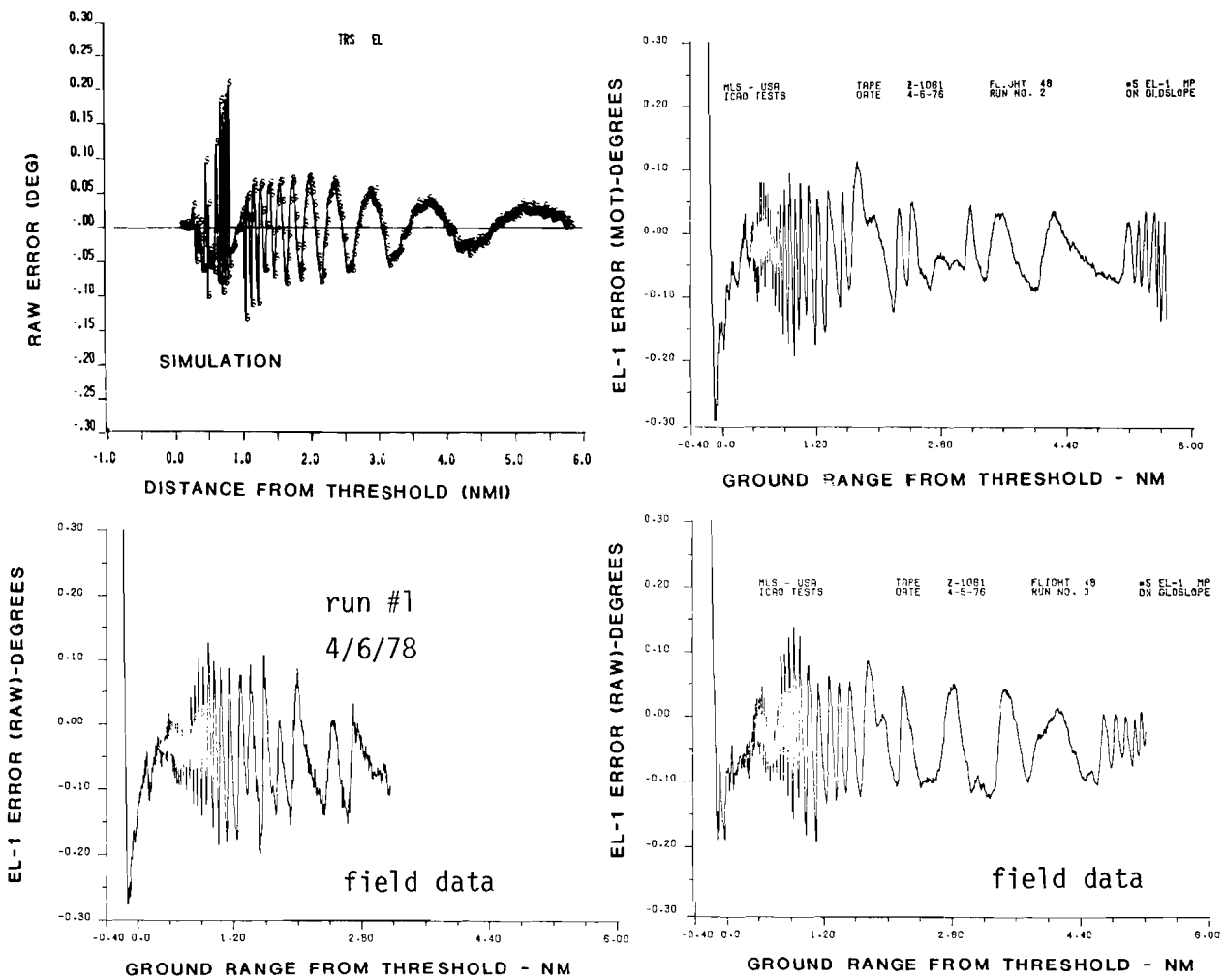
Fig. 2-28 EL errors, simulation and experimental, for "elevation multipath on glide slope" (2° approach).
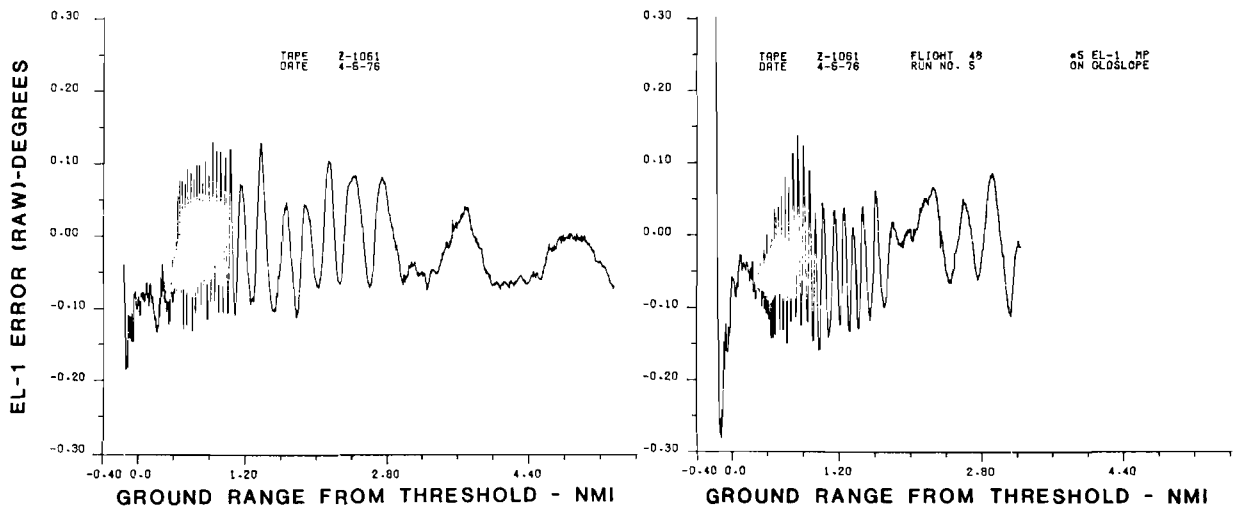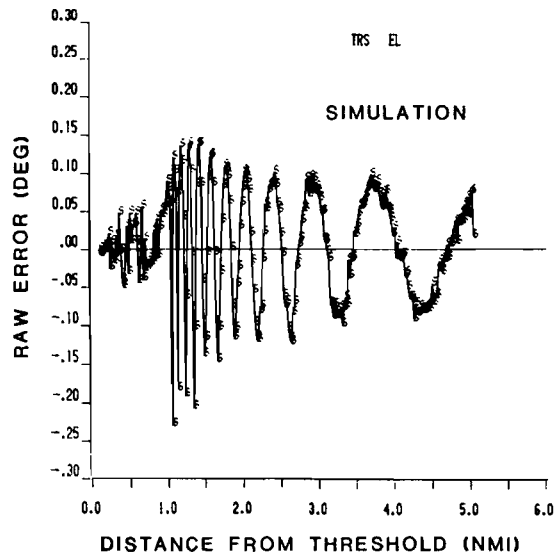
Fig. 2-29 EL errors, simulation and experimental, for "elevation multipath on glide slope" (3° approach).

simulation results and field data, a second set of simulations were made, in which the actual tracker history was used to generate the simulation flight profile. Two simulations of this type were performed; one using the previously mentioned five plate model for the screen and the other utilizing a single plate model. Figures 2-30 and 2-31 show the results for these simulations.

Comparing Figures 2-30 and 2-31 with 2-28 and 2-29, we see that a much better agreement has been obtained in the outer portion of the approach where aircraft heading changes (especially at turn-on) are the major factor in the observed error frequencies. However, the agreement near threshold (e.g., 1.0 nmi) is not significantly improved. The differences in the near in region are felt to arise primarily from the complicated (poorly known) nature of the screen warping, as well as unmodelled near-field effects (the screen to antenna distance = $0.3 \ L^2/\lambda$).

(ii). Hangar Multipath Tests at JFK Airport

The field tests at John F. Kennedy (JFK) International Airport, New York, in December, 1977 and February, 1978, provided an opportunity to measure TRSB response to both in-beam reflection and diffraction signals as illustrated in Figure 2-32. Both van tests and flight tests were conducted at the airport. The van test results, together with the corresponding airport model, were described in Volume I, Chapter 3, Section A of this report. Thus, the discussion here will focus on the flight test results, which were rather more complicated to model due to the greater number of obtacles which may be of concern.

Figure 2-33 shows some of JFK runway 13L environment near the MLS elevation sites used. Some idea of the obstacle density near the airport end can be obtained from the horizon survey data shown in Figure 2-34. The same runway end was also used as the basis for several of the ICAO standard multipath scenarios (repeated in Volume III of this report).

The two principal multipath threats in the AWOP comparative scenarios were the Seaboard cargo building and hangars 3-4-5. Figure 2-35 shows the front view of the Seaboard cargo building and the exaggerated profile assumed
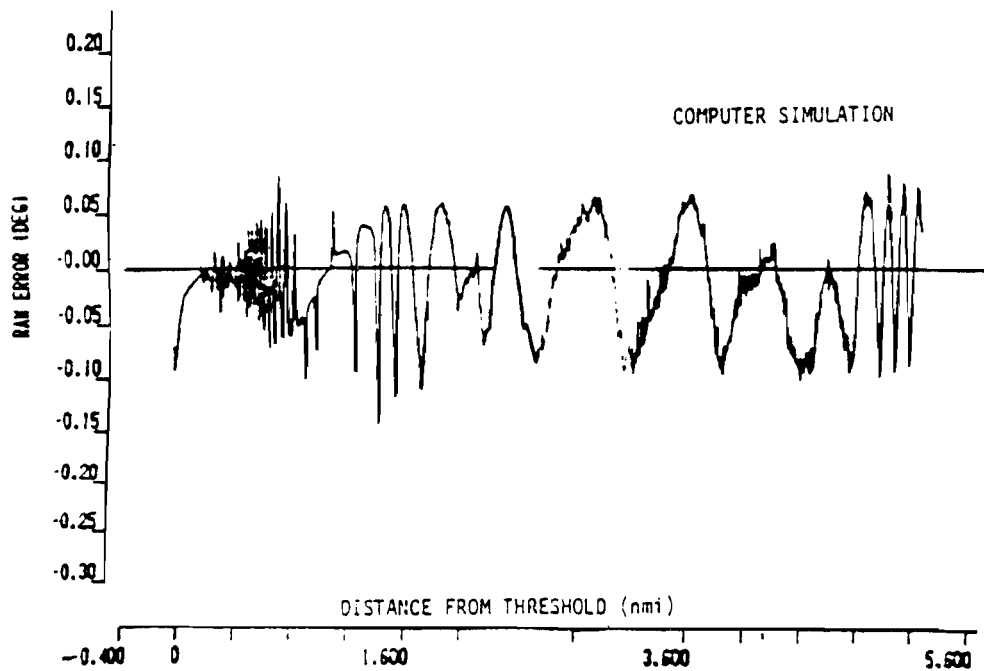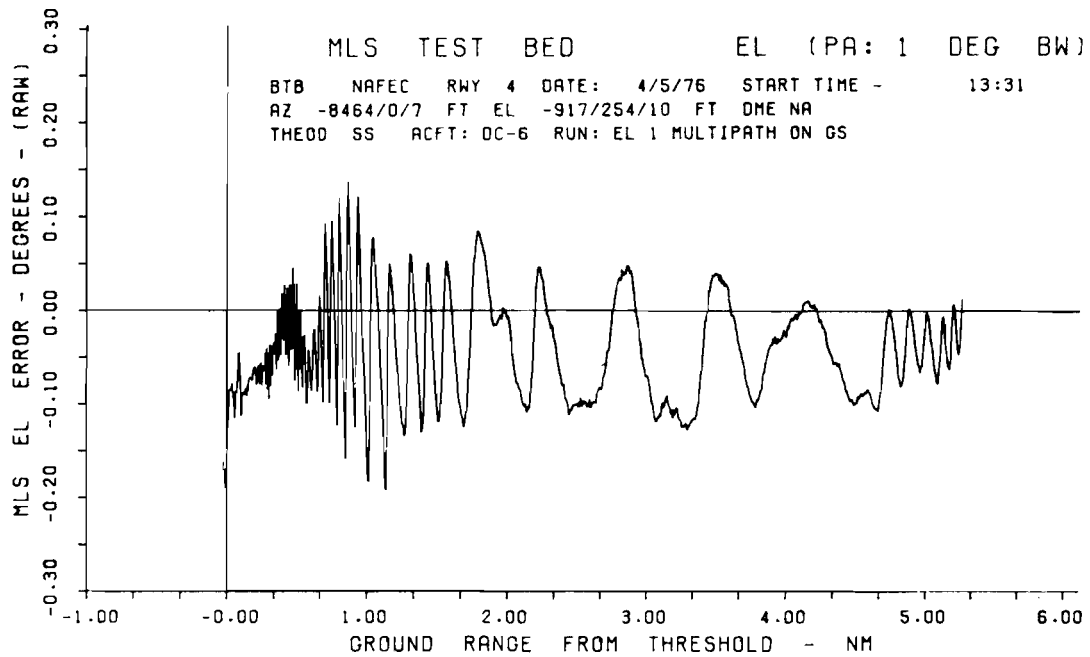
Fig. 2-30 Comparison of field data and computer simulation for elevation multipath field test.
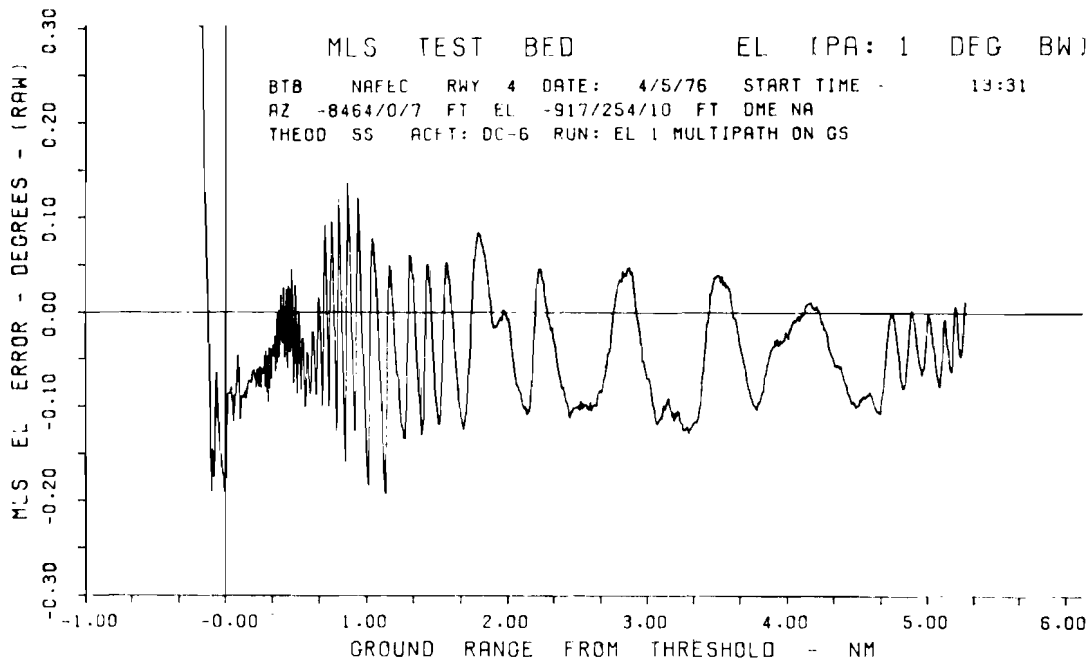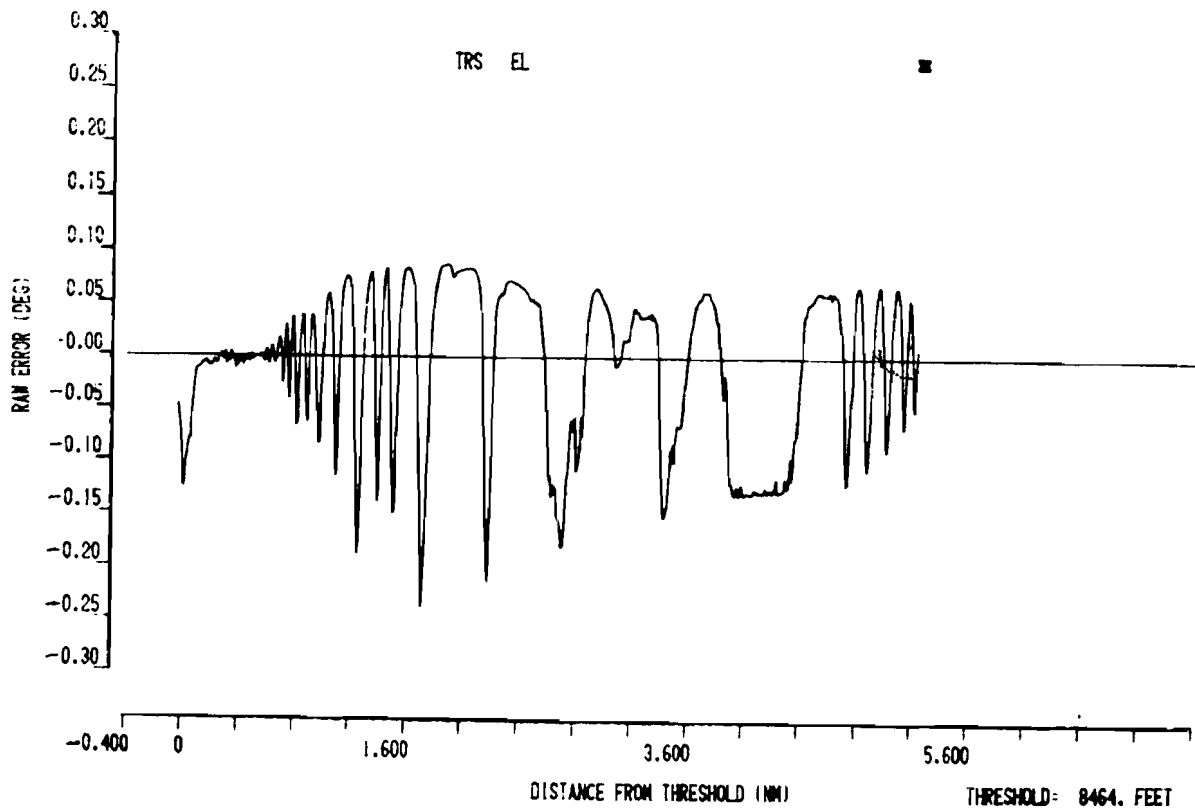
Fig. 2-31 Comparison of field data and simulation with
single plate screen model.

MULTIPATH
REGIONS

DIFFRACTION
REGION

5 N MILE ARC

-38°

38°

2000 FT
38° RADIAL

DIFFRACTION

EL

HANGARS 3,4,5

REFLECTIONS

38°   38°

AZIMUTH
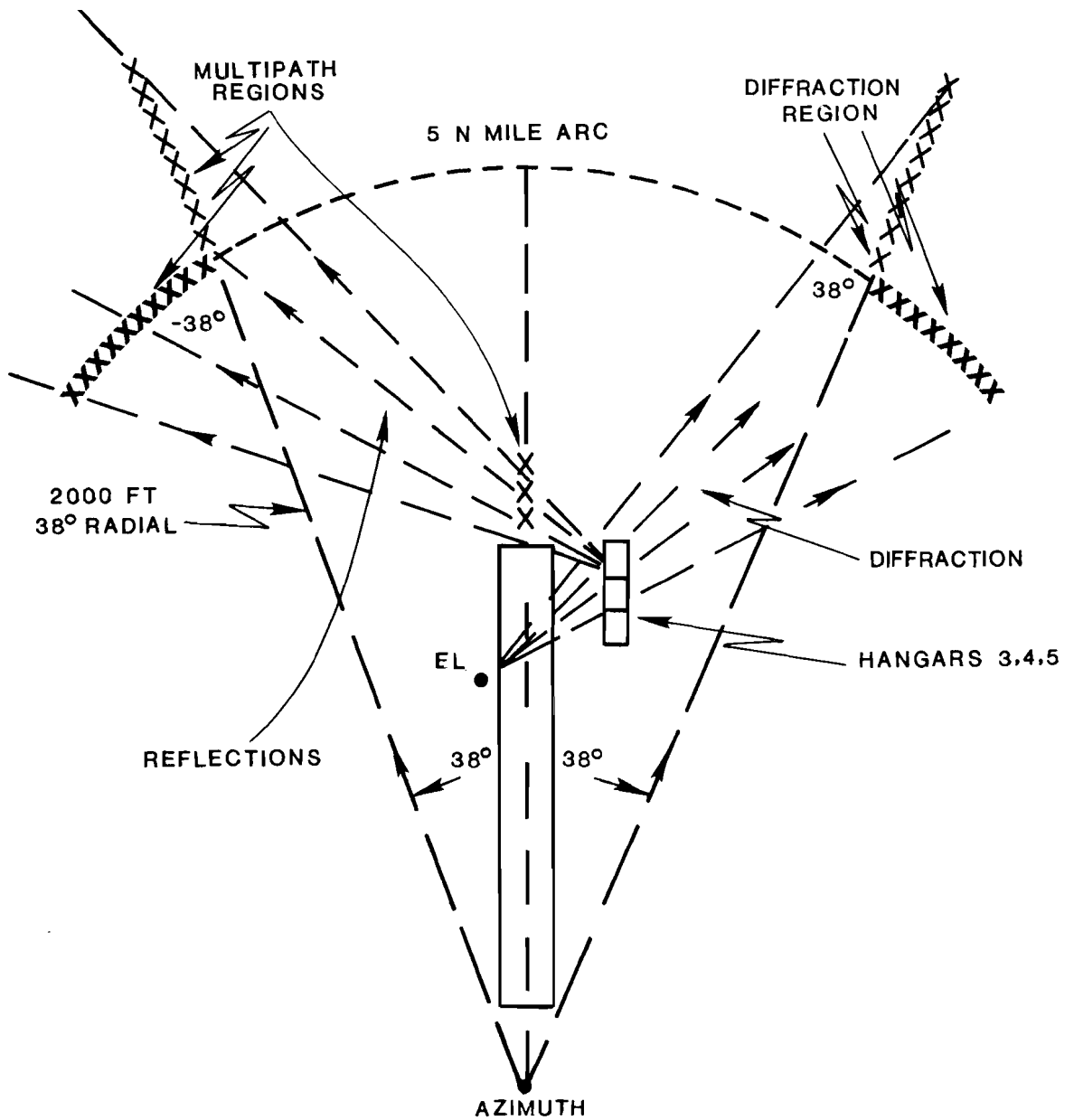
NOTE: 1) DIMENSIONS
NOT TO SCALE

Fig. 2-32 Coherent interference phenomena encountered during TRSB
field tests at JFK airport.

2-41

① SEABOARD CARGO
② HANGARS 3,4,5
③ JAL/SAS
④ TEL. CO.
⑤ MEDICAL SERVICE
⑥ POST OFFICE

□ = MLS ELEVATION SITES
FOR TESTS 1977-78

JFK
AIRPORT

① ② ③

MIDDLE
MARKER 13L

LOCALIZER
TRANSMITTER

BLAST
FENCE

ILS GLIDE PATH 13L

FENCE

④ ⑤ ⑥

13
L

DENOTES BUILDINGS

0   600   1200   1600
FEET
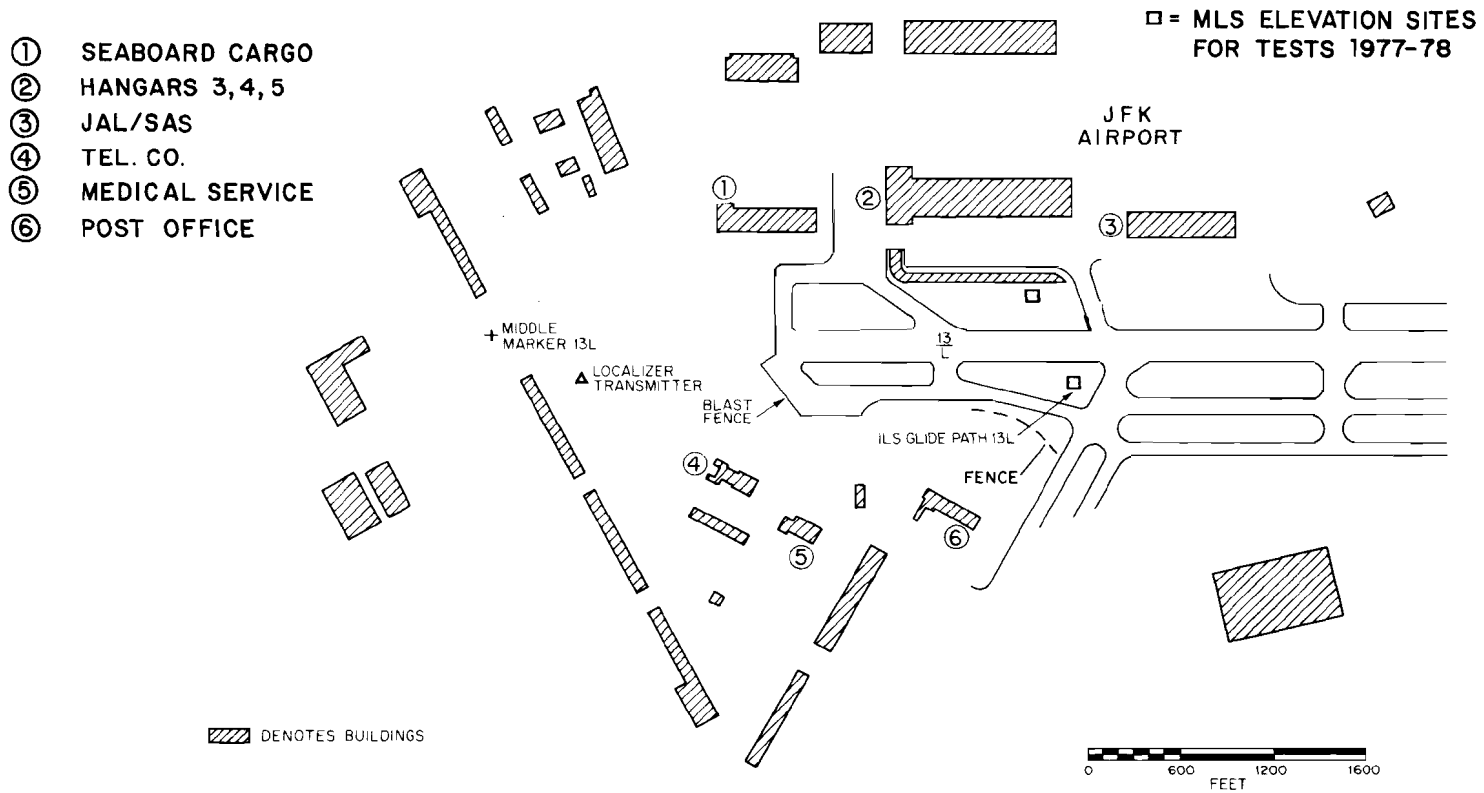
Fig. 2-33 JFK airport environment near MLS elevation sites.
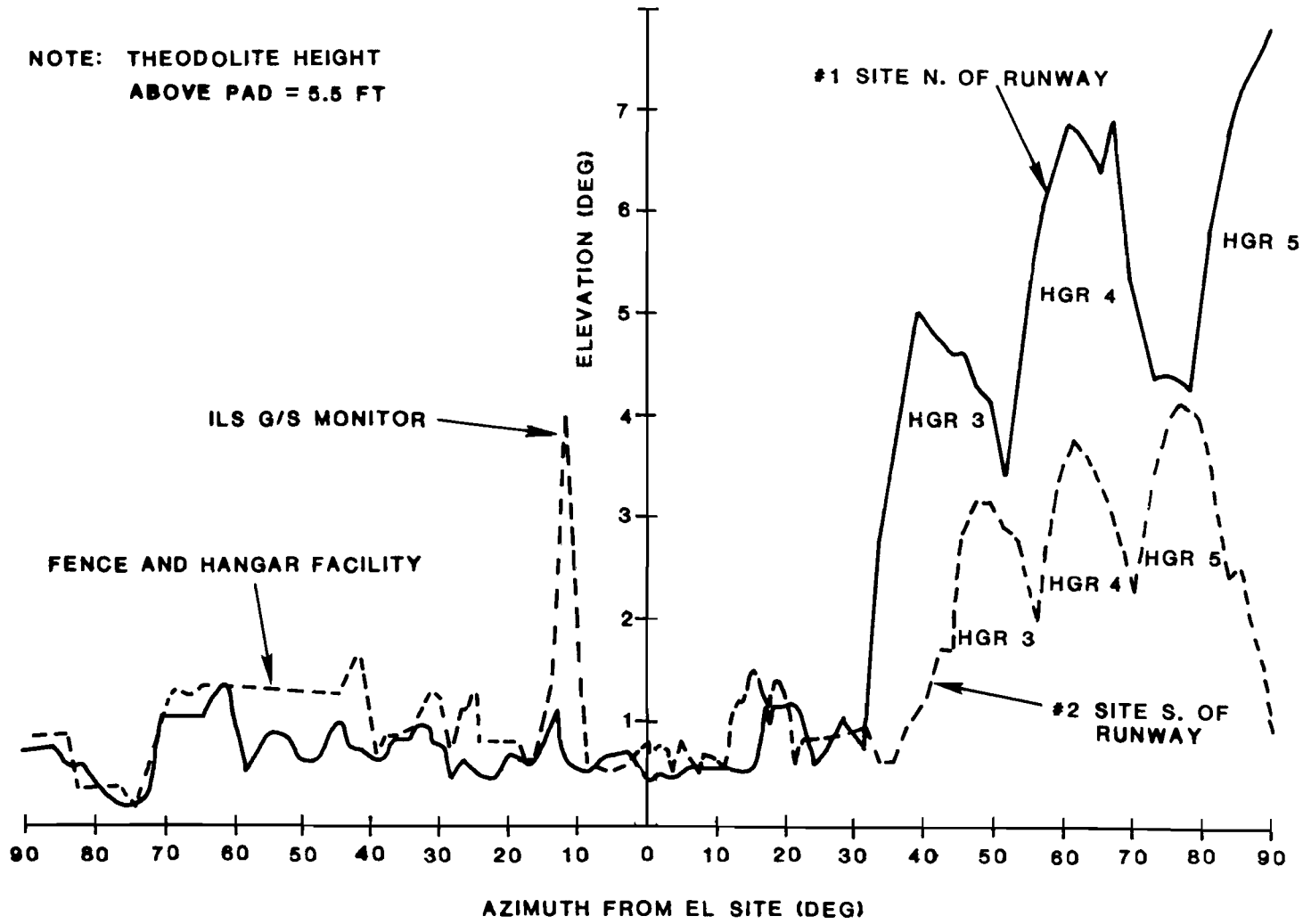
Fig. 2-34   JFK test site horizon survey data.

PROFILE ASSUMED FOR AWOP

"SYSTEM SENSITIVITY"

SCENARIOS

WALL ASSUMED TO BE A HOMOGENEOUS FLAT
SURFACE

Metal Corrugation RFI

12'

32'

20'

← 12' → window 6'

8'

Truck Bays and Loading Platform

ACTUAL
PROFILE

← 700' →
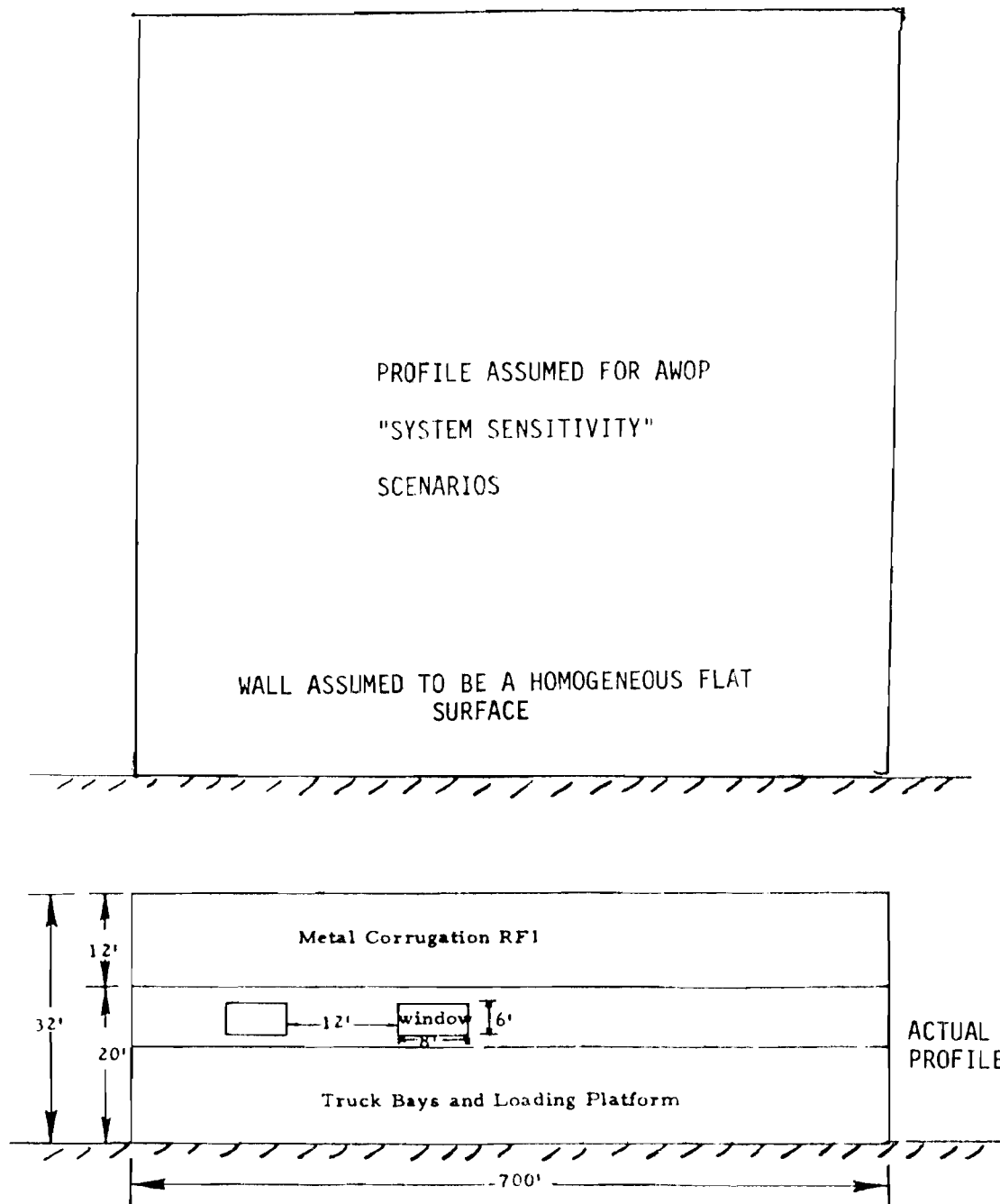
Fig. 2-35 JFK, sea board building.

for the AWOP comparative scenarios. The actual building height is such that it presents no threat even though the exaggerated profile did yield some effects in the AWOP scenarios.

Hangars 3, 4, and 5 are identical except for a small brick building between hangars 3 and 4. Figure 2-36 compares the actual building profile with the profile assumed in the AWOP comparative simulations (photographs of the hangar front surface are shown in Volume I of this report).

Although the assumed profile was higher than the actual profile, the actual profile is still quite high.* Moreover, some features of the actual hangar (specifically, the doors and top rim) are more reflective than was assumed for the AWOP simulations. Other complicating features of the actual building include:

1. The staggering of the hangar doors which produces a more complicated spatial pattern of multipath than was the case for the AWOP scenarios.

2. Curvature of the top edge versus the rectangular shape characteristic of most buildings.

3. Marked inhomogeneity in reflectivity between various surfaces on the building.

To take account of this complexity, several different building models were developed to obtain an optimized representation for various reflection geometries. Figure 2-37a shows the 50 plate model used for orbital and radial simulations where the hangar top is the prime multipath threat. For shadowing situations, only the silhouette is of concern. Figure 2-37b shows the 10 plate model used to approximate the building front and roof as seen from the elevation site on the south (far) side of Runway 13L-31R. The Fresnel reflection coefficients for the hangar material were determined from van tests described in Volume I of this report.

---

*The hangar exceeds the ICAO Annex 10 obstruction clearance limit at this point (49 feet) by some 30 feet.

FOR AWOP COMPARATIVE SIMULATIONS, FRONT SURFACE WAS ASSUMED TO BE FLAT HOMOGENEOUS
MATERIAL WITH FRESNEL REFLECTION COEFFICIENT OF 0.7
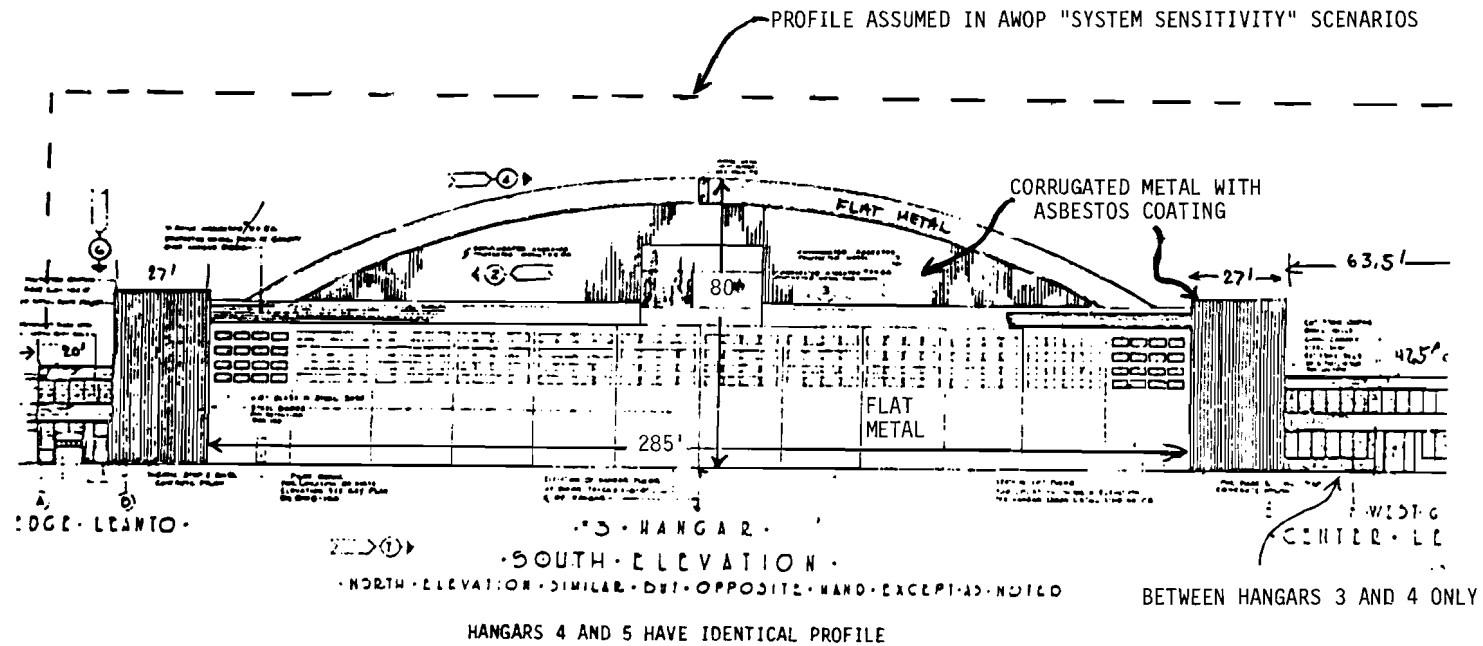
Fig. 2-36   Runway facing profile of hangar 3 at JFK.

FRONT PROFILE

48.26'

8
9 39' 10 45' 11 12 13 17' 14 80' 15 16 17 18 19 20
(50) 41 42 43 44 22' 45 46 47 48 49 50

1 2 3 4 5 6 7
21 22 23 24 25 26 27 28 29 30 31 32
33 34 35 36 37 38 39

DOOR STAGGERING

10.5"
7.5'
3.175'
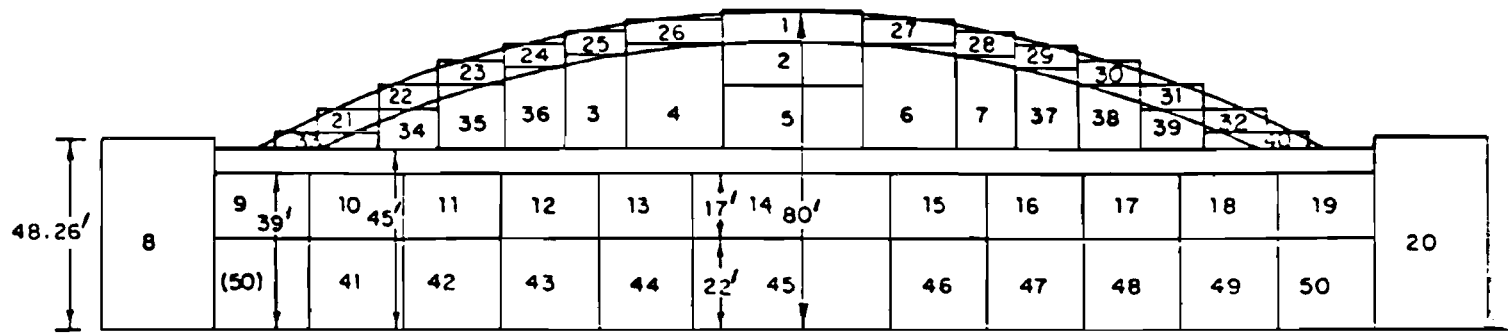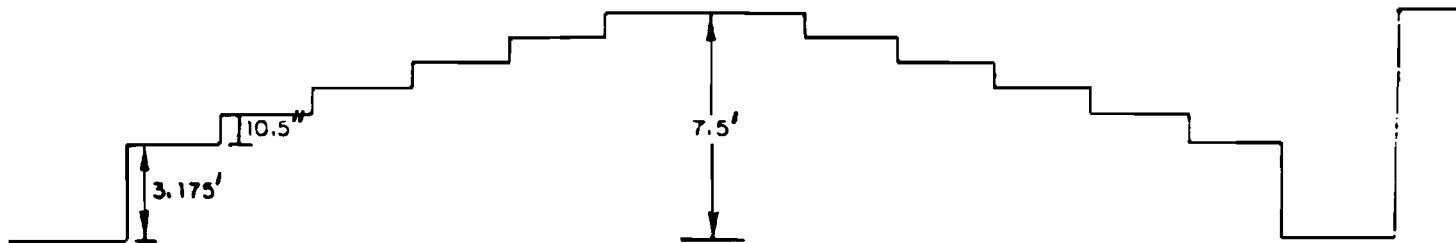
Fig. 2-37a   Model for hangar 3 reflection multipath studies.

FRONT VIEW

FEET

79.0

48.3

10   9   8 7   6   5   4   3   2

Z

X

BASE HEIGHT ASSUMED TO BE AT HEIGHT OF 2.5 FEET
WITH RESPECT TO ELEVATION TRANSMITTER BASE

HT = 79.0'

1

229'

191'

X

Y

TOP VIEW

1 CM = 15.08' IN X AND Z
1 CM = 60.32' IN Y
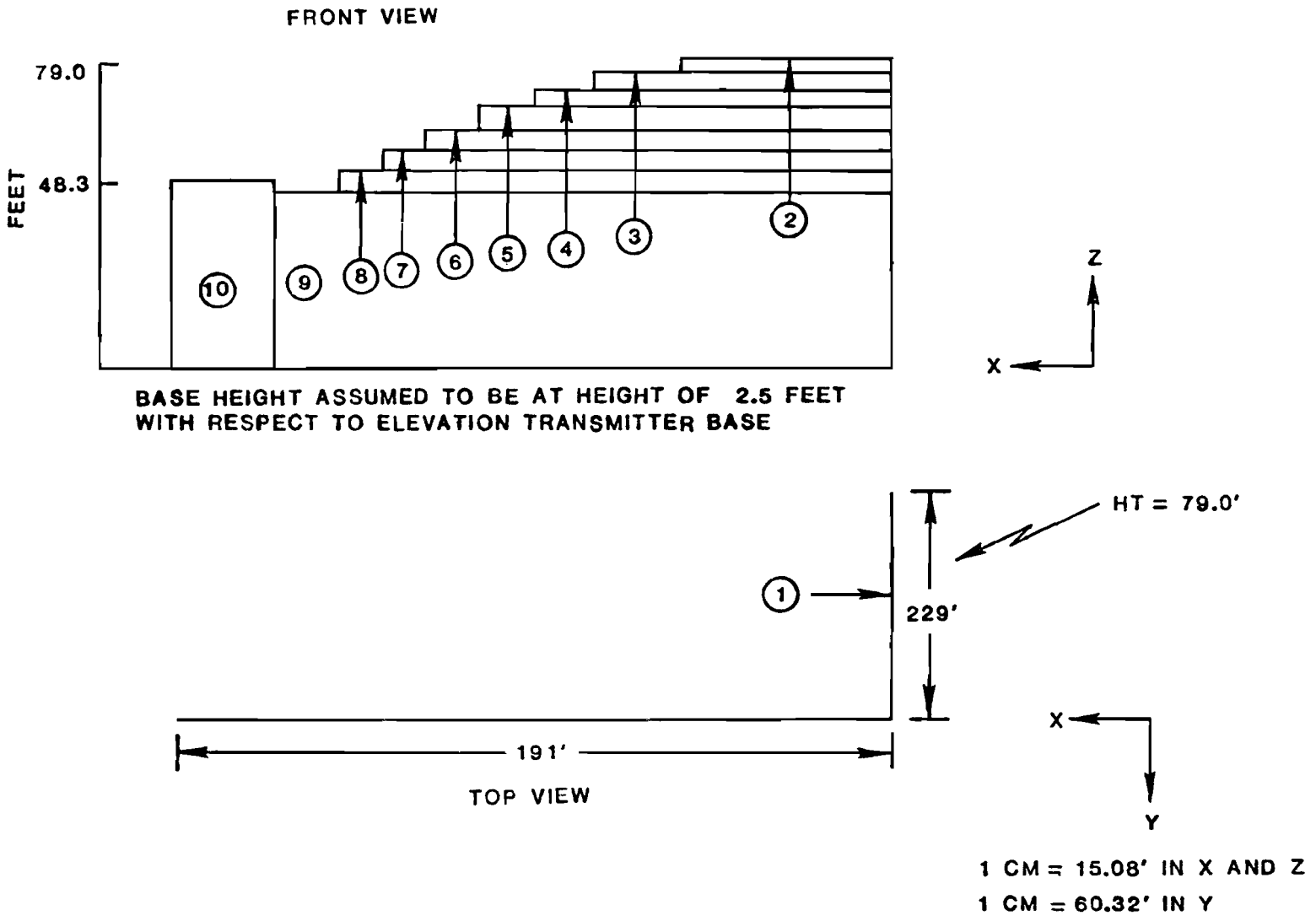
Fig. 2-37b Model of JFK hangar 3 for shadowing simulations.

The terrain at JFK is very flat, and was modelled by a flat plate. The only other features explicitly considered for the simulations described here were shadowing by a fence and the post office building to the south of the runway. These were represented by six rectangular plates with heights determined from the site horizon data of Figure 2-34.

No tracked centerline approach data was available for the December 1977 January 1978 flight tests; however, some was available for the March 1978 tests where the elevation antennas were on the south side of the runway. Figure 2-38 compares TRSB test results with the computer simulation results for a 2.86° glideslope. Comparing the various results, the flight test data is seen to be noticeably noisier throughout the approach region. This additional noise is believed to reflect a combination of tracker error, scanning and receiver noise not modelled in the computer simulations. In particular, it should be noted that the van tests, reported in Volume I of this report, (which did not involve a tracker) in the same region gave much better correspondence with simulation results.

TRSB test flights were made at constant altitude along a +38° radial from the azimuth site, with the elevation antenna at the south of the runway. The flights at roughly 2000 feet altitude experienced considerable shadowing effects from hangar 3, and thus were good candidates for simulation. Simulations were made for TRSB using a flight profile based on the tracker (x, y, z) position data and the hangar shadowing model of Fig. 2-37.

Figure 2-39 compares TRSB flight test results with simulation results. The simulated results are seen to be generally in good agreement with the actual errors. Some difference arises because the vertical rectangular plates do not in all cases give a good approximation to the curved roof line. This is an area for future model refinement. It should be noted that the shadowing error here is very sensitive to the shadowing geometry (it was found in preliminary simulations that the error could change by 0.05° for a change in the hangar height of 2 feet). This illustrates the need for precise building location and flight path data in some cases if good error waveform agreement is to be obtained.
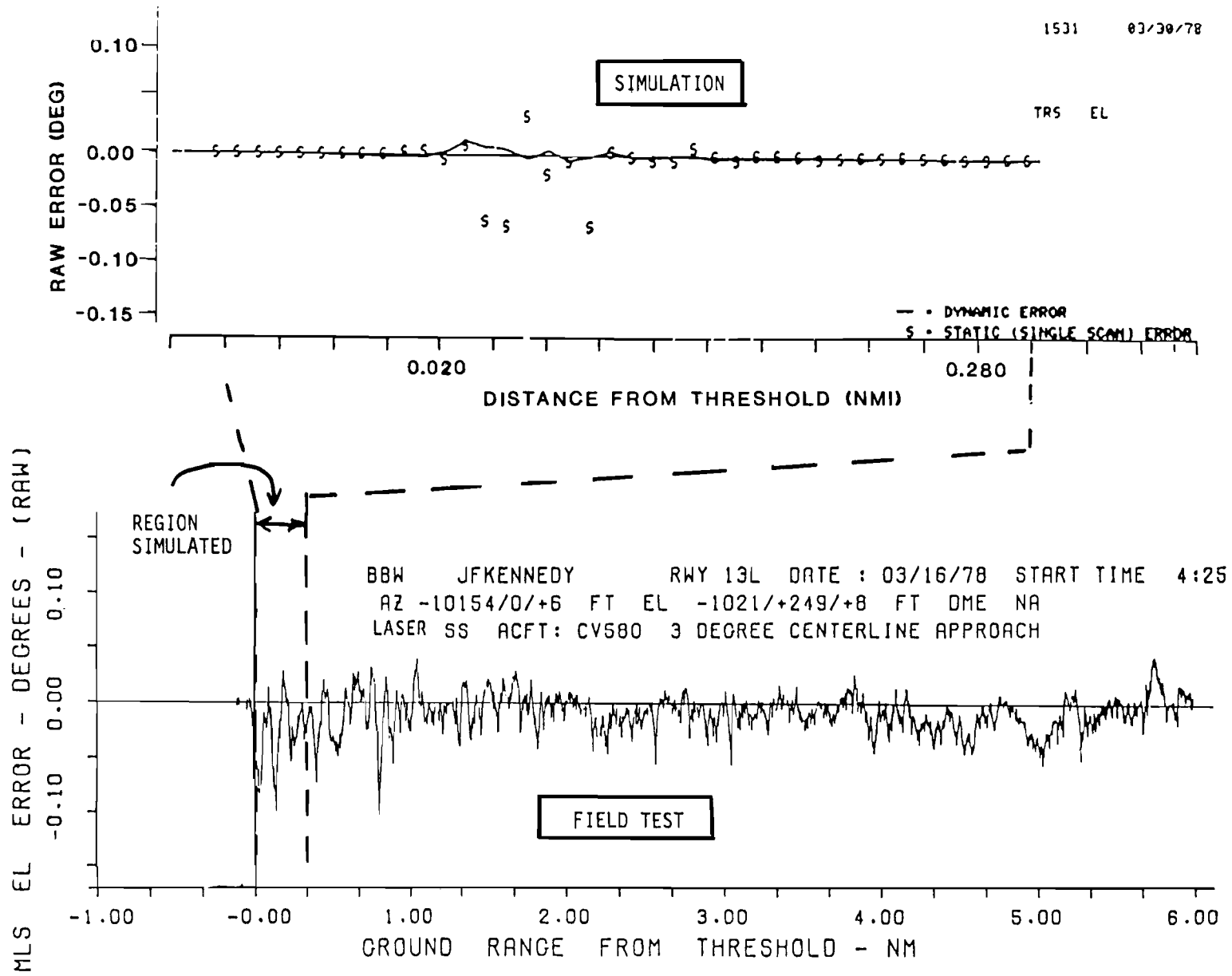
Fig. 2-38 Comparison of TRSB simulation with JFK field data for CL approach.
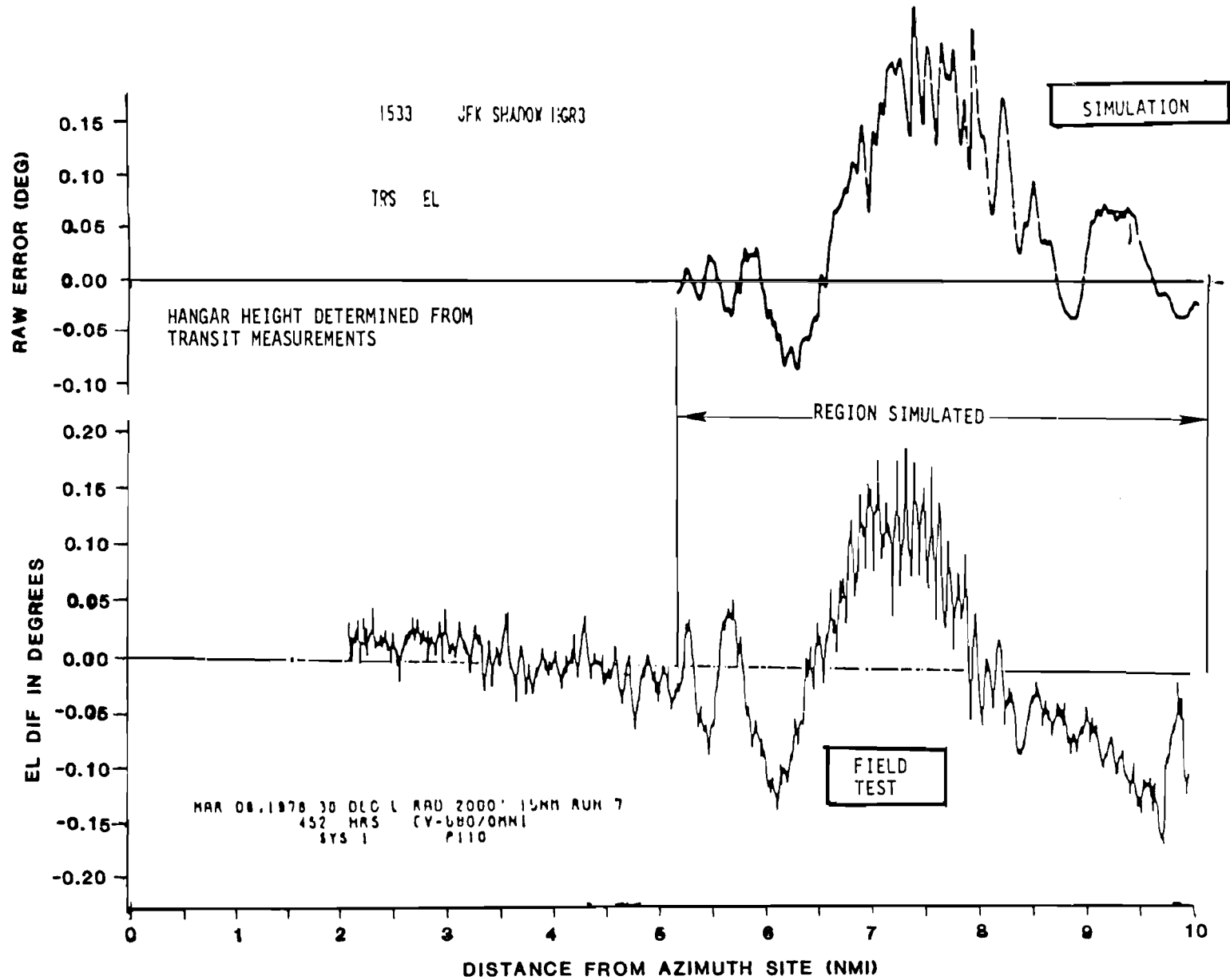
Fig. 2-39 Comparison of simulation with JFK +38° radial field test.

TRSB flights were made at constant altitude along a -38° radial from the azimuth site. The flights at roughly 2000 feet altitude experienced reflection effects from hangar 3 as well as shadowing by the fence and building to the south of the runway centerline. Two of these 2000 feet altitude runs were simulated. The flight profile models were based on tracker (x, y, z) position data and the hangar 3 modelled as shown in Fig. 2-37.

Figure 2-40 compares the TRSB simulation results with the corresponding flight results. Both the TRSB simulation and the flight test generated a system flag at approximately 8.3 nmi. Some of the high frequency noise on both flight tests near the start of the run is believed to arise from a low signal to noise condition created by the combined effects of shadowing and reflections.

Orbital flights were conducted in a 5nmi. circle centered on the JFK VORTAC. The profiles at approximately 1500 feet encountered reflection multipath near -38° azimuth, and shadowing near +38° azimuth. One of the TRSB flights was simulated, using tracker (x, y, z) data to generate the flight path model and Figure 2-37 as the hangar model.

Figure 2-41 compares the simulation result with the corresponding flight test data. The simulated error and the observed errors are seen to be in generally good correspondence except for one spike in the near -46° azimuth. The computer simulation shows larger single scan errors (e.g., 0.2 degrees peak) at that point, which suggests that the larger error in the field data arose from a difference between the point in the TRSB jitter sequence used in the computer simulation versus that of the ground system at the time of measurement.

(iii). Shadowing by ILS Glideslope Monitor at Buenos Aires

Figure 2-42 shows the runway layout and TRSB antenna locations at Aeroparque Jorge Newbery, Buenos Aires, Argentina. Figure 2-43 shows details of the airport near the MLS elevation sites. Elevation signal reflections from the OSN building (see Figure 2-43) were generally shielded by the trees,
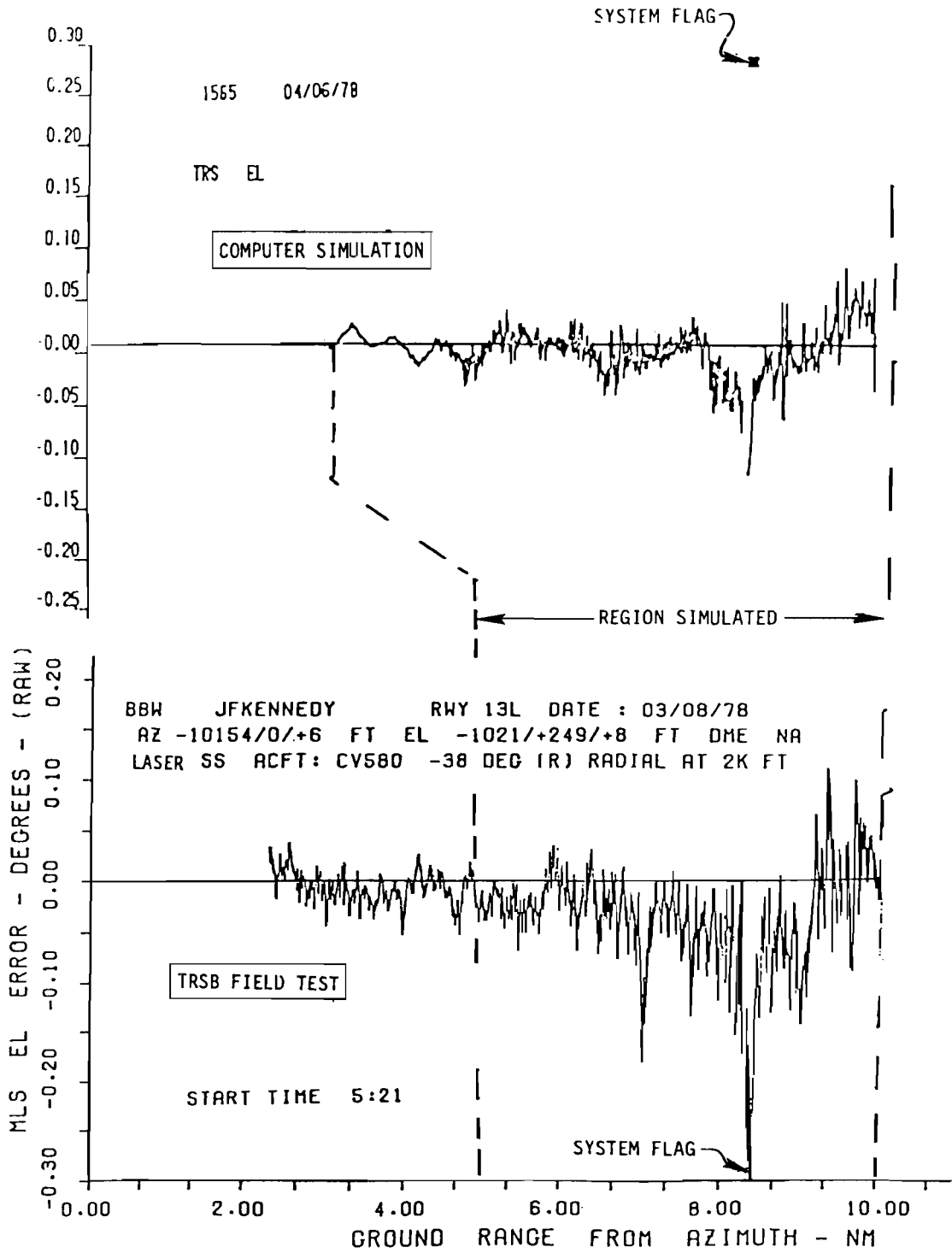
Fig. 2-40 Comparison of simulation with JFK -38° radial field test.
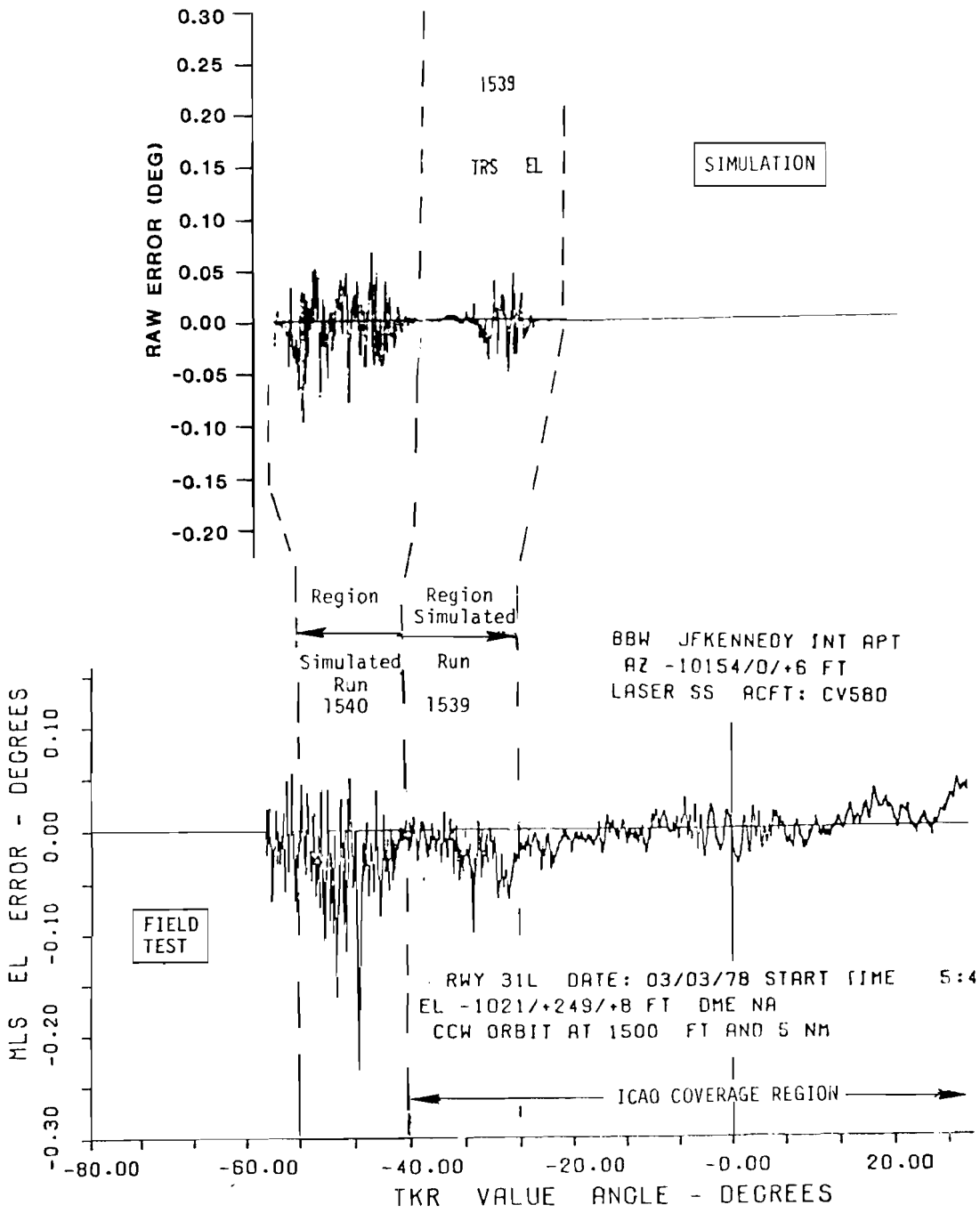
Fig. 2-41 Comparison of TRSB simulation with JFK orbital
flight test data.

TRSB MLS INSTALLATION
BUENOS AIRES, ARGENTINA
JORGE NEWBERY AEROPARQUE

CONTROL
TOWER

397'
121m

Elev 20'

475'
145m

75'
30m

ILS

6890'
2100m

427'
130m

958'
292m

TRSB
EL SITE

Elev 16'

LOCALIZER

TRSB
AZ SITE

FEET

1000   0   1000   2000   3000

500   0   500   1000
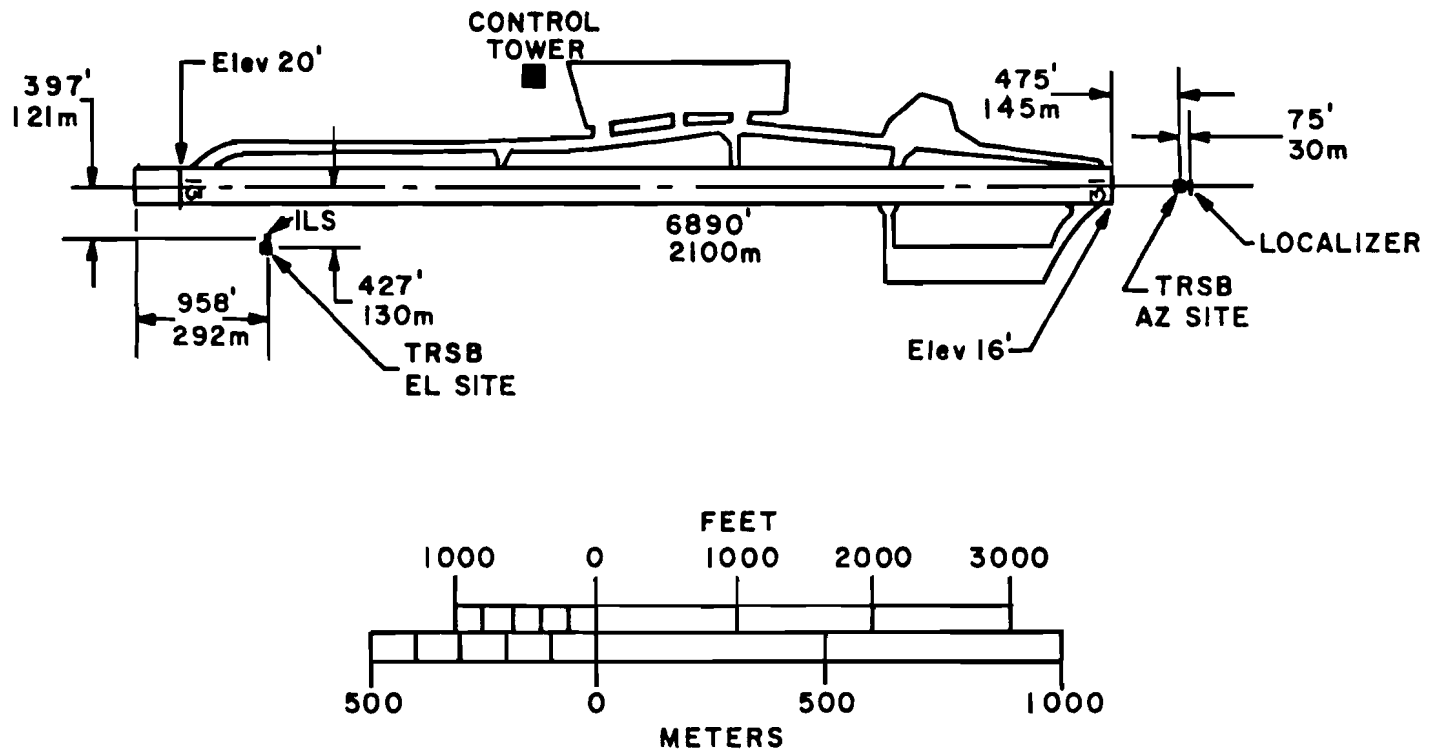
METERS

Fig. 2-42 Buenos Aires test site.
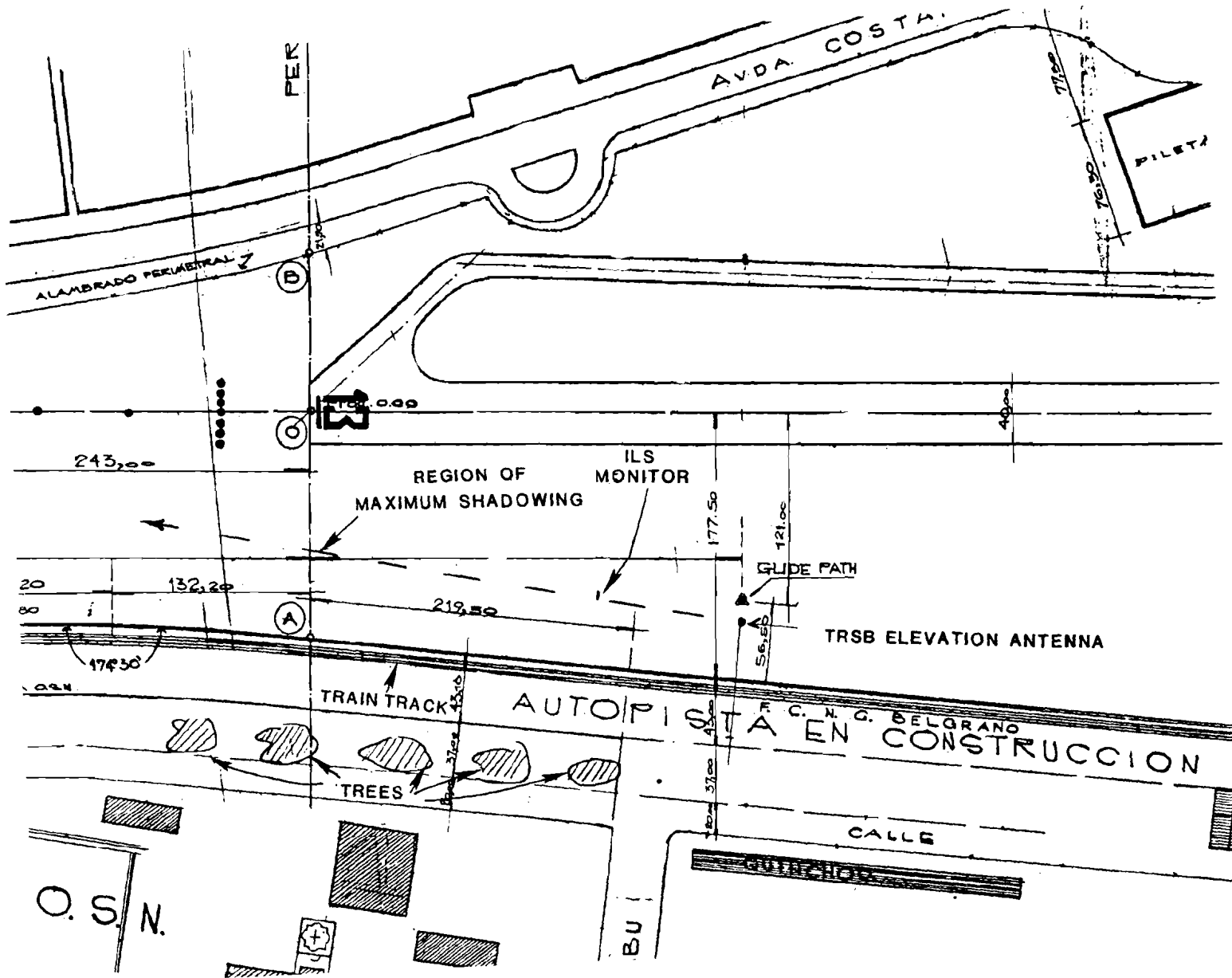
Fig. 2-43   TRSB elevation site at Buenos Aires.

while reflection from the moving trains on the adjacent track were of a very transient nature. The only discernible multipath effects arose from a large (1 meter square) ILS glideslope monitor which was located forward and inboard from the TRSB elevation antenna.[*] Figures 2-44 and 2-45 are photographs showing the B-737 during the turn onto the extended centerline and when on the final approach. The ILS monitor yields diffraction signals which have much the same character of in-beam reflection multipath.

The monitor was modeled by a single shadowing plate, while the flight path points were determined from the analog flight tracker traces. The aircraft velocity was assumed to be 116 knots in all cases.[**] The TRSB system model consisted of the TRSB Phase III receiver together with the model of the 1.5° beamwidth Bendix Basic Narrow elevation antenna discussed in Chapter I.

Figures 2-46 and 2-47 compare the observed TRSB errors with the simulation results for two flights. The simulation results have been scaled to yield horizontal and vertical scales which approximate those of the field data. In some cases, the simulation horizontal scale has been offset slightly to correct what are felt to be offsets in the tracker range.

The simulation results are seen to replicate the peak-to-peak[***] magnitudes and spatial character quite well. At the outer range, there is some difference in the spatial period; however, this may only reflect the fact that the distance scale for the flight trials data was estimated from the known flight profile as opposed to being measured by a precise tracker.

_____

[*]At a distance of 82.6 meters and elevation angle of approximately 1.65° elevation angle with respect to the elevation system phase antenna.

[**]This assumption is viewed as being non-critical due to the very low scalloping frequencies which arose here.

[***]Peak-to-peak error magnitude is the most relevent measure in cases such as this where trackers of limited precision are being utilized.
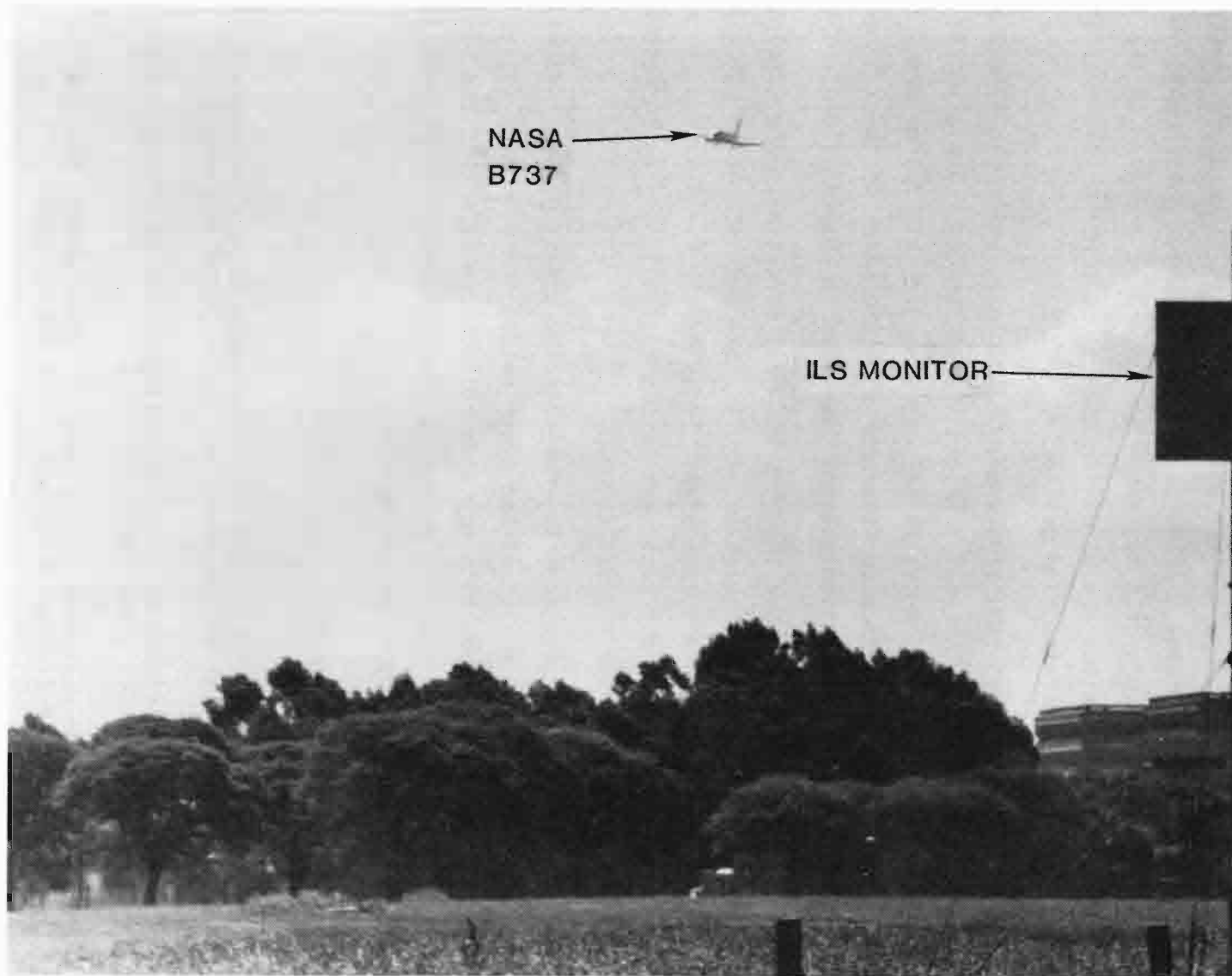
Fig. 2-44   View from TRSB elevation site at Aeroparque.

NASA
B737

ILS MONITOR
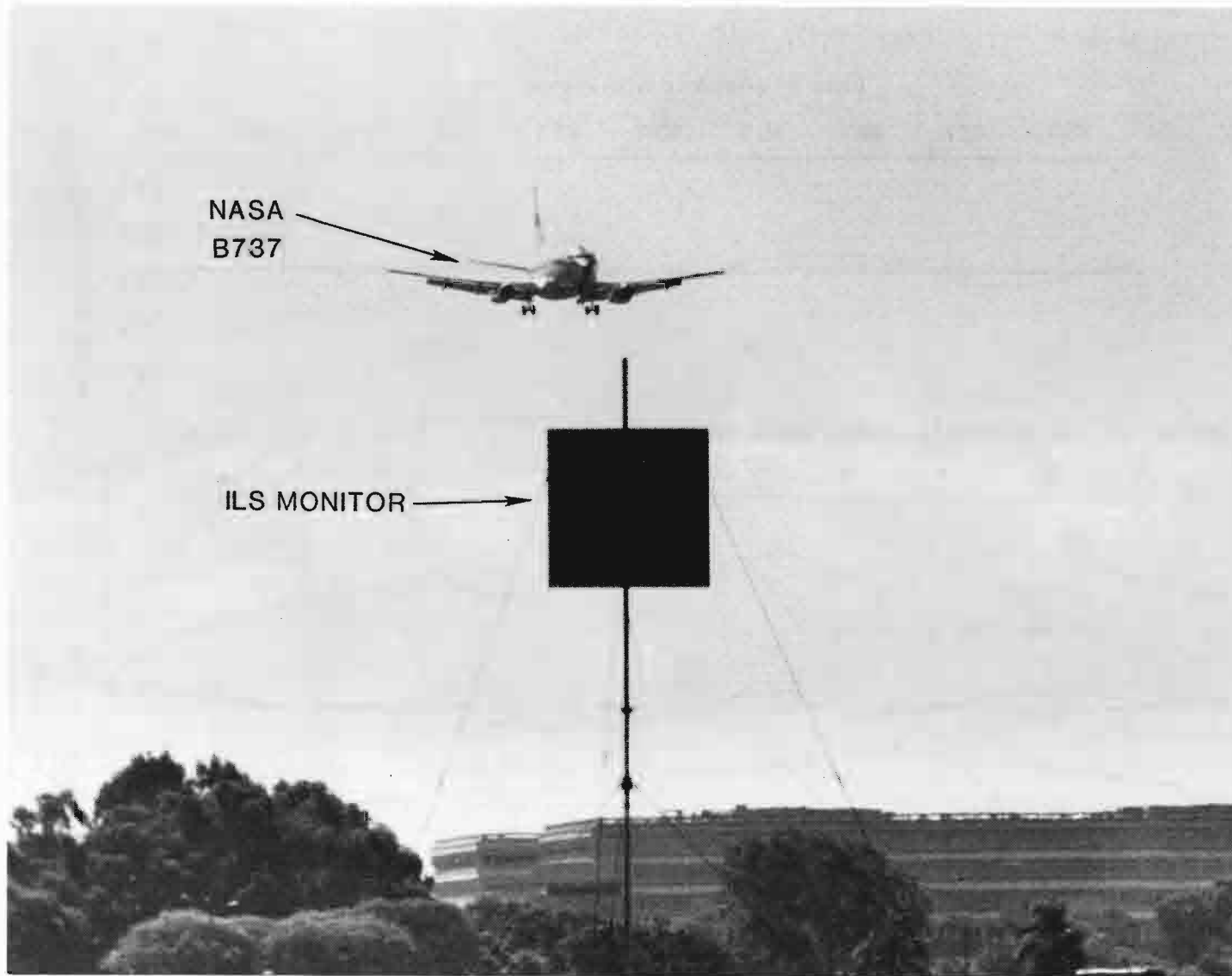
Fig. 2-45   View from TRSB elevation site at Aeroparque.

JORGE NEWBERY AEROPARQUE
BUENOS AIRES, ARGENTINA
DATE: 11-4-77   RUN: 8
AIRCRAFT: NASA B-737
AZ: CENTERLINE   EL: 3.0°

FLIGHT DATA
3° TRACKER ANGLE

ELEVATION TRACKER ANGLE

ELEVATION ERROR

ELEVATION TRSB ANGLE

ELEVATION ERROR DEGREES

.2
.1
0
.1
.2

ACTUAL RESULT

0   .1   .2   .3   .4   .5   .6   .7   .8   .9   1.0   1.1   1.2

GROUND RANGE FROM THRESHOLD — NAUTICAL MILES

RAW ERROR (DEG)

0.40
0.20
-0.00
-0.20
-0.40

SIMULATION

TRS EL

0.100   0.204   0.308   0.412   0.516   0.620   0.724   0.828   0.932   1.036

DISTANCE FROM THRESHOLD (NMI)

Fig. 2-46 Comparison of TRSB simulation with Buenos Aires field data.
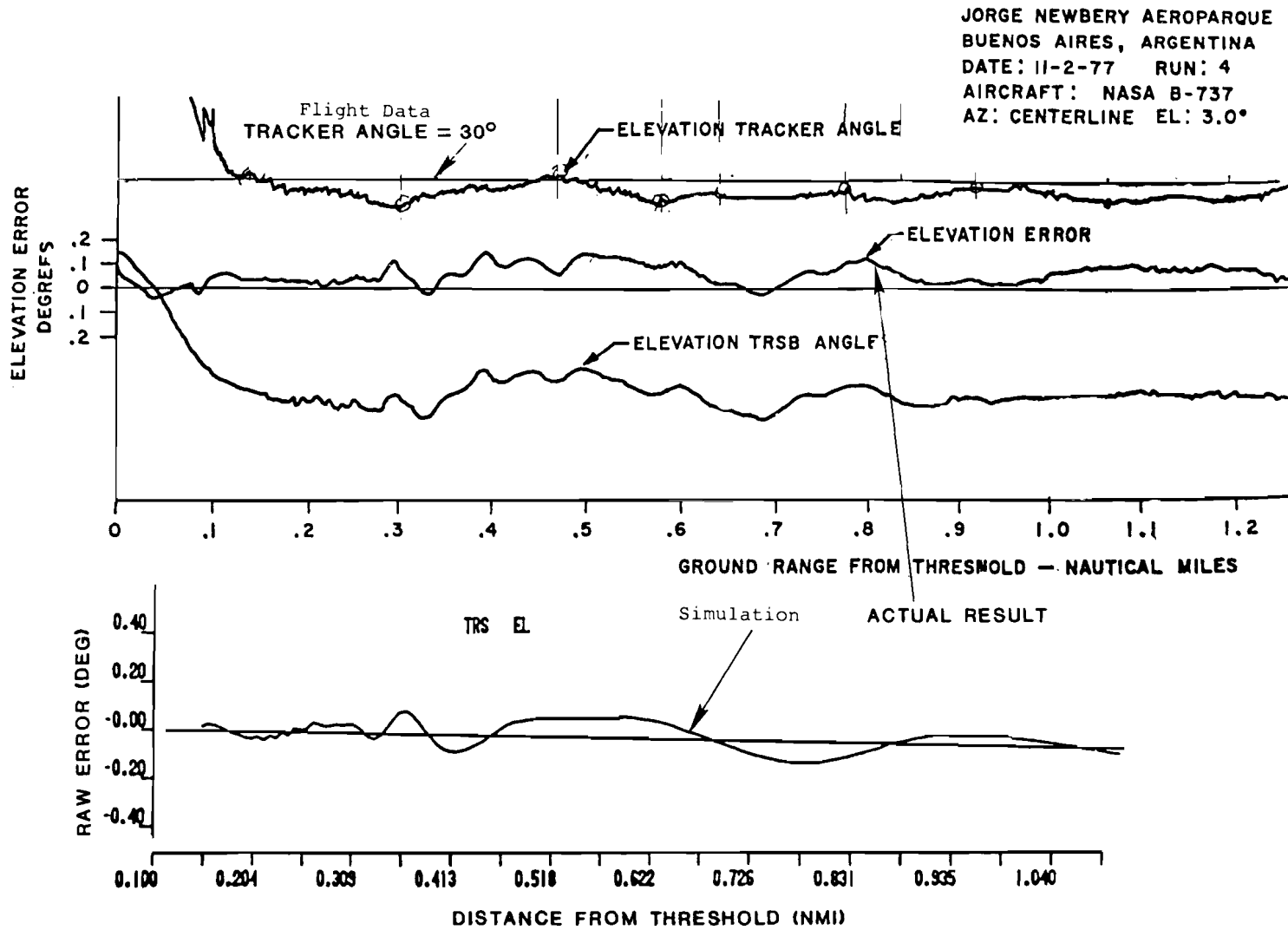
Fig. 2-47 Comparison of TRSB simulation with Buenos Aires field data.

Figure 2-48 compares the observed TRSB error on a run with a simulation result for a flight profile corresponding to a 3° approach. The actual profile differed at some points from 3° (by an unknown amount); however, the main features of the error are seen to be quite similar.

(iv.) Elevation Shadowing by Hercules Aircraft at Brussels National Airport

A series of TRSB and DMLS field tests were held at Brussels National Airport (Belgium). Figure 2-49 shows the MLS antenna sites as well as many of the principal scatterers. Azimuth multipath simulation results are reported in Volume III, thus, the discussion here will focus on reflection effects.

None of the buildings at Brussels National were oriented to yield in-beam elevation multipath in an operationally relevant region and the Brussels terrain is fairly flat. Thus, elevation effects due to multipath were expected to be very small. However, some effects were artificially introduced by parking two Hercules aircraft in front of the elevation transmitter as shown in Figures 2-50 and 2-51.

Discernible multipath errors were encountered on 2° glideslope centerline approaches with these aircraft present. These cases were used to develop several "airport specific" scenarios. Figure 2-52 shows the rectangular plates used to model the Hercules aircraft nearest threshold (as the other aircraft's geometry was such that it did not shadow centerline approaches).

The elevation profiles were determined from the published plots of tracker angle versus distance from theshold. Evidently, the aircraft were tracked in one axis only, so it was assumed that the aircraft were above the extended centerline at all times. Any lateral weaves that did occur would result in a different shadowing geometry than assumed here. In particular, the point at which the line of sight passes through or above the tail would be at a different distance from threshold than was assumed in these simulations.

As before, the field data result contains non-multipath related effects, such as tracker errors. However, since this was created multipath condition, "clean accuracy" results with the shadowing aircraft not present per-
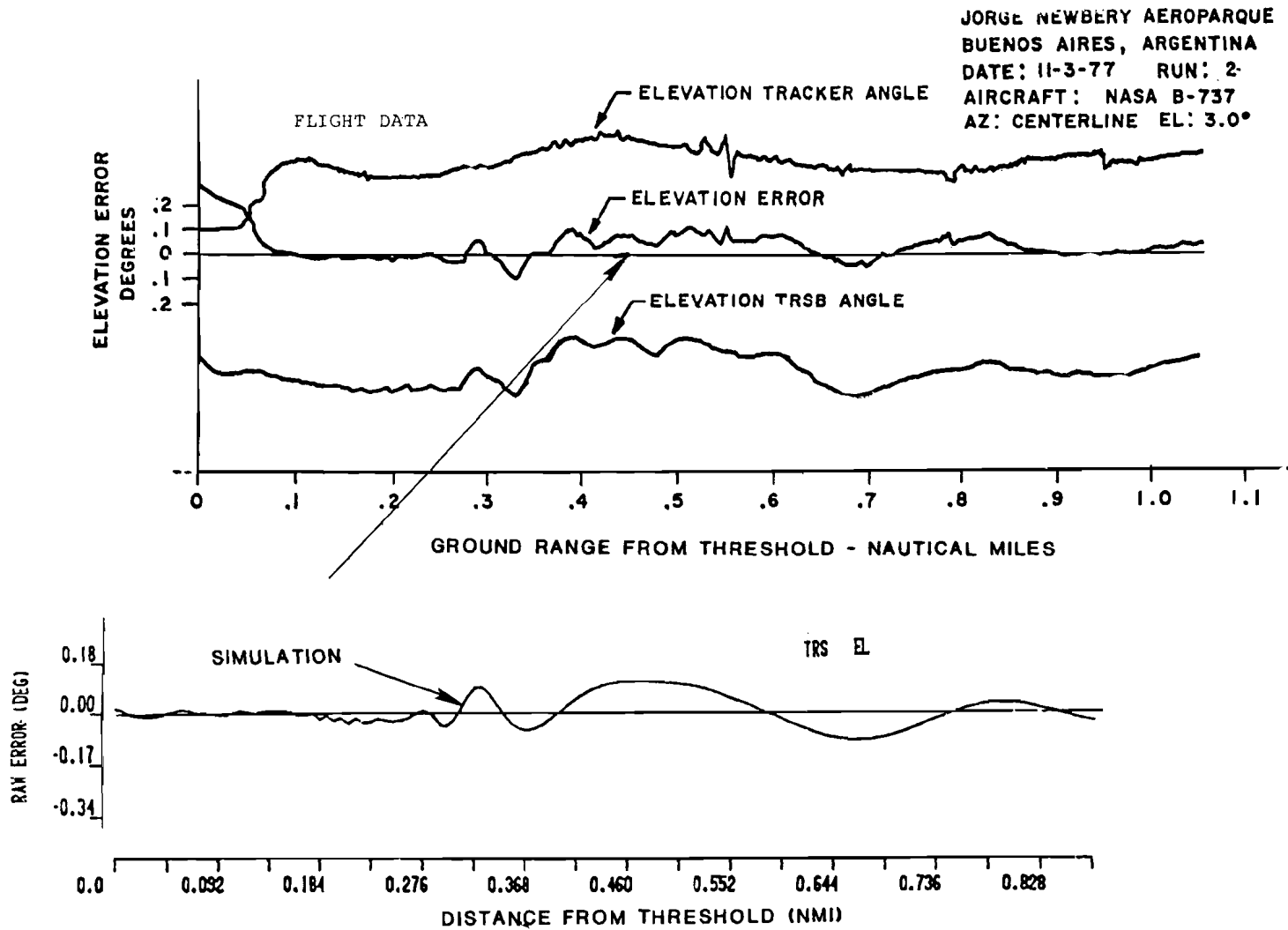
Fig. 2-48 Comparison of TRSB simulation with Buenos Aires field data.

ZAVENTUM NATIONAL AIRPORT
BRUSSELS, BELGIUM
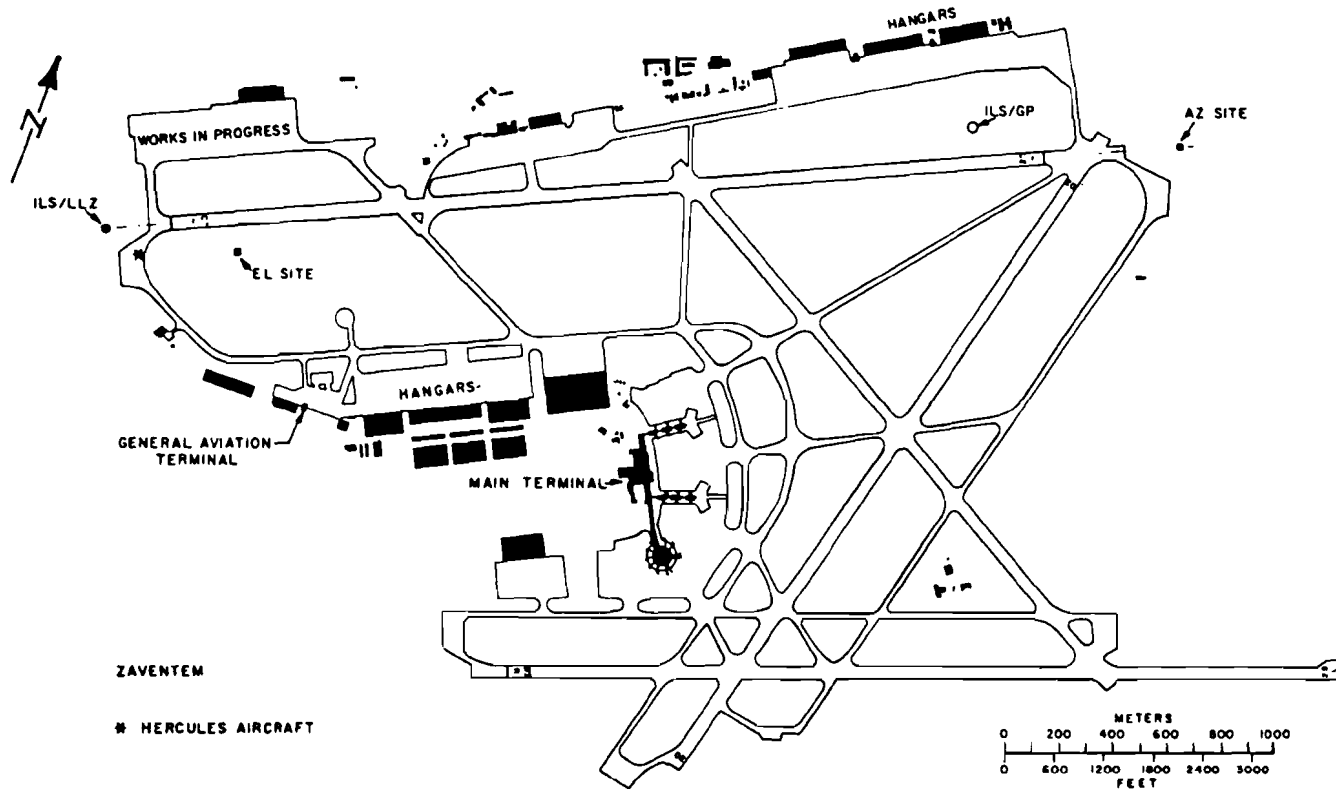
Fig. 2-49a Brussles Belgium airport layout and MLS test sites.
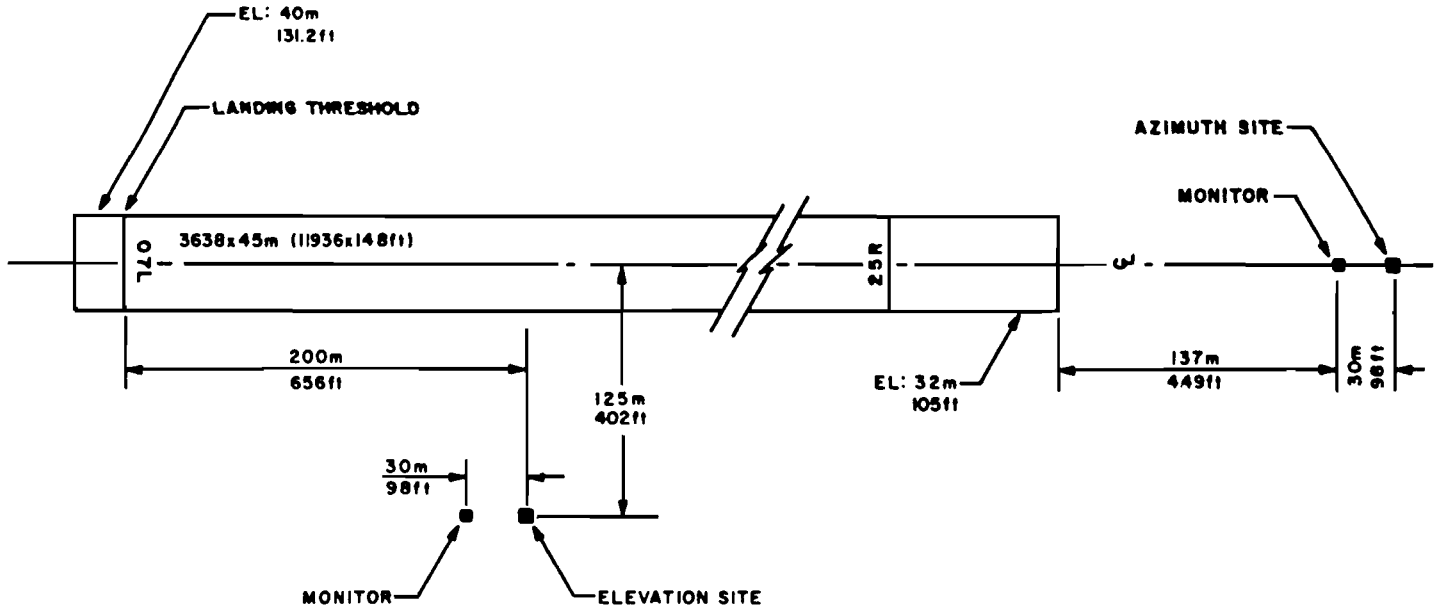
Fig. 2-49b MLS test sites along Brussels runway 07L-25R.

DATA FURNISHED BY MR. DE BACKER, RVA ENGINEER
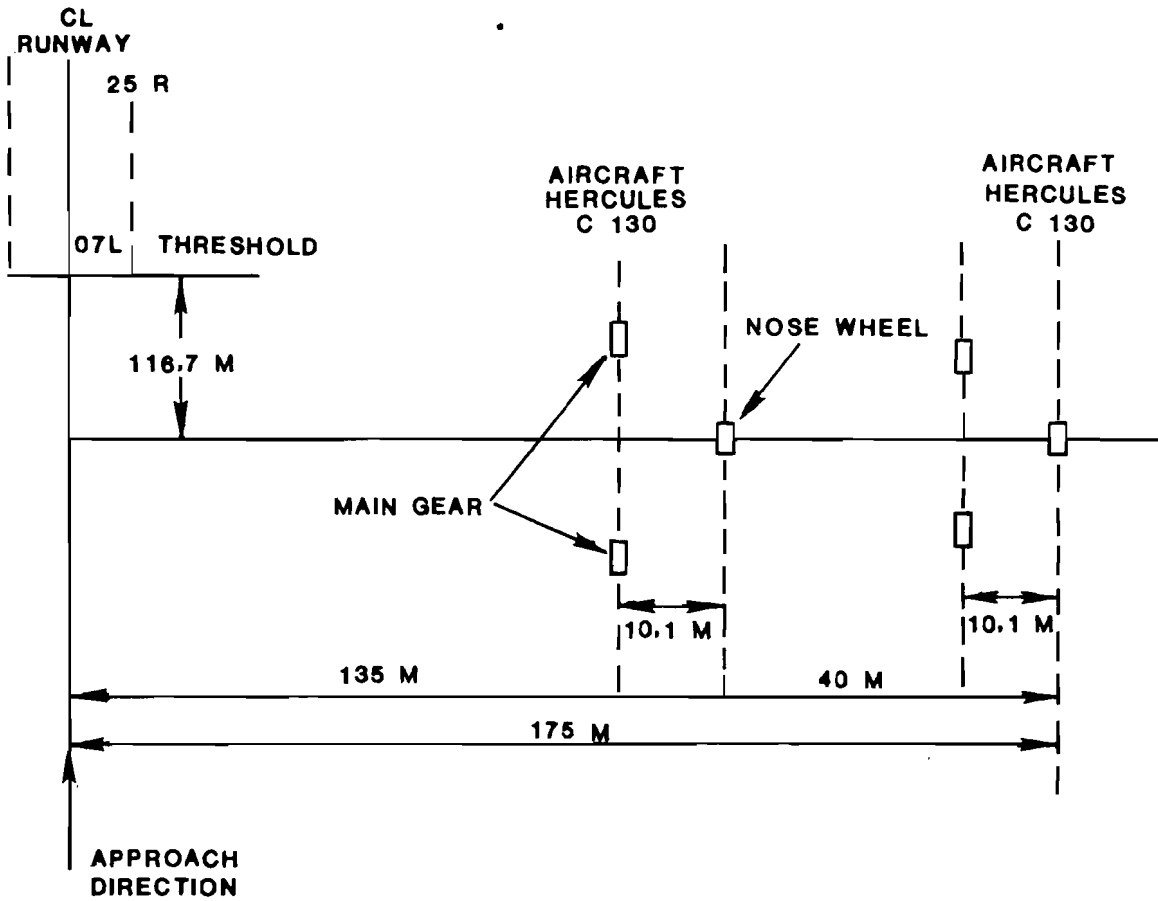
Fig. 2-50 Geometry of Brussels C-130 shadowing tests.

2-66
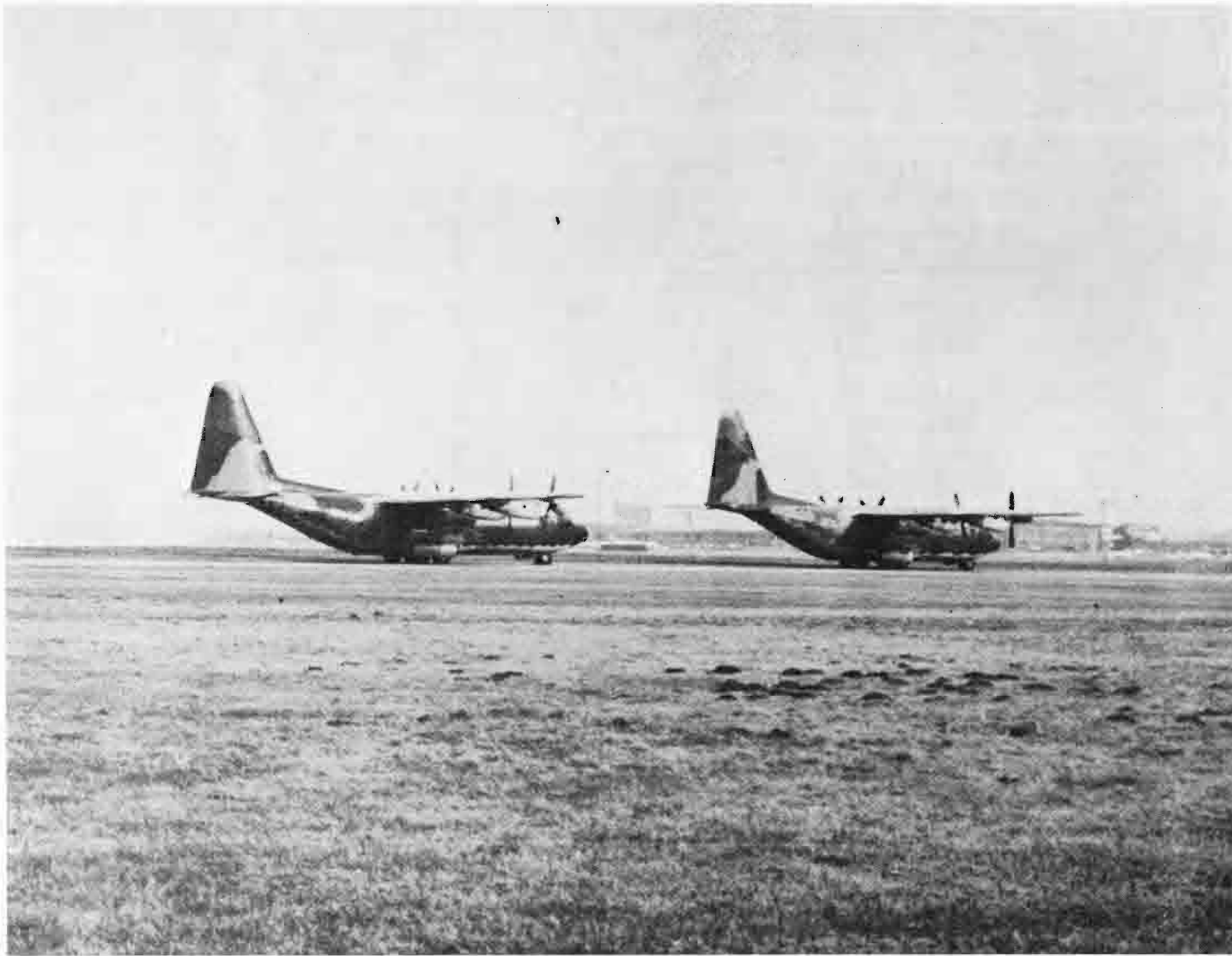
Fig. 2-51 Hercules aircraft near threshold end of runway in line with TRSB elevation antenna.
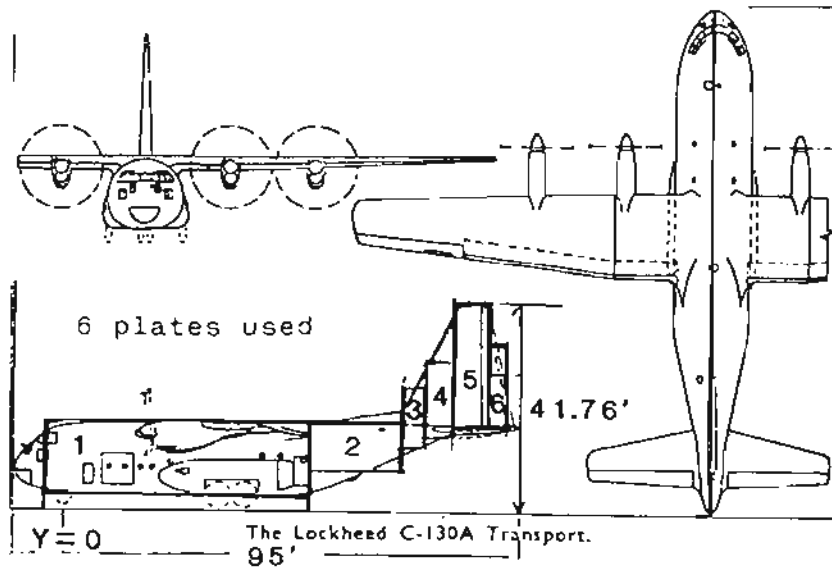
Fig. 2-52 Shadowing profile model for C-130 aircraft.

mit some assessment of these factors. Figure 2-53 shows a TRSB field result for a 2° glideslope with no shadowing aircraft present.

Figures 2-54 and 2-55 compare simulation results for scenarios with the Hercules aircraft present with corresponding field results. The location of the peak errors is somewhat different, but the peak-to-peak error and frequency content are quite similar. The peak location differences are believed to arise from the aircraft lateral weaves, which could not be included in the simulation flight profile model due to lack of data.

D. Tolerancing of TRSB Simulation Model

The simulation results and the MLS field test data from a number of airports (see Table 2-2) and multipath sources have been compared for a variety of TRSB systems and flight profiles. In some cases, as was anticipated by AWOP [66], error sources not considered in the multipath simulation (e.g., tracker errors and low signal to noise effects) are evident in the field test data. In all cases, insufficient accuracy in airport geometry and aircraft flight path data meant that only the gross error features (e.g., peak error, frequency content and error region) could be quantitatively compared. Keeping these factors in mind, the overall agreement between simulations and the field data is regarded as quite good.

Given these good agreements between the field tests and simulation to within the uncertainty limits imposed by the lack of knowledge as to exact field test conditions and TRSB errors, the principal basis for tolerancing the TRSB simulation model has been CALSPAN bench simulator data. Table 2-3 summarizes the total tolerancing errors which were applied to the TRSB system AWOP scenario simulations. It is believed that a similar tolerance is applicable to the models of the Bendix Phase III basic narrow and small community antennas (except for a greater uncertainty regarding the azimuth sidelobe levels at wide angles).

US TIME REFERENCE SCANNING BEAM SYSTEM
BRUSSELS NATIONAL R/W 07L

DATA PROCESSED BY U.K.

FACILITY - EL1   TRANSMITTER - BASIC WIDE
DATE - 4/2/78   RECEIVER - P101
FLIGHT No - C6   RUN No - 04
AZIMUTH ANGLE - 0   ELEVATION ANGLE - 2
ANTENNA BEAMWIDTH = 1 DEGREE

SYSTEM ERROR

0.3

0.2

0.1

ICAO FULL CAPABILITY 2-SIGMA NOISE SPEC

0.0

TRACKER OSCILLATIONS

-0.1

TRACKER
NOISE

-0.2

-0.3

DEGREES

| 0.0 | 1.0 | 2.0 | 3.0 | 4.0 | NM 5.0 | 6.0 |

| 0 | 6080 | 12160 | 18240 | 24320 | 30400 | 36480 |

C.: R/W THRESHOLD   GROUND RANGE FROM THRESHOLD   FEET

Fig. 2-53 TRSB Brussels field test data without shadowing aircraft present.

1544

RAW ERROR (DEG)

0.10

0.05

-0.00

-0.05

0.10

TRS EL

CENTERLINE SIMULATION USING TRACKER

DATA TO OBTAIN HEIGHT PROFILE

0.0   1.039   2.078   3.117   4.156

DISTANCE FROM THRESHOLD (NM)   THRESHOLD= 10000. FEET

SYSTEM ERROR

0.3

0.2

0.1

0.0

-0.1

DATA PROCESSED BY U.K.

US TIME REFERENCE SCANNING BEAM SYSTEM
BRUSSELS NATIONAL R/W 07L

FACILITY - EL1	TRANSMITTER - BASIC WIDE
DATE - 31/1/78	RECEIVER - P101
FLIGHT No - 03	RUN No - 06
AZIMUTH ANGLE - 0	ELEVATION ANGLE - 2

ANTENNA BEAMWIDTH = 1 DEGREE

O C-130 HERCULES IN FRONT OF ELEVATION ANTENNA

ICAO FULL CAPABILITY 2-SIGMA NOISE SPEC

TRACKER
ERRORS

1.0   2.0   3.0   4.0   NM   5.0   6.0

0   6080   12160   18240   24320   30400   36480

T : R/W THRESHOLD   GROUND RANGE FROM THRESHOLD   FEET

Fig. 2-54 Comparison of TRSB simulation with Brussels field data.

RAW ERROR (DEG)

1544

0.10
0.05
-0.00
-0.05
0.10

TRS EL

CENTERLINE SIMULATION USING TRACKER
DATA TO OBTAIN HEIGHT PROFILE

0.0   1.039   2.078   3.117   4.156

DISTANCE FROM THRESHOLD (NM)   **THRESHOLD= 10000. FEET**

SYSTEM ERROR

US TIME REFERENCE SCANNING BEAM SYSTEM
BRUSSELS NATIONAL R/W 07L

0.3   DATA PROCESSED BY U.K.

FACILITY - EL1   TRANSMITTER - BASIC WIDE
DATE - 31/1/78   RECEIVER - P101
FLIGHT No - 03   RUN No - 06
AZIMUTH ANGLE - 0   ELEVATION ANGLE - 2

ANTENNA BEAMWIDTH = 1 DEGREE

0.2

○ C-130 HERCULES IN FRONT OF ELEVATION ANTENNA

0.1   ICAO FULL CAPABILITY 2-SIGMA NOISE SPEC

0.0

-0.1   TRACKER
        ERRORS

        1.0   2.0   3.0   4.0   NM 5.0   6.0

0   6080   12160   18240   24320   30400   36480

T : R/W THRESHOLD   GROUND RANGE FROM THRESHOLD   FEET

Fig. 2-55 Comparison of TRSB simulation with Brussels field data.

TABLE 2-2

TRSB MULTIPATH SIMULATION VALIDATION DATA OBTAINED
FROM OPERATIONAL AIRPORTS

| Airport | TRSB Ground System | Discernible Multipath Error Effects | | Utility for Model Validation |
		Azimuth	Elevation	
Buenos Aires Argentina	Basic Narrow	none	shadowing by ILS monitor	modelling done and reported in this chapter
Honduras	Small community	both small due to rough terrain		insufficient terrain data and flight profile available
Kristiansand, Norway	Basic Narrow	small errors at low angles due to rough terrain shadowing and reflections		insufficient terrain and flight profile available
Brussels	Testbed	very small	shadowing by C-130 aircraft	modelling done and reported in this chapter
Charleroi, Belgium	Small community	none or small errors due to terrain		insufficient terrain and flight profile data no significant phenomena of interest
Dakar, Senegal	"	"		"
Nairobi, Kenya	"	"		"
Cape May, NJ	"	"		"
Crows Landing, California	Basic Narrow and Small Community	none	shadowing by monitor poles	not modelled in view of other studies of same phenomena
JFK, New York	Basic Narrow and Testbed	none	reflections and/or shadowing	modelling done and reported in this chapter
NAFEC, NJ	Basic Narrow and	none or very small		--
	Small Community	shadowing by monitor poles		modelling done and reported in Chapter IV of Volume I
	Testbed	a/c shadowing, screen multipath reflections		modelling done and reported in this chapter

TABLE 2-3

TRSB SIMULATION TOLERANCING

	Inbeam Error	Out-of-Beam-Error
Azimuth Filled	±5%*	0% to 75% overestimate
Density Tapered	±5%	±25% (2 dB)
Elevation (COMPACT)	±5%	±12% (1 dB)

*Based on CALSPAN comparisons.

III. DMLS MODEL

A computer model has been developed for predicting the multipath performance of the Doppler Microwave Landing System (DMLS) which was proposed to ICAO by the United Kingdom. The computer model is based on the DMLS system as described in the U.K. proposal [7] and various papers presented at the meetings of the ICAO All Weather Operations Panel (AWOP), and by U.K. representatives in private discussions.

The DMLS computer model characterizes the signal processing and antenna models for the azimuth and elevation angle scan processing, as these were the functions considered in the AWOP comparative simulation activity. The antennas modeled here consist of 1° fixed and commutated reference azimuth arrays as well as the 1° fixed reference elevation array, as these were the antennas considered in the AWOP assessment activity.

We must emphasize that the DMLS system model described here corresponds to the proposed DMLS characteristics as of February 1977. It is not clear to what extent the DMLS hardware corresponds to the proposed implementation. Consequently, this version of the DMLS system model may not be completely appropriate for end-to-end validation by comparison with UK field test data.

A. U.K. Angle Subsystems

In this section we describe the Doppler scan system which has been modeled. Our objective here is to briefly bring together descriptive material by the UK which appears in the UK proposal [7], CAA reports [67], and minutes of the AWOP WG-A multipath subgroup [66].

The U.K. angle subsystems operate according to the Doppler scan principle. In a Doppler system, angle information is transmitted via a CW signal radiated into the coverage volume. This signal is spatially modulated so that the frequency transmitted towards a particular point in space is a monotone function of the angular coordinate of that point. In order to counteract the effect of A/C-induced Doppler shift, a CW reference tone is transmitted simultaneously at a neighboring frequency. The airborne receiver measures the difference in frequency between the two received signals (the difference frequency

is essentially free of any dependence on aircraft motion) in order to estimate the angular coordinate, as illustrated in Fig. 3-1. Both received signals are, of course, subject to contamination by coherent interference (i.e., multipath) generated by the scattering obstacles in an airport environment.

The U.K. proposes ground system antennas (electronically commutated line arrays) which generate the Doppler signal by simulating the motion of an RF source. The angle encoding varies sinusoidally with angle, and the array beamwidth increases in proportion to the sine of the off-boresight angle. The natural coordinates of the resulting angle subsystems are conical. During an angle data frame, the commutated source makes several scans across the antenna aperture. These scans can be in either direction. The choice of direction as a function of scan number is a system parameter known as the scan format. The number of scans per frame varies with angle function. The angle receiver makes use of all these scans in deriving an angle estimate. In doing so, it may incur a beneficial phenomenon known variously as "motion averaging" or "multipath averaging." These terms refer to the fact that over the duration of a large number of scans, the relative phases of the direct and multipath signals may change significantly due to the changes in differential path lengths which accumulate as the aircraft moves. If the differential phase change is large enough over the frame, multipath-induced bias in the angle estimate may vary from positive to negative and ultimately be "averaged out". Since motion averaging is a potentially important aspect of Doppler scan MLS performance, care is taken to see that it is properly introduced into the Lincoln Laboratory simulation.

The primary source of angle measurement error attributable to multipath phenomena derives from the method of frequency estimation employed by the airborne receiver. The receiver (which derives timing information from the incoming signal and thus operates synchronously with it) can be regarded as an approximation to the "optimal" estimator for a single sinusoid in white Gaussian noise. "Optimal" processing would involve setting up a bank of filters

Narrow (equivalent) beamwidth commutated array

$F_C + \delta_1 F$

Wide beamwidth reference antenna

$F_C - F_O + \delta_1 F$

Transmitter

Frequency sources and antenna coding generator

Frequency of received array signal

$F_C + \delta_1 F + F_D + \delta_2 F$
and
$F_C - F_O + \delta_1 F + \delta_2 F$

RF

Frequency of received reference signal

IF

Detector

$F_O + F_D$

Frequency measurement

Angle output digital and analogue

F_C = Basic transmission frequency
F_O = Offset frequency
$\delta_1 F$ = Tx drift
$\delta_2 F$ = Doppler shift due to Rx motion
F_D = Doppler shift due to Tx commutation $[= (V/\lambda) \sin\theta]$

Fig. 3-1 Doppler scan concept.

matched to expected Doppler frequencies and determining the filter with the largest output. To avoid an excessive number of filters, one typically spaces filters at frequencies separated by (scan duration)$^{-1}$ and then interpolates between adjacent filters which bracket the expected frequency. This interpolation can be realized by forming sum and difference filter outputs and dividing the difference output by the sum output.* Classic detection/estimation theory [103] shows that the matched filters can be realized by correlation in time.

The sum and difference matched filters are realized by correlating the received signals with internally generated sinusoids at the tracked frequency, as illustrated in Figure 3-2. The correlation products are weighted by Taylor coefficient time tapers, $\Gamma_\Sigma(k)$, $\Gamma_\Delta(k)$, in order to reduce the effective sidelobes. The interpolation output is exponentially smoothed to update the correlator frequency on each scan during the data frame. The correlator frequency for the start of the next frame is obtained by block averaging the scan-by-scan interpolation outputs, and this frequency is converted to an equivalent receiver angle and output to the user.

The receiver utilizes an automatic gain control (AGC) circuit to prevent the incoming signal from lying outside the range of the A/D converter. The AGC gain can vary significantly over a scan, thus putting an additional time taper on the received data.

Multipath generates errors by causing the sum and difference filter outputs to deviate from their "no multipath" values. In particular, if the multipath Doppler frequency lies within the passband of the matched filters, i.e., it is inbeam, significant errors can occur on single scans. Multipath at frequencies outside the matched filter passbands is generally of concern only when it is so large that the receiver may inadvertently lock onto it. To minimize the likelihood of the receiver locking onto multipath and/or outputting erroneous data, a number of acquisition and validation (ACQ/VAL) tests are performed on the received data.

---

*Readers familiar with radar/beacon processing will recognize that this technique is quite similar to monopulse processing [104]. A detailed discussion of radar frequency discriminators using correlator systems quite similar to the U.K. Doppler receiver is given in Ref. [105].
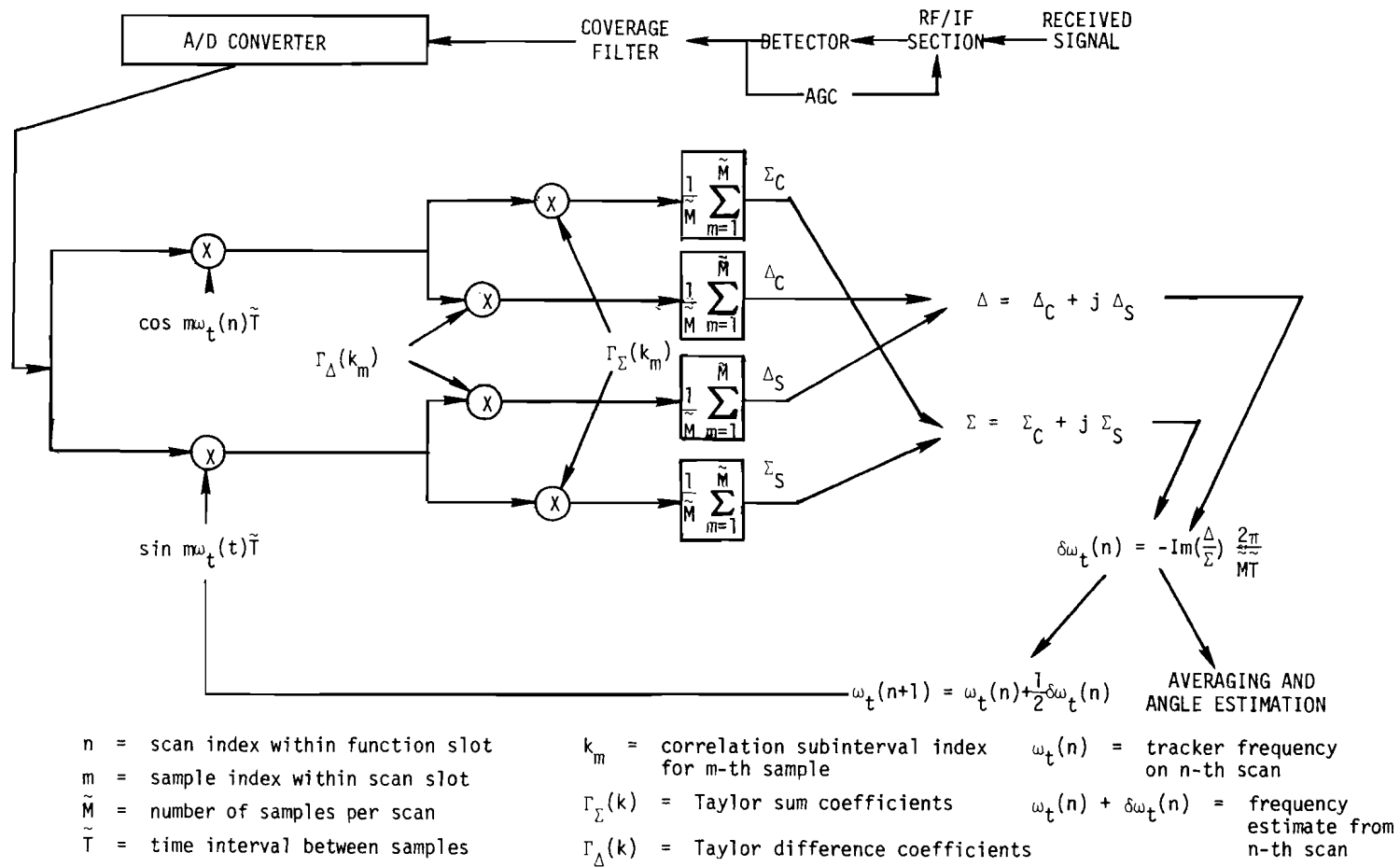
Fig. 3-2   Functional diagram of DMLS digital correlator processor.

1. Transmitted Signal Model

The reference signal is an RF tone of frequency $\omega_r \mp .5\,\omega_{off}$. The frequency of the angle signal takes on the values $\omega_r \pm .5\,\omega_{off}$. The sign of the offset in both cases is governed by the scan direction. The commutation process is modeled by assuming that the source traverses the antenna aperture (L) at a constant velocity (v_s) over the duration of a scan (T_s);[*] obviously

$$L = v_s T_s \tag{3-1}$$

A total of 2N scans are transmitted. It is assumed that the angle signal takes on the upper frequency value $\omega_r + .5\,\omega_{off}$ on the first N scans, and the lower frequency $\omega_r - .5\,\omega_{off}$ on the last N scans. The reference alternates in the opposite sequence, i.e., N scans at $\omega_r - .5\,\omega_{off}$ followed by N scans at $\omega_r + .5\,\omega_{off}$.[†] By advancing the time origin an amount T_s on each scan, we can write for the transmitted signal:[**]

Angle:

$$s(t) = \begin{cases} \text{expj}[(\omega_r + 0.5\,\omega_{off})t] & ; \text{ first N scans} \\[2em] \text{expj}[(\omega_r - 0.5\,\omega_{off})t] & ; \text{ last N scans} \end{cases} \tag{3-2}$$

---

[*]The discussion here considers the case of a filled array. The model for a thinned azimuth array using a commutated reference is discussed in Section C.

[†]This alternation of sidebands preserves the angle coding at a fixed angular direction when the scan reverses, i.e., the received frequency alternates between two values which are equidistant from the reference frequency. At baseband, this appears as a constant frequency.

[**]The process known as phase cycling (or stepping or digitization) which is employed at the angle transmitter is intentionally neglected in the model. This feature is employed to reduce granularity error in the angle estimate with zero crossing counters, but since this is an instrumentation-related, not a multipath-related, problem, it need not be of concern here. Phase cycling also helps reduce filter transient effects.

Reference:

$$s'(t) = \begin{cases} \exp j[(\omega_r - 0.5\ \omega_{off})t] & ; \text{first N scans} \\ \\ \exp j[(\omega_r + 0.5\ \omega_{off})t] & ; \text{last N scans} \end{cases} \tag{3-3}$$

A stationary observer located on the radial defined by the angular co-ordinates (θ, Φ) where θ is the (planar) scan plane coordinate angle (e.g., azimuth in the AZ system, etc.), and Φ is the orthogonal coordinate, sees a linear combination of $s'(t)$ and a Doppler shifted version of $s(t)$. Each signal is weighted by the transmitting antenna pattern in the direction (θ, Φ); these patterns are designated as $P'(\theta, \Phi)$, and $P(\theta, \Phi)$, respectively. Each of these patterns is assumed to factor into a product of an azimuth and an elevation pattern as follows:

$$P(\theta, \Phi) = P_a(\theta)\ P_b(\Phi) \tag{3-4}$$

$$P'(\theta, \Phi) = P'_a(\theta)\ P'_b(\Phi) \tag{3-5}$$

The fractional Doppler shift of $s(t)$ depends only on the source velocity vector and the conical scan plane angle θ_c corresponding to (θ, Φ). The co-ordinate systems are defined such that $\theta_c = 0$ corresponds to the plane normal to the line array axis (i.e., centerline in AZ, parallel to the ground in EL and flare). The commutated source velocity vector points in the direction $\theta_c = +90°$ on the upper sideband scan and $\theta_c = -90°$ on the lower. Therefore, the angle frequency observed at coordinate θ_c is

$$(\omega_r \pm 0.5\ \omega_{off})\ (1 \pm \frac{v_s}{c} \sin \theta_c), \tag{3-6}$$

the + or - sign depending upon the scan direction.

The proportionality constant in the angle-to-frequency mapping is called the coding factor, and is denoted by K; from (3-6) it is evident that

$$K = \frac{\omega_r v_s}{c}(\text{rad/sec})/\text{rad} \tag{3-7}$$

(to within $\pm$ $\dfrac{.5\ \omega_{off}}{\omega_r}$ $\approx \pm$ 8 ppm). A more enlightening expression for K can be given in terms of the scan duration and the aperture size in wavelengths, or simpler yet, the antenna beamwidth in degrees (θ_{BW}):

$$K = \frac{\pi}{180\ T_s} \quad \left(\frac{L}{\lambda}\right) = \frac{1}{\theta_{BW}\ T_s} \quad \text{Hz/deg} \tag{3-8}$$

An additional Doppler shift occurs if the observer (aircraft) is not stationary. The A/C-induced fractional Doppler shift is expressed as $(v_a \cos \beta)/c$, where v_a denotes the A/C velocity and β is the conical angle between the A/C velocity vector and the direction toward the incident signal. Both reference and angle signals are subject to this effect. Therefore, the reference and angle frequencies observed at a moving receiver are

$$(\omega_r \mp 0.5\ \omega_{off})\ \left(1 + \frac{v_a}{c} \cos \beta\right) \tag{3-9}$$

and

$$(\omega_r \pm 0.5\ \omega_{off})\ \left(1 \pm \frac{v_s}{c} \sin \theta_c + \frac{v_a}{c} \cos \beta\right) \tag{3-10}$$

Table 3-1 lists the values used in the simulation for the transmitter parameters defined above. The transmitter and receiver antenna patterns are described in Section D.

2. Received Signal

The received signal expression consists of a superposition of terms. One of these represents the direct path component, and the others represent the multipath propagation components. Receiver noise is excluded because

(1) the preliminary link budgets and avionics specification for DMLS indicates that nominal operation will occur at high signal-to-noise ratio, and

(2) the principal objective in this MLS simulation was the comparative effect of multipath propagation upon the operation of the various systems.

TABLE 3-1

TRANSMITTER PARAMETER VALUES FOR U.K. DOPPLER MLS SIMULATION

Parameter	Function	Symbol	Value	Units	Comments
Carrier Frequency	AZ, EL1	$\frac{1}{2\pi}\omega_r$	5.08	GHz	
Offset Frequency	AZ, EL1	$\frac{1}{2\pi}\omega_{off}$	83.2	kHz	
Scan Time	AZ	T_s	2.5	msec	54λ
	EL1	"	1.25	"	"
Number of Scans	AZ	2N	12		54λ aperture
	EL1	"	40		" "
Coding Factor	AZ	K	378	Hz/deg	at $\theta=0°$
	EL1	"	756	"	"
Commutation Speed	AZ	v_s	4.2	ft/msec	
	EL1	"	8.4	"	
Reference/Array Emphasis Ratio	AZ	R	2.0		= 6 dB
	EL1	"	4.47		= 13 dB
Reference/Array Phase Center Displacement	AZ	D_{ref}	27.0	wavelengths	
	EL1	"	1.0	"	

Each component of the received signal is characterized by 9 parameters; specifically, the i-th angle component is described by

$$\rho_i = \text{amplitude} \tag{3-11}$$

$$\tau_i = \text{path delay} \tag{3-12}$$

$$\phi_i = \text{change in phase angle due to i-th path reflection} \tag{3-13}$$

$\theta_i =$ planar transmission angle to the scattering point
on the i-th reflector in the measured coordinate $\tag{3-14}$

$\Phi_i =$ planar transmission angle to the scattering point
on the i-th reflector in the orthogonal coordinate $\tag{3-15}$

$\tilde{\theta}_i, \tilde{\Phi}_i =$ planar heading and elevation angles of scattering
point from the receiver wrt the aircraft velocity
vector $\tag{3-16}$

$$r_i = \text{fractional source-induced Doppler shift} \tag{3-17}$$

$$\tilde{r}_i = \text{fractional A/C-induced Doppler shift} \tag{3-18}$$

A similar set of parameters characterizes the reference signal; these are designated as ρ_i', τ_i', ϕ_i', θ_i', Φ_i', $\tilde{\theta}_i'$, $\tilde{\Phi}_i'$, r_i', and $\tilde{r}_i'$. Note that $r_i' \equiv 0$ for all components because the reference source velocity is zero. The values of the parameters are calculated for each reflector in the scattering portion of the program.* It has been assumed that the reference and angle antennas are

---

*The scattering models are described in Refs. [28] and [29].

colocated.[*] In those cases for which the antenna patterns of the two are identical, the multipath parameters will be identical as well. The received frequencies will not, of course, be equal due to the difference in transmitted frequency and the commutated source Doppler, but their A/C-dependent Dopplers will essentially be the same. A brief summary of the considerations which enter into the determination of each of the multipath parameters is given below.

The amplitude is computed by an appropriate electromagnetic wave propagation technique (e.g., knife-edge diffraction, Fresnel zones, bistatic cross-sections, etc.) as though the transmitting and receiving antennas were omnidirectional. The amplitude so computed (call it A_i) is weighted in the receiver program by the actual transmitting and receiving antenna patterns:

$$\rho_i = A_i P(\theta_i, \Phi_i) \quad \cdot \quad \tilde{P}(\tilde{\theta}_i, \tilde{\Phi}_i) \tag{3-19}$$

The reference amplitude ρ_i' is computed in a similar manner.

The path delay is computed according to the formula

$$\tau_i = \frac{R_{ti} + R_{ri}}{c} \tag{3-20}$$

where

R_{ti} = distance from angle transmitter to scattering point on
     i-th obstacle (3-21)

R_{ri} = distance from scattering point on i-th obstacle
     to receiver (3-22)

---

[*]A reference antenna displacement variable is provided in the program. It is assumed to be small enough so as to affect only the relative phases of the reference components.

The reference delay τ'_i is set equal to τ^*_i.

The scattering phase is computed from the electromagnetic boundary conditions at the scattering surface. If, for example, the i-th scatterer were an infinitely large planar perfect conductor, $\phi_i = 180°$.

Given the positions of the transmitter and the scatterer, the angles θ_i, $\tilde{\theta}_i$, Φ_i and $\tilde{\Phi}_i$ are found by simple geometry.

The fractional source- and A/C-induced Doppler shift r_i, $\tilde{r}_i$, $\tilde{r}'_i$ are expressed in terms of three conical angles derived from (θ,Φ), $(\tilde{\theta},\tilde{\Phi})$, $(\tilde{\theta}',\tilde{\Phi}')$. The angle between the commutated source velocity vector (on the first scan) and the vector from the angle signal transmitter to the scattering point on the reflector is denoted γ_i; the angles between the aircraft velocity vector and the vector from the receiver to the scattering point for the angle and reference antennas are denoted β_i, β'_i, respectively. Illustration is provided in Fig. 3-3. For the direct components, the reflectors are absent, and the propagation path is rectilinear. The fractional Doppler shifts are computed as

$$r_i = \frac{v_s}{c} \cos \gamma_i \tag{3-23}$$

$$\tilde{r}_i = \frac{v_a}{c} \cos \beta_i \tag{3-24}$$

$$\tilde{r}'_i = \frac{v_a}{c} \cos \beta'_i \tag{3-25}$$

---

*The reference delay should differ from the main array delay by approximately $\Delta\tau'_i = -(2\pi D_{ref}) (\sin \theta^{az}_{ci})/\omega_r$, where D_{ref} is the displacement in wavelengths of the reference array phase center from the main array phase center (assumed to be entirely in the azimuth plane) and θ^{az}_{ci} is the conical azimuth angle of the i-th component. To avoid roundoff error, this delay differential is incorporated by the receiver program as an equivalent adjustment $\Delta\phi'_i = -\omega_r \Delta\tau'_i$ to the reference phase.
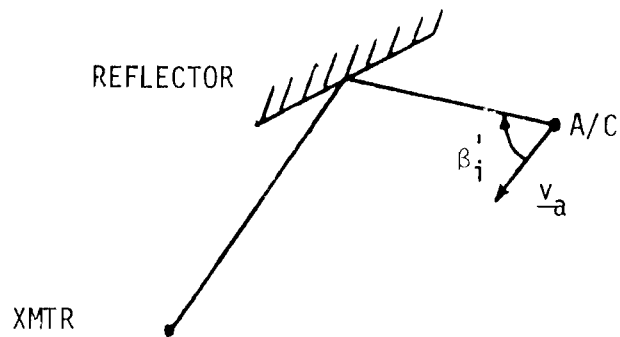
(a) Reference Frequency
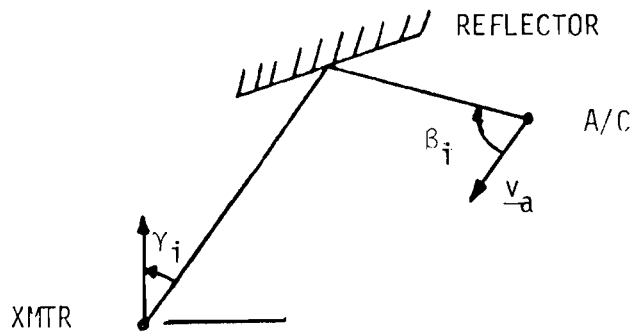
(b) Angle Frequency

Fig. 3-3   Geometry for Doppler frequency calculations.

In order to complete the received signal calculation, the time dependent delays along each of the paths must be evaluated. For the angle signal, the nominal delay τ_i represents the path delay at the middle of the first scan. The time dependent delay for the first scan is[*]

$$\tau_i(t) = \tau_i - \frac{v_a \cos \beta_i}{c} t - \frac{v_s \cos \gamma_i}{c} t \qquad (3\text{-}26)$$

Equation (3-26) can be modified to yield the delay for the n-th scan by accommodating the changes in the scan direction and updating the delay corresponding to the aircraft position at the beginning of the n-th scan. This is done in such a way that the time reference is reset to t = 0 at the middle[†] of each scan.

$$\tau_{in}(t) = \tau_i - \left(\frac{v_a \cos \beta_i}{c}\right) [t + (n-1)T_s] - d(n) \left(\frac{v_s \cos \gamma_i}{c}\right) t \qquad (3\text{-}27)$$

where

$d(n) \equiv$ scan direction indicator

$$= \begin{cases} +1 \text{ for first N scans} \\ -1 \text{ for last N scans} \end{cases} \qquad (3\text{-}28)$$

The delay formula for the reference signal is simpler, since there is no source Doppler component:

$$\tau'_{in}(t) = \tau'_i - \left(\frac{v_a \cos \beta'_i}{c}\right) [t + (n-1)T_s] \qquad (3\text{-}29)$$

---

[*]If the multipath parameters are computed with respect to the array center, t goes from $-T_s/2$ to $+T_s/2$ on the first scan.

[†]This midpoint convention might seem peculiar, but is warranted by the fact that all multipath characteristics, including delay, are computed with respect to the array midpoint.

The time dependent delays in (3-27) and (3-29) may alternatively be expressed in terms of the fractional Doppler shifts r_i, $\tilde{r}_i$, $\tilde{r}_i'$.

The total received signal can be written in terms of the parameters defined above. The i-th angle component of the n-th scan is $\rho_i y_{in}(t)$, and the corresponding i-th reference component is $\rho_i' y_{in}'(t)$, where

$$y_{in}(t) = \exp j\{[\omega_r + 0.5\, d(n)\omega_{off}]\,[t - \tau_{in}(t)] + \phi_i\} \qquad (3\text{-}30)$$

$$y_{in}'(t) = \exp j\{[\omega_r - 0.5\, d(n)\,\omega_{off}]\,[t - \tau_{in}'(t)] + \phi_i'\} \qquad (3\text{-}31)$$

Using (3-27) and (3-29) we can also write (3-30) and (3-31) in the form

$$y_{in}(t) = \exp j\,(\omega_{in} t + \phi_{in}) \qquad (3\text{-}32)$$

$$y_{in}'(t) = \exp j\,(\omega_{in}' t + \phi_{in}') \qquad (3\text{-}33)$$

where

$$\omega_{in} = [\omega_r + 0.5\, d(n)\,\omega_{off}]\left[1 + \frac{v_a \cos \beta_i}{c} + d(n)\frac{v_s \cos \gamma_i}{c}\right] \qquad (3\text{-}34)$$

$$\omega_{in}' = [\omega_r - 0.5\, d(n)\,\omega_{off}]\left[1 + \frac{v_a \cos \beta_i'}{c}\right] \qquad (3\text{-}35)$$

$$\phi_{in} = [\omega_r + 0.5\, d(n)\,\omega_{off}]\left[(n-1)T_s\frac{v_a \cos \beta_i}{c} - \tau_i\right] + \phi_i \qquad (3\text{-}36)$$

$$\phi_{in}' = [\omega_r - 0.5\, d(n)\,\omega_{off}]\left[(n-1)T_s\frac{v_a \cos \beta_i'}{c} - \tau_i'\right] + \phi_i' \qquad (3\text{-}37)$$

Since the commutated and reference signals are transmitted simultaneously, the n-th scan received signal is the sum $r_n(t)$:

$$r_n(t) = \text{Re}[y_n(t) + y_n'(t)] \qquad (3\text{-}38)$$

where

$$y_n(t) = \sum_{i=0}^{M} \rho_i y_{in}(t) \qquad (3\text{-}39)$$

$$y_n'(t) = \sum_{i=0}^{M} R\rho_i' y_{in}'(t) \qquad (3\text{-}40)$$

and R is the reference-to-array emphasis factor.

3. Receiver Processing

Figure 3-4 shows a block diagram of the U.K. receiver. The input sum signal is translated through three IF stages. The third output is applied to a final detector which has a nonlinear characteristic. The video output of this signal contains a term proportional to the product of the angle and reference signals centered in the vicinity of ω_{off} (83.2 kHz), and this is essentially the signal upon which the angle measurement is based.

Figures 3-5 and 3-6 are detailed block diagrams of the linear detector and AGC loop. The low pass filter in the feedback loop causes the AGC gain to vary so as to maintain a roughly constant (short time) average envelope out of the detector. On the other hand, the bandpass filter preceding the A/D converter has an output corresponding to the cross product between the received reference and array signals.

The basic angle tracker processing was shown in Fig. 3-2. The Taylor weightings applied are [*]

k	Time Within a Scan	$16\Gamma_{\Sigma}(k)$	$16\Gamma_{\Delta}(k)$	t_k
1	-8T to -6T	1.0	-1.1875	-7T
2	-6T to -4T	1.5	-1.5	-5T
3	-4T to -2T	2.5	-1.4375	-3T
4	-2T to 0	3.0	-0.625	- T
5	0 to 2T	3.0	0.625	T
6	2T to 4T	2.5	1.4375	3T
7	4T to 6T	1.5	1.5	5T
8	6T to 8T	1.0	1.1875	7T

$T \equiv$ integration time/16 $= 0.95 \ T_s/16$

t_k = midpoint of k-th subinterval $= (2k-9)T$

---

[*] Note that the relative weights are normalized such that $\sum_{k=1}^{8} \Gamma_{\Sigma}(k) = 1$. The difference coefficient values are taken from [68]; the sum coefficients were modified slightly from those reported in [68] as a result of UK/LL discussions in February 1977 [78].
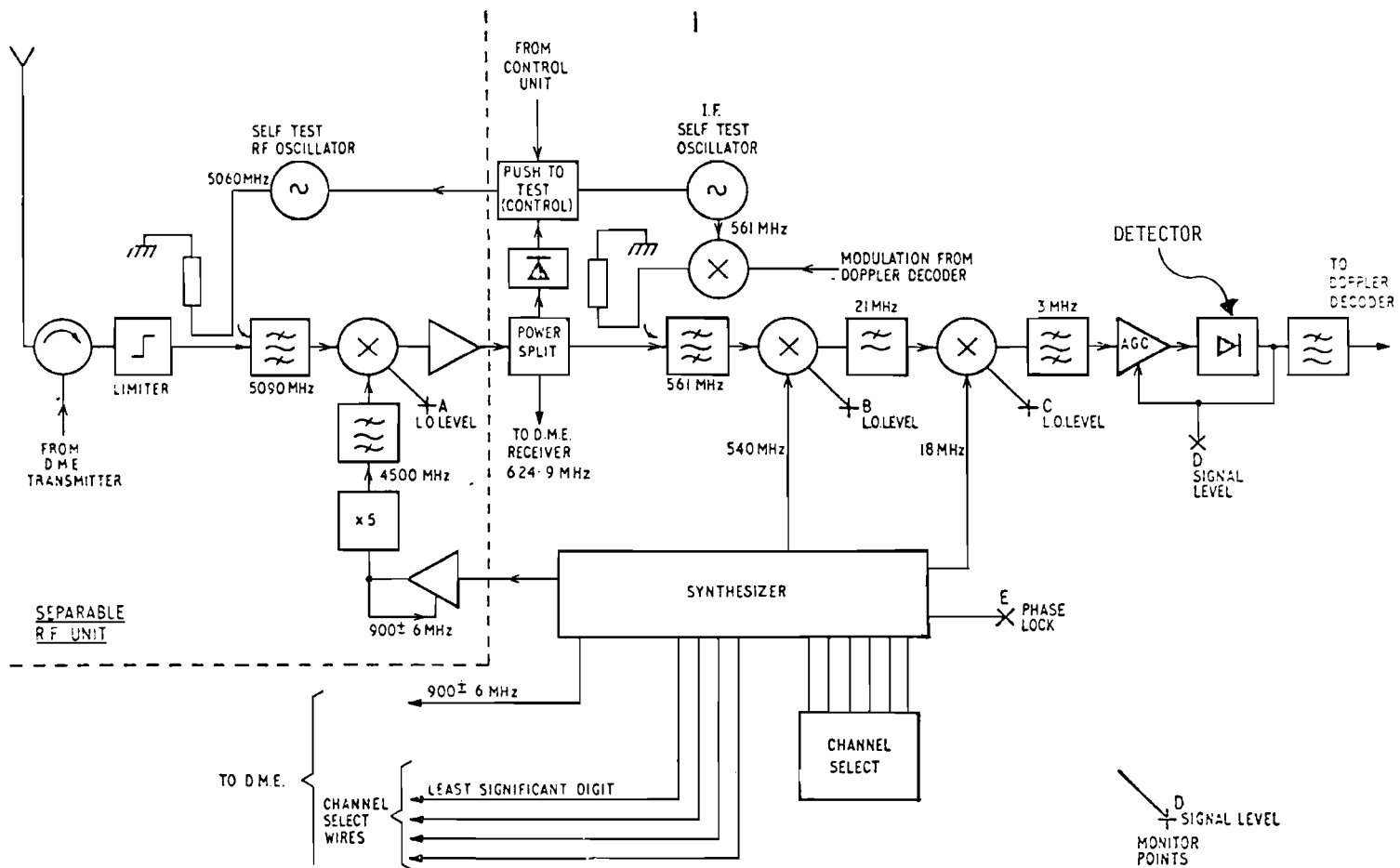
Fig. 3-4 Full capability DMLS receiver RF/IF circuits.
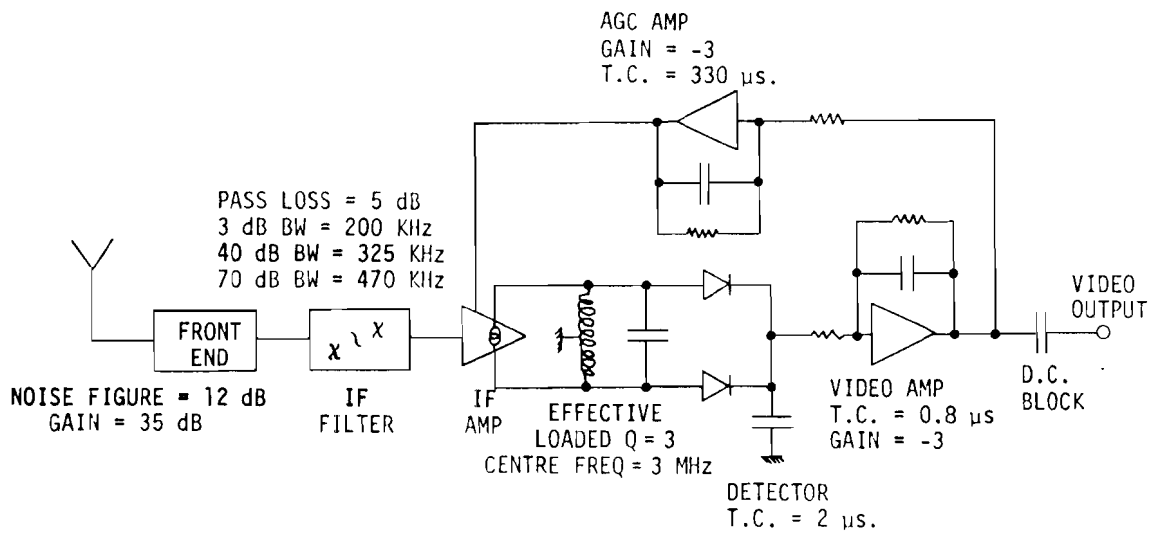
Fig. 3-5 Block diagram of DMLS receiver (from [66]).
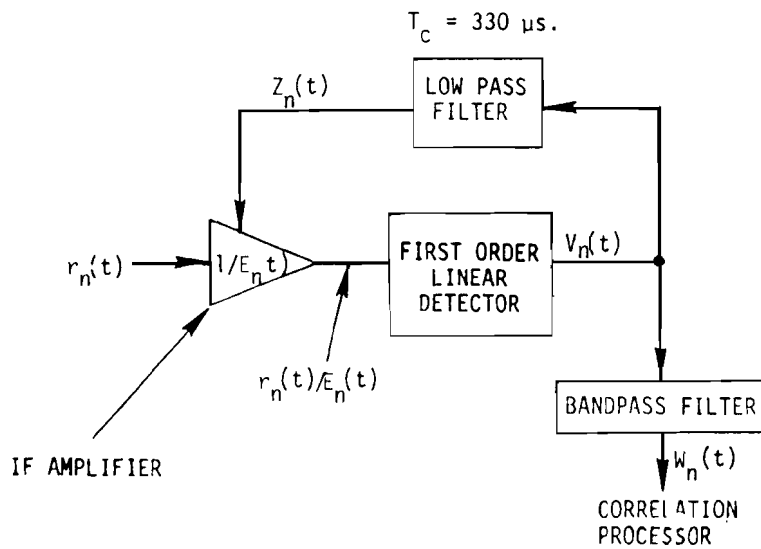
Fig. 3-6 AGC computer model.

4. Acquisition and Validation (ACQ/VAL)

In this section, we briefly present the ACQ/VAL procedure proposed by the UK for the digital correlator DMLS receiver implementation. Figure 3-7, which is taken from [67], summarizes the ACQ/VAL process. Figures 3-8 and 3-9 are detailed flow charts of the DMLS ACQ/VAL process which were supplied by the UK in July 1976 [66].[*]

The acquisition procedure consists of two stages. First, the detected signal is correlated with a set of coarsely spaced frequencies spanning the coverage region; a rough frequency estimate is determined by maximizing the correlation outputs by pairs. Then a more closely spaced set of correlation frequencies is centered around this estimate, and the procedure is repeated to obtain an initial setting for the tracker frequency.

The principal validation input from the tracker is the sum (Σ) correlation value. Three classes of tests occur:

(1) current $|\Sigma| > \frac{1}{8}$ long term time average of $|\Sigma|$

(2) short term time average of $|\Sigma| > \frac{1}{4}$ long term time average of $|\Sigma|$

(3) long term time average of $|\Sigma| \times 1.91 >$ coarse bin pairwise
search peak.[**]

A new Σ value is determined on each scan. Failing test (1) causes that scan to be ignored. Test (2) is intended to give a "fast dropout" if the tracked signal "disappears." Test (3) is the principal test for a larger out-of-beam signal. In addition to these three tests, there is an outlier check which truncates the frame angle estimate if it differs from the previous estimate by more than 0.2°.

---

[*]Additional data regarding the DMLS ACQ/VAL was obtained in Feb. 1977 as a byproduct of UK/LL discussions regarding DMLS tests in the US [78]. In particular, bin widths were increased by (and correlation times reduced by) 5% from the values given in the flow charts.

[**]The origianl UK documentation (see Fig. 3-8) used 1.625 as the comparison ratio; however, during the course of UK/LL discussions concerning the UK receiver for the proposed DMLS tests in the US [78], it was learned that 1.91 was the current preferred value.

'SHORT TERM' TRACKER BIN

'LONG TERM' TRACKER BIN

ORDINARY BINS

HOMING BINS

SPECTRUM OF DETECTOR OUTPUT

R_D A_D

-40°   0°   +40°
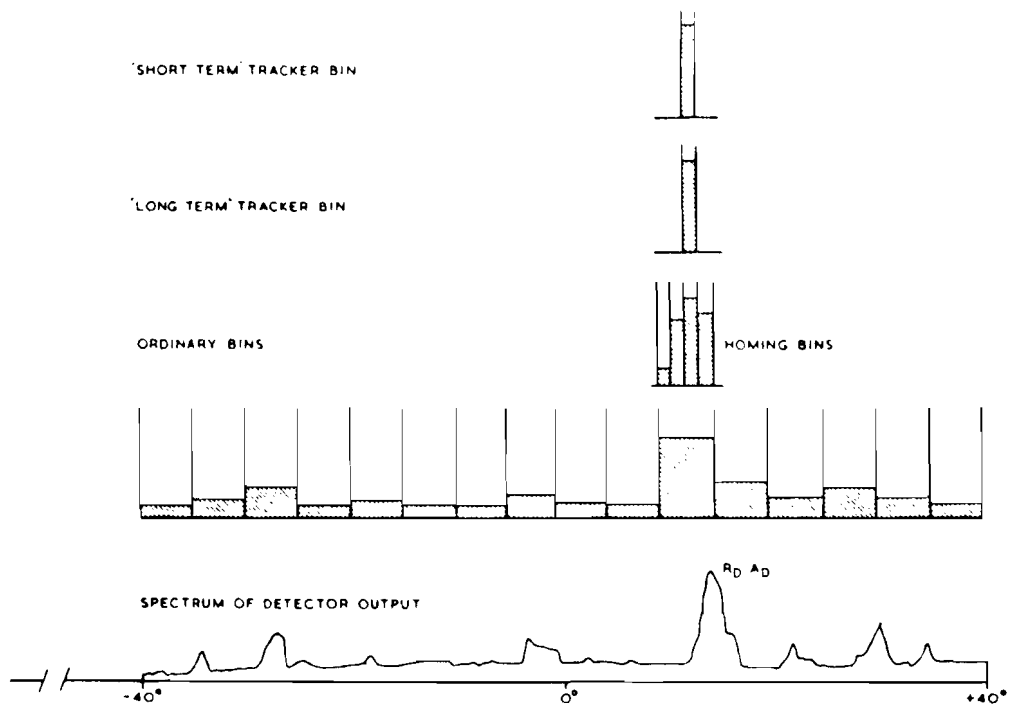
INITIAL ACQUISITION

(a) Coverage sub-divided into 16 bins.

(b) Signal content in each bin measured.

(c) Largest bin or pair of bins gives coarse position by interpolation.

FINE ACQUISITION

(a) 4 narrow bins set around coarse position.

(b) Process repeated, establishes position within half beamwidth.

(c) Set track process to fine position.

VALIDATION

(a) Continue measurement of all bins.

(b) Confirm that tracked signal corresponds to largest bin position.

CONFIDENCE

(a) Confidence timer (1 sec) incremented when validation is satisfactory, and

(b) tracked signal level is satisfactory compared with its previous history, and

(c) outlier not exceeded,

(d) Otherwise confidence decremented.

Fig. 3-7 Summary of DMLS ACQ/VAL (from CAA report [67]).

PREFERRED VALUE (PV) ROUTINE

If bins A & B contribute
to y_{pk}, Contents of bin A = C_A

START

$C_A > C_B$?

No → EXCHANGE C_A & C_B

Yes

$\delta = .5 \times 595$ Bw   BW = BIN WIDTH

$C_A > 2C_B$?

No

Yes

$\delta = .25 \times 595$ Bw

CENTRE
FREQUENCY = $Freq_A - \delta \frac{A-B}{|A-B|}$
CHOICE

RETURN

A →

SET ORD BINS TO
LEVEL NOMINAL

B

SPEND 1 SCAN MEASURING SIGNAL CONTENT
IN ALL ORD BINS. USE FORMULA

$C_{bin\ t} = \frac{1}{N} x + \frac{N-1}{N} C_{bin\ t-1}$

FOR EACH BIN.

TAKE BIN CONTENT BY PAIRS, USING FORMULA

$y = Bin_i + Bin_{i+1} + .25\ |Bin_i - B_{i+1}|$

AND SWEEP i, LOOKING FOR LARGEST VALUE OF
$y(=y_{pk})$

DOES y_{pk}
EXCEED 2.2 x AVERAGE
BIN CONTENT (BINS CONTRIBUTING
TO y_{pk} EXCLUDED)
?

No

Yes

SET 4 "HOMING" BIN LEVELS TO
STARTING VALUE REMEMBER y_{pk}

USING PV ROUTINE TO SET
4 HOMING BIN FREQUENCIES

HOMING BINS DEPLOYED

$\pm \frac{1}{2}$ & $\pm 1\frac{1}{2} \times 595$ Hz

(BIN WIDTHS) ABOUT CENTRE FREQUENCY

SPEND 1 SCAN MEASURING SIGNAL
CONTENT IN EACH HOMING BIN.
USE RECURSION FORMULA ABOVE

$(C_{bin\ t} = \frac{1}{N} x + \frac{N-1}{N} C_{bin\ t-1})$

TAKE BIN CONTENT BY PAIRS
TO OBTAIN y'_{pk} AS BEFORE

DOES Y'_{pk}
EXCEED 3 x AVERAGE
CONTENT OF THE BINS NOT
CONTRIBUTING TO Y'_{pk}
?

No

Yes

USE PV ROUTINE TO POSITION
TRACKER MECHANISM

SET TRACKED LONG TERM ANGLE BIN TO 1.5 x Y_{pk}
SET SHORT TERM TRACKED ANGLE BIN TO .5 x Y_{pk}
SET CONFIDENCE COUNTER TO VALUE 3

GO TO TRACK MODE

Fig. 3-8 DMLS ACQ/VAL flow chart (from [66]).

COMMENCED
TRACKING

CORRELATE AGAINST i/p SIGNAL
WITH TRACKING MECHANISM
NOTE i/p SIGNAL LEVEL
FROM SUM CORRELATION

UPDATE SHORT TERM AND LONG
TERM TRACKED ANGLE BINS
(τ_s = 1 sec, τ_L = 8 sec)

DID TRACKED
SIGNAL LEVEL DURING
SCAN EXCEED 1/8 OF LONG TERM TRACKED
ANGLE BIN CONTENT?

No

Yes

EVALUATE f_{dopp}, APPLY TO THE
AVERAGE RESULT (ALSO BY
RECURSION PROCESS, τ = 200 ms)

DOES SHORT
TERM TRACKED ANGLE
BIN EXCEED ¼ LONG TERM TRACKED
ANGLE BIN
?

No   RESTART
      ACQUISITION

Yes

ON EVERY 4th SCAN UPDATE ALL
ORDINARY ANGLE BINS
(τ = 8 secs)

TAKE BIN CONTENTS BY PAIRS
TO FIND Y_{pk}

DOES
LONG TERM
TRACKED ANGLE BIN
x 1.625 EXCEED
Y_{pk}?

Yes   No   NOTE
                       RESULT:Y

NOTE
RESULT:X

END OF
FUNCTION
DURATION

No

Yes

IS
NEW ANGULAR
POSITION WITHIN .2°
OF LAST STORED
RESULT?

No

Yes

STORED OUTPUT (AND
OUTPUT MADE AVAILABLE
TO PILOT) IS ALTERED
ONLY BY .2°

STORED OUTPUT IS
ALTERED TO NEW VALUE

DID
NO OF X's
EXCEED NO OF Y's
?

Yes

No

IS
FLAG ALREADY
DISPLAYED?

No

Yes

INCREMENT CONFIDENCE COUNTER

DECREMENT CONFIDENCE COUNTER   RESTART ACQUISITION

WAIT

Fig. 3-9 Acquisition/Validation for correlation
processor (cont.).

3-22

B. Angle Processor Model

The angle processor model incorporates the following features which were deemed necessary to achieve representative error models:

(1) The modulation products between the angle and reference signals are retained. Thus, effects due to multipath on both signals should emerge.

(2) Scalloping of both the angle and reference signals is included by representing the scan-to-scan phase coherence of each received component.

(3) A model of the tracker dynamics is included. By tracking on the previous angle estimate rather than the true A/C position, the "pulling" effect of inbeam multipath will be observed. This effect tends to give higher and more realistic errors than would otherwise be predicted using fixed frequency tracking.

(4) A model for the AGC dynamic behavior is included. By considering the changes in AGC gain within a scan, the modification of time weighting (and, mainlobe and sidelobe characteristics) due to multipath will be observed. This tends to give a more realistic estimate of errors than would be predicted by assuming no AGC gain variations.

(5) A model for the ACQ/VAL tests is included for the filled array system. By considering the acquisition process and the degree to which angle scan data is rejected by the validation tests, a more realistic estimate of the system performance is obtained.

The details of the processing model follow.

1. AGC Model

The AGC model is explained by reference to Fig. 3-6. The detector output $V_n(t)$ for the n-th scan is taken to be

$$V_n(t) = \frac{1}{E_n(t)} \sqrt{r_n^2(t)} \qquad (3-41)$$

or, using (3-38) and ignoring terms at twice the carrier frequency,

$$V_n(t) = \frac{1}{E_n(t)} \sqrt{\frac{1}{2}|y_n(t)|^2 + \frac{1}{2}|y_n'(t)|^2 + \text{Re}[y_n(t)y_n'^*(t)]} \qquad (3\text{-}42)$$

The low pass filter in the AGC feedback loop eliminates the reference-array cross product term, and it also eliminates those angle signal multipath component cross products $y_{in}^*(t) \, y_{jn}(t)$ contributing to $|y_n(t)|^2$ (see Eq. 3-39)) for which the frequency difference $\omega_{in} - \omega_{jn}$ lies outside the 3 kHz filter passband. This means that such component pairs should be added incoherently, rather than coherently as indicated by (3-39), in order to determine their effect on the AGC gain. Therefore, in the AGC model, the term $|y_n(t)|^2$ in (3-42) is replaced by $\sum_\ell |y_n^\ell(t)|^2$, where the $\{y_n^\ell(t)\}$ denote coherent sums

over angle signal components within $\pm$ 1.5 kHz of a set of center frequencies covering the range of received signal frequencies, i.e.,

$$y_n^\ell(t) = \sum_{i \in I_n^\ell} y_{in}(t) \qquad (3\text{-}43)$$

such that the I_n^ℓ are non-overlapping and together include all the component indices, and $i \in I_n^\ell$, $j \in I_n^\ell$ implies $\frac{1}{2\pi}|\omega_{in} - \omega_{jn}| < 3$ kHz. The frequencies of the neglected terms are also outside the passband of the filter immediately preceding the digital correlator, so they may be dropped from (3-42) altogether. There is no corresponding decomposition of the reference signal, because the aircraft-induced Doppler shifts are assumed to be small enough that all the reference component cross products are within the 3 kHz filter passband.

Using the argument above and expanding the square root in (3-42) to first order, we re-write the detector output as

$$V_n(t) = \frac{1}{E_n(t)} [V_n^0(t) + V_n^1(t)] \qquad (3\text{-}44)$$

with

$$V_n^0(t) = \sqrt{\frac{1}{2}|y_n'(t)|^2 + \frac{1}{2}\sum_\ell |y_n^\ell(t)|^2} \qquad (3\text{-}44a)$$

$$V_n^1(t) = \frac{1}{2} \text{Re}\left[y_n'(t) y_n'^*(t)/V_n^0(t)\right] \tag{3-44b}$$

The output of the low pass filter $Z_n(t)$ is just the first term in (3-44)

$$Z_n(t) = V_n^0(t)/E_n(t) \tag{3-45}$$

The feedback loop is assumed to be in quasi steady state when $Z_n(t)$ is constant, i.e.,

$$E_n(t) = R_n \sqrt{\frac{1}{2} |y_n'(t)|^2 + \frac{1}{2} \sum_\ell |y_n^\ell(t)|^2} \tag{3-46}$$

The constant R_n is chosen so as to make the complex magnitude of the sum output of the angle processor equal to unity whenever only the direct signal is present and the tracker is positioned on it exactly. This results in

$$R_n = \frac{1}{2} \frac{R\rho_0'\rho_0}{R^2\rho_0'^2 + \rho_0^2} \tag{3-47}$$

where the reference-to-array emphasis ratio. See Eqs. (3-54) and (3-58) below.

To yield a practicable computation time, it is assumed that $E_n(t)$ is constant over each of the eight subintervals of a single function scan (the same subintervals over which the Taylor weights are taken to be constant), i.e.,

$$E_n(t) \approx E_n(t_k) \qquad \text{if } t \in [t_k - T, t_k + T] \tag{3-48}$$

where

$$t_k = (2k-9)T, \ k = 1,2,\ldots,8$$

$$T = \frac{1}{16} \text{ (integration time)} = .95 \ T_s/16$$

For azimith, the subinterval length is 295 µsec, which is well matched to the low pass filter time constant. For elevation, the subinterval length is 147 µsec so the approximation is even better.

2. Angle Processor

a. Input Signal to Digital Correlator

The bandpass filter preceding the correlation processor admits only that part of the detector output represented by the second term in (3-44). Using the expression (3-46) for $E_n(t)$, we write this term as

$$\frac{V_n^1(t)}{E_n(t)} = \frac{R_n}{E_n^2(t)} \frac{1}{2} \operatorname{Re}[y_n(t) \, y_n^{'*}(t)] \qquad (3-49)$$

or, using (3-39), (3-40),

$$\frac{V_n^1(t)}{E_n(t)} = \frac{R_n}{E_n^2(t)} \frac{1}{2} \sum_{i=0}^{M} \sum_{j=0}^{M} \rho_i R \rho_j' \operatorname{Re}[y_{in}(t) \, y_{jn}^{'*}(t)] \qquad (3-50)$$

Finally, referring to (3-32) and (3-33) and denoting by $H(\omega) \, e^{j\psi(\omega)}$ the filter transfer function within its passband, we obtain an explicit expression for the input signal to the digital correlator

$$W_n(t) = \frac{R_n}{E_n^2(t)} \frac{1}{2} \sum_{i=0}^{M} \sum_{j=0}^{M} \rho_i \, R\rho_j' \cos(\omega_{ijn}t + \alpha_{ijn}) H(\omega_{ijn}) \qquad (3-51)$$

where the frequency and phase of the (i,j) component are given by

$$\omega_{ijn} = \omega_{in} - \omega_{jn}' \qquad (3-52)$$

$$\alpha_{ijn} = \phi_{in} - \phi_{jn}' + \psi(\omega_{ijn}) \qquad (3-53)$$

b. Frequency/Angle Estimator Model

The portion of the digital correlator processor which forms the sum (Σ) and difference (Δ) values in Fig. 3-2 is modeled as an analog processor because:

(1) There is a negligible difference between the analog and discrete time results, if a sufficiently high sampling rate is used.

(2) The analysis for the analog case is much easier to follow.

From Fig. 3-2 and Eq. (3-51), we find that the correlator outputs can be written as

$$\Sigma(n) = \sum_{k=1}^{8} \Gamma_\Sigma(k) \, S_n(k) \qquad\qquad (3\text{-}54)$$

$$\Delta(n) = \sum_{k=1}^{8} \Gamma_\Delta(k) \, S_n(k) \qquad\qquad (3\text{-}55)$$

where

$$S_n(k) = \frac{1}{2T} \int_{t_k-T}^{t_k+T} W_n(t) \, e^{j\omega_t(n)t} \, dt$$

$$= \frac{1}{2} \frac{R_n}{E_n^2(t_k)} \sum_{i=0}^{M} \sum_{i=0}^{M} \rho_i R\rho_j' \frac{H(\omega_{ijn})}{2T} \int_{t_k-T}^{t_k+T} \cos(\omega_{ijn}t + \alpha_{ijn}) e^{j\omega_t(n)t} \, dt$$

$$= \frac{1}{4} \frac{R_n}{E_n^2(t_k)} \sum_{i=0}^{M} \sum_{j=0}^{M} \rho_i R\rho_j' \, [F(\omega_t(n)+\omega_{ijn},t_k)e^{j\alpha_{ijn}} + F(\omega_t(n)-\omega_{ijn},t_k)e^{-j\alpha_{ijn}}]H(\omega_{ijn})$$

$$(3\text{-}56)$$

and

$$F(\omega,t) = e^{j\omega t} \frac{\sin \omega T}{\omega T} \tag{3-57}$$

One of the frequencies $\omega_t(n) \pm \omega_{ijn}$ is approximately twice the reference-array offset frequency, so the terms in (3-56) involving the corresponding $F(\omega_t(n) \pm \omega_{ijn}, t_k)$ are negligible. Therefore, $S_n(k)$ is computed in the program as

$$S_n(k) = \frac{1}{4} \frac{R_n}{E_n^2(t_k)} \sum_{i=0}^{M} \sum_{j=0}^{M} \rho_i R \rho_j' \, F(\omega_t(n)-d(n)\omega_{ijn}, t_k) \, \exp j(-d(n)\alpha_{ijn}) \, H(\omega_{ijn}) \tag{3-58}$$

The tracker frequency error for the n-th scan is estimated to be

$$\delta\omega_t(n) = -\mathrm{Im} \frac{\Delta(n)}{\Sigma(n)} \frac{2\pi}{16T} \tag{3-59}$$

and the tracker frequency for the next scan is updated according to

$$\omega_t(n+1) = \omega_t(n) + \frac{1}{2} \delta\omega_t(n) \tag{3-60}$$

At the end of the data frame the frequency estimates from all validated scans are averaged to yield the tracker frequency $\hat{\omega}_t$ for the start of the next frame

$$\hat{\omega}_t = \frac{1}{N_v} \sum_{\substack{\text{valid} \\ \text{scans} \\ n}} [\omega_t(n) + \delta\omega_t(n)] \tag{3-61}$$

where N_v is the number of valid scans. The (conical) angle estimate $\hat{\theta}_c$ for the frame is obtained from $\hat{\omega}_t$ by applying the angle coding factor (see Eq. (3-7))

$$\hat{\theta}_c = \sin^{-1}[(\hat{\omega}_t - \omega_{off})/K] \tag{3-62}$$

3-28

3. Acquisition/Validation

   a. Acquisition

The initial setting of the tracker frequency is obtained as the result of the two-stage acquisition procedure depicted in Figs. 3-7 to 3-9. While in either acquisition phase the input signal $W_n(t)$ is correlated with sinusoids and cosinusoids at each of the bin center frequencies $\omega_b(m)$ for an integration time $2T_b$ matched to the bin widths.

$$C_n(m) = \frac{1}{2T_b} \int_{t_b(m)-T_b}^{t_b(m)+T_b} W_n(t) \, e^{j\omega_b(m)t} \, dt \qquad (3-63)$$

where

$$\omega_b(m) = \omega_b(m-1) + \Delta\omega_b, \quad m = 2,\ldots,B \qquad (3-64)$$

$$2T_b = \frac{2\pi}{\Delta\omega_b}{}^{\dagger} \qquad (3-65)$$

with the number of bins B, bin width $\Delta\omega_b$, and first bin center frequency $\omega_b(1)$ specified by antenna for each acquisition phase (see Table 3-2 below).

The integral in (3-63) is evaluated in the same manner as the one in (3-56). The center correlation times $t_b(m)$ for ordinary acquisition vary with bin number across the scan time, as the correlator computational capacity is time-shared among the bins. To reduce computation time, it is assumed that the AGC factor $R_n/E_n^2(t)$ is constant over the correlation interval, and $E_n^2(t)$ is replaced by a suitable average $\bar{E}_n^2(m)$ over nearby $\{t_k\}$ of the squared envelopes during the 8 basic scan time subintervals, $\{E_n^2(t_k), k=1,\ldots,8\}$. The values of $t_b(m)$ and $\bar{E}_n^2(m)$ used in the program are listed in Table 3-2.

The correlation output $C_n(m)$ is used to update the contents $B_n(m)$ of the m-th bin according to the formula

$$B_n(m) = \frac{N_b-1}{N_b} B_{n-1}(m) + \frac{1}{N_b} |C_n(m)| \qquad (3-66)$$

---

† Except $2T_b = \frac{\pi}{\Delta\omega_b}$ in homing acquisition mode for the elevation function, because the scan time is too short to accommodate the integration time specified by (3-65).

where $\dagger \cdot \dagger$ denotes an approximation to the complex magnitude function,[*]

$$\dagger Z \dagger \equiv |\text{Re}(Z)| + |\text{Im}(Z)| + \frac{3}{8} \Big| |\text{Re}(Z)| - |\text{Im}(Z)| \Big| \qquad (3\text{-}67)$$

The time constant N_b and initial bin settings $B_0(m)$ are listed in Table 3-2.

Each acquisition phase is deemed to be complete as soon as a preferred bin pair emerges. The pair contents are calculated as

$$P_n(m) = B_n(m) + B_n(m+1) + \frac{1}{4}|B_n(m) - B_n(m+1)| \qquad (3\text{-}68)$$

and the $\hat{m}$-th pair is selected as the preferred pair on the $\hat{n}$-th scan provided that

$$P_{\hat{n}}(\hat{m}) > P_{\hat{n}}(m) \qquad \text{for all } m \neq \hat{m} \qquad (3\text{-}69)$$

and

$$P_{\hat{n}}(\hat{m}) > K_b \frac{1}{B-2} \sum_{\substack{m \neq \hat{m}, \\ \hat{m}+1}} B_{\hat{n}}(m) \qquad (3\text{-}70)$$

See Table 3-2 for the values of the comparison factor K_b.

When a preferred bin pair $\hat{m}$ is chosen on the $\hat{n}$-th scan, a frequency estimate $\hat{\omega}_b$ is calculated as

$$\hat{\omega}_b = \frac{1}{2}[\omega_b(\hat{m}) + \omega_b(\hat{m}+1)] + \frac{1}{4} \Delta\omega_b \, I_{\hat{n}}(\hat{m}) \qquad (3\text{-}71)$$

where

$$I_{\hat{n}}(\hat{m}) = \begin{cases} +1 & \text{if } B_{\hat{n}}(\hat{m}+1) > 2B_{\hat{n}}(\hat{m}) \\ -1 & \text{if } B_{\hat{n}}(\hat{m}) > 2B_{\hat{n}}(\hat{m}+1) \\ 0 & \text{otherwise} \end{cases} \qquad (3\text{-}72)$$

---

[*]Note that $\dagger Z \dagger$ varies from $1.375 \, |Z|$ to $1.510 \, |Z|$, depending on the phase of Z, so the approximation $\dagger \cdot \dagger$ includes roughly a 3 dB emphasis.

TABLE 3-2
ACQUISITION PARAMETERS

	ORDINARY ACQ		HOMING ACQ	
	AZ	EL	AZ	EL
B	16	8	4	4
$\frac{1}{2\pi}\Delta\omega_b$	2506 Hz	2506 Hz	627 Hz	627 Hz
$\frac{1}{2\pi}\omega_b(1)$	64403 Hz	84109 Hz	*	*
N_b	120	400	120	400
$B_{\hat{n}}(m)$ [†] (same for all m)	.076	.076	.038	.054
K_b	2.2	2.2	3.0	3.0
$t_b(m)$	t_1, m=1,2,3,4 t_3, m=5,6,7,8 t_5, m=9,10,11,12 t_7, m=13,14,15,16	t_2, m=1,2,3,4 t_6, m=5,6,7,8	0	0
$\bar{E}_n^2(m)$	$E_n^2(t_b(m))$	$\frac{1}{3}\sum_{k=1}^{3}E_n^2(t_k),$ m=1,2,3,4 $\frac{1}{3}\sum_{k=5}^{7}E_n^2(t_k),$ m=5,6,7,8	$\frac{1}{8}\sum_{k=1}^{8}E_n^2(t_k)$	$\frac{1}{8}\sum_{k=1}^{8}E_n^2(t_k)$

*Homing bin frequencies are centered around the estimate $\hat{\omega}_b$ obtained from ordinary acquisition, i.e., $\omega_b(1) = \hat{\omega}_b - 1.5\,\Delta\omega_b$.

[†]$\hat{n} = 0$ for start of ORDINARY ACQ, $\hat{n}$ = last scan from ORDINARY ACQ for start of HOMING ACQ.

The homing bin frequencies $\omega_b(m)$ are centered around the frequency estimate $\hat{\omega}_b$ obtained from ordinary acquisition. The tracker frequency $\omega_t(\hat{n}+1)$ for the first scan in track is initialized to the frequency estimate $\hat{\omega}_b$ obtained from homing acquisition.

b. Validation

Once acquisition is finished, the tracker frequency is updated according to (3-60) or (3-61) and angle estimates are obtained from (3-62) as long as the validation tests are passed. The confidence counter is initialized at the value 3 upon completion of acquisition and it increments by 1 (up to a saturation value 9) at the end of every validated frame. When it reaches the value 8, the system flag is raised and the frame angle estimates are accepted. Once raised, the system flag is only lowered if a series of frames with validation failures causes the confidence counter to decrement to the value 3.

Most of the validation checks focus on the time history of the tracker sum output $\Sigma(n)$. Long- and short-term tracker averages $T_L(n)$, $T_S(n)$ are computed recursively as follows.

$$T_L(n) = \frac{N_L - 1}{N_L} \, T_L(n-1) + \frac{1}{N_L} \, |\Sigma(n)| \qquad (3-73)$$

$$T_S(n) = \frac{N_S - 1}{N_S} \, T_S(n-1) + \frac{1}{N_S} \, |\Sigma(n)| \qquad (3-74)$$

where

$$N_L = \begin{cases} 480 & \text{for AZ} \\ 1600 & \text{for EL} \end{cases} \qquad (3-75)$$

$$N_S = \begin{cases} 60 & \text{for AZ} \\ 200 & \text{for EL} \end{cases} \qquad (3-76)$$

The initial values of T_L and T_S are determined from the contents of the peak bin pair from the _ordinary_ acquisition phase.[*]

$$T_L (\hat{n}_h) = 1.5 \, P_{\hat{n}_0} (\hat{m}_0) \qquad\qquad (3\text{-}77)$$

$$T_S (\hat{n}_h) = 0.5 \, P_{\hat{n}_0} (\hat{m}_0) \qquad\qquad (3\text{-}78)$$

At the same time the ordinary acquisition bins are updated on every 4th scan while in track.

$$B_{4n}(m) = \frac{N_b - 1}{N_b} \, B_{4n-4}(m) + \frac{1}{N_b} \left| C_{4n}(m) \right| \qquad\qquad (3\text{-}79)$$

N_b is unchanged from its acquisition phase value, so the effective time constant is increased by a factor of 4 (to match that of the long-term tracker average).

The validation tests are expressed in terms of these quantities as follows.

(1) Individual scans are invalidated whenever

$$\left| \Sigma(n) \right| < \frac{1}{8} T_L(n) \qquad\qquad (3\text{-}80)$$

Such scans do not contribute to the frame angle estimate in (3-61), and they do not cause the tracker frequency to be updated as in (3-60).

(2) If at any time the short-term average becomes too small, specifically,

$$T_S(n) < \frac{1}{4} T_L(n) \qquad\qquad (3\text{-}81)$$

track mode is immediately halted and acquisition is restarted from scratch.

---

[*] $\hat{n}_0$, $\hat{n}_h$ = last scan from ordinary, homing acquisition, respectively.

$\hat{m}_0$ = preferred ordinary bin pair

(3) On each ordinary bin update, it is determined whether

$$P_{4n}(m) > 1.91 \ T_L(4n) \qquad \text{for some bin pair } m \qquad (3\text{-}82)$$

If condition (3-82) prevails for at least half the checks within a frame, the confidence counter is decremented. Furthermore, if confidence is already low enough that the system flag was not raised at the beginning of the frame, acquisition is restarted, but the ordinary bins are not re-initialized.

In addition to these three tests, there is an outlier test which affects the confidence counter, the output angle estimate, and acquisition restarts due to validation test (3).

(4) Whenever the new angle estimate $\hat{\theta}_c = \sin^{-1}[(\hat{\omega}_t - \omega_{off})/K]$ given by (3-62) differs from the previous frame angle estimate $\hat{\theta}_c^{\circ}$ by more than θ_{max} (= 0.2°), the new estimate is truncated,*

$$\hat{\theta}_c^{trunc} = \hat{\theta}_c^{\circ} + \theta_{max} \ \text{sgn} \ \{\hat{\theta}_c - \hat{\theta}_c^{\circ}\} \qquad (3\text{-}83)$$

the confidence counter is decremented, and validation test (3) is bypassed. The tracker frequency for the next frame remains at the value determined by (3-61).

There is one situation that is not addressed in the U.K. flow chart (Fig. 3-8). If every scan within a frame fails validation test (1) above, there is no data from which to compute the frequency estimate in (3-61). In the computer model, this situation causes the confidence counter to decrement and no frame angle estimate is returned. The tracker frequency and the saved angle estimate for the outlier comparison do not change from their values at the start of the frame. The frame is still subjected to validation tests (2) and (3), but not to the outlier test.

There is no provision in the U.K. flow chart for restarting acquisition based on the confidence counter alone. Thus, it is possible for the confidence counter to decrement all the way to 0 (as a result of outlier failure or frames with no valid scans) and remain there indefinitely. Since a string of

---

*The function sgn(x) is defined by sgn x = +1 if x > 0 and -1 otherwise.

of outlier failures causes validation test (3) to be bypassed, it may be difficult to drop a faulty track under these circumstances. Because it is felt that this might have been an unintentional oversight, the DMLS model permits an option which causes acquisition to be started from scratch whenever the confidence counter reaches the value 0. However, this option has not been employed in any of the simulations.

C. Uniformly Thinned Azimuth Array Model

The UK has proposed that uniformly thinned azimuth arrays (such as those used in the RAE field tests) be used at nondifficult sites [7]. For difficult sites, it is proposed that filled arrays would be utilized. Since 1) the WG-A scenarios were intended to be "difficult" sites, and 2) only a filled azimuth array has operated with the proposed TDM format, it was felt appropriate to initially model the thinned array in lesser detail than was done for the filled arrays.

The model for the density tapered array contains the following features which were deemed necessary for an initial model:

(1)   The modulation products between the angle and reference signals are retained. Thus effects due to multipath on both signals should emerge.

(2)   Scalloping of both the angle and reference signals is included by representing the scan-to-scan phase coherence of each received component.

(3)   A model of the tracker dynamics is included. By tracking on the previous angle estimate rather than the true A/C position, the "pulling" effect of inbeam multipath will be observed. This effect tends to give higher and more realistic errors than would otherwise be predicted using fixed frequency tracking.

(4)   The discrete commutation process is modeled so that the multipath "grating lobes" characteristic of this form of array will be considered.

Neither the AGC dynamic model nor the full acquisition/validation tests are incorporated in the model. Rather, a fixed AGC gain is assumed and the tracker is initialized at the frequency of the direct signal.

We now describe the tracker model for uniformly thinned azimuth arrays. Since the properties of these arrays have been described in other Lincoln publications (see section 4.3.3 of [28]) as well as in the UK proposal (see Appendix C.3 of [7]), it will be assumed here that the reader is conversant with the theory of operation and single multipath signal analysis for such arrays.

To minimize the complexity of the resulting expressions, we assume that hard switching is used. This increases spectrum splatter into adjacent channels, but essentially does not affect the multipath performance for the channel of concern.

The reference array is assumed to consist of $N_f = 2L + 1$[*] elements spaced δ wavelengths apart while the main array consists of $N_m - 8(2J + 1)$[*] elements spaced $N_f \delta$ wavelengths apart.[†] The main array source is stepped between adjacent positions at a rate $1/N_f T_\delta$ while the reference array source commutates between its elements at a rate $1/T_\delta$.[†] When the reference array reaches its last element, it "jumps back" to its starting position on the next commutation. The reference array steps of size δ are in the opposite direction to the main array commutation, so that the separation between reference and main array sources increases by δ every T_δ seconds.

Let the main array element index be denoted by m and the reference array index by ℓ. Each measures in the commutation direction for its array the element's position with respect to the center of that array in units of the interelement spacing.[**] The (ℓ,m) element pair is active for times t in the interval

$$t \, \varepsilon \, I_{\ell m} \equiv \left[t_{\ell m} - \frac{T_\delta}{2} \, , \, t_{\ell m} + \frac{T_\delta}{2} \right] \qquad (3\text{-}84)$$

---

[*]L and J may be either integer or half-integer quantities.

[†]In the current thinned array model, $N_f = 2$, $N_m = 48$, $\delta = 0.57$, $T = 26.3$ μsec.

[**]ℓ may be either integer of half-integer; m must be half-integer because N_m is assumed to be divisible by 8.

where

$$t_{\ell m} = (\ell + m \, N_f)T_\delta \qquad (3\text{-}85)$$

For times within any interval $I_{\ell m}$ the sources are stationary, so the received angle and reference signals are computed in the same manner as the reference signal in Section A, except that a phase differential corresponding to the displacement of the (ℓ,m) elements from the array centers must be included.

$$y_{in}(t) = \exp j \, (\omega^o_{in} t - \phi_{in} + \xi_{inm}), \quad t \, \epsilon \, I_{\ell m} \qquad (3\text{-}86)$$

$$y'_{in}(t) = \exp j \, (\omega'_{in} t + \phi'_{in} + \xi'_{in}), \quad t \, \epsilon \, I_{\ell m} \qquad (3\text{-}87)$$

where ω'_{in}, ϕ_{in}, ϕ'_{in} are the same frequency and phases defined in (3-35) to (3-37), and the angle frequency ω^o_{in} is obtained from (3-34) by setting v_s to zero.

$$\omega^o_{in} = [\omega_r + 0.5 \; d(n) \; \omega_{off}] \left(1 + \frac{v_a \cos \beta_i}{c}\right) \qquad (3\text{-}88)$$

The angle encoding is now contained in the element-dependent phase differentials, ξ_{inm}, $\xi'_{in\ell}$, which are defined as

$$\xi_{inm} = d(n) \; 2\pi m \, N_f \delta \, \cos \gamma_i \qquad (3\text{-}89)$$

$$\xi'_{in\ell} = - \, d(n) \; 2\pi \ell \delta \, \cos \gamma'_i \qquad (3\text{-}90)$$

The input signal to the correlator is written in a manner analogous to (3-51)[*]

$$W_n(t) = \frac{1}{2} \sum_{i=0}^{M} \sum_{j=0}^{M} \rho_i \, R\rho'_j \; \cos \, (\omega^o_{ijn} t + \alpha_{ijn} + \xi_{inm} - \xi'_{jn\ell}),$$

$$t \, \epsilon \, I_{\ell m} \qquad (3\text{-}91)$$

---

[*]The AGC factor $\dfrac{R_n}{E_n^2(t)}$ is not incorporated in the thinned array model, and the sector filter transfer function is assumed to be flat, $H(\omega) = 1$, $\psi(\omega) = 0$.

where α_{ijn} is as defined in (3-53) and

$$\omega^o_{ijn} = \omega^o_{in} - \omega'_{jn} \qquad\qquad (3\text{-}92)$$

The correlator output for the k-th integration subinterval is given by a discrete version of the integral in (3-56). It is assumed that the sampling rate for the correlator multiplications is equal to $1/T_\delta$. The correlation time 2T is taken to be 1/8 times the main array scan time, i.e.,

$$2T = \frac{1}{8} N_m N_f T_\delta = (2J + 1) N_f T_\delta \qquad\qquad (3\text{-}93)$$

Thus, the center of the k-th subinterval is given by

$$t_k = (2k - 9)T = J_k N_f T_\delta \qquad\qquad (3\text{-}94)$$

where

$$J_k = (2k - 9) (J + \frac{1}{2}) \qquad\qquad (3\text{-}95)$$

In terms of these quantities the correlator output is represented as

$$S_n(k) = \sum_{m=J_k-J}^{J_k+J} \sum_{\ell=-L}^{L} W_n(t_{\ell m}) e^{j\omega_t(n)t_{\ell m}} \frac{1}{N_f (2J + 1)} \qquad (3\text{-}96)$$

Referring to (3-89)-(3-91) and expanding $\cos(\cdot)$ as $\frac{1}{2}[e^{j(\cdot)} + e^{-j(\cdot)}]$, we evaluate $S_n(k)$ as

$$S_n(k) = \frac{1}{4} \sum_{i=0}^{M} \sum_{j=0}^{M} \rho_i R \rho'_j \left[\exp j(J_k N_f v^+_{ijn} + \alpha_{ijn}) F_J(N_f v^+_{ijn}) F_L(v'^+_{ijn}) \right.$$

$$\left. + \exp j(J_k N_f v^-_{ijn} - \alpha_{ijn}) F_J(N_f v^-_{ijn}) F_L(v'^-_{ijn}) \right]$$

$$(3\text{-}97)$$

where

$$v^+_{ijn} = (\omega_t(n) + \overset{o}{\omega}_{ijn})T_\delta + d(n)\ 2\pi\delta\ \cos\ \gamma_i \qquad (3\text{-}98)$$

$$v^-_{ijn} = (\omega_t(n) - \overset{o}{\omega}_{ijn})T_\delta - d(n)\ 2\pi\delta\ \cos\ \gamma_i \qquad (3\text{-}99)$$

$$v'^+_{ijn} = (\omega_t(n) = \overset{o}{\omega}_{ijn})T_\delta + d(n)\ 2\pi\delta\ \cos\ \gamma'_j \qquad (3\text{-}100)$$

$$v'^-_{ijn} = (\omega_t(n) - \overset{o}{\omega}_{ijn})T_\delta - d(n)\ 2\pi\delta\ \cos\ \gamma'_j \qquad (3\text{-}101)$$

and the Fourier series kernel is given by[*]

$$F_Q(\nu) = \frac{1}{2Q+1}\ \sum_{q=-Q}^{Q}\ e^{j\nu q}$$

$$= \frac{\sin\ (2Q+1)\ \dfrac{\nu}{2}}{(2Q+1)\ \sin\ \dfrac{\nu}{2}}\ . \qquad (3\text{-}102)$$

Analogously to the evaluation of $S_n(k)$ for filled arrays in (3-56), (3-58), only one of the terms inside the brackets in (3-97) is retained in the computer algorithm for each scan type. $S_n(k)$ is approximated as

$$S_n(k) = \frac{1}{4}\ \sum_{i=0}^{M}\ \sum_{j=0}^{M}\ \rho_i R\rho'_j\ \exp j(J_k N_f v_{ijn} - d(n)\ \alpha_{ijn})\ F_J(N_f v_{ijn})\ F_L(v'_{ijn})$$

$$(3\text{-}103)$$

where

$$v_{ijn} = (\omega_t(n) - d(n)\ \overset{o}{\omega}_{ijn})T_\delta - 2\pi\delta\ \cos\ \gamma_i \qquad (3\text{-}104)$$

$$v'_{ijn} = (\omega_t(n) - d(n)\ \overset{o}{\omega}_{ijn})T_\delta - 2\pi\delta\ \cos\ \gamma'_j \qquad (3\text{-}105)$$

---

[*]The evaluation of F_Q is valid for both integer and half-integer values of Q. At points ν for which the denominator in (3-102) vanished (namely, ν = 0, $\pm\pi$, $\pm2\pi$, $\pm3\pi$,. . .), $F_Q(\nu)$ = 1.

The sum and difference outputs are computed as in (3-54) and (3-55), and equations (3-59) to (3-62) are used to update the tracker frequency and determine the angle estimate.[†] The angle estimate is subjected to the outlier test (test (4) in Sec.b.3.b), and it is truncated according to (3-83) if the test is failed. No other validation checks are performed.

D.   Antenna Models

The various DMLS antenna patterns assumed for the simulation are depicted in Figs. 3-10 to 3-15. The sector filter response is shown in Figs. 3-16 and 3-17. Each figure includes the computer simulation pattern and one measured or proposed by the UK. For convenience, the various patterns are catalogued in Table 3-3.

E.   Limitations of the DMLS Model

In this section, we discuss the following factors which should be considered in utilizing this version of the DMLS system model:

(a)   relationship of system model to field test equipment

(b)   near field effects

(c)   low signal to noise ratio effects

(d)   coverage limits

(e)   effects of receiver memory on error behavior

and (f)   spatial variation of multipath characteristics.

Our intent here is to make the reader aware of these factors, so as to minimize the possibility of erroneous conclusions being drawn from the model results.

As indicated in the introduction, the system model here is based on the system proposed by the UK for ICAO assessment, as opposed to replication in all respects of the existing test hardware. Attempts have been made to obtain confirmation of the receiver processing algorithm details and measured ground

3-40

O dB

5

10

15

-90 -70 -50 -30 -10 0 10   30   50   70   90

AZIMUTH ANGLE (deg)
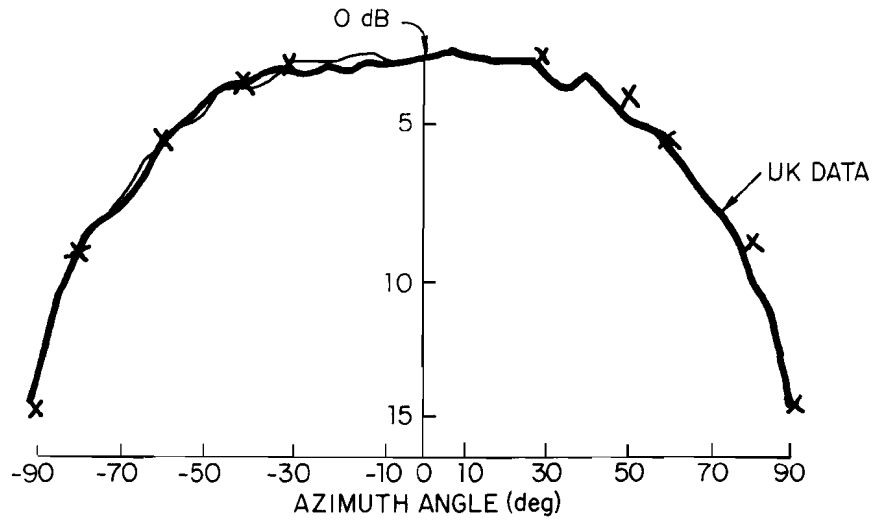
UK DATA

X = POINTS FOR PIECEWISE LINEAR INTERPOLATION

UK DATA [66]

AZIMUTH HORIZONTAL PATTERN OF COLUMN ELEMENT

0.0

-2.5

-5.0

-7.5

-10.0

-12.5

-15.0

-90   -60   -30   0   30   60   90

AZIMUTH IN DEGREES

AZIMUTH PATTERN (DB)

MODEL
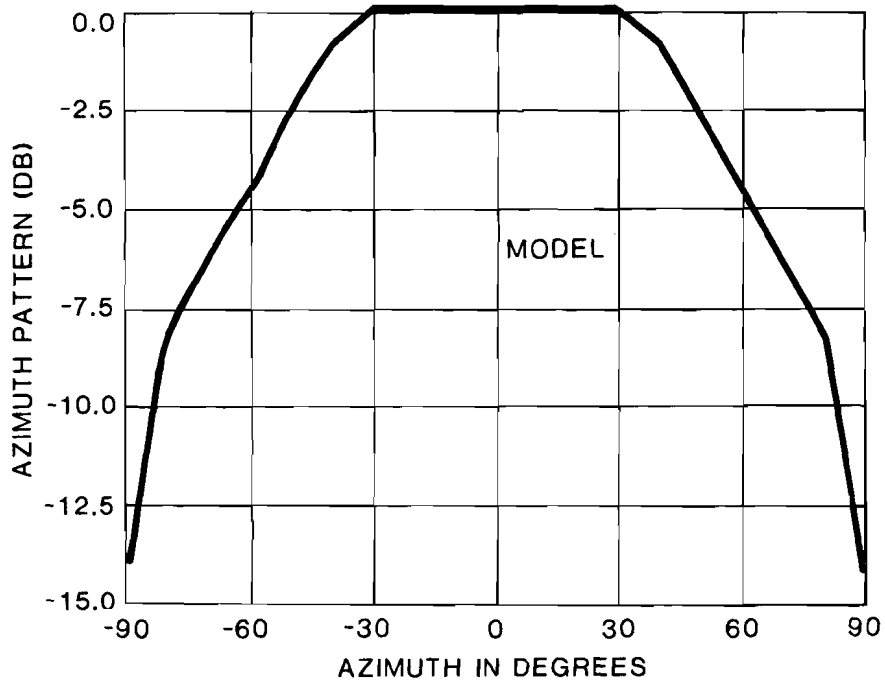
Fig. 3-10 Azimuth pattern of DMLS azimuth main array and reference
array without centerline emphasis.

ELEMENT WEIGHTS ⟶ $\dfrac{\dot{E}}{16}$ $\dfrac{\dot{E}}{8}$ $\dfrac{\dot{E}}{8}$ $\dot{E}$ $\dfrac{\dot{E}}{8}$ $\dfrac{\dot{E}}{8}$ $\dfrac{\dot{E}}{16}$

|0.75λ|0.75λ| 1λ |

GAIN (DB)

UK DATA [66]

SINGLE ELEMENT

TYPICAL MODIFIED
REFERENCE

AZIMUTH ANGLE

MODEL

AZIMUTH PATTERN (DB)

AZIMUTH IN DEGREES
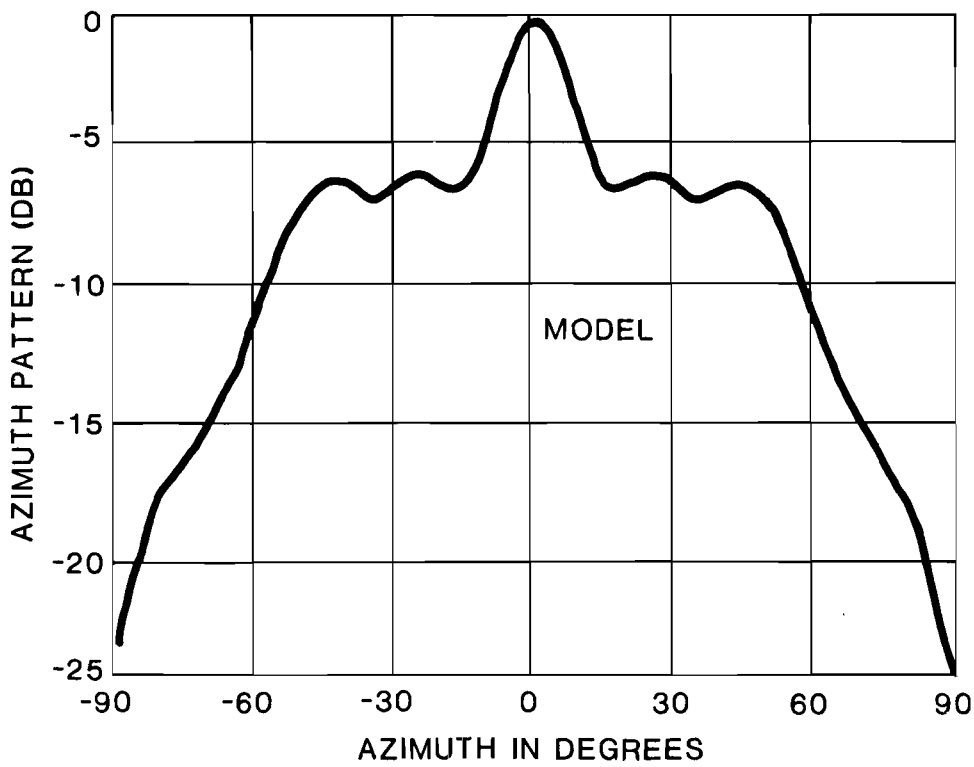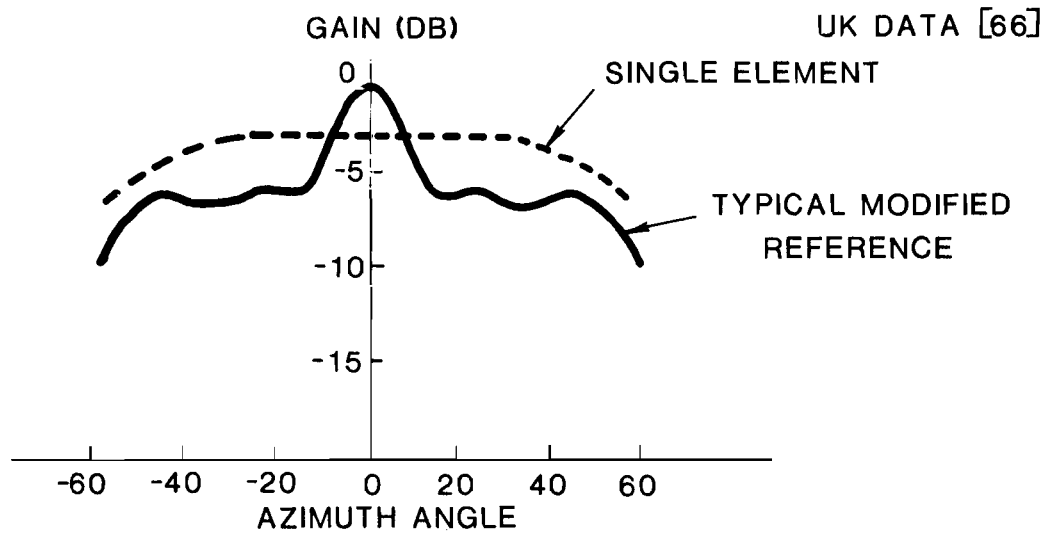
Fig. 3-11   Azimuth pattern of DMLS azimuth reference array
with centerline emphasis.

3-42

0 = points for interpolation

UK data

Measured Pattern (from Fig. 2.3.13b
of Ref. [7]).

MODEL PATTERN
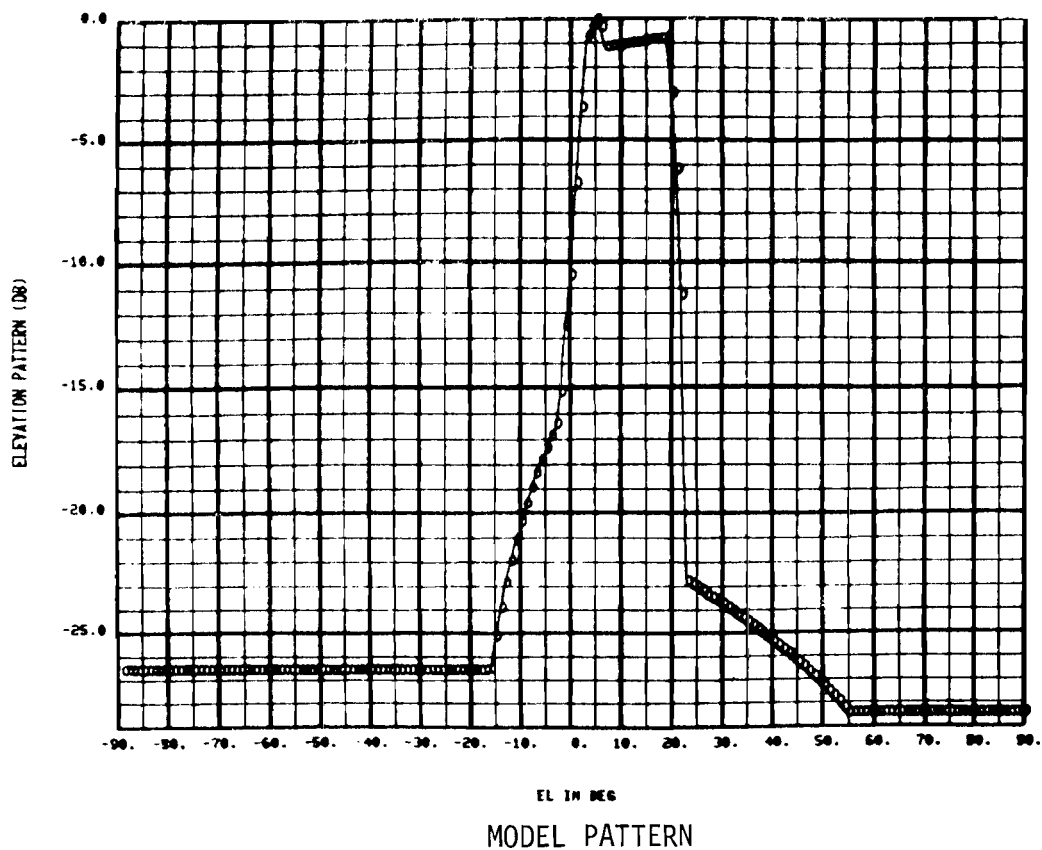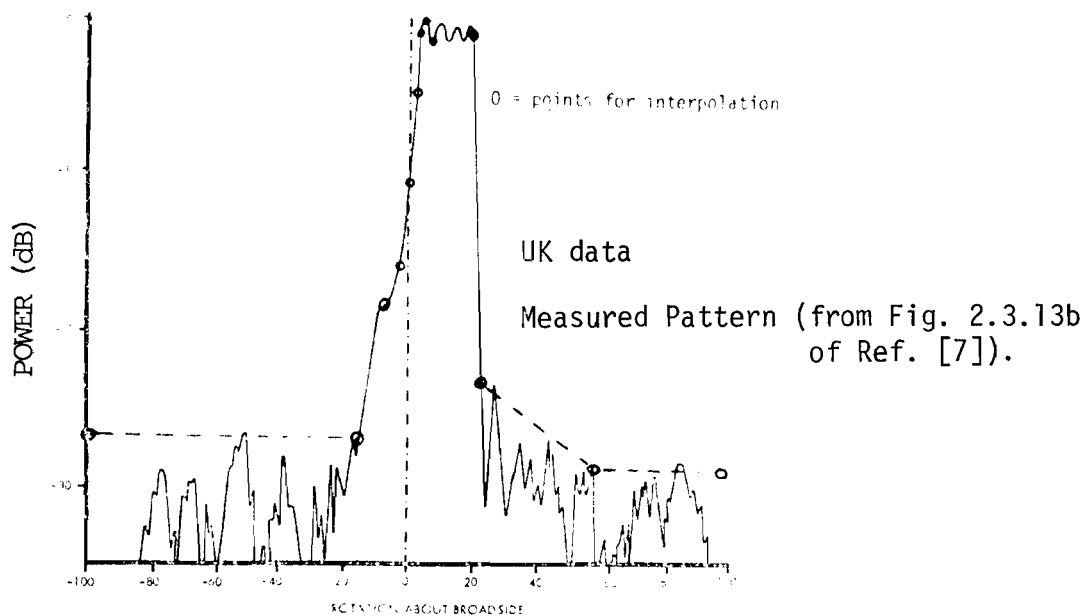
Fig. 3-12 Elevation pattern of DMLS azimuth main and reference arrays.

Without External Flares

With External Flares

X = Points for Piecewise Linear Approximation

Relative Amplitude (dB)

Patterns taken from [66]

Proposed Pattern

Pattern of UK Field Equipment

Azimuth, (Degrees)
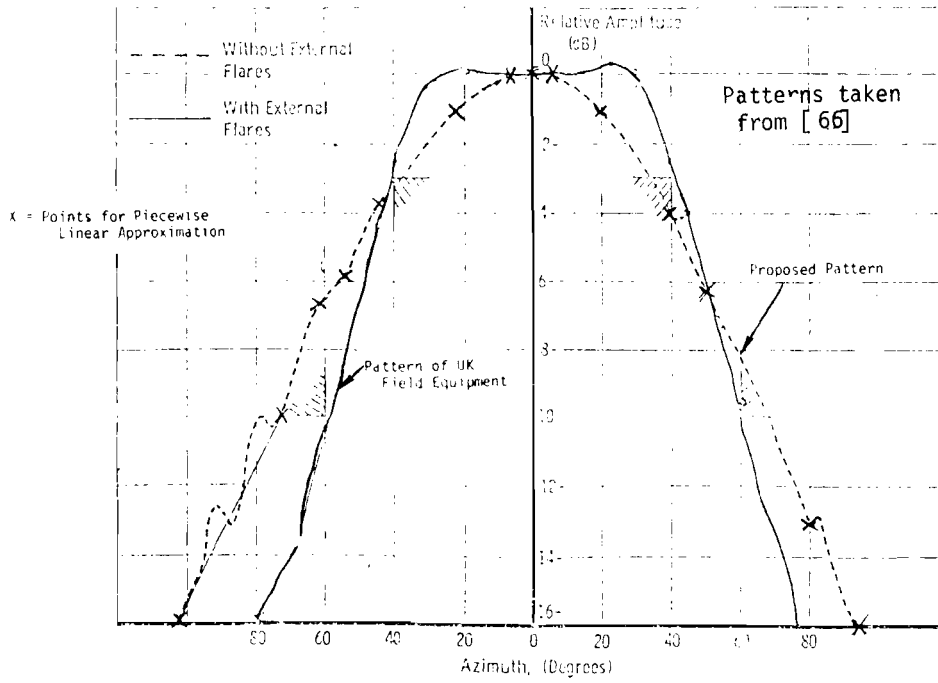
AZIMUTH RADIATION PATTERN OF DMLS ELEVATION ARRAY

AZIMUTH PATTERN (DB)

-0.0

-2.5

-5.0

-7.5

-10.0

-12.5

-15.0

MODEL

-90. -80. -70. -60. -50. -40. -30. -20. -10. 0. 10. 20. 30. 40. 50. 60. 70. 80. 90.

AZ IN DEG
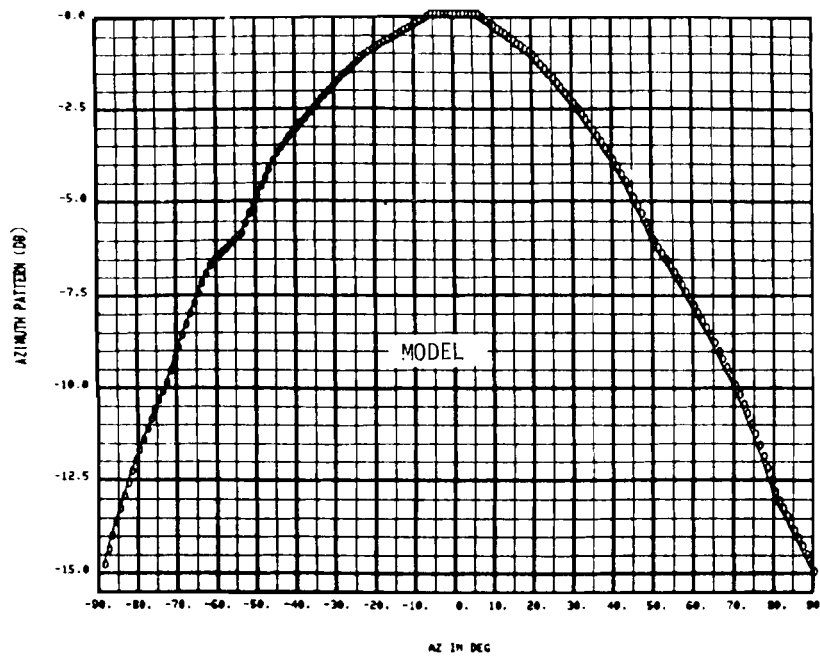
Fig. 3-13   Azimuth pattern of DMLS elevation main and reference arrays.
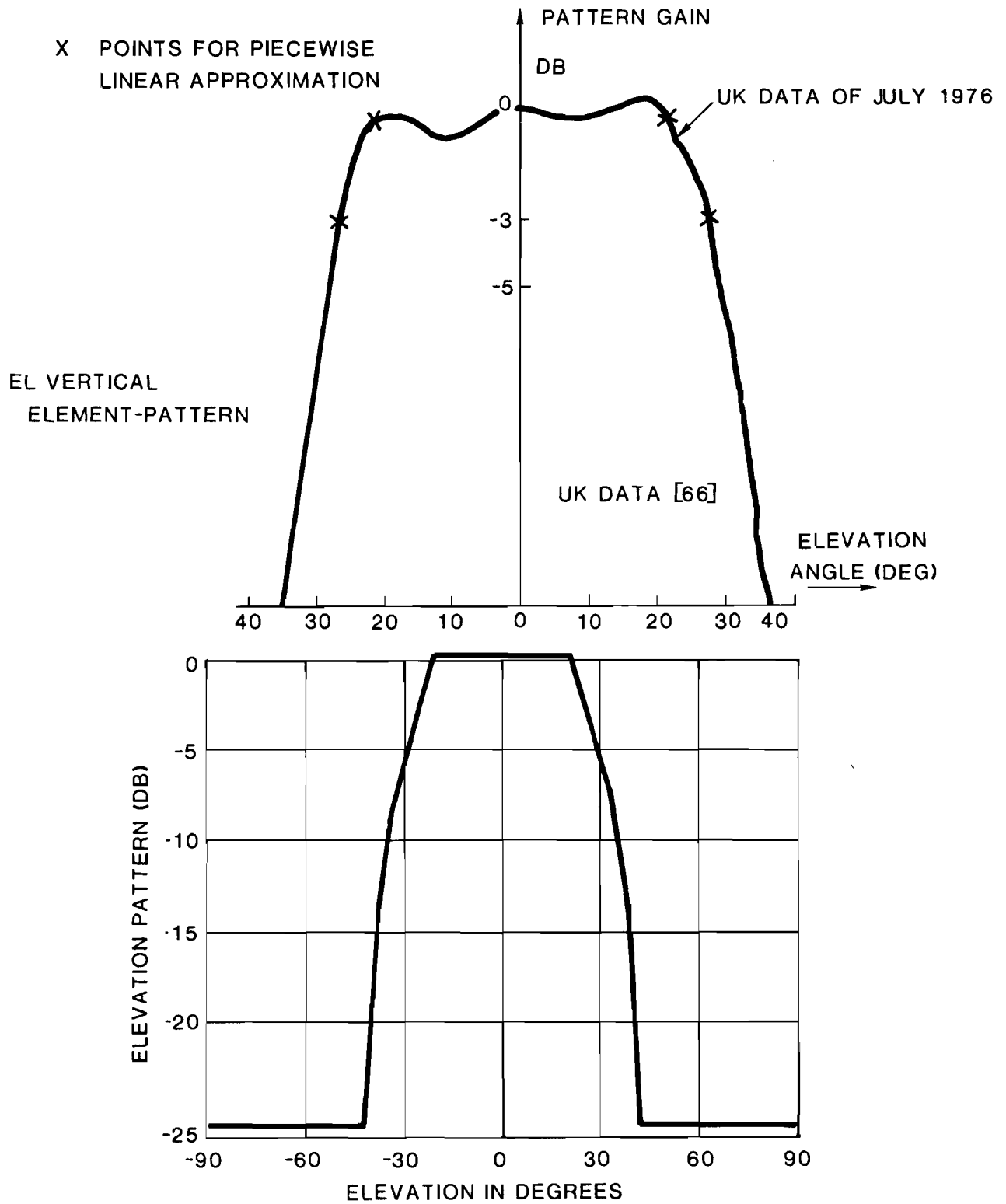
Fig. 3-14 Elevation pattern of DMLS elevation main array.
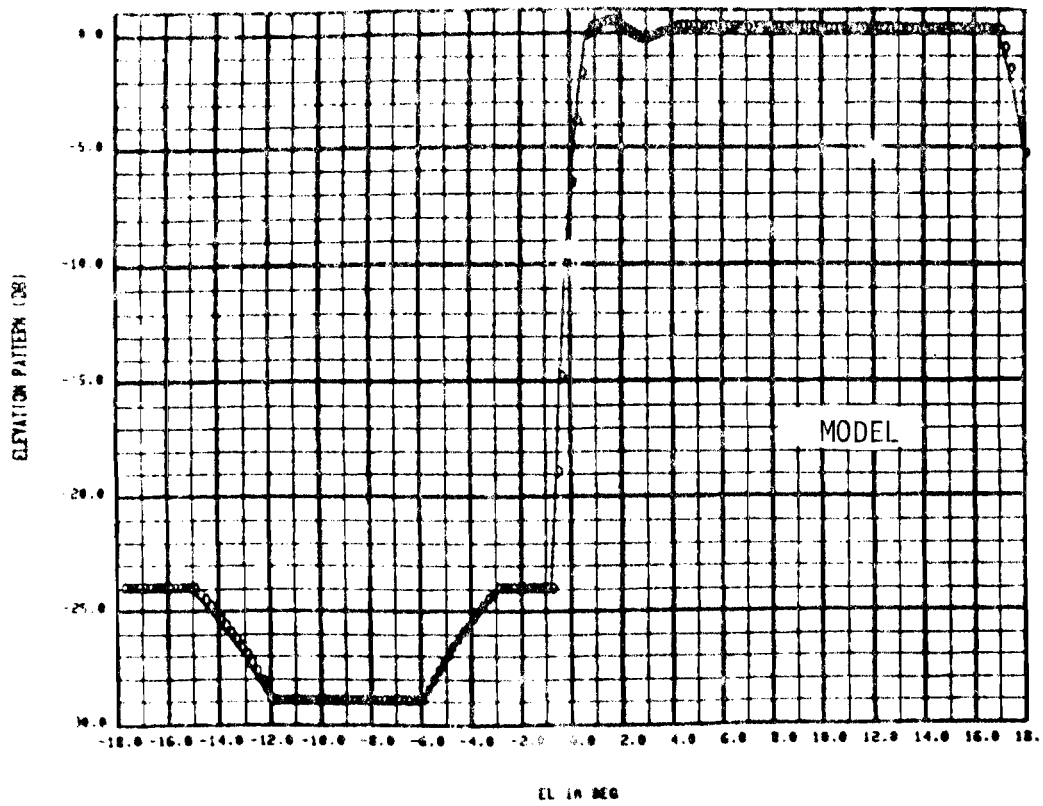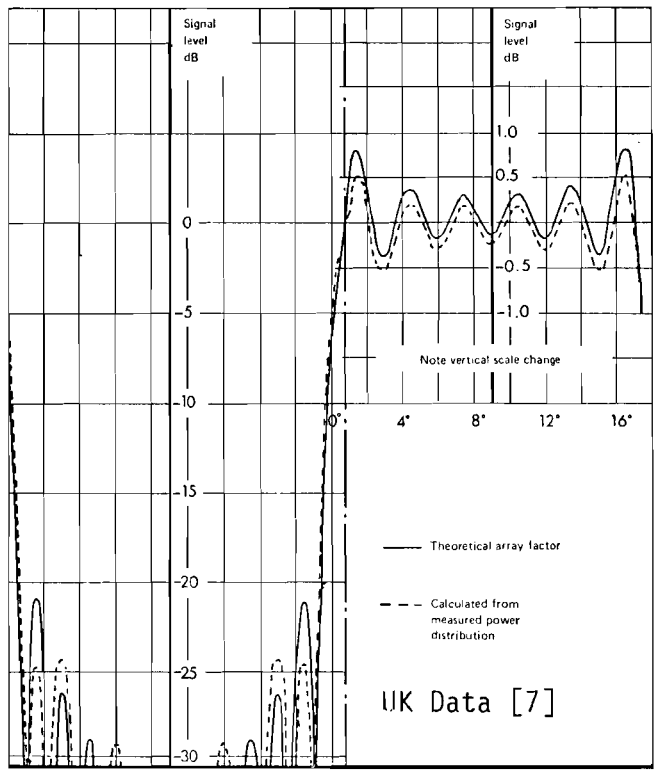
Fig. 3-15   Elevation pattern of DMLS elevation reference array.
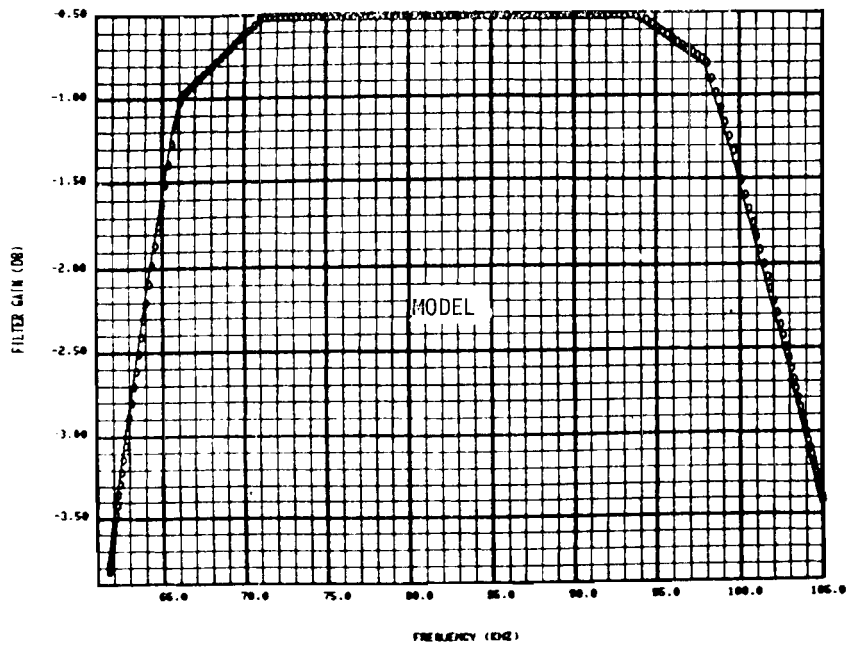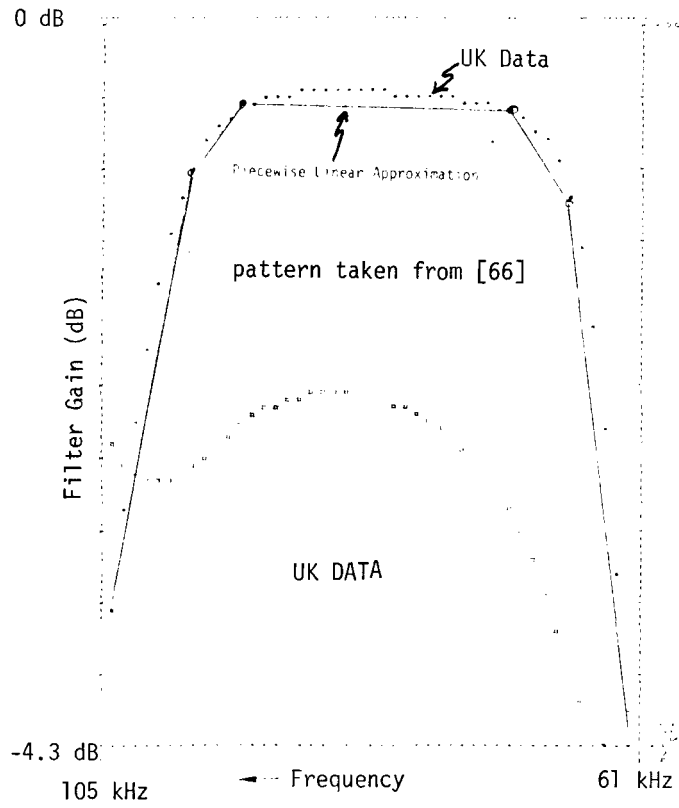
Fig. 3-16   DMLS sector filter gain.

MODEL

UK DATA

Phase of Sector Filter (deg)

o Points used in Piecewise
   Linear Approximation

o Points from UK Computer
   Printout

   Pattern taken
   from [66]
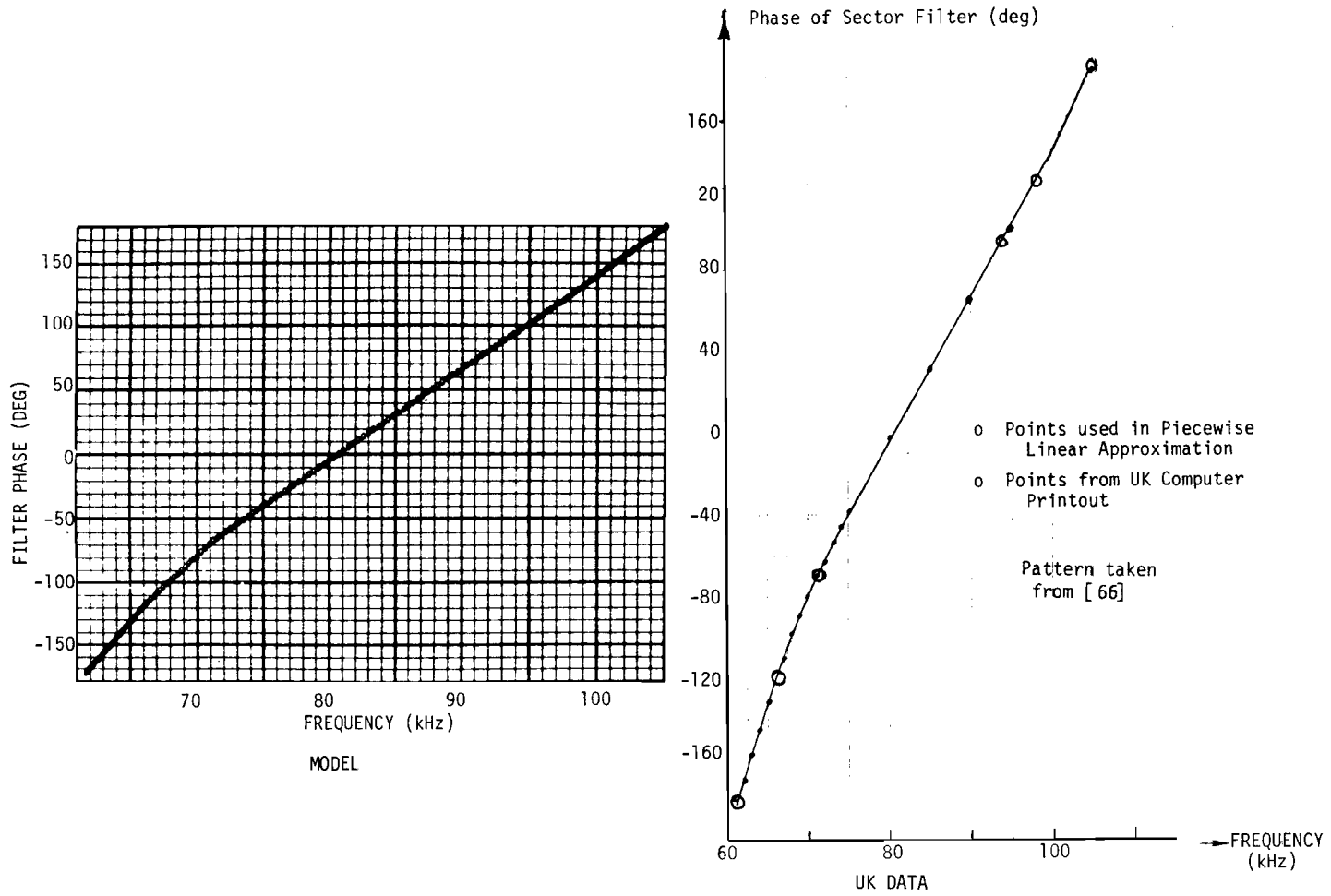
Fig. 3-17 DMLS sector filter phase characteristics.

TABLE 3-3

DMLS MODEL ANTENNA PATTERNS

ARRAY TYPE OR OTHER PATTERN TYPE	PATTERN SYMBOL IN TEXT	FUNCTION	COORDINATE	DESCRIPTION
Main Array	P	AZ	Azimuth Angle	see Fig. 3-10
			Elevation Angle	see Fig. 3-12
		EL-1	Azimuth Angle	see Fig. 3-13
			Elevation Angle	see Fig. 3-14
Reference Array	P'	AZ	Azimuth Angle	see Fig. 3-11 (with CL emphasis) or Fig. 3-10 (without CL emphasis)
			Elevation Angle	see Fig. 3-12
		EL-1	Azimuth Angle	see Fig. 3-13
			Elevation Angle	see Fig. 3-15
Aircraft Antenna	P	All	Azimuth and Elevation Angles	Omni; P = 1
Sector Filter Gain	H	All	Frequency	see Fig. 3-16
Sector Filter Phase	ι	All	Frequency	see Fig. 3-17

and airborne antenna characteristics, but this data has not always been provided. We currently believe there are differences in at least the following respects:

(a) elevation pattern of the azimuth array - our understanding is that the field equipment pattern rolloff at the horizon is considerably less than that assumed. However, the TRSB azimuth array elements, which have a measured pattern rolloff better than that assumed for DMLS, could be utilized for a DMLS array.

(b) airborne antenna pattern - the current model assumes an omni pattern, whereas actual patterns tend to have more gain in the forward direction than to the sides of the aircraft.

(c) azimuth pattern of elevation array - it is our understanding that the actual elevation array is not "flared" to the same extent as the proposed array. Also, we understand that the DMLS elevation radome was changed since the original patterns were measured.

(d) the receiver acquisition/validation logic for reduced aperture systems (e.g., 2° azimuth) has not been described by the UK.

The received signal model used here assumed that the diffracted and/or reflected signals can be represented by plane waves. Although this approximation in generally satisfactory for large plate reflectors (e.g., the AWOP screens) within the antenna near field, it is not valid for repeaters. Nor is it valid for shadowing obstacles (e.g., light poles) in the near field when utilizing the original Lincoln propagation model [29].

No check is currently made for very low received signal power levels. Thus, the model may not adequately represent system behavior in certain "deep shadowing" situations.

The actual DMLS receiver accomplished the out of coverage indication (OCI) by a not yet specified combination of angle checks and comparison of OCI signal levels with in coverage signal levels. This has not been modeled in the

DMLS program. The acquisition/validation logic will attempt to locate a trackable signal in any case. Thus, it is the responsibility of the user to insure that the direct signal is indeed within the desired coverage limits.

Section B has discussed how many of the AC /VAL tests rely on various time averages of the tracked signal and the "ordinary bins" correlation sums. Consequently, when driving the model with multipath inputs that do not represent "realistic" time sequences, one must be alert for the possibility that spurious effects may arise from the choice of input sequence. To illustrate, situations can arise (e.g., with two inbeam multipath signals) in which the tracker has several equilibrium points such that different past inputs result in several possible error values for a given "current" multipath input.

It is implicitly assumed in the multiple scan processing computation that the multipath characteristics are essentially fixed for each scatterer[*] over the duration of a single frame (except for the rf phase, which is incremented linearly in accordance with the scalloping frequency). This appears to be a reasonable assumption for most practical geometries; e.g., for an aircraft approach velocity of 200 feet per second, a single frame corresponds to a receiver displacement of 6 to 10 feet. However, if the multipath geometry were such to yield very fast variations in multipath characteristics for some particular scatterer, then the current model would need some modification to yield representative results. For instance, multipath parameters could be computed scan-by-scan instead of frame-by-frame. Of course, any such refinement would greatly increase the running time for both the propagation and receiver model programs.

---

[*]However, the net multipath signal level (= sum of signals from all the various scatterers) may change fairly rapidly if the scalloping rates are sufficiently different.

IV. DMLS MODEL VALIDATION

The validity of the DMLS simulation model has been confirmed by comparison with data recorded from bench tests and field tests performed on an actual DMLS receiver. In addition, analytical studies have been conducted both to explain observed error phenomena and to predict situations which might give rise to significant errors.

A. Error Analysis

In order to analyze the DMLS error mechanisms, we observe from (3-59) that the angle frequency estimate from the nth scan, $\omega_t(n)$, + $\delta\omega_t(n)$, is obtained by adding to the tracked frequency a correction proportional to the imaginary part of the ratio of the outputs $\Delta(n)$, $\Sigma(n)$ of the difference and sum filters:

$$\omega_t(n) + \delta\omega_t(n) = \omega_t(n) - \text{Im}\left[\frac{\Delta(n)}{\Sigma(n)}\right] \frac{2\pi}{16T} \qquad (4-1)$$

where 16T is the total integration time for the scan. The estimate $\hat{\omega}_t$ for an entire data frame is obtained as an average of validated single scan estimates according to (3-61).

$$\hat{\omega}_t = \frac{1}{N_v} \sum_{\substack{\text{valid} \\ \text{scans } n}} [\omega_t(n) + \delta\omega_t(n)] \qquad (4-2)$$

where N_v is the number of valid scans.

The angle estimate $\hat{\theta}_c$ is obtained by applying the angle coding relation to the frequency estimate, as in (3-62),

$$\hat{\theta}_c = \sin^{-1} [(\hat{\omega}_t - \omega_{off})/K] \qquad (4-3)$$

where K is the angle coding factor and ω_{off} is the reference-to-array offset frequency. The angle error $\hat{\varepsilon}$ for the data frame is the difference between

$\hat{\theta}_c$ and the actual conical angle of the direct signal θ_c,

$$\hat{\varepsilon} = \hat{\theta}_c - \theta_c . \qquad (4\text{-}4)$$

As long as the error is small, a first order expansion of $\sin^{-1}x$ around $x = \sin\theta_c$ can be used to produce the approximation

$$\hat{\varepsilon} = \frac{\hat{\omega}_t - \omega_{off} - K\sin\theta_c}{K\cos\theta_c} . \qquad (4\text{-}5)$$

It is convenient to write this expression in terms of the single scan estimates as

$$\hat{\varepsilon} = \frac{1}{N_v} \sum_{\substack{valid \\ scans\ n}} \varepsilon(n) \qquad (4\text{-}6)$$

where

$$\varepsilon(n) = \frac{\omega_t(n) + \delta\omega_t(n) - \omega_{off} - K\sin\theta_c}{K\cos\theta_c} . \qquad (4\text{-}7)$$

Using the same first order expansion of $\sin^{-1}x$, we can interpret the term $\varepsilon(n)$ as the approximate angle error corresponding to the nth scan frequency estimate $\omega_t(n) + \delta\omega_t(n)$. Thus, we define $\varepsilon(n)$ to be the single scan angle error.

The single scan error is calculated from the ratio of the outputs of the difference and sum filters,

$$\varepsilon(n) = \frac{\omega_t(n) - \omega_{off} - K\sin\theta_c}{K\cos\theta_c} - \frac{\theta_B}{\cos\theta_c}\ \text{Im}\left[\frac{\Delta(n)}{\Sigma(n)}\right] \qquad (4\text{-}8)$$

where

$$\theta_B = \frac{2\pi}{16KT} \qquad (4\text{-}9)$$

By substituting the expression (3-7) for the angle coding factor, $K = \omega_r \, v_s/c$, we observe that θ_B is the angular beamwidth of an antenna with effective aperture length $16v_sT$ at wavelength $2\pi c/\omega_r$.

The first term in (4-8) is the initial tracker error at the beginning of the nth scan, and the second term is the receiver's estimate of this error based on the nth scan measurement. The difference between them is usually, to first order, independent of the initial tracker error. Thus, we shall often make the simplifying assumption that the tracker frequency at the beginning of a scan is equal to the direct signal frequency. The single scan frequency error is then simply the false correction $\delta\omega_t(n)$ determined by the receiver from the $\Delta(n)/\Sigma(n)$ ratio.

To compute the difference-to-sum ratio, we use equations (3-57), (3-58) to rewrite equations (3-54), (3-55) in the form

$$\Sigma(n) = \frac{1}{4} \sum_{i=0}^{M} \sum_{j=0}^{M} \rho_i R\rho_j' \; H_\Sigma^n(d(n)\omega_{ijn} - \omega_t(n)) \; \exp j(-d(n)\alpha_{ijn})H(\omega_{ijn})$$

$$(4\text{-}10)$$

$$- \Delta(n) = \frac{1}{4} \sum_{i=0}^{M} \sum_{j=0}^{M} \rho_i R\rho_j' \; jH_\Delta^n(d(n)\omega_{ijn} - \omega_t(n)) \; \exp j(-d(n)\alpha_{ijn})H(\omega_{ijn})$$

$$(4\text{-}11)$$

where the sum and difference filter frequency responses are evaluated as

$$H_\Sigma^n(\omega) = \frac{\sin\omega T}{\omega T} \sum_{k=1}^{8} \frac{\Gamma_\Sigma(k)}{E_n^2(t_k)/R_n} \; \exp j \; (-\omega t_k) \qquad (4\text{-}12)$$

$$-jH_\Delta^n(\omega) = \frac{\sin\omega T}{\omega T} \sum_{k=1}^{8} \frac{\Gamma_\Delta(k)}{E_n^2(t_k)/R_n} \; \exp j \; (-\omega t_k) \qquad (4\text{-}13)$$

Note that the frequency responses are scan-dependent, because the effective time tapers are modified by the AGC factors $E_n^2(t_k)/R_n$. This time taper

distortion can cause a significant departure from the desired sidelobe structure produced by the Taylor taper alone. In Volume III, we will study this effect more closely. For most of our analytical results, we shall assume that the sum and difference patterns are undistorted by AGC effects.

In the absence of AGC variations $(E_n^2(t_k)/R_n = 1)$, the sum and difference filter frequency responses are independent of scan number n and are denoted simply as $H_\Sigma(\omega)$, $H_\Delta(\omega)$:

$$H_\Sigma(\omega) = \frac{\sin\omega T}{\omega T} \sum_{k=1}^{8} \Gamma_\Sigma(k) \, e^{-j\omega(2k-9)T} \tag{4-14}$$

$$-jH_\Delta(\omega) = \frac{\sin\omega T}{\omega T} \sum_{k=1}^{8} \Gamma_\Delta(k) \, e^{-j\omega(2k-9)T} \tag{4-15}$$

Because the Taylor weights $\Gamma_\Sigma(k)$, $\Gamma_\Delta(k)$ have even and odd symmetry, respectively, around midscan (i.e., $\Gamma_\Sigma(k) = \Gamma_\Sigma(9-k)$, $\Gamma_\Delta(k) = -\Gamma_\Delta(9-k)$), $H_\Sigma(\omega)$ and $H_\Delta(\omega)$ are both real, $H_\Sigma(\omega)$ is even, and $H_\Delta(\omega)$ is odd.

Figures 4-1 and 4-2 show the Taylor weighted sum and difference patterns. The frequency responses are seen to be analogous to the sum and difference patterns of an amplitude comparison monopulse radar with beamwidth θ_B.

The cross-product multipath components contributing to (4-10) and (4-11) can be divided into two types: <u>mainlobe</u> components with frequencies $d(n)\omega_{ijn}$ falling near the tracked frequency $\omega_t(n)$, and <u>sidelobe</u> components with frequencies $d(n)\omega_{ijn}$ separated from $\omega_t(n)$ by more than about 2 beamwidths. As with TRSB, mainlobe components are produced by scatterers which are angularly inbeam, but in DMLS additional mainlobe components may arise from out-of-beam reflections of the reference signal. To see this, we calculate the cross-product frequencies from (3-52), (3-34), (3-35), ignoring terms of the order of $\omega_{off} v_s/c$ or $\omega_{off} v_a/c$.

$$d(n)\omega_{ijn} = \omega_{off} + \omega_r \left[\frac{v_s \cos\gamma_i}{c} + d(n) \frac{v_a(\cos\beta_i - \cos\beta_j')}{c} \right] \tag{4-16}$$
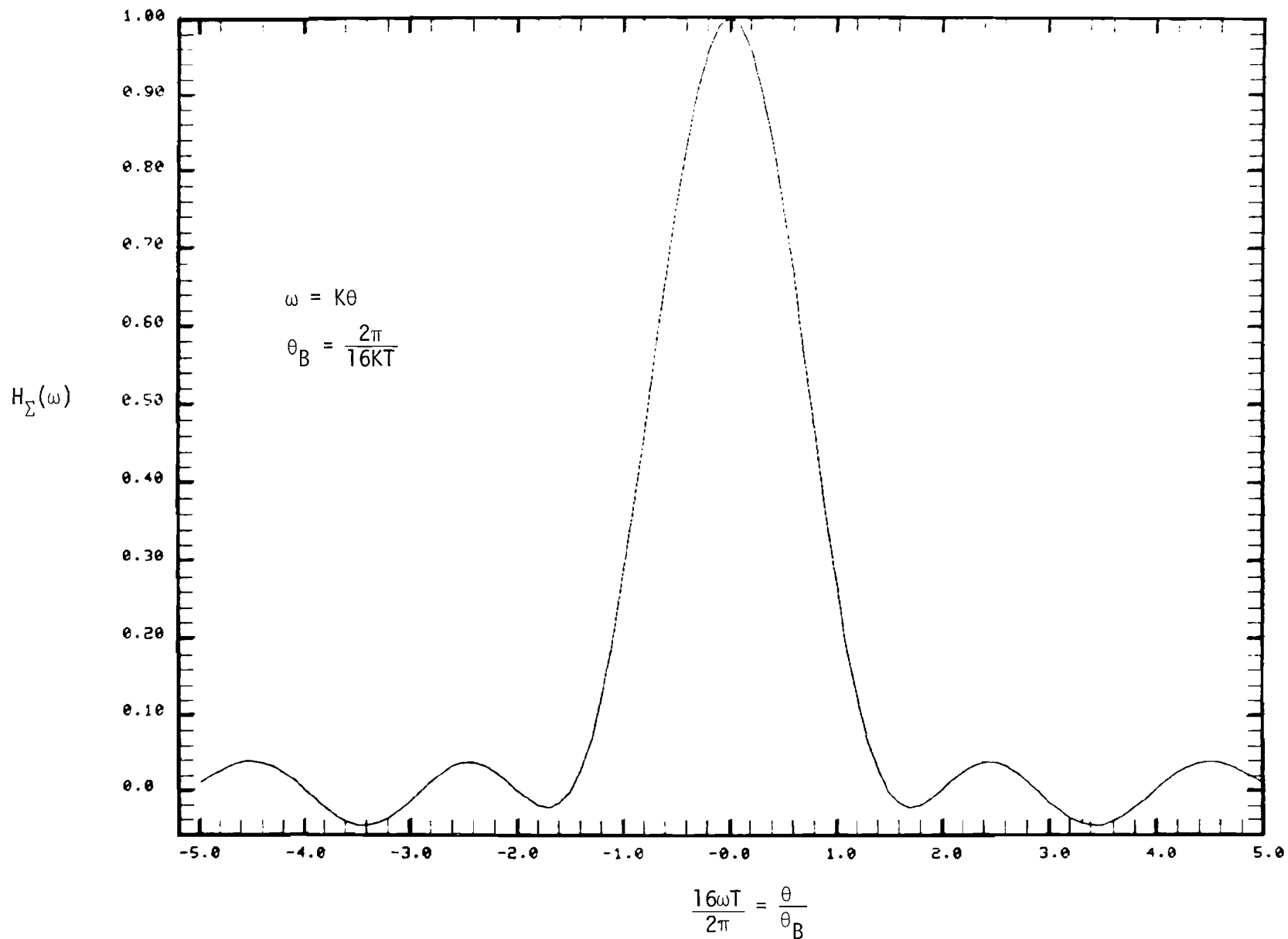
Fig 4-1 Sum filter frequency response function (uniform AGC weighting).

$\omega = K\theta$

$\theta_B = \dfrac{2\pi}{16KT}$

$H_\Delta(\omega_i)$

$\dfrac{16\omega T}{2\pi} = \dfrac{\theta}{\theta_B}$
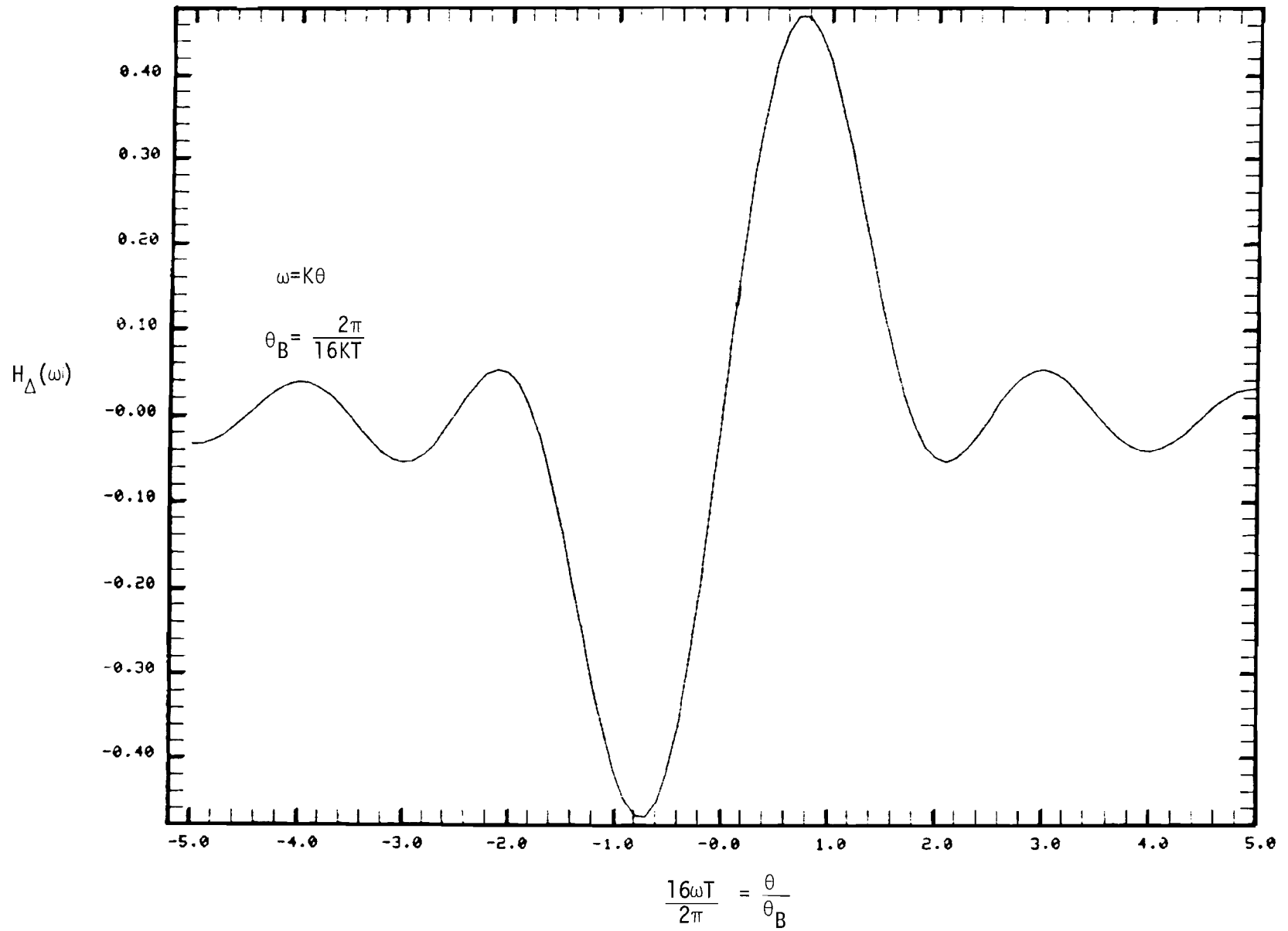
Fig. 4-2   Difference filter frequency response function (uniform AGC weighting).

or relative to the direct signal frequency $d(n)\omega_{00n}$,

$$d(n)\omega_{ijn} = d(n)\omega_{00n} + \omega_i{}^a + d(n)(\omega_i{}^S - \omega_j'{}^S) \qquad (4\text{-}17)$$

where we have introduced notation for the relative <u>angle frequency</u> $\omega_i{}^a$ of the ith component and for the relative <u>scalloping frequencies</u> $\omega_i{}^S$, $\omega_j'{}^S$ of the array and reference signal components, with respect to the direct components:

$$\omega_i{}^a = \omega_r \frac{v_s(\cos\gamma_i - \cos\gamma_0)}{c} \qquad (4\text{-}18)$$

$$\omega_i{}^S = \omega_r \frac{v_a(\cos\beta_i - \cos\beta_0)}{c} \qquad (4\text{-}19)$$

$$\omega_j'{}^S = \omega_r \frac{v_a(\cos\beta_j' - \cos\beta_0')}{c} \qquad (4\text{-}20)$$

In obtaining (4-16) and (4-17), we have ignored the term $\frac{1}{2}\frac{\omega_{off}}{\omega_r}(\omega_i{}^S + \omega_j'{}^S)$, which is retained in the simulation model for accuracy but may be neglected for analytical purposes.

As long as the system is operating well, the tracked frequency $\omega_t(n)$ is nearly equal to the direct component frequency $d(n)\omega_{00n}$, so the problem of identifying the mainlobe components typically reduces to determining whether $\omega_i^a + d(n)(\omega_i^S - \omega_j'{}^S)$ is smaller than the beamwidth of the sum and difference filter frequency responses. For typical aircraft velocities and airport geometries, the scalloping term is generally less than a mainlobe half-width. The angle frequency ω_i^a is within the mainlobe if the multipath angle γ_i is in-beam. This includes the special case i = 0 (direct component of array signal), which is important because mainlobe multipath also results from cross products of the direct array signal with scalloping reflected components (j ≠ 0) of the reference signal, even when these components are angularly out of beam.

The direct signal frequency is calculated on the assumption that the array and reference scalloping angles β_0, β_0' in (4-16) are approximately equal. This assumption is valid as long as the phase centers of the reference and array antennas are approximately colocated with respect to the transmitter-reflector distances. The result is conveniently written in terms of the angle coding factor.

$$d(n)\omega_{00n} = \omega_{off} + K \cos \gamma_0$$
$$= \omega_{off} + K \sin \theta_c \tag{4-21}$$

We observe that the direct signal frequency $d(n)\omega_{00n}$ is independent of the scan direction.[*]

Returning to the single scan error expression (4-8), we let $\Delta\omega_t(n)$ denote the amount by which the tracker frequency differs from the direct signal frequency at the start of the nth scan[**],

$$\omega_t(n) + \Delta\omega_t(n) = d(n)\omega_{00n} = \omega_{off} + K \sin \theta_c \tag{4-22}$$

The sum and difference equations (4-10), (4-11) take the explicit form

$$\Sigma(n) = \frac{1}{4} \sum_{i=0}^{M} \sum_{j=0}^{M} \rho_i R \rho_j' \, H_\Sigma^n(\Delta\omega_t(n) + \omega_i{}^a + d(n)(\omega_i{}^s - \omega_j'{}^s))$$
$$\times \text{expj}(-d(n)\alpha_{ijn}) \, H(\omega_{ijn}) \tag{4-23}$$

---

[*]The terms ignored in writing (4-16), along with any perturbations caused by unequal direct signal scalloping angles, actually make the direct signal frequency slightly scan-dependent, but these effects are negligible.

[**]The notation $\Delta\omega_t(n)$ should be distinguished from the notation $\delta\omega_t(n)$, which designates the receiver's _estimate_ of $\Delta\omega_t(n)$ after the nth scan measurement.

$$- \Delta(n) = \frac{1}{4} \sum_{i=0}^{M} \sum_{j=0}^{M} \rho_i R \rho_j' \quad jH_\Delta^n \left(\Delta\omega_t(n) + \omega_i^a + d(n) (\omega_i^S - \omega_j'^S) \right)$$

$$\times \exp j(-d(n)\alpha_{ijn}) \, H(\omega_{ijn}) \; . \tag{4-24}$$

The cross-product phases α_{ijn} appearing in (4-23), (4-24) are obtained from (3-53), (3-36), (3-37), in the form[*],

$$\alpha_{ijn} = \alpha_{00n} + (\tilde{\phi}_i - \tilde{\phi}_j') + (\omega_i^S - \omega_j'^S) (n-1)T_s + \psi(\omega_{ijn}) - \psi(\omega_{00n})$$

$$- \frac{1}{2} d(n) \; \omega_{off} (\tilde{\tau}_i + \tilde{\tau}_j') \tag{4-25}$$

where $\psi(\cdot)$ is the phase of the sector filter transfer function, T_s is the scan time, and $\tilde{\tau}_i$, $\tilde{\tau}_j'$, $\tilde{\phi}_i$, $\tilde{\phi}_j'$ are the relative midscan time delays and phases (on the first scan) for the ith angle signal and jth reference signal components:

$$\tilde{\tau}_i = \tau_i - \tau_0 \tag{4-26}$$

$$\tilde{\tau}_j' = \tau_j - \tau_0' \tag{4-27}$$

$$\tilde{\phi}_i = (\phi_i - \phi_0) - \omega_r (\tau_i - \tau_0) \tag{4-28}$$

---

[*]The right side of (4-25) should contain an additional term equal to $\frac{1}{2} d(n) \frac{\omega_{off}}{r} (\omega_i^S - \omega_j'^S) (n-1)T_s$. As with the similar term missing from (4-17), this term is retained in the simulation model, but it is small enough to be ignored for analytical purposes. The last term in (4-25) is also proportional to the relatively small reference-array offset frequency ω_{off}, and so it is usually negligible too. However, is some cases, the relative multipath time delay $\tilde{\tau}_i$ or $\tilde{\tau}_j'$ is long enough that this term makes a difference (see the discussion on reference scalloping errors in Volume III of this report).

$$\tilde{\phi}'_j = (\phi'_j - \phi'_0) - \omega_r (\tau'_j - \tau'_0) \tag{4-29}$$

where τ_i, τ'_j are the absolute midscan time delays and ϕ_i, ϕ'_j are the phase changes due to reflection.

Expressions (4-22) to (4-29) are used to evaluate the single scan error expression (4-8). It is convenient to express the error in the form

$$\varepsilon(n) = \varepsilon^o(n) + [\varepsilon(n) - \varepsilon^o(n)] \tag{4-30}$$

where $\varepsilon^o(n)$ is the single scan error that would result if the tracker error at the beginning of the scan were zero; i.e.,

$$\varepsilon^o(n) = -\frac{\theta_B}{\cos \theta_c} \; \mathrm{Im} \left.\left[\frac{\Delta(n)}{\Sigma(n)}\right]\right|_{\Delta\omega_t(n) = 0} \tag{4-31}$$

As long as the initial tracker error is small, the correction term in (4-31) may be evaluated as

$$\varepsilon(n) - \varepsilon^o(n) = -\frac{\Delta\omega_t(n)}{K \cos \theta_c} - \frac{\theta_B \, \Delta\omega_t(n)}{\cos \theta_c} \; \frac{d}{d\Delta\omega_t(n)} \; \mathrm{Im} \left.\left[\frac{\Delta(n)}{\Sigma(n)}\right]\right|_{\Delta\omega_t(n) = 0} \cdot \tag{4-32}$$

This is the most general error formulation which we shall consider. To gain further insight, it is helpful to make some simplifying assumptions for the sake of analytical clarity. In the next subsection, therefore, we shall assume the following:

(1) The tracker frequency error $\Delta\omega_t(n)$ at the beginning of each scan is zero; i.e., $\varepsilon(n) = \varepsilon^o(n)$.

(2) The sector filter transfer function is assumed to pass all frequencies in its passband without distortion, i.e., $H(\omega) \, e^{j\psi(\omega)} = 1$.

(3) The AGC gain is assumed to be uniform, $E_n^2(t_k)/R_n = 1$, which means that the scan-dependent sum and difference filter frequency respones $H_\Sigma^n(\omega)$, $H_\Delta^n(\omega)$ are replaced by the Taylor time taper responses $H_\Sigma(\omega)$, $H_\Delta(\omega)$ shown in Figs. 4-1, 4-2.

(4) The last term in the expression (4-25) for the cross-product phases α_{ijn} is assumed to be negligible, i.e.,
$$\frac{1}{2} \omega_{off} (\tilde{\tau}_i + \tilde{\tau}_j') \ll 2\pi.$$

(5) The validation tests are ignored, so that N_v is equal to the total number of scans in a data frame, 2N, and the summations in (4-2) and (4-6) are over all 2N scans.

a. Static Errors

In a static situation, the receiver is motionless, and the scalloping frequencies are zero. For any given array component i, the cross-product frequencies are the same for all reference components j. Thus, the expressions (4-23) (4-24) for $\Sigma(n)$, $\Delta(n)$ reduce to single sums over the array components. Using assumptions (1) to (4) above, we evaluate the single scan error from (4-31), (4-23), (4-24),

$$\varepsilon^o(n) = \frac{\theta_B}{\cos \theta_c} \; Re \left[\frac{\displaystyle\sum_{i=0}^{M} \rho_i H_\Delta(\omega_i{}^a) \, e^{j\tilde{\phi}_i}}{\displaystyle\sum_{i=0}^{M} \rho_i H_\Sigma(\omega_i{}^a) \, e^{j\tilde{\phi}_i}} \right] \qquad (4\text{-}33)$$

The i=0 term in the numerator of (4-33) is zero because $H_\Delta(0) = 0$, and the i=0 term in the denominator equals ρ_0 because $H_\Sigma(0) = 1$. A first-order expansion of (4-33) yields

$$\varepsilon^o(n) \approx \varepsilon_1^o(n) \equiv \frac{\theta_B}{\cos \theta_c} \sum_{i=1}^{M} \tilde{\rho}_i \, H_\Delta(\omega_i{}^a) \cos \tilde{\phi}_i \qquad (4\text{-}34)$$

where $\{\tilde{\rho}_i\}$ are the __relative__ multipath amplitudes

$$\tilde{\rho}_i = \rho_i/\rho_0 \qquad\qquad (4\text{-}35)$$

This DMLS error expression is analogous to the results obtained earlier for TRSB. For example, if the direct angle is $\theta_c = 0°$ (boresight) and the multipath anlges differ from the direct angle by a small amount $\tilde{\theta}_i$, then

$$\tilde{\theta}_i = \gamma_i - \gamma_0 \qquad\qquad (4\text{-}36)$$

$$\omega_i{}^a \approx K\tilde{\theta}_i \qquad\qquad (4\text{-}37)$$

and

$$H_\Delta(\omega_i{}^a) \approx \sum_{k=1}^{8} (2k\text{-}9)\, \Gamma_\Delta(k) \quad \omega_i{}^a\, T\ . \qquad\qquad (4\text{-}38)$$

The second expression is obtained from (4-15) under the assumption of small $\omega_i{}^a$. The Taylor weights $\Gamma_\Delta(k)$ are designed to satisfy the normalization condition[*],

$$\sum_{k=1}^{8} (2k\text{-}9)\, \Gamma_\Delta(k) = \frac{16}{2\pi} \qquad\qquad (4\text{-}39)$$

---

[*]This normalization is desirable, because it enables the receiver to correct an initial tracker error $\varepsilon_t(n)$ (exactly, to first order) whenever only the direct signal is present. The actual DMLS receiver weights are computationally efficient approximations to the desired weights, and they satisfy

$$\sum_{k=1}^{8} (2k\text{-}9)\, \Gamma_\Delta(k) = (1.019)\, \frac{16}{2\pi}.$$

and thus the evaluation of $H_\Delta(\omega_i{}^a)$ reduces to

$$H_\Delta(\omega_i{}^a) \approx \frac{16KT}{2\pi} \; \tilde{\theta}_i = \tilde{\theta}_i/\theta_B \qquad (4\text{-}40)$$

Combining (4-34) and (4-40), we obtain

$$\varepsilon_1^0(n) = \sum_{i=1}^{M} \tilde{\rho}_i \tilde{\theta}_i \cos \tilde{\phi}_i \qquad (4\text{-}41)$$

which is equivalent to the expression (2-3) for the small-amplitude, small-angle error performance of TRSB.

We note from (4-33) that the single scan error in a static situation does not vary with scan number n. Thus, the motion averaging effect does not produce any error reduction, and the average error $\hat{\varepsilon}^0$ for the data frame is equal to the single scan error.

b.   Dynamic Errors

In a dynamic situation, both the array and reference scalloping frequencies are generally nonzero and must be included when evaluating the expressions (4-23), (4-24) for the sum and difference filter outputs. The single scan error is calculated as

$$\varepsilon^0(n) = \frac{\theta_B}{\cos\theta_c} \; \mathrm{Re} \left[\frac{\displaystyle\sum_{i,j=0}^{M} \rho_i \rho_j' \; H_\Delta(\omega_i^a + d(n)(\omega_i^s - \omega_j^s)) \exp j(\tilde{\phi}_i - \tilde{\phi}_j' + (\omega_i^s - \omega_j^s)(n-1)T_s)}{\displaystyle\sum_{i,j=0}^{M} \rho_i \rho_j' \; H_\Sigma(\omega_i^a + d(n)(\omega_i^s - \omega_j^s)) \exp j(\tilde{\phi}_i - \tilde{\phi}_j' + (\omega_i^s - \omega_j^s)(n-1)T_s)} \right]$$

$$(4\text{-}42)$$

In this expression, the $i = j = 0$ term equals zero in the numerator and $\rho_0 \rho_0'$ in the denominator, as a result of the properties of $H_\Delta(\omega)$, $H_\Sigma(\omega)$. A first-order expansion of the single-scan error retains the $i \neq 0$, $j = 0$ terms and

the $i = 0$, $j \neq 0$ terms, and it may be written in the following form:

$$\varepsilon^0(n) \approx \varepsilon_1^0(n) \equiv \varepsilon_1^a(n) + \varepsilon_1^r(n) \qquad (4\text{-}43)$$

where

$$\varepsilon_1^a(n) = \frac{\theta_B}{\cos \theta_c} \sum_{i=1}^{M} \tilde{\rho}_i \, H_\Delta(\omega_i^a + d(n)\omega_i^s) \cos (\tilde{\phi}_i + \omega_i^s(n-1)T_s) \qquad (4\text{-}44)$$

$$\varepsilon_1^r(n) = \frac{\theta_B}{\cos \theta_c} \sum_{j=1}^{M} \tilde{\rho}_j' \, H_\Delta(-d(n)\omega_j'^s) \cos (\tilde{\phi}_j' + \omega_j'^s(n-1)T_s) \qquad (4\text{-}45)$$

and $\tilde{\rho}_i$, $\tilde{\rho}_j'$ are the relative multipath amplitudes

$$\tilde{\rho}_i = \rho_i / \rho_0 \qquad (4\text{-}46)$$

$$\tilde{\rho}_j' = \rho_j' / \rho_0' \ . \qquad (4\text{-}47)$$

i. Array Scalloping Effects

The first term in (4-43) is analogous to the first-order static error expression (4-34). The multipath angle frequencies ω_i^a are shifted from their static values by the array scalloping frequencies ω_i^s, the direction of the shift depending on the scan direction. The array scalloping frequencies are normally small enough that the angle frequencies are the sole determinant of whether $\omega_i^a + d(n) \omega_i^s$ is within the beamwidth of $H_\Delta(\omega)$. In other words, the array scalloping effect does not cause mainlobe errors whenever the multipath angle is well out of beam.

Linearizing (4-44) around the angle frequencies ω_i^a, we obtain

$$\varepsilon_1^a(n) = \frac{\theta_B}{\cos \theta_c} \sum_{i=1}^{M} \tilde{\rho}_i \, [H_\Delta(\omega_i^a) + d(n) \, \omega_i^s \, H_\Delta'(\omega_i^a)] \cos(\tilde{\phi}_i + \omega_i^s(n-1)T_s)$$

$$(4\text{-}48)$$

where

$$H'_\Delta(\omega) = \frac{d}{d\omega} H_\Delta(\omega) .$$ (4-49)

The error perturbation caused by the array scalloping changes sign with each change of scan direction, provided that the scalloping frequency is small enough that the cosine factor in (4-48) remains relatively constant from scan to scan. Thus, in a quasi-static situation in which $\omega_i^S < < 2\pi/T_S$, the first order array scalloping perturbation to the motion averaged data frame error is zero. A more extensive discussion of array scalloping is given in Chapter 2 of Volume III of this report.

ii. Reference Scalloping

The second term in (4-43) represents the reference scalloping error effect. Unlike the array scalloping effect, which is merely a perturbation to an existing error term, reference scalloping errors are produced even when all multipath sources are well out of beam.

The reference scalloping frequency $\omega_j^{'S}$ is almost always within the main-lobe of $H_\Delta(\omega)$; hence we observe by comparing (4-44) and (4-45) that the reference scalloping error component $\epsilon_1^r(n)$ is quite analogous to the array error component $\epsilon_1^a(n)$ produced by inbeam multipath. The one critical difference between the two is that the reference scalloping error changes sign with scan direction; this follows from the fact that $H_\Delta(\omega)$ is odd, implying that

$$H_\Delta(-d(n)\omega_j^{'S}) = - d(n) H_\Delta(\omega_j^{'S}) .$$ (4-50)

Thus, as with array scalloping, reference scalloping errors will average out to zero over a data frame in a quasi-static situation. However, under less static conditions which produce significant scan-to-scan variations in the cosine factor in (4-45), the error averaging is less effective. A detailed study of the reference scalloping phenomenon is presented in Chapter 2 of Volume III.

iii. Motion Averaging Effects

Whenever the scalloping frequencies are large enough to cause the phase of the cosine factor in (4-44) or (4-45) to change significantly from scan to scan, the sequencie of single scan errors $\varepsilon^o(n)$ may oscillate over the length of a data frame, resulting in smaller average error. To illustrate this phenomenon, we consider the result of averaging the angle frequency component of the array error $\varepsilon_1^a(n)$, i.e., the component of (4-44) which corresponds to retaining the first term inside the brackets in (4-48). We write

$$
\varepsilon_1^{aa}(n) = \frac{\theta_B}{\cos\theta_c} \sum_{i=1}^{M} \tilde{\rho}_i \, H\Delta(\omega_i^a) \cos\left(\tilde{\phi}_i + \omega_i^s (n-1)T_s\right) \tag{4-51}
$$

and calculate the corresponding component of the average data frame error as

$$
\hat{\varepsilon}_1^{aa} = \text{Re}\left[\sum_{i=1}^{M} \tilde{\rho}_i \, H\Delta(\omega_i^a) \, A(\omega_i^s T_s) \, e^{j\tilde{\phi}_i} \right] \tag{4-52}
$$

where $A(\cdot)$ is the Fourier transform of the finite discrete sequence $a(n) = 1$, $n = 0,1,\ldots,2N-1$; i.e.,

$$
A(\alpha) = \frac{1}{2N} \sum_{n=0}^{2N-1} e^{jn\alpha} \tag{4-53}
$$

Figure 4-3 shows the grating lobe structure of the averaging factor $A(\cdot)$ for the case of the $1°$ azimuth system ($2N = 12$, $T_s = 2.5$ msec).

A similar formulation is possible for evaluating the effects of averaging the error components due to scalloping. Because these error components change sign with scan direction, the motion averaging factor $A(\cdot)$ is replaced by the Fourier transform of the scan direction sequence $d(n + 1)$. For further details, the reader is referred to Chapter 2 of Volume III. In the analysis there, error contributions higher than first order are also considered.

ARRAY ERROR MOTION AVERAGING FUNCTION $A(\omega_1{}^s T_s)$

ARRAY SCALLOPING FREQUENCY IN Hz ($\frac{1}{2\pi} \omega_1{}^s$)
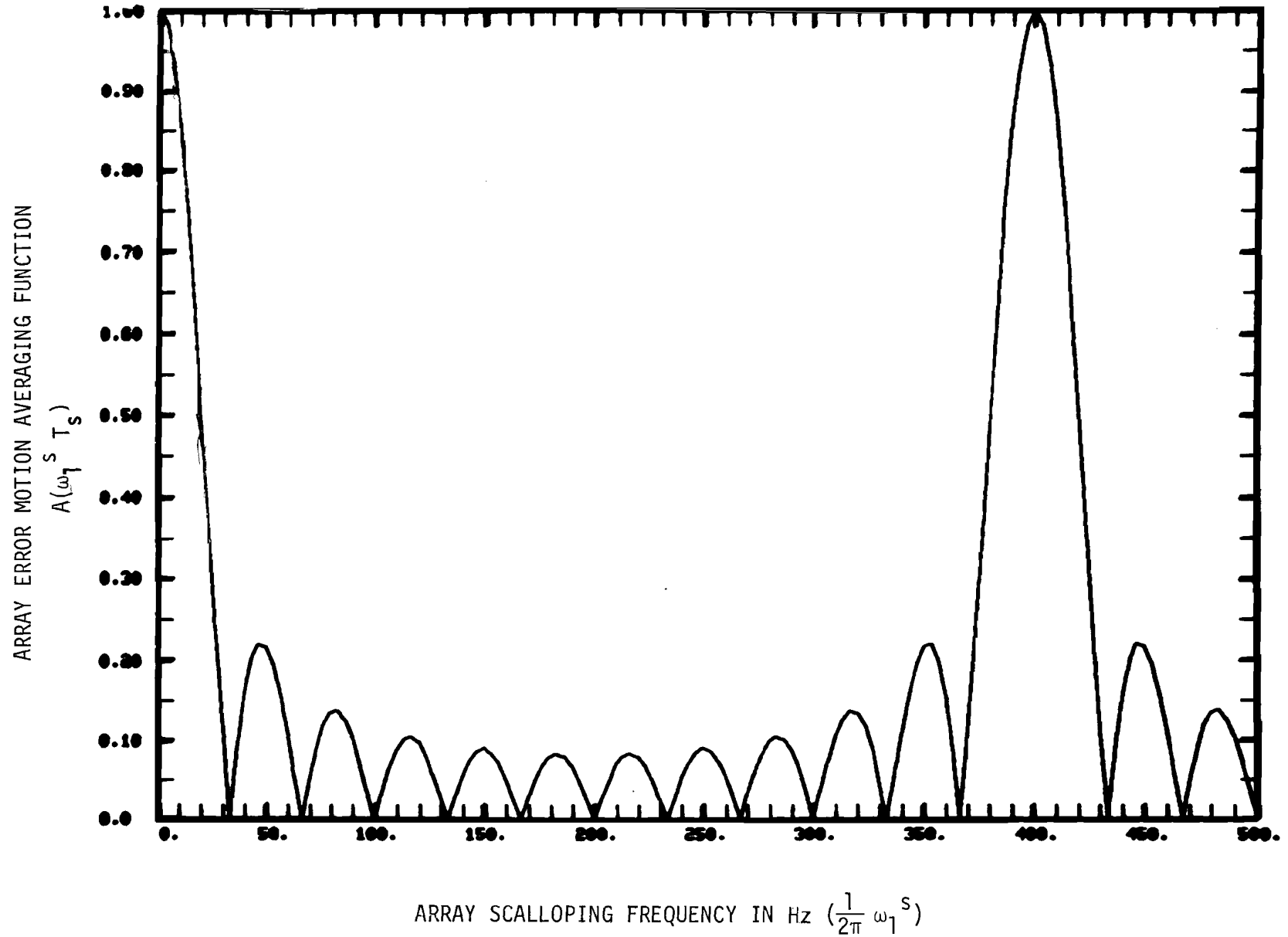
Fig. 4-3 Array error motion averaging function for the 1° azimuth system (2N = 12, T_s = 2.5 msec).

B.   Bench Tests

The primary source of data for validating the DMLS computer models was the RAE hybrid bench simulator [7]. Tests were performed in the UK on this simulator to determine the error characteristics of an actual DMLS receiver subjected to certain single-component multipath conditions. Three types of data were considered most useful:

(1) static errors

(2) dynamic inbeam errors

(3) reference scalloping errors.

Comparisons of the bench test error traces with the predictions of the computer simulation are shown in Figs. 4-4 to 4-6 which depict, respectively, static error as a function of separation angle, dynamic inbeam elevation error as a function of scalloping frequency, and out-of-beam azimuth reference scalloping error as a function of scalloping frequency. For all the bench test results, the multipath relative phase was smoothly cycled during the measurement period, and hence the error traces are oscillatory, as indicated by (4-41). The corresponding computer simulation prediction in each case is an estimate of the outer envelope of the oscillations, obtained by cycling the multipath phase at each measurement point and determining either the largest error (in magnitude), the peak positive and negative errors, or the peak-to-peak error spread. In all cases, the computer predictions agree very well the the measured errors, except for

1) overestimating the reference scalloping errors in the region 130 Hz to 200 Hz. This is believed to arise from unmodelled AGC loop dynamic effects which are particularly important in contributing to errors when the scalloping frequency is a subharmonic of the peak error frequency (this point is discussed further in Volume III). To illustrate, with the original UK scan format of d(n) = +1 on even scans and -1 on odd scans, the simulator model showed good agreement (see figure 4-7) with the
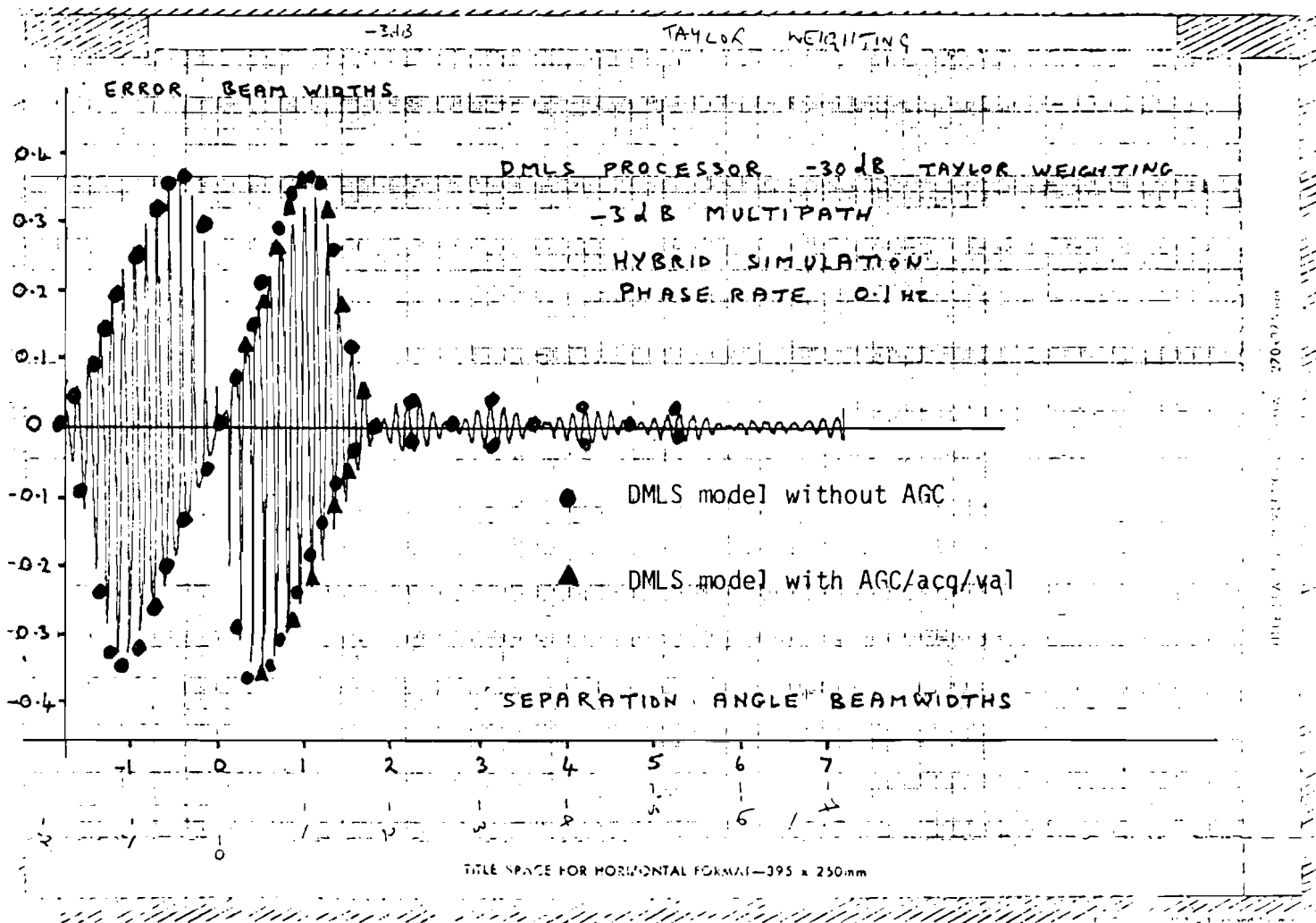
Fig. 4-4a Comparison of DMLS computer model results with RAE hyrbrid
bench simulator data for static errors due to -3 dB multipath.
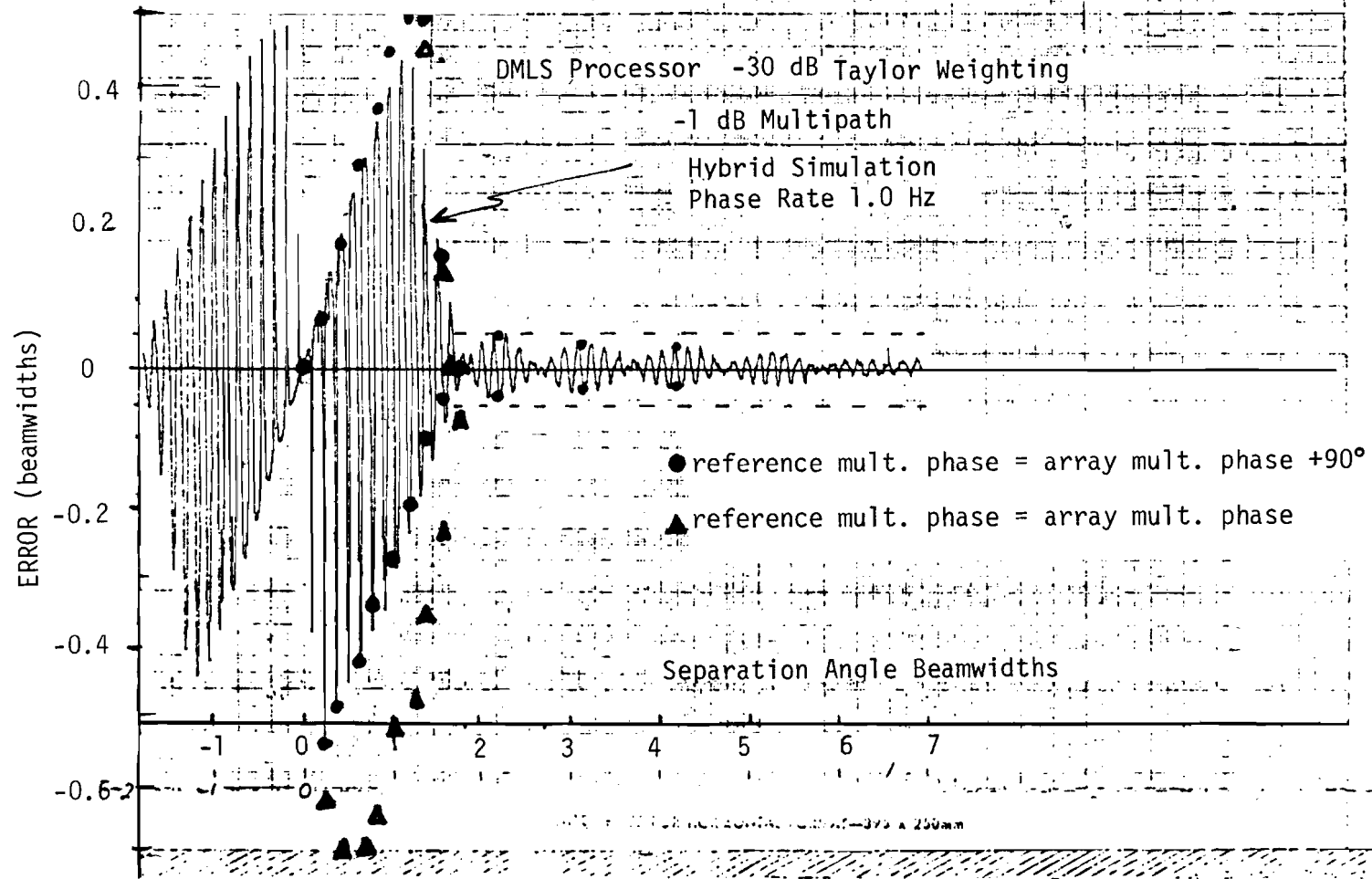
Fig. 4-4b Comparison of DMLS computer model results with RAE hybrid bench simulator data for static errors due to -1 dB multipath.
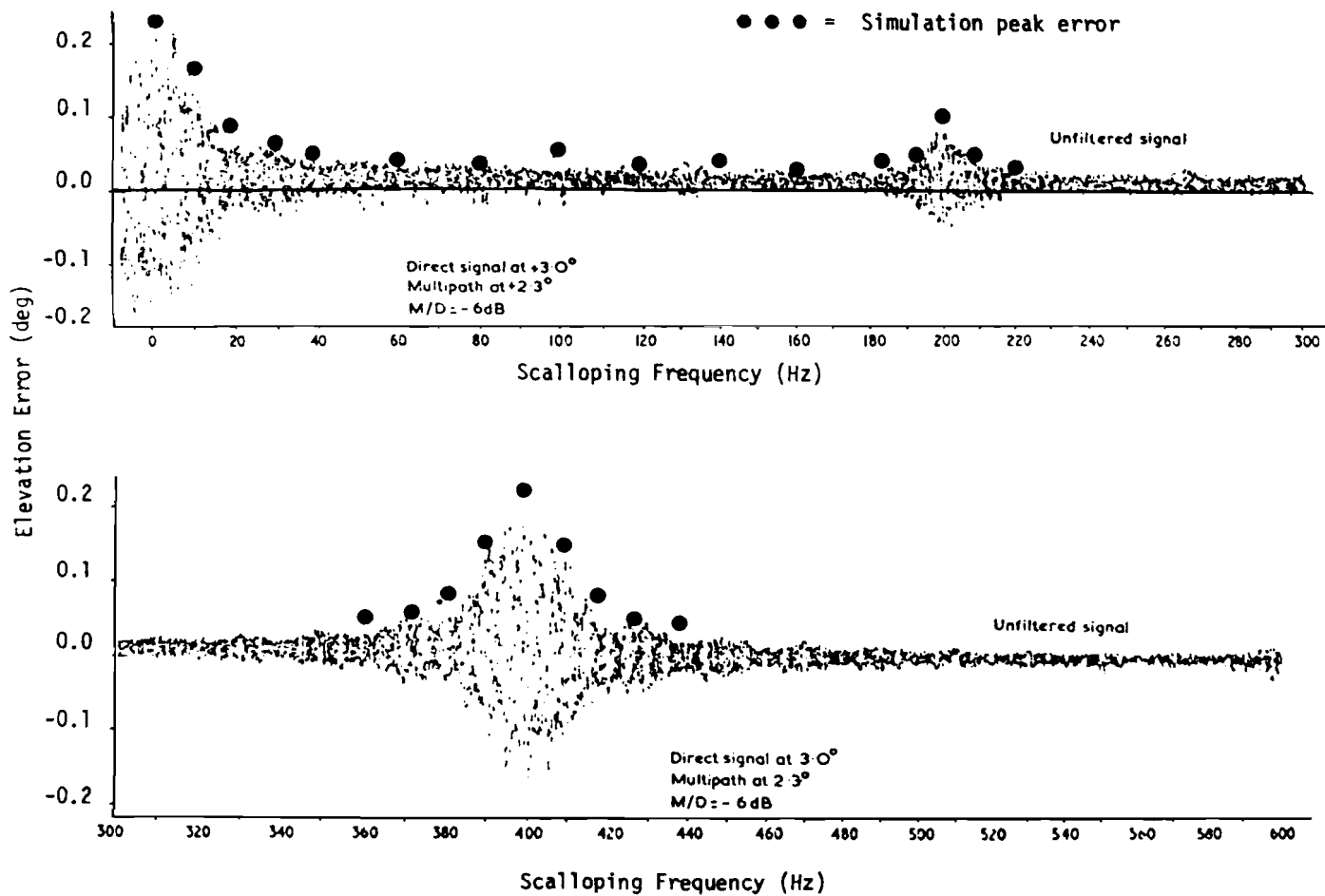
Fig. 4-5 Comparison of DMLE computer model with RAE hybrid bench simulator
data for dynamic inbeam elevation errors.
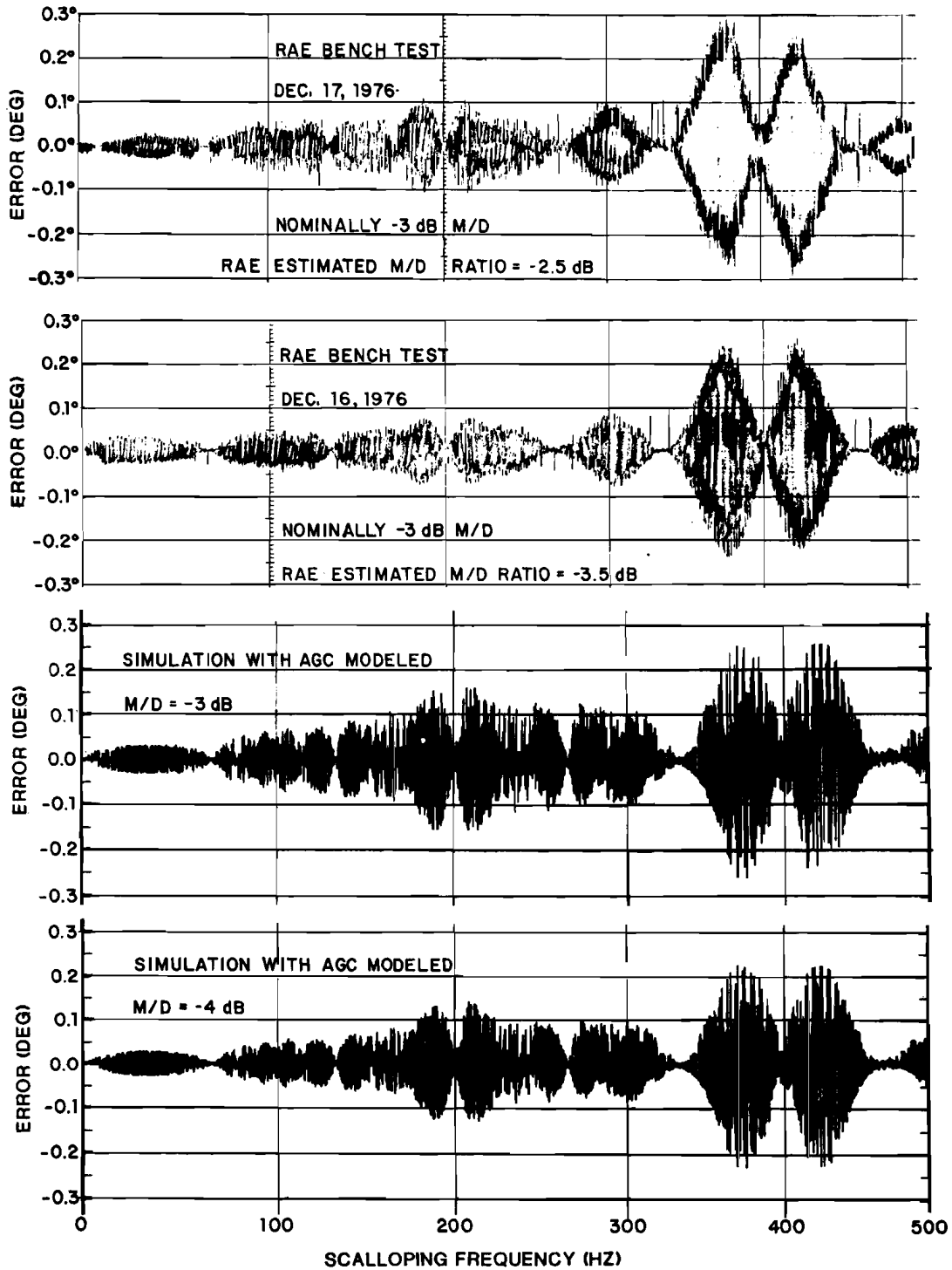
Fig. 4-6a Comparison of DMLS computer model results with RAE hybrid bench simulator data for azimuth reference scalloping errors. Multipath level = -3 dB.
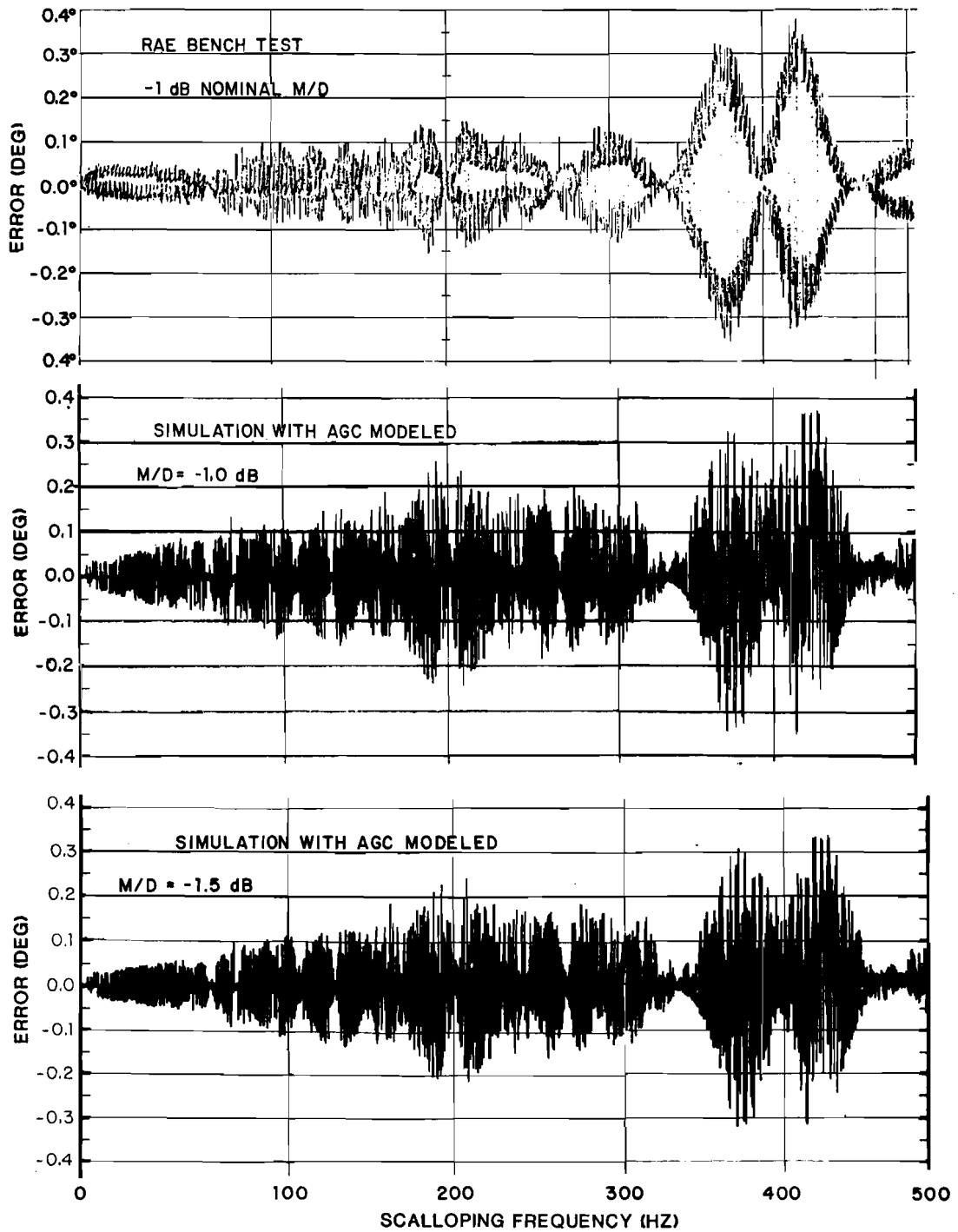
Fig. 4-6b Comparison of DMLS computer model results with RAE hybrid bench simulator data for azimuth reference scalloping errors. Multipath level = -1 dB.
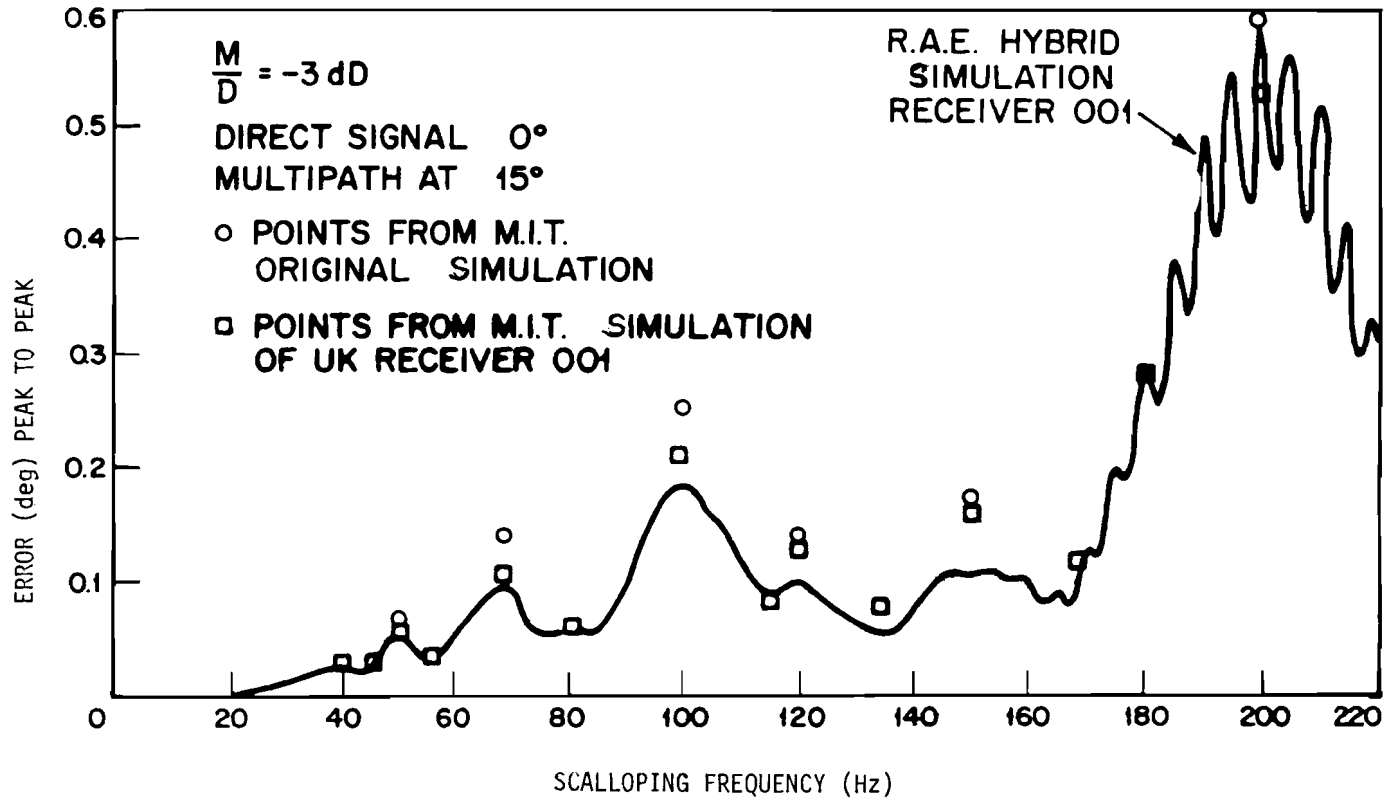
Fig. 4-7 Comparison of DMLS simulation model with RAE hybrid bench simulation results for azimuth reference scalloping errors, using original DMLS scan format.

simulator data at the peak error frequency of 200 Hz and overestimated the errors at 100 Hz.

2) sensitivity of static errors at high M/D level to the uncontrolled (and unmeasured) phase of the reference signal multipath relative to that of the signal multipath (i.e., $\tilde{\phi}_1'$ relative to $\tilde{\phi}_1$) in the bench simulator. As shown in Fig. 4-4b, this phase can influence the results by virtue of its effect on the AGC time taper $E_n(t)$.

C. Field Tests

There was a much smaller amount of relevant DMLS field test data appropriate for model validation studies since the proposed DMLS implementation differed significantly[*] from the implementation utilized for the ICAO testing [7]. The major source of detailed field data in a non-benign multipath environment was the series of tests performed at Kennedy airport just after the TRSB tests described in Chapter 2. Also, there were some tests of elevation shadowing by a C-130 aircraft at Brussels.

1. Tests at J. F. Kennedy Airport, New York

As with TRSB, the major flight simulation interest focused on the elevation errors caused by shadowing and reflections from the three large hangars shown in Fig. 2-36. Identical multi-plate hangar models were used for simulating both the TRSB amd DMLS tests (see Fig. 2-37). Flight profiles were also nominally the same (because the field tests were supposed to be comparative), but it was necessary to incorporate the more accurate position data available from the tracker for each individual run.

One set of flights was made through the region south of runway 13L (see Fig. 2-32) which experienced reflections from hangar 3 as well as shadowing by a fence (not shown) and buildings to the south of the centerline. Fig. 4-8

---

[*]The differences included array length (120λ vs. 54λ), scan format (FDM vs. TDM) and velocity as well as receiver processing (analog filters vs. digital correlator).

DOP EL

SIMULATION

RAW ERROR (DEG)

0.30
0.25
0.20
0.15
0.10
0.05
0.00
-0.05
-0.10
-0.15
-0.20
-0.25
-0.30

5.1   7.55   10   12.45

GROUND RANGE FROM AZIMUTH (NMI)
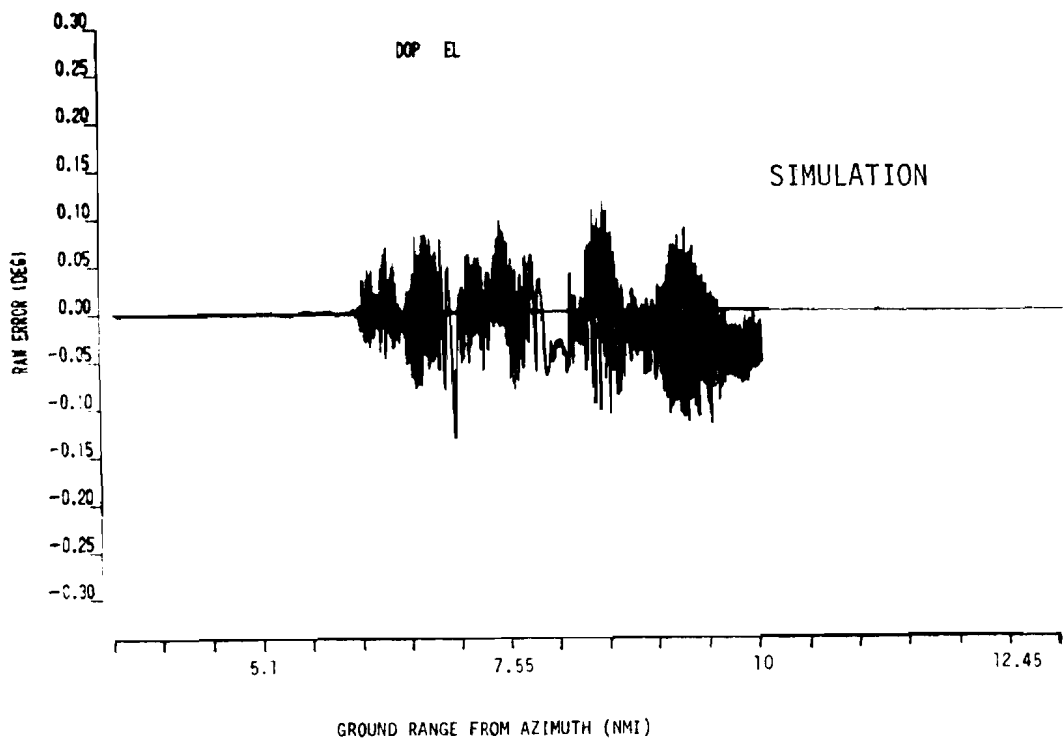
PLESSEY   JFK APT   RWY 13L DATE : 03/22/78 START TIME 6:11
AZ -10154/0/- FT EL -1021/+249/- FT DME NA
LASER SS ACFT: CV680   38 DEO (R) RADIAL AT 2K FT

FIELD TEST

ICAO LIMIT (2σ)

MLS EL ERROR - DEGREES - (RAW)

0.30
0.20
0.10
0.00
-0.10
-0.20
-0.30

0.00   2.00   4.00   6.00   8.00   10.00   12.00   14.00

GROUND RANGE FROM AZIMUTH - NM
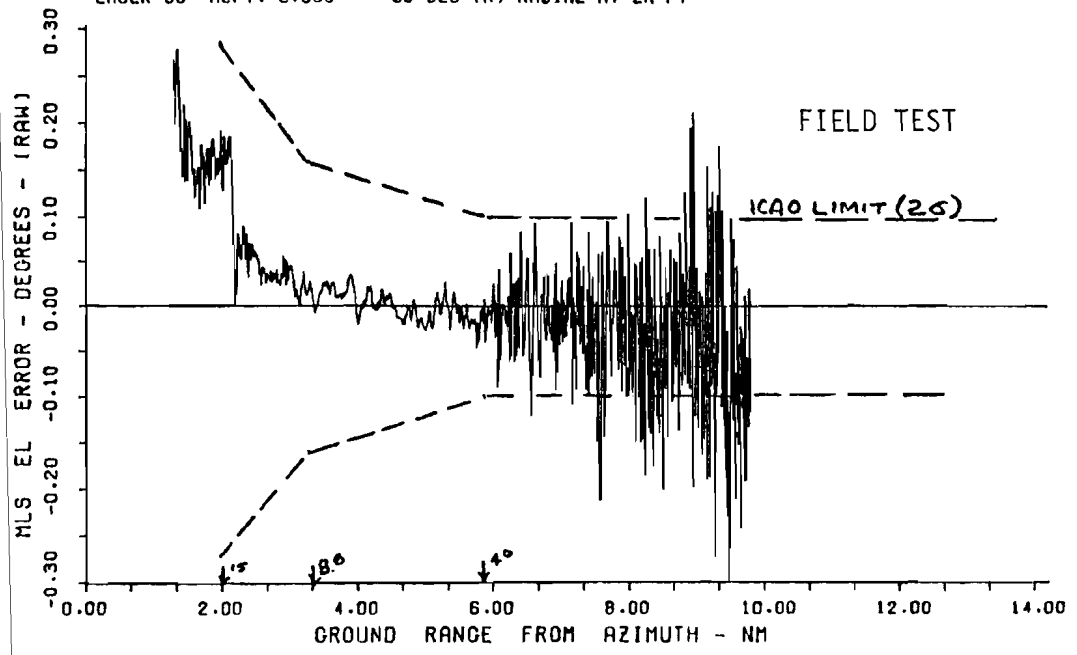
Fig. 4-8 Comparison of DMLS simulation and flight test on -38°
radial at 2000 feet at JFK airport.

4-26

compares the DMLS simulation results with the corresponding flight test data for a flight at approximately 600 meters altitude along the -38° radial from the MLS azimuth transmitter site. The simulated error is seen to have much the same character as the field record, but it is smaller in amplitude. The added noise in the field test data is believed to arise from front-end noise effects.

Flights were also made through the shadowing region to the north of runway 13L. Figure 4-9 compares the simulation results with flight test data for a flight at approximately 600 meters altitude along the +38° radial from the MLS azimuth. The overall error magnitude and waveform are seen to be in reasonably good agreement.

Figure 4-10 compares the DMLS flight test errors with simulation results for a centerline approach along a 3° glideslope. As in the case of the TRSB system, the flight errors near threshold are considerably larger than the simulation data. However, these differences are believed to arise primarily from tracker errors since 1) they are similar in nature to the TRSB flight test errors (recall Fig. 2-38), and 2) TRSB van tests in the same region give much smaller errors (see Figs. 3-9 to 3-18 in Volume I of this report).

2. Tests at Brussels National Airport

During the course of MLS tests at Brussels National Airport, two C-130 aircraft were located in front of the elevation site so as to produce shadowing effects when the landing aircraft was on final approach. The locations of the DMLS antenna and C-130 aircraft relative to the runway were described in Chapter 2 of this volume (see Figs. 2-49 to 2-52). As in the case of the TRSB system, the landing aircraft was tracked only in the elevation plane. Thus, it was assumed that the landing aircraft flew precisely along the extended runway centerline. Figure 4-11 shows the DMLS "clean accuracy" errors while Fig. 4-12 compares the simulation results for a 2° and 3° glideslope with the DMLS field test data. We see that the peak-to-peak errors are similar for simulation and field tests; however, the detailed error waveforms are quite different. A similar result was obtained for the TRSB tests. It is believed that the major cause for these differences was variations in the landing aircraft

NM FROM AZIMUTH PHASE CENTER
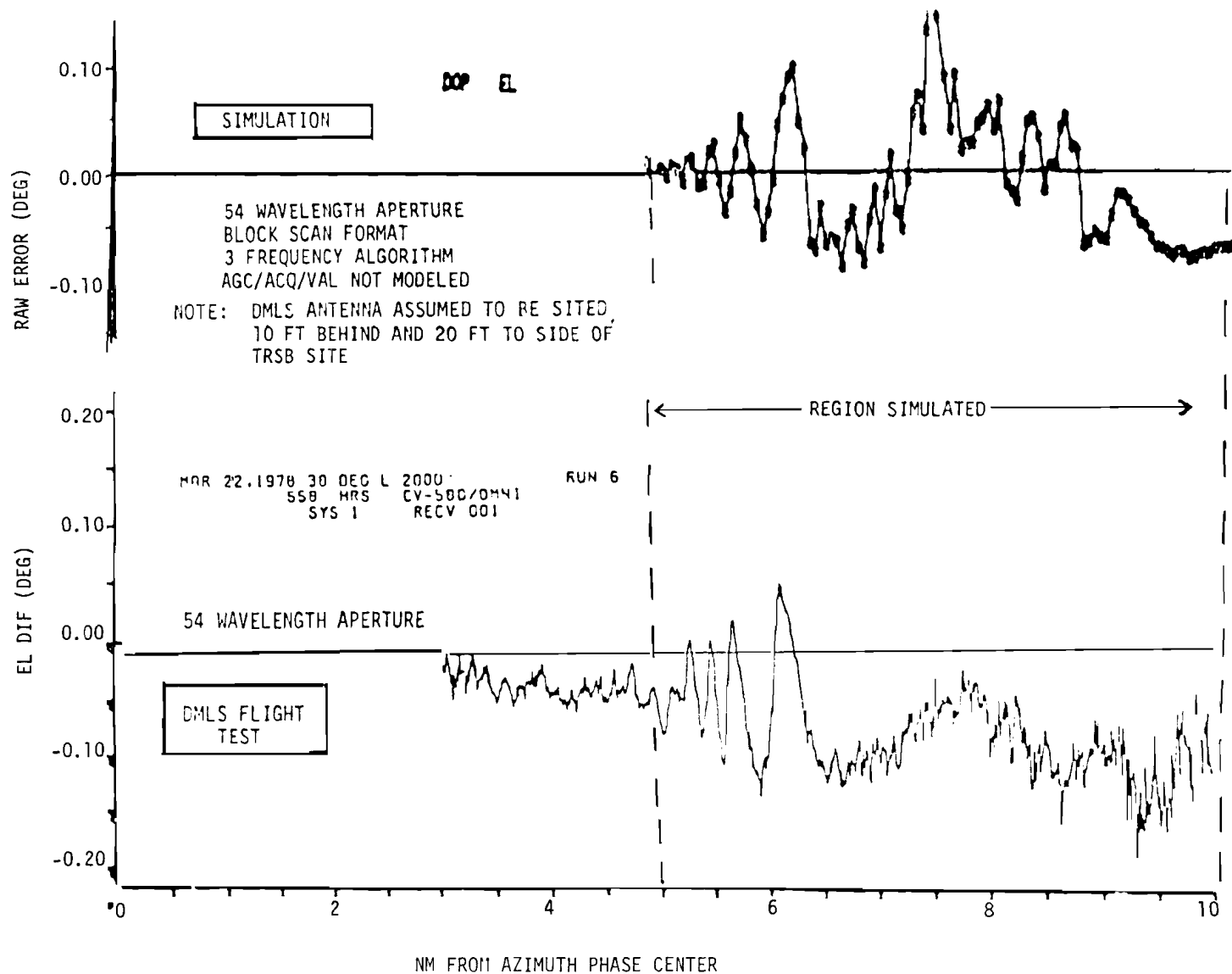
Fig. 4-9 Comparison of DMLS simulation and flight test on +38° radial at
2000 feet at JFK airport.
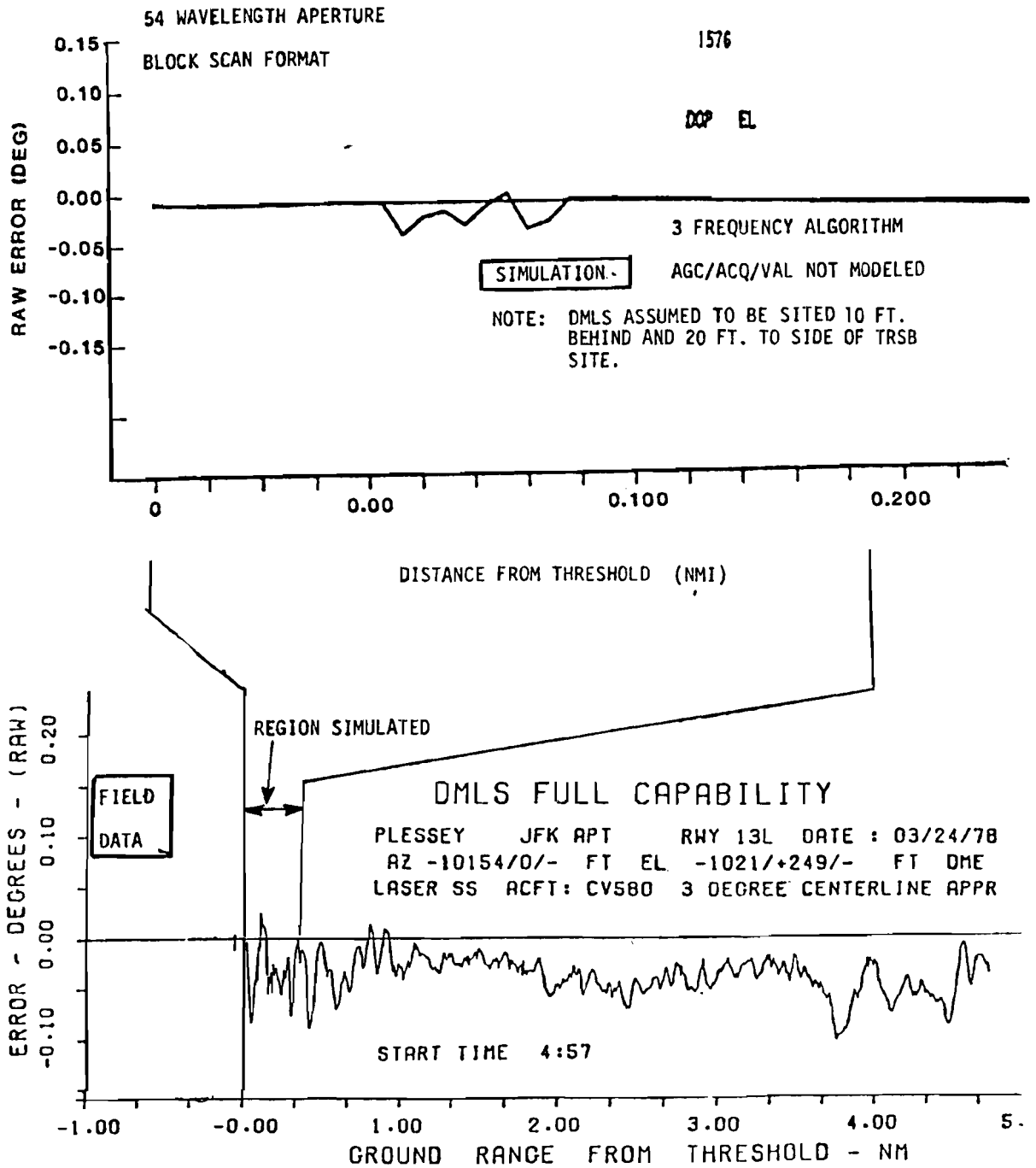
Fig. 4-10 Comparison of simulation with DMLS JFK centerline approach data.

DATA PROCESSED BY U.K.   OFFSET = 2.000 EG

ELEVATION, CENTERLINE, 2° APPROACH

RESULT INCLUDES TRACKER NOISE AND
SMALL DROP-OUTS

ICAO FULL CAPABILITY 2-SIGMA NOISE SPEC
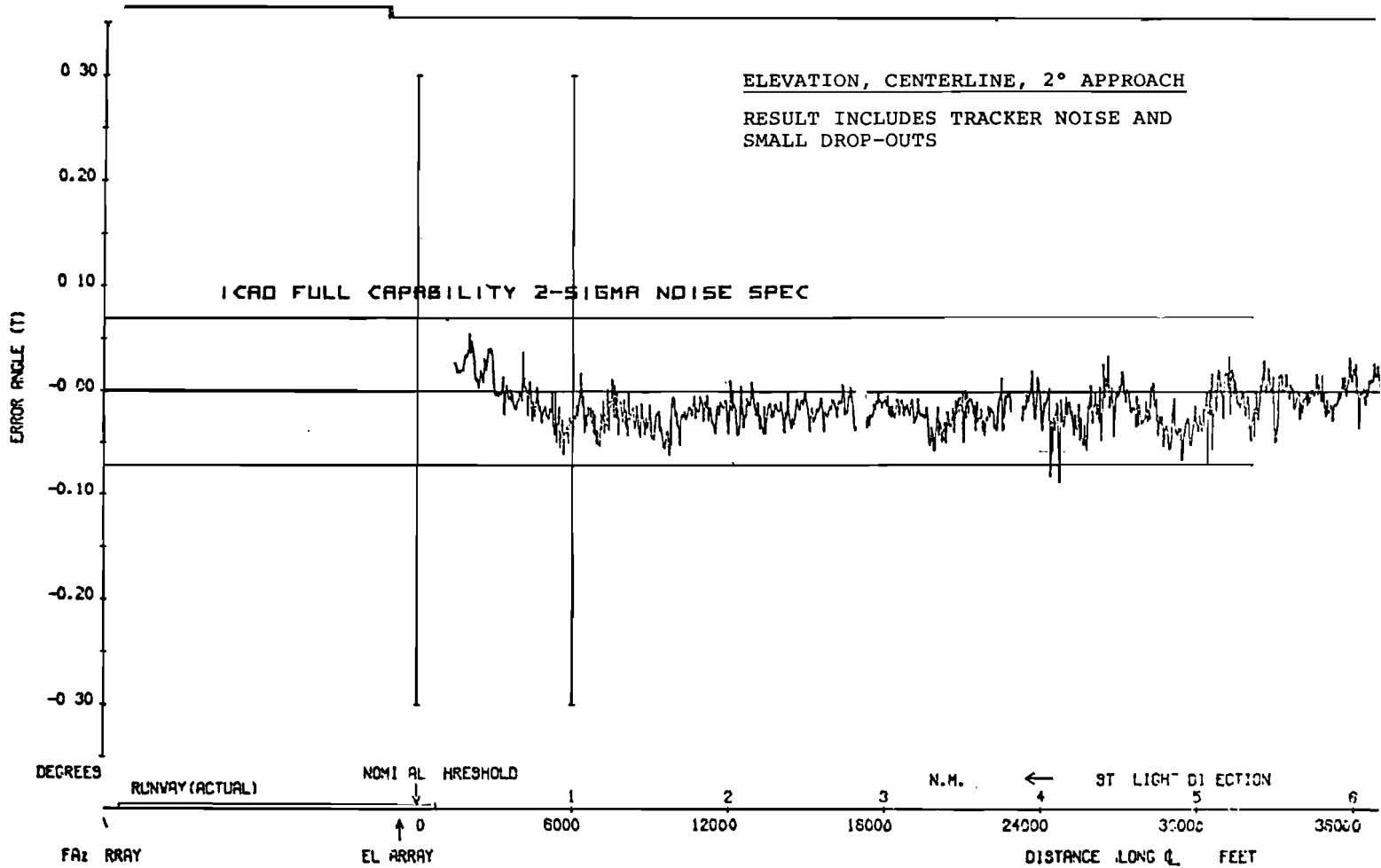
BRUSSELS NAT VAL AIRPORT

Fig. 4-11 DMLS "clean accuracy" errors at Brussels National Airport.

1569

54 wavelength aperture

3 frequency processor

AGC/VAL not modeled

DOP EL

0.10

0.05

-C.00

-0.05

-0.10

RAW ERROR (DEG)

centerline simulation with

height profile determined from

telescroscope data

0.0   1.000   2.000   3.000   4.000   5.000

DISTANCE FROM THRESHOLD (NM)

DMLSFD-UT50/ 7-EL-PC -10/01/78

OFFSET = 2.000 DEG

2° APPROACH WITH HERCULES PARKED

RESULT INCLUDES TRACKER CYCLIC
NOISE AND SMALL DROP OUTS

ICAO 2σ

0.10

-0.00

-0.10

ERROR ANGLE (T)

NOISE LIMITS

RUNWAY (ACTUAL)   NOMINAL THRESHOLD   N.M.   ← TEST FLIGHT DIRECTION

FAI ARRAY   EL ARRAY   0   6000   12000   18000   24000   30000   35000

1   2   3   4   5   6

DISTANCE ALONG ⊄   FEET

Fig. 4-12 Comparison of simulation with DMLS data for Hercules shadowing test.

lateral location with respect to the extended runway centerline since good agreement was obtained in the JFK data where one had precise tracker data in both planes.

D.   Tolerancing of DMLS Simulation Model

DMLS model validation by comparison with measurements on actual hardware was complicated by

(a)   the lack of controlled multipath field test data on the proposed ground arrays, signal format and airborne receiver

(b)   a lack of bench test data on the final proposed signal format and receiver algorithms (e.g., no elevation data was provided by the UK for the final scan format and processor algorithm).

Consequently, several complicating factors in DMLS performance (e.g., the effects of reference to sideband ratio on inbeam multipath error characteristics) were not completely resolved during the AWOP assessment.

The UK suggested [66] that the hybrid bench simulator test data should be utilized for quantitative assessment of DMLS simulations. It was found that:

(a)   The static multipath error characteristics for the DMLS computer model agree very closely with the RAE hybrid simulator data within the uncertainty limits that arise because the DMLS simulator does not control nor measure a key DMLS multipath parameter (the phase of the reference multipath signal with respect to the commutated array multipath signal)

(b)   The dynamic out-of-beam azimuth multipath (e.g., reference scalloping) error characteristics of the DMLS computer model also agree well with the RAE hybrid simulator results within the uncertainty limits that arise because:

(1) The DMLS hybrid simulator does not tightly
control the M/D level.

(2) The DMLS reference scalloping error at certain
frequencies is very sensitive to M/D levels.

As an illustration of points (1) and (2), RAE simulations on successive days
at nominally -3 dB M/D yielded a 40 percent change in error near 200 Hz.

Accordingly, the specific criterion adopted for comparing the simulation
data to the RAE simulator data was to deem the agreement quite good if the com-
puter data at an M/D level within 0.5 dB of the RAE estimated level showed
close agreement with the RAE data. In cases where such close agreement was
not obtained, the difference has been characterized in terms of the difference
in respective M/D levels to give close agreement. Using the criterion, it is
concluded that:

(1) The computer model and the RAE data show quite good
agreement for scalloping frequencies below 150 Hz
and above 300 Hz. These frequencies include the range
of azimuth multipath encountered in the AWOP scenarios
as well as various other scenarios discussed in Volume
III of this report.

(2) The computer model and RAE data appear to differ by
1.0 to 1.5 dB for scalloping frequenices between
150 Hz and 300 Hz. This frequency range includes
one building in one of the AWOP scenarios.

V. DLS MODEL DESCRIPTION

A. Introduction

The DME Based Landing System (DLS) is the microwave landing system pro-
posed by the Federal Republic of Germany [6, 84]. It is based on an improved
version of the distance measuring equipment (DME) which is a standard ICAO
system used for measuring distances for en route and short range navigation.
It operates in a frequency range near 1 GHz.

DLS is envisioned as comprising (see Fig. 5-1) of an airborne component
consisting of an interrogator and signal decoder and a ground component con-
sisting of two receiver antenna arrays (one for azimuth and one for elevation)
with processing and a transponder for replies. Each receiver antenna array
is used to sample the transmissions from the interrogator and feed that in-
formation to a processor. One receiver/antenna array/processor (RAP) combina-
tion yields time of arrival and azimuth angle, while the other RAP yields the
elevation angle. This information is fed to a transponder, colocated with
the azimuth receiver/processor, which transmits the DME pulse-pair and angle
information back to the airplane using pulse position modulation.

The interrogator would be identical to the standard DME interrogator ex-
cept with regard to the incorporation of a greater variety of pulse-pair spac-
ings in order to increase the effective number of channels available. Each
ground station has associated with it an address composed of a frequency and
pulse-pair spacing and will respond only when addressed. The distance meas-
uring aspect of DLS operates in a manner identical to DME. The data from the
azimuth sensor is processed to determine an estimate of azimuth position, and
this information is coded by pulse position modulation relative to the DME
pulse-pair response. Data from the elevation sensor is similarly processed,
coded, and transmitted. (Auxiliary data may also be included in the trans-
ponder reply). A summary of the signal format is illustrated in Fig. 5-2.

Historically, civil navigation aids have been "air-derived" systems in
which the position parameter (e.g., azimuth) is measured in airborne receivers
by analyzing a signal transmitted from the ground. By contrast, the angle

Fig. 5-1   DLS BLOCK DIAGRAM

DME
Interrogation

DME   azimuth   elevation

$T_{oe} + T_e$

$T_{od} + T_d$ $T_{oa} + T_a$

50μs

(Tod)

Toa = 5 msec

Ta = 18.2 μ sec × θa

Toe = 12 msec

Te = 18.2 μ sec × (θe + 5°)

θa, θe = azimuth and elevation in deg
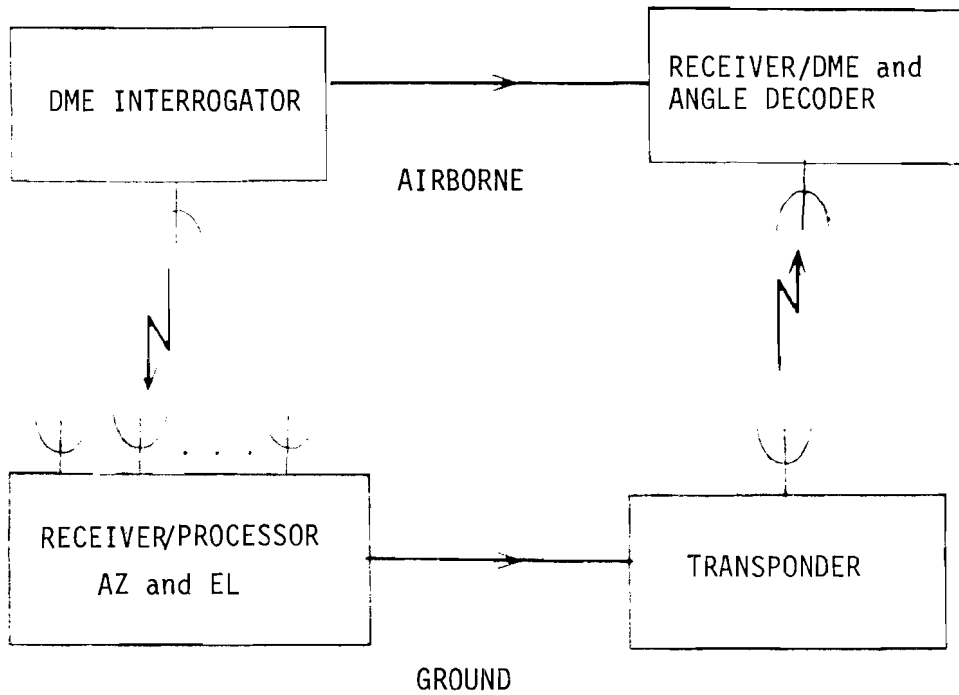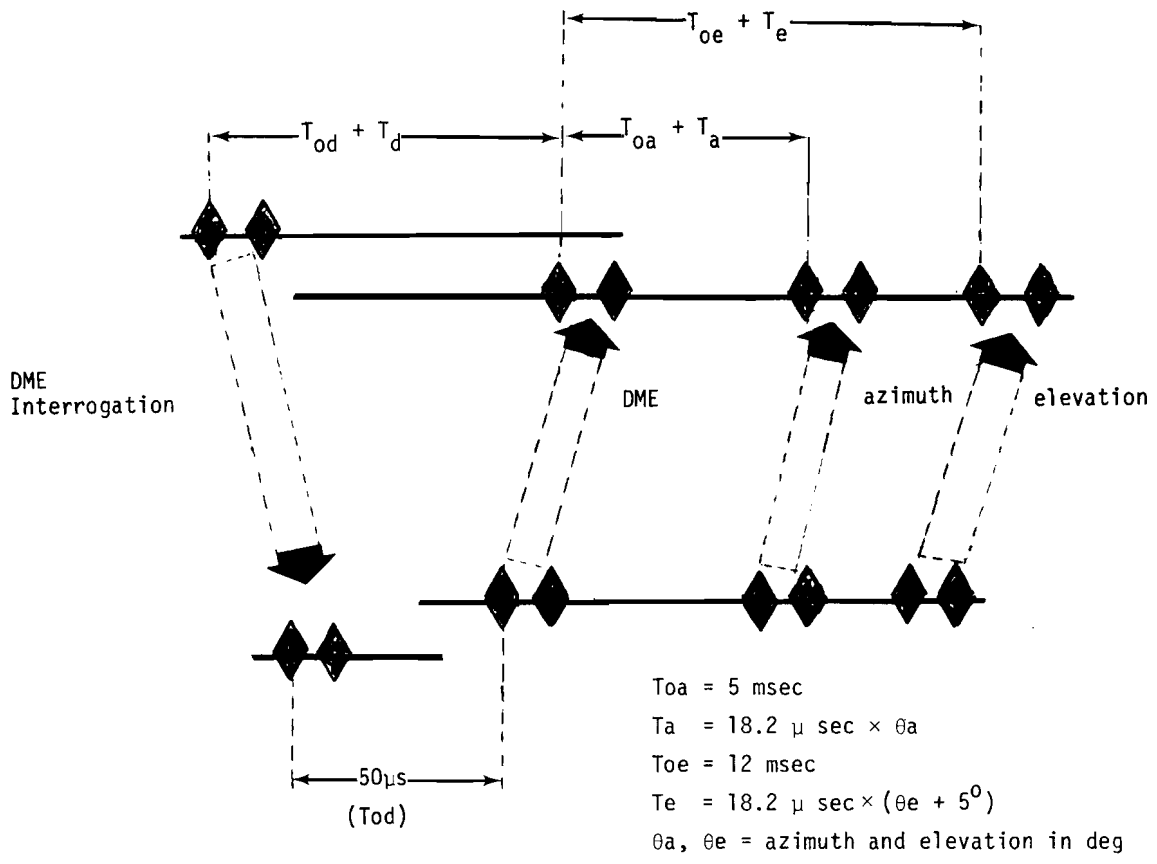
Ta - time equivalent to azimuth
Td - time equivalent to distance
Te - time equivalent to elevation
Toa, Tod, Toe - bias time intervals

Fig. 5-2   DLS signal format.

portion of DLS is a "ground-derived" system in which the position parameter is measured by a ground based receiving system analogous to the air space traffic control surveillance radars. Thus, a short discussion of some differences between DLS and the air-derived MLS techniques (DMLS and TRSB) is in order (see reference [83] for a more general discussion of air versus ground-derived MLS techniques).

Several advantages achieved by this approach are: (1) a lower cost for the airborne equipment if DME is considered to be on every MLS equipped aircraft [9], (2) some multipath reduction is obtained by sampling the leading edge of the downlink DME pulse, since although the multipath signal is rising similar to the direct signal, it has risen, at the sampling time, to a lesser extent than the signal (this difference is dependent on the pulse shape and the multipath time delay), (3) greater flexibility exists as to the type, size, and geometric location of ground antennas, and, (4) the potential for more flexible and sophisticated signal processing that exists for data processing with a large computer.

These, in turn, are countered by the following disadvantages: (1) the 1 foot wavelength at 1 GHz forces the antennas to be physically much larger than those of the C band system ($\lambda\approx0.2$ foot) for similar beamwidths, (2) each angle estimate is made on the ground independent of all prior knowledge of the aircraft position, and (3) the need to complete all processing for an angle estimate within a short time duration (e.g., 5 msec) results in the use of the computationally simple, but suboptimal approach of multiple baseline interferometry[*] for aircraft locations. The resulting sensitivity to ambiguity resolution errors at high multipath levels is exacerbated by (2) since knowledge of the past aircraft locations cannot be utilized in the ambiguity resolution process. However, there is an airborne tracker which can discard highly erroneous ground estimates in many cases.

---

[*] The signal processing approach described is that which was proposed to and assessed by the ICAO AWOP. Subsequently, it has been suggested [84] that a more nearly optimal FFT beamforming technique [85] could be utilized for aircraft angle location at difficult sites.

The nucleus of the DLS simulation model is (1) its antenna arrays, (2) the phase measurement receiver, and (3) the digital processing of the receiver outputs. These and other relevant aspects of DLS are described below.

B. DLS Antenna Arrays

The deployment of antenna arrays for the highest performance DLS is illustrated in Fig. 5-3. The azimuth antennas, which are located on centerline near the stop end of the runway, consist of five antenna arrays (Fig. 5-4). In the center is a 19 element circular array, out to each side are dipole arrays, and at the extremities are two six-element linear arrays.

The azimuth circular array provides full 360° coverage with the estimate being made using interferometric techniques. Azimuth angle estimates are made with a sequence of increasing baselines. The small baseline estimates are used only to resolve the ambiguities with the largest baseline (the full diameter) results used for the estimate transmitted to the aircraft. If this estimate is less than 40 degrees in magnitude, then it too is utilized as an ambiguity resolution input and the process is extended with continually increasing baselines achieved by utilizing the dipoles and the six-element linear arrays as a compound interferometer. The final baseline is 96.45 feet, corresponding to the linear array physical separation.

The elevation antenna (Figs. 5-3 and 5-5) is located to one side of the runway near the threshold. It can be thought of as a 30 element linear array. In order to narrow the horizontal beamwidth of the pattern, lateral diversity has been used and the 30 elements are spread over 5 columns of six elements each. In addition, a reference element has been added at the base of each column. This is used to reference respectively each colummn measurement and thus allow for the intermeshing of the five columns of data measurements into, effectively, a single vertical linear array.

The elevation array estimates the elevation angle by interferometer pairs of increasing baseline. The interferometer elements are "synthetic antennas" obtained by summing the complex received signal on a number of adjacent physical elements so as to achieve a directional pattern. Also, beam steering is
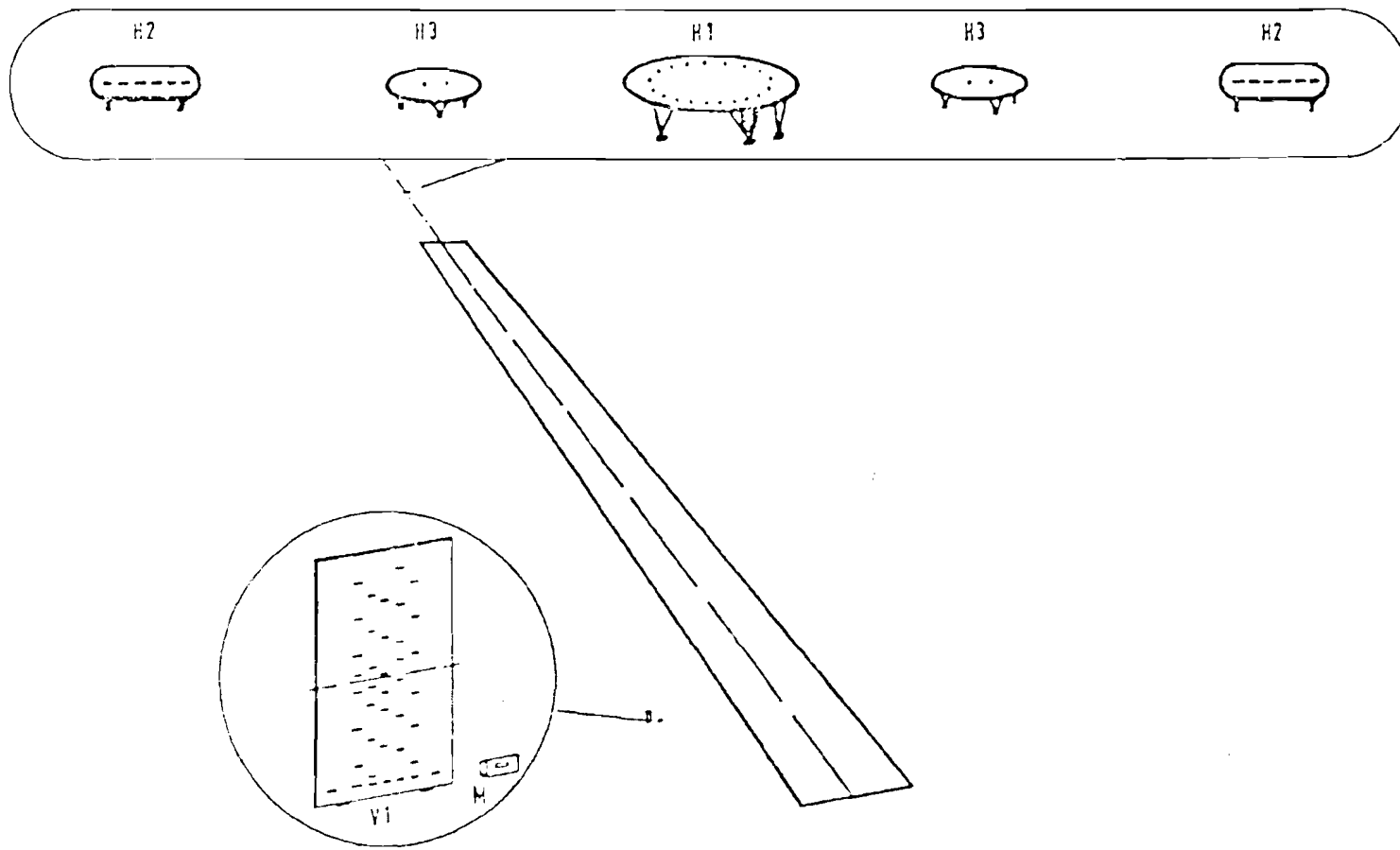
Fig. 5-3   DLS ground system configuration.

RUNWAY CENTERLINE

5.45 λ

1.22 .9 .8 1.03 1.5λ

SUBARRAY EXPANDED VIEW

DIPOLE

CIRCULAR ARRAY

DIPOLE

28 λ

14 λ

7 λ

14 λ

28 λ
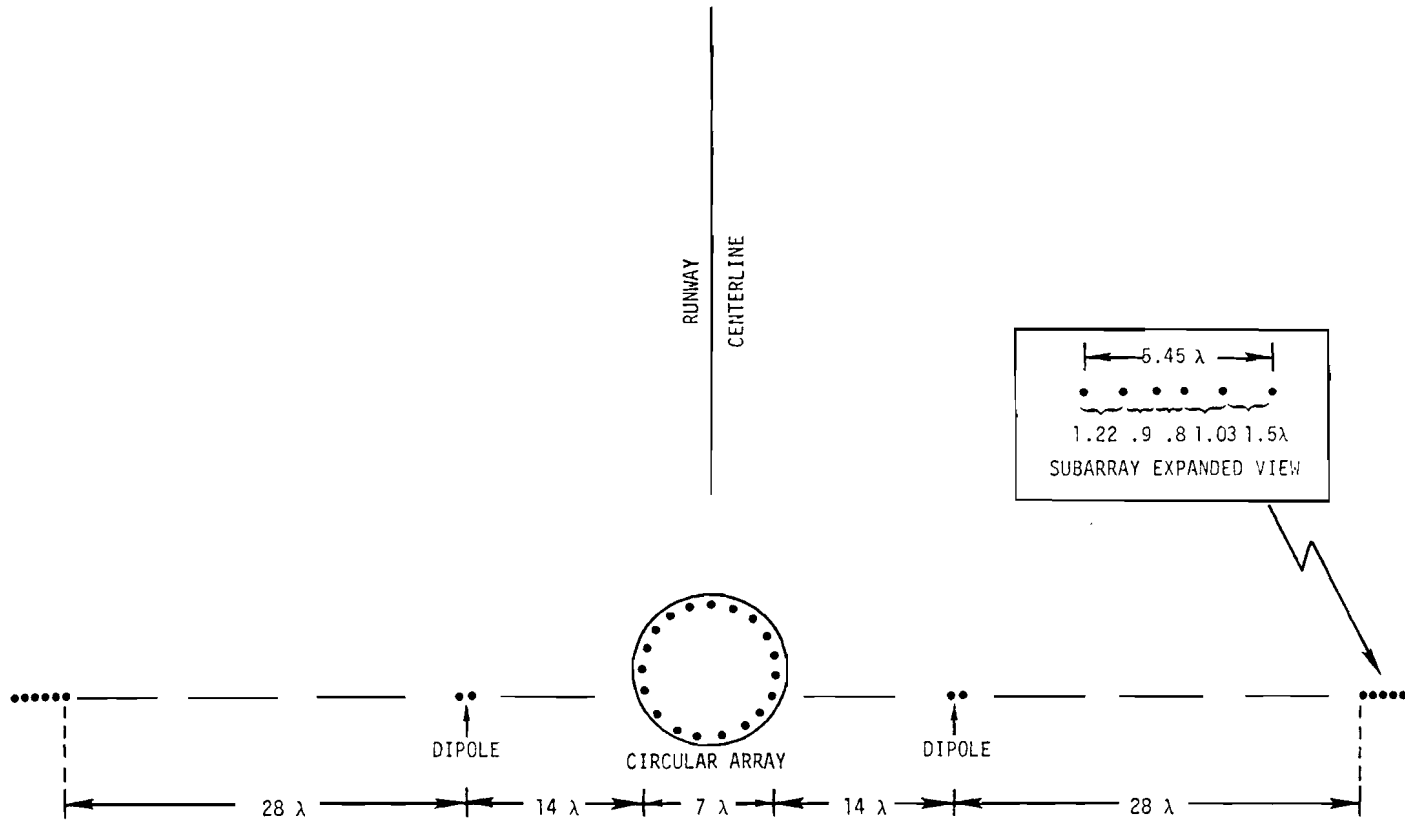
Fig. 5-4 DLS azimuth antenna arrays.
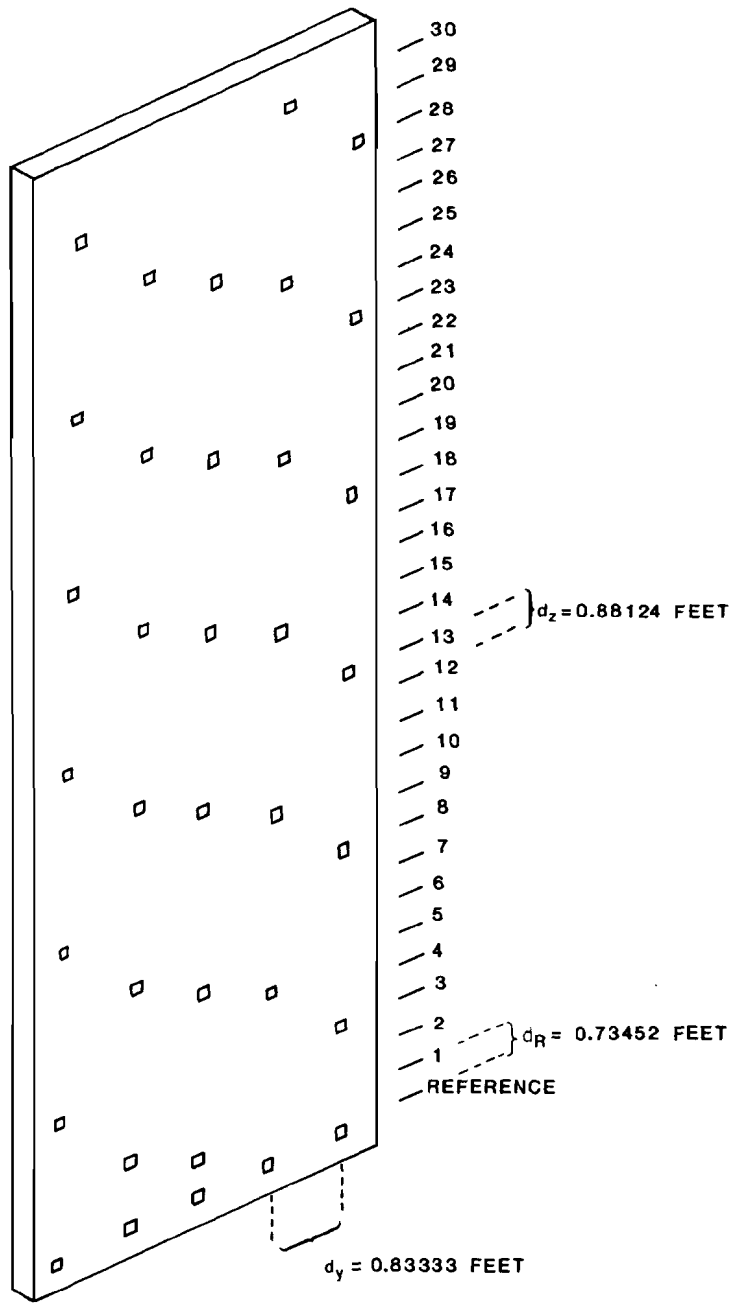
Fig. 5-5   DLS elevation antenna element positions.

used in the synthetic antenna formation in such a way as to prevent ground bounce from arriving on the main lobe [86].

In order to precisely and efficiently describe the modeling of the signals, phases, and processing of the measurement data, it behooves us to place these quantities in the context of a mathematical framework which will be described next.

C.   Mathematical Framework for System Modeling

This section is devoted to introducing the mathematical framework and nomenclature to be utilized throughout.

We begin by defining the reference phase point for each antenna array as the physical center of the elements used in forming the array. The vector, $\underline{d}_k$ is defined as the displacement of the kth element from this reference phase point. There is assumed to be one direct and M multipath signals impinging on each element and we denote the direct signal by subscript zero and the mth multipath by subscript m, $1 \leq m \leq M$. Each signal received at an antenna is assumed to be in the form of a plane wave with the vector $\underline{n}_m$ as its directional vector; i.e., specifying the direction of propagation of the plane wave. If we designate the planar azimuth angle by θ_m and the conical elevation angle by ϕ_m, then the vector $\underline{n}_m$ can be written as:

$$\underline{n}_m = -(\cos \phi_m \cos \theta_m, \cos \phi_m \sin \theta_m, \sin \phi_m). \tag{5-1}$$

The signal modulating the carrier has the pulse shape $p(t)$

$$p(t) = \begin{cases} e^{-1.423(t/\tau)^2} & |t| \leq 4 \times 10^{-6} \\ 0 & |t| > 4 \times 10^{-6} \end{cases} \tag{5-2}$$

where $\tau = 2.5 \times 10^{-6}$ sec and t is in seconds. We designate the magnitude of the mth signal by ρ_m and the phase at the reference point by $\alpha_{mk}^{\dagger}$, τ_m is the

---

$^\dagger\alpha_{mk}$ includes the phase shift due to reflections and the phase of the antenna elements.

time delay of the mth multipath pulse relative to the direct, ω_m the carrier frequency, $\Delta\omega_m$ the doppler frequency, and Δt the time difference between DME interrogations. Finally, designating $G_k(\theta_m, \phi_m)$ as the antenna pattern of the kth element, then we can write the total received signal at the kth element, S_k, as

$$S_k = D_k + M_k \tag{5-3}$$

where

$$D_k = \rho_0 \, p(-T) \, |G_k (\theta_0, \phi_0)| \, e^{j(\alpha_{0k} + \Delta\alpha_{0k})} \tag{5-4a}$$

$$M_k = \sum_{m=1}^{M} \rho_m \, p(-T-\tau_m) \, |G_k(\theta_m, \phi_m)| \, e^{j(\alpha_{mk} + \Delta\alpha_{mk} + \omega_{mk}\tau_m)}$$

$$\underset{=}{\Delta} \; |M_k| \, e^{j\beta_k} \tag{5-4b}$$

where $T = 10^{-6}$ sec and

$$\Delta \alpha_{mk} = -\frac{2\pi}{\lambda} \; (\underline{d}_k, \underline{n}_m) \tag{5-5}$$

where we use the notation $(\underline{a}, \underline{b})$ to denote the inner product between vectors $\underline{a}$ and $\underline{b}$.

As a computational convenience to reduce calculations, it is assumed that the individual signal amplitudes do not change significantly over 0.2 sec. Therefore, by adjusting the phases, the same amplitudes are used to generate the N signals received in a fifth of a sec. Normal interrogation rates are 15 Hz and 40 Hz with the latter used during the time the aircraft is in the glide slope. These correspond to N=3 and 8, respectively. The N replies are averaged in the airborne receiver so that the final data rate is approximately 5 Hz. Since each rf phase is modified between interrogations by an amount $\Delta\omega_m \Delta t$, then we can represent N successive received signals at the

k^{th} antenna element by

$$S_{kn} = D_{kn} + M_{kn} \quad \text{for } n=0,1\cdots,N-1 \tag{5-6}$$

where

$$D_{kn} = \rho_0 \; p(-T) \; |G_k \; (\theta_0, \; \phi_0)| \; e^{j(\alpha_{ok} + \Delta\alpha_{ok} + \Delta\omega_0 \; n\Delta t)} \tag{5-7a}$$

$$M_{kn} = \sum_{m=1}^{M} \rho_m \; p(-T-\tau_m) |G_k \; (\theta_m, \; \phi_m)| \; e^{j(\alpha_{mk}+\Delta\alpha_{mk}+\omega_m t_m+\Delta\omega_m n\Delta t)}$$

$$\triangleq |M_{kn}| \; e^{j \; \beta_{kn}} \qquad\qquad n=0,1,\cdots,N-1 \tag{5-7b}$$

We define γ_{kn} as the rf phase difference of the $(n+1)^{st}$ interrogation $(n=0,1,\ldots,N-1)$ at the kth antenna element relative to the reference point so that in terms of the above quantaties

$$\gamma_{kn} = \alpha_{ok} + \Delta\alpha_{ko} + \Delta\omega_0 \; n\Delta t \tag{5-8}$$

$$+ \tan^{-1} \left\{ \frac{|M_k| \; \sin \; [\beta_{kn} - (\alpha_{ok} + \Delta\alpha_{ok} + \Delta\omega_0 \; n\Delta t)]}{\rho_0 + |M_k| \; \cos \; [\beta_{kn} - (\alpha_{ok} + \Delta\alpha_{ok} + \Delta\omega_0 \; n\Delta t)]} \right\} + a_k \; 2\pi$$

$$n=0,1,\ldots,N-1$$

where the a_k are integers corresponding to the proper resolution of the phase data; i.e., a_k is known if γ_{kn} is correctly resolved. We relegate the details of the ambiguity resolution procedure and issues to Appendix G and assume here that the data have been correctly resolved.

With this notation, we are now in a position to efficiently specify and model the signal to be processed by each antenna receiver.

D. Azimuth Circular Array Model

The azimuth circular array has 19 elements, is configured as shown in Fig. 5-4, and has a radius, r, of about 3.5 feet. The displacement vector $\underline{d}_k$ for each element is

$$\underline{d}_k = r \left(\cos \frac{(2k-1)\pi}{19} \, , \, - \sin \frac{(2k-1)\pi}{19} \, , \, 0 \right) \tag{5-9}$$

$$k = 1, 2, \ldots, 19$$

so that for the kth element

$$\Delta\alpha_{km} = \frac{2\pi}{\lambda} \, r \left[\cos \frac{(2k-1)}{19} \pi \cos \phi_m \cos \theta_m \right.$$

$$\left. - \sin \frac{(2k-1)}{19} \pi \cos \phi_m \sin \theta_m \right] \tag{5-10}$$

$$= \frac{2\pi}{\lambda} \, r \, \cos \, \phi_m \, \cos \left(\theta_m + \frac{(2k-1)}{19} \pi \right).$$

The omni directional elements do not have a symmetrical ground plane so that the pattern in the direction going radially outward is different from that going radially inward towards the center of the circle. The amplitude and phase patterns of a vertical plane cut are given in Fig. 5-6. The two lobes of amplitude pattern correspond to the outward radial and inward directions which we designate $G_0(\phi)$ and $G_I(\phi)$, respectively.

We make the assumption that the pattern varies linearly in both amplitude and phase as the direction rotates from $\theta = 0°$ (outward) to $\theta = \pi$ (inward) directions so that the pattern for element 1 is:

$$G_1(\theta, \phi) = G_0(\phi) \left(1 - \frac{|\theta|}{\pi} \right) + G_I(\phi) \left(\frac{|\theta|}{\pi} \right) \tag{5-11}$$

The pattern for element k is the same except that it has been rotated by $\frac{(2k-1)\pi}{19}$ radians so that
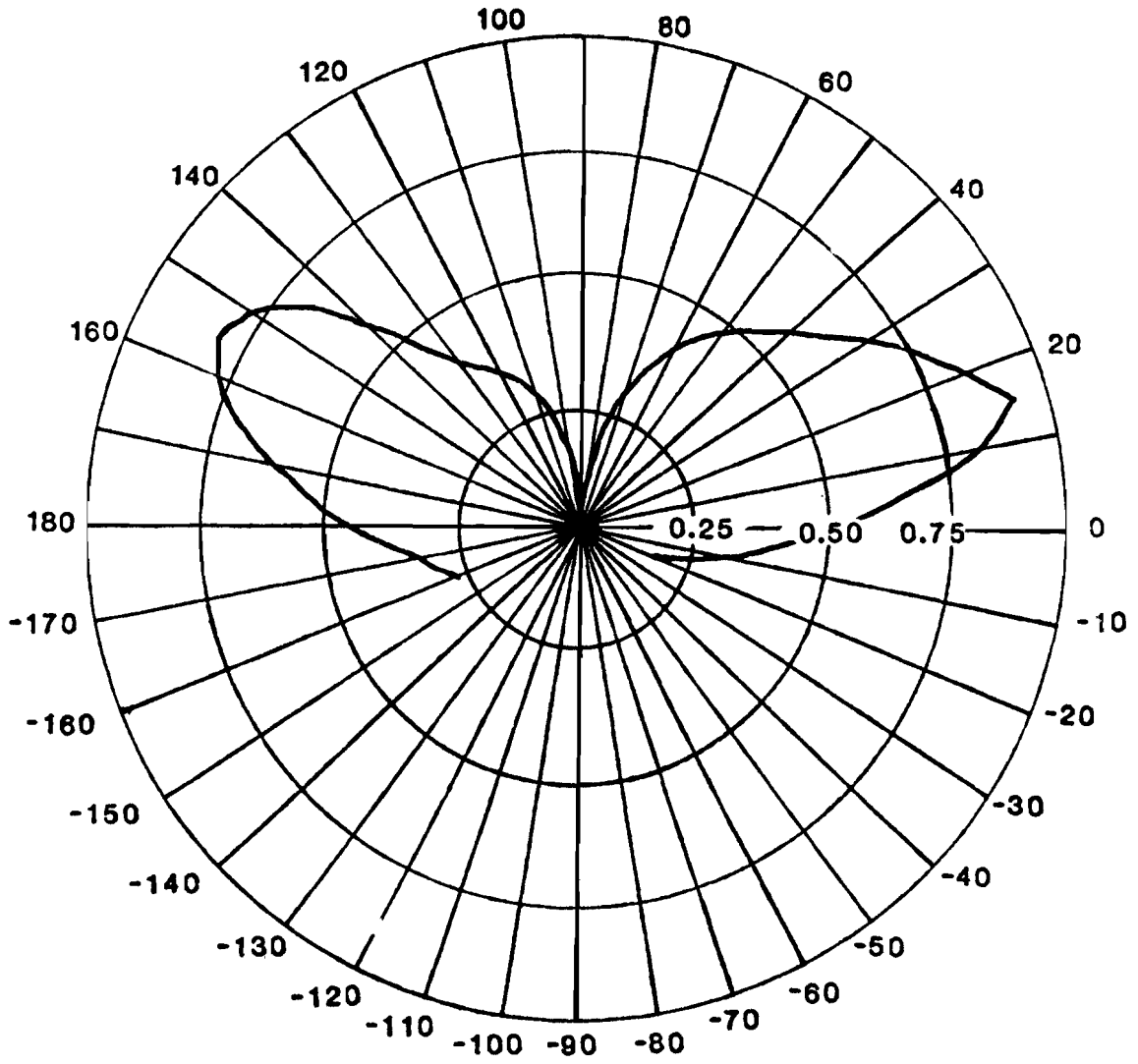
Fig. 5-6a Elevation pattern (magnitude) of DLS
circular array "omni" elements.
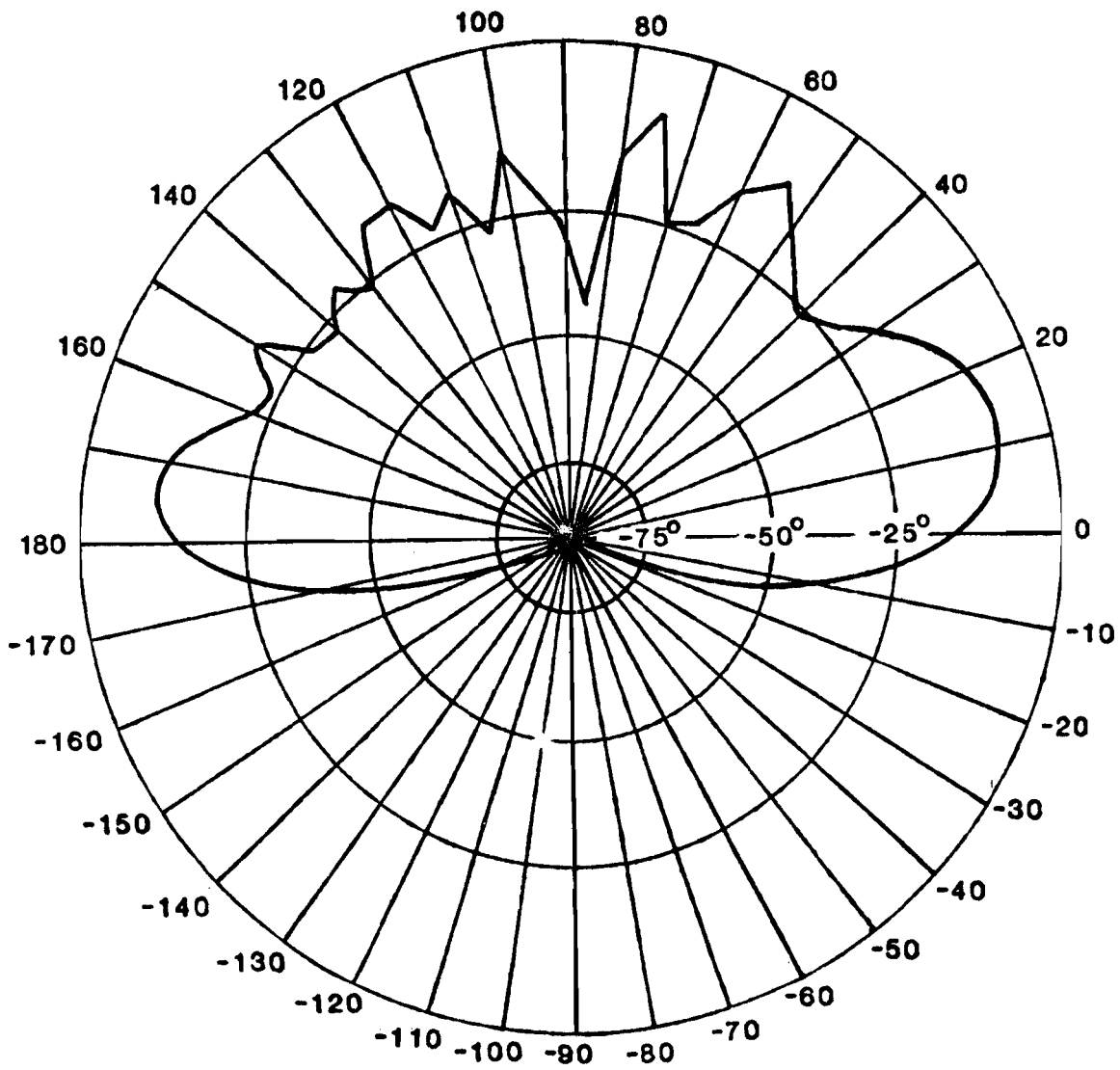
Fig. 5-6b Elevation pattern (phase) of DLS
circular azimuth elements.

$$G_k(\theta,\phi) = G_0(\phi) \left(1 - \left|\frac{\theta}{\pi} - \frac{(2k-1)}{19}\right|\right) + G_I(\phi) \left|\frac{\theta}{\pi} - \frac{(2k-1)}{19}\right| \qquad (5\text{-}12)$$

$$k = 1, 2, \ldots, 19$$

The estimate is made by forming $\Delta\gamma_{k,n}$

$$\Delta\gamma_{k,n} = \begin{cases} \gamma_{a,n} - \gamma_{b,n} & \begin{array}{l} a = (k-1)/2 + 5 \\ b = (k-1)/2 + 14 \end{array} \quad \text{for } k \text{ odd} \\ \\ \gamma_{c,n} - \gamma_{d,n} & \begin{array}{l} c = k/2 + 4 \\ d = k/2 + 14 \end{array} \quad \text{for } k \text{ even} \end{cases} \qquad (5\text{-}13)$$

$$k = 1, 2, \ldots, 19 \quad \text{and} \quad n = 0, \ldots, N\text{-}1$$

then defining

$$S_n = -\sum_{k=1}^{19} \Delta\gamma_{k,n} \, \sin(k-1)\frac{\pi}{19}$$

$$\qquad (5\text{-}14)$$

$$C_n = \sum_{k=1}^{19} \Delta\gamma_{k,n} \, \cos(k-1)\frac{\pi}{19} \qquad n = 0, 1, \ldots, N\text{-}1$$

one has the azimuth estimate

$$\hat{\theta}_{p,n} = \tan^{-1} \frac{C_n}{S_n} \qquad (5\text{-}15)$$

when the subscript p denotes that the angle is a planar angle as opposed to conical.

These estimates are transmitted to the aircraft possible with some data link error. If we ignore the data link error, then the final estimate as averaged on the aircraft is of the form

$$\hat{\theta}_p \approx (1/N) \sum_{n=1}^{N-1} \hat{\theta}_{p,n} \qquad (5\text{-}16)$$

If the estimate $|\hat{\theta}_{p,n}|$ is less than 40°, the ambiguity resolution process is continued employing the azimuth linear arrays to yield a wider baseline. If $40° \leq |\hat{\theta}_{p,n}| \leq 140°$, the estimate $\hat{\theta}_{p,n}$ is transmitted. If $140° \leq |\hat{\theta}_{p,n}| \leq 180°$, then the dipoles are used for a final back azimuth estimate.

E. Azimuth Linear Array Model

If the angle estimate, as determined by the circular array, has a magnitude less than 40° then the process continues utilizing the linear arrays. The first requirement is to convert the planar angle estimate into a conical angle so as to be consistent with the type of angle estimate to be generated by the linear arrays. This is done by means of the conversion formula

$$\theta_{cn} = \sin^{-1} (\cos \phi_c \sin \theta_{pn}) \tag{5-17}$$

where θ_p is as defined in (15) and with S and C as in (5-14), so

$$\ell = \sqrt{c^2 + s^2} \tag{5-18}$$

and

$$D = \ell / \ell \text{ max}; \quad \ell \text{ max} = 416.4059 \tag{5-19}$$

then

$$\cos \phi_{cn} = D \tag{5-20}$$

Noise may cause D to be greater than 1 so a limit of 1 is placed on D for use in (5-20).

Elements six and fifteen of the circular array are in line with the dipoles and the outer arrays (Fig. 5-4). Using the conical azimuth angle as obtained from (5-17), further estimates corresponding to increasing baselines are determined using various combination of antennas and ending with a baseline of 63 feet. This estimate, θ', is used to steer the six element arrays and to resolve the phase difference measurement made by the pair of six element arrays.

The details and issues of these more or less standard [87] intermediate steps are relegated to Appendix G and we proceed under the assumption that the angle θ' has been correctly resolved. The six element outer linear arrays has a steerable pattern which is aimed in the direction θ' so that the normalized array pattern is

$$E_a(\theta, \theta') = \frac{\cos \theta'}{6} \sum_{k=1}^{6} e^{j2\pi w_k (\sin \theta - \sin \theta')} \qquad (5\text{-}21)$$

where the w_k,

$$w_k = \begin{cases} -2.61 & k=1 \\ -1.39 & k=2 \\ -0.49 & \text{for} \quad k=3 \\ 0.31 & k=4 \\ 1.34 & k=5 \\ 2.84 & k=6 \end{cases}$$

are defined relative to the 6 element subarray phase center. Note that these two outer subarrays are identical and not mirror images of one another. The final baseline is 96.45 feet.

Designating the linear element pattern by $G(\theta, \phi)$ (shown in Fig. 5-7), the total subarray pattern is $G_A(\theta_m, \phi_m, \theta') = G(\theta_m, \phi_m)E_a(\theta_m, \theta')$. The terms $\Delta \alpha_{mk}$ for this array are

$$\Delta \alpha_{mk} = 96.45 \, k\pi \cos \phi_m \sin \theta_m, \text{ for } k = \pm 1 \qquad (5\text{-}22)$$

so that substituting this in (5-8) we can obtain values for $\gamma_{1,n}$ and $\gamma_{-1,n}$ and the final estimate is

$$\hat{\theta}_{c,n} = \sin^{-1} \left(\frac{\gamma_{1,n} - \gamma_{-1,n}}{192.9\pi} \right) \qquad (5\text{-}23)$$

F. The Elevation Antenna Model

The elevation antenna array is illustrated in Fig. 5-5. It consists of 30 elements spread in five columns and five reference elements at the base of each column. The spreading allows for a narrower horizontal beam pattern to help reduce multipath. The phase data on each element is taken relative to reference element in its own column. The data is then combined as if it were from a single vertical linear array.

Several passes are made in processing the data. On the first pass, the data from elements 8 to 23 form one array and 9 to 24 a second. The amplitudes and phases are chosen so that the broad clearance pattern of Fig. 5-8 results.
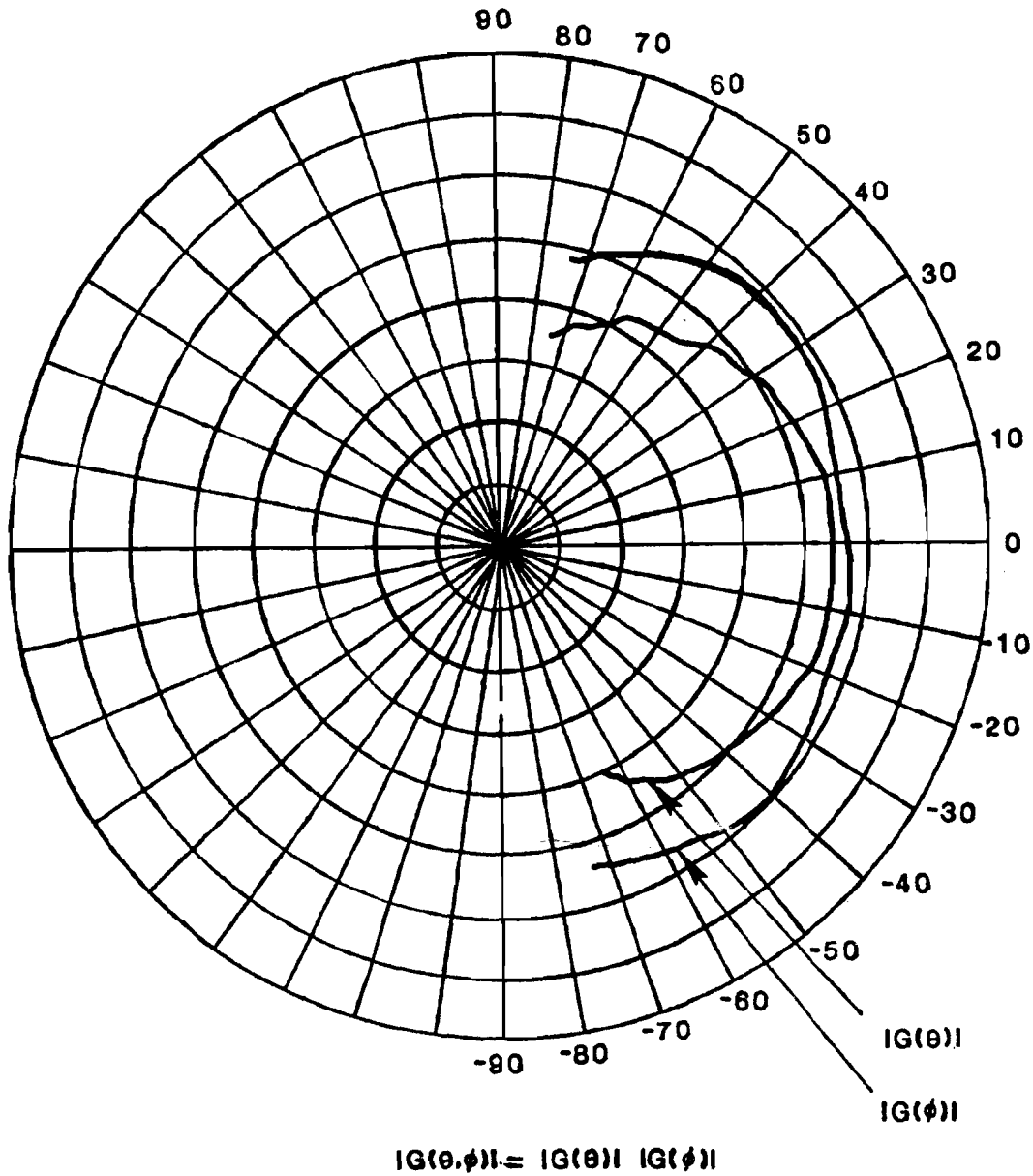
Fig. 5-7a   Pattern (amplitude) of DLS linear
array elements.

$$|G(\theta,\phi)| = |G(\theta)| \; |G(\phi)|$$
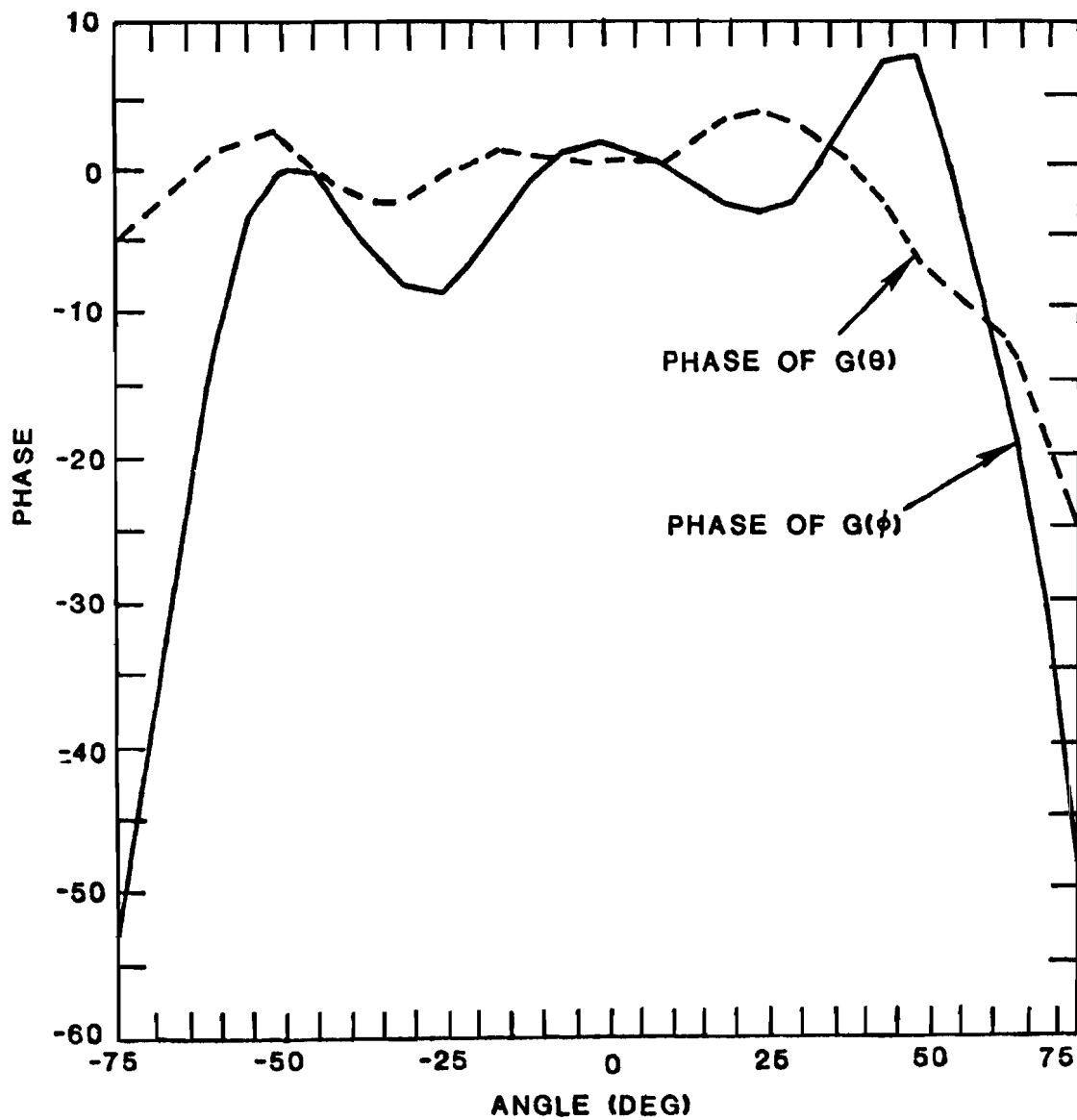
Fig. 5-7b   Phase characteristic of DLS linear array element.
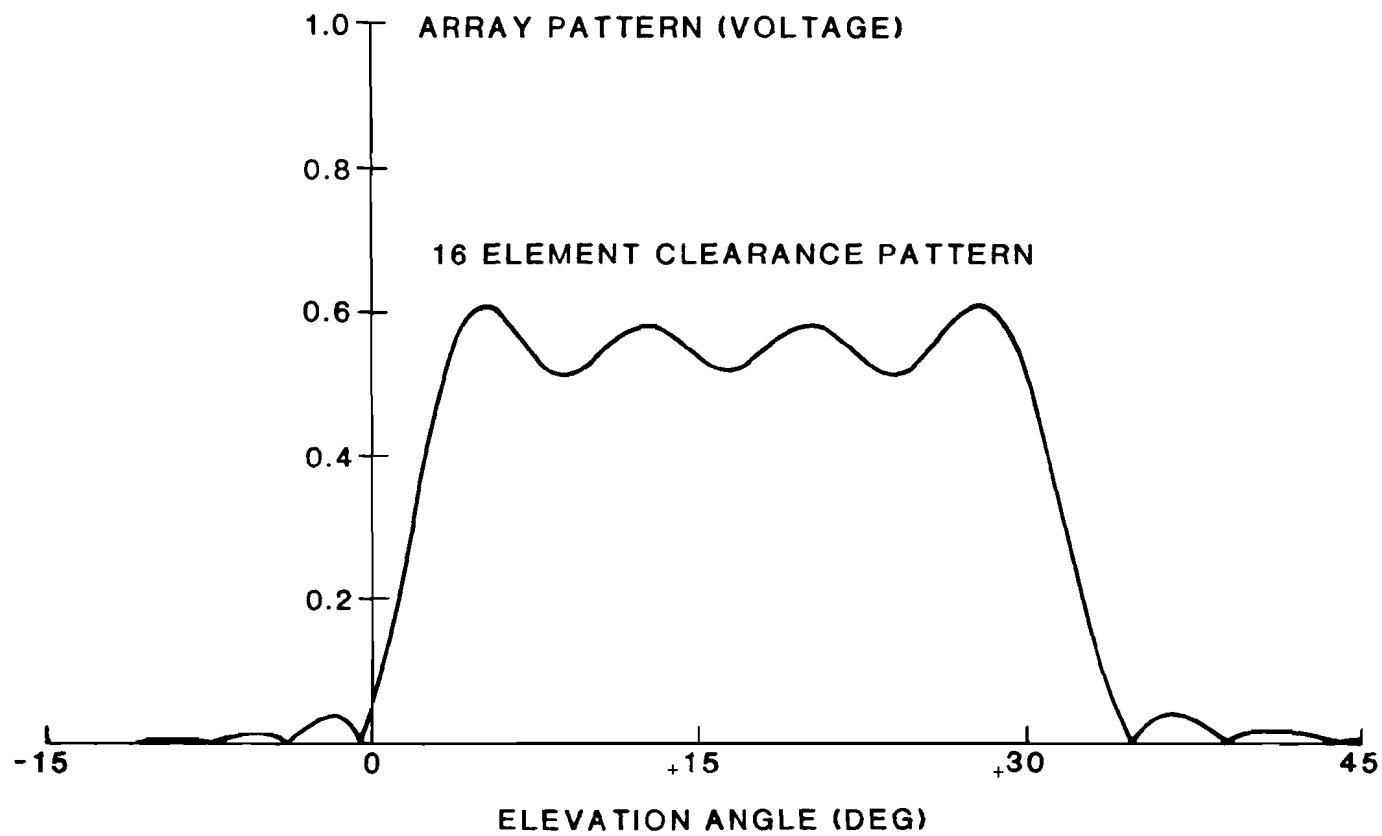
Fig. 5-8 Synthetic element "clearance" array pattern used in DLS elevation
array initial processing.

Note that ground reflections at negative angles are significantly reduced by this pattern. An elevation angle estimate is made based on the phase difference at the output of these two arrays which have a phase center separation of 0.88142 feet.

A new array combination of 15 elements is utilized to form the narrow beam of Fig. 5-9 which is steered toward the estimated elevation angle. In order to prevent ground reflections from coming in on the main beam an adjustment to the steering angle is made when the estimated angle is below 7.5°. The beam is never pointed below 5.3° for which case the 1st null is on the horizon. For estimates less than 2° the beam is steered to 5.3°. For estimates between 2° and 7.5° a beam steering angle ϕ_s is determined by the linear equation:

$$\phi_s = 0.4\hat{\phi} + 4.5° \text{ for } 2° \le \hat{\phi} < 7.5° \tag{5-24}$$

where $\hat{\phi}$ is the estimated elevation angle from the previous pass.

The interferometer pair separation increases on successive estimates by factors of 2, 2.5, and 3 so that the final separation is (15) x (0.88142) = 13.2 feet. A total of 4 passes have been made, the first with the clearance pattern and three with the steered narrow beam pattern. Again ambiguity resolution algorithms are relegated to appendix G.

The location of the pth element, relative to the antenna center, is

$$d_p = (0, \frac{5}{6}f\left\{ p \text{ mod } 5\right\}, (0.88142)(-15.5 + p)) \tag{5-25}$$

where

$$f\left\{n\right\} = \begin{cases} -2 & n=4 \\ -1 & n=2 \\ 0 & \text{for} & n=1 \\ 1 & n=0 \\ 2 & n=3 \end{cases} \text{ and } p = 1, 2, \ldots, 30$$

The five reference elements can be considered as elements 31 through 35 located at

$$d_p = \left(0, \frac{5}{6}f\left\{p \text{ mod } 5\right\}, (-0.88142)(15.333)\right) \text{ for } p = 31, \ldots, 35 \tag{5-26}$$
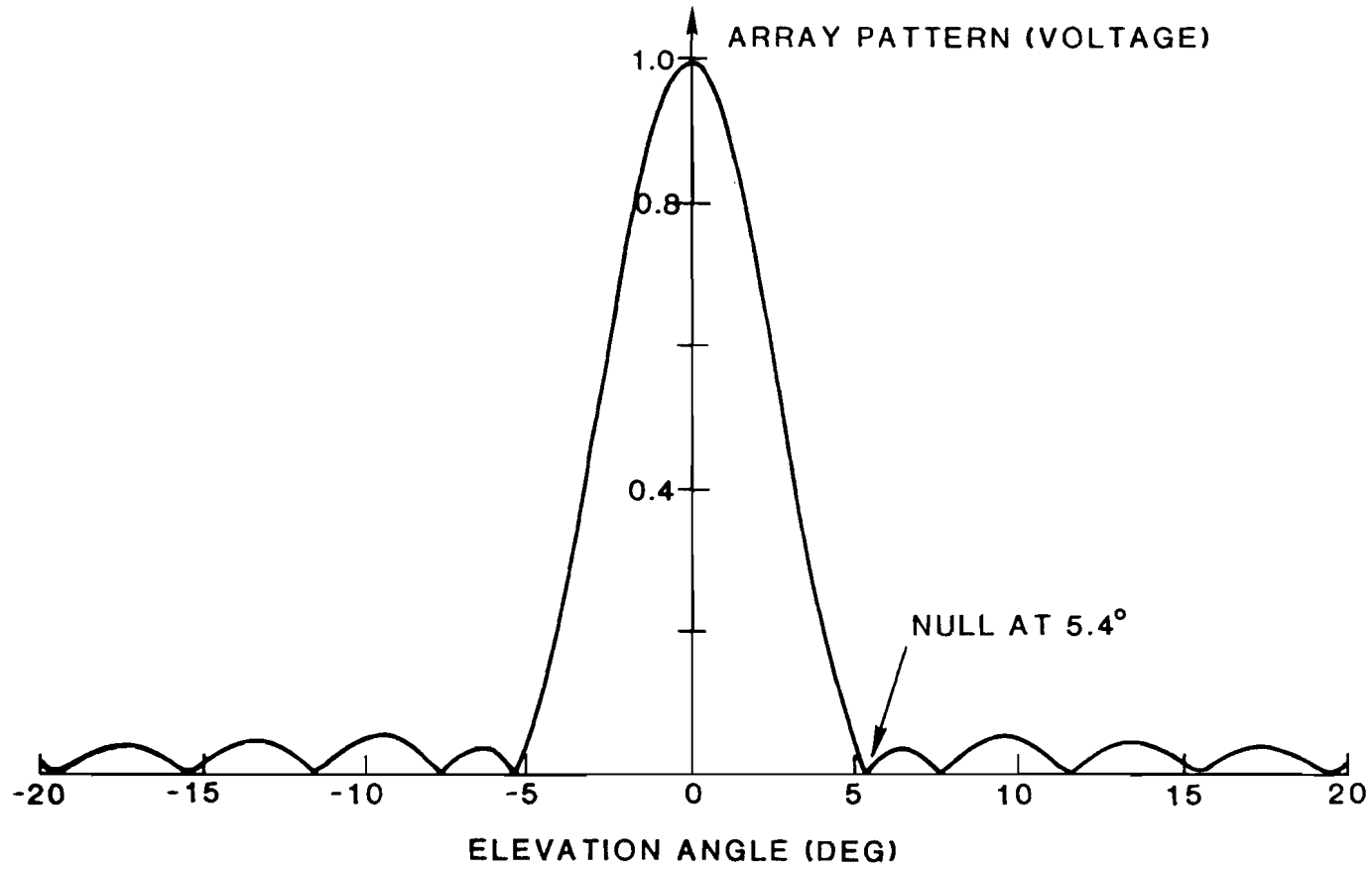
Fig. 5-9   Steered beam array pattern used in DLS elevation array final
stage of interferometric processing.

In addition to the array coefficients which produce the array patterns $E_A(\theta,\phi,\phi_S)$ of Figs. 5-8 and 5-9, there are the measured element amplitude and phase patterns which are assumed identical to the element of the azimuth linear arrays. The overall antenna pattern becomes

$$G_E(\theta_m,\phi_m) = G_A(\theta_m)\ G_E(\phi_m)\ E_A(\theta_m,\phi_m,\phi_S).$$

For the final pass we can consider the weighted sum over element p=1 to 15 as a single antenna port and p=16 to 30 as a second with phase centers at $\underline{d}_k$,

$$d_k = \{0,\ 0,\ (0.88142)\ (\tfrac{15}{2})\ k\} \qquad \text{for} \quad k=1,\ -1 \qquad (5\text{-}27)$$

G.   Multipath On The Data Uplink

Since the coding of angle information is done by pulse position modulation and the adaptive threshold detection is done on the leading edge, then different pulse distortions will be translated into decoding errors. The distortions in the shape of the ground station pulses associated with distance and angle data need not be identical since they are transmitted at time differences ranging from 5 msec to 15 msec. Thus, multipath with scalloping frequencies above 30 Hz are of greatest concern. Such scalloping frequencies are typically associated with reflections from buildings or aircraft when the receiver is nearing the threshold. Three factors tend to mitigate the likelihood of such errors:

(1)   such multipath typically has sizable delays and would thus be reduced by time delay discrimination

(2)   the data link coding factor of 0.056°/μ sec means that the data link angle errors will be small if the DME subsystem design (e.g., waveform, ground antenna, thresholding) is such as to yield the desired accuracy of 0.07 μsec (100 foot rms ranging error), and

(3)   a motion averaging rms improvement of approximately $1/\sqrt{8}$ may arise.

These factors suggest that the data uplink error will be much smaller in most cases than the angle estimation errors on the downlink and has, therefore, been ignored for the purpose of the simulations reported here.

H. The Tracker in the Aircraft Receiver

The estimates received on the aircraft are modified by a tracker and it is the tracker output estimates $\hat{\theta}_{TR}$ which are used as an aid to landing guidance. Its main function is to reject clearly incorrect estimates such as might arise from an ambiguity resolution problem in the ground processing and, for these, substitute the extrapolated value derived from the tracker logic.

There are many parameters which are associated with the tracker algorithm but the central part of the tracker is that section which determines how a new input estimate and previous tracker output estimates are combined to yield a new output estimate. This part is described briefly without detailing the parameter values.

The central part of the proposed tracker is as follows: a difference Δ between the last tracker estimate $\hat{\theta}_{TR}$ and the new raw estimate $\hat{\theta}(\Delta = \hat{\theta}_{TR} - \hat{\theta})$ is formed and compared in magnitude to 0.7031°. If the magnitude of the difference is greater than 0.7031°, it is rejected and the tracker estrapolates a new estimate without the use of this $\hat{\theta}$ and the fact of rejection is noted. If $|\Delta|$ is found to be less than 0.7031°, then a residue term $\Sigma\Delta(\Sigma\Delta = 0$ and $\hat{\theta}_{TR} = \hat{\theta}$ for first estimate) is modified by adding Δ. Next, both a "velocity" term V (V is zero for first estimate) and $\hat{\theta}_{TR}$ are modified by subtracting CH

where
$$CH = \text{Int} \left[\frac{|\Sigma\Delta|}{IDD} \right] \text{sign}(\Sigma\Delta) \ (0.01099°) \tag{5-28}$$

where Int[x] is the integer part of x and IDD is a tracker parameter nominally set to 8. $\Sigma\Delta$ is equal to the modulo IDD addition of the Δ and the final $\Sigma\Delta$ generated from the previous pass through the tracker.

Next the magnitude of V is limited to 2.8125° and V is added to a velocity residue term $\Sigma V(\Sigma V$ is zero for the initial estimate). In a fashion similar to the above

$$CHV = \text{INT} \left[\frac{|\Sigma V|}{IDV} \right] \text{sign}(\Sigma V) \ (0.01099°) \tag{5-29}$$

$$\hat{\theta}_{TR} = \hat{\theta}_{TR} + CHV \tag{5-30}$$

$$\Sigma V = \Sigma V - IDV + CHV \tag{5-31}$$

(nominal value of tracker parameter IDV = 3) where the resulting value of ΣV is the modulo IDV sum of V and the previous ΣV.

If the percentage of rejections becomes too great the tracker goes out of track by reinitializing and starting a new track record.

The actual Fortran program for the DLS airborne tracker logic was provided by the FRG and incorporated directly into the simulation model without any changes.

VI. DLS MODEL VALIDATION

The validation for the DLS system model proceeded somewhat differently from that for TRSB or DMLS in that the system concept did not lend itself to hybrid bench simulation and no "standard" AWOP multipath field test results were reported by the FRG. On the other hand, the problem of justifying a DLS computer model is much easier since virtually all of the proposed DLS signal processing is to be carried out in a digital computer.

A. Analytical Verification

In those cases where the proposed DLS antenna processing coincides with well studied angle determination schemes (e.g., two element interferometers), validation consisted primarily of showing that the model response to multipath coincided with the previously known results [88, 89]:

$$\epsilon \approx \left(2\pi \frac{D}{\lambda} \cos \theta_D\right)^{-1} \left[\tan^{-1}\left(\frac{\rho \sin \phi_1}{1 + \rho \cos \phi_1}\right) - \tan^{-1}\left(\frac{\rho \sin \phi_2}{1 + \rho \cos \phi_2}\right)\right] \qquad (6\text{-}1)$$

where $\frac{D}{\lambda}$ = pair separation in wavelengths

θ_D = direct signal (conical) angle

ρ = M/D ratio taking into account the antenna patterns of the individual interferometer elements

$$\phi_1 = \phi + (\pi D/\lambda)(\sin \theta_m - \sin \theta_D) \qquad (6\text{-}2)$$

$$\phi_2 = \phi - (\pi D/\lambda)(\sin \theta_m - \sin \theta_D) \qquad (6\text{-}3)$$

ϕ = multipath phase relative to direct signal phase at interferometer midpoint

θ_m = multipath signal (conical) angle

It follows from Eq. (6-1) that the multipath error

(1) will be zero whenever the multipath angle coincides with a null in the element antenna pattern

and

(2) for small separation angles $(\theta_{sep} = \theta_m - \theta_D)$ and ρ,

$$\varepsilon \approx (2\pi \frac{D}{\lambda} \cos \theta_D)^{-1} (\rho \sin\phi_1 - \rho \sin\phi_2)$$

$$= (2\pi \frac{\sim}{\lambda} \cos\theta_D)^{-1} 2\rho\cos\phi \sin[\frac{\pi D}{\lambda} (\sin\theta_m - \sin\theta_D)]$$

$$\approx (2\pi \frac{D}{\lambda} \cos\theta_D)^{-1} 2\rho\sin[\pi(D\theta_{sep}/\lambda) \cos\theta_D] \qquad (6\text{-}4)$$

$$\approx \rho\theta_{sep} \cos\phi \qquad (6\text{-}5)$$

Equation (6-4) shows the linear dependence on separation angle, ρ and $\cos\phi$ which was encountered previously in both the TRSB and DMLS models.

Figure (6-1) shows the results of simulating the DLS elevation error using the steered beam pattern of Fig. 5-9. We see that the error nulls are at the proper angles and that the error at small separation angles has the linear dependence on θ_{sep} indicated by Eq. (6-4). These (and similar) results verified that the system model equations were programmed properly (including the antenna patterns).

B.   Validation of Ground Processor Model

Validation of the model for the ground processor phase error model was provided by the experiment[*] whose block diagram is shown in Fig. 6-2. With that set up it is possible to synthesize the signal which would result from 1 to 3 wavefronts arriving simultaneously at a pair of antennas being used as the sensors for an interferometric measurement. It is then possible to compare the measured result with that of the model. Such a comparison is illustrated in Fig. 6-3 for a two wavefront case. The directions for the wavefronts relative to boresight are 0 and 5 degrees. Designating the 0 degree wavefront as the signal and the 5 degree wavefront as the multipath signal we see six values of direct to multipath ratio (M/D) plotted. The phase difference generated at the antenna channels correspond to an antenna separation $d/\lambda = 2$. The solid lines are the results of the model while the

---

[*] The experimental signal generation and phase measurement electronics were built at Lincoln Laboratory in connection with a Dept. of Defense program; however, the phase measurement circuits for DLS should show a multipath response which is identical to that of the Lincoln circuits.

ϕ(rf PHASE OF MULTIPATH RELATIVE TO THE DIRECT) = 0°   M/D RATIO = -6 dB
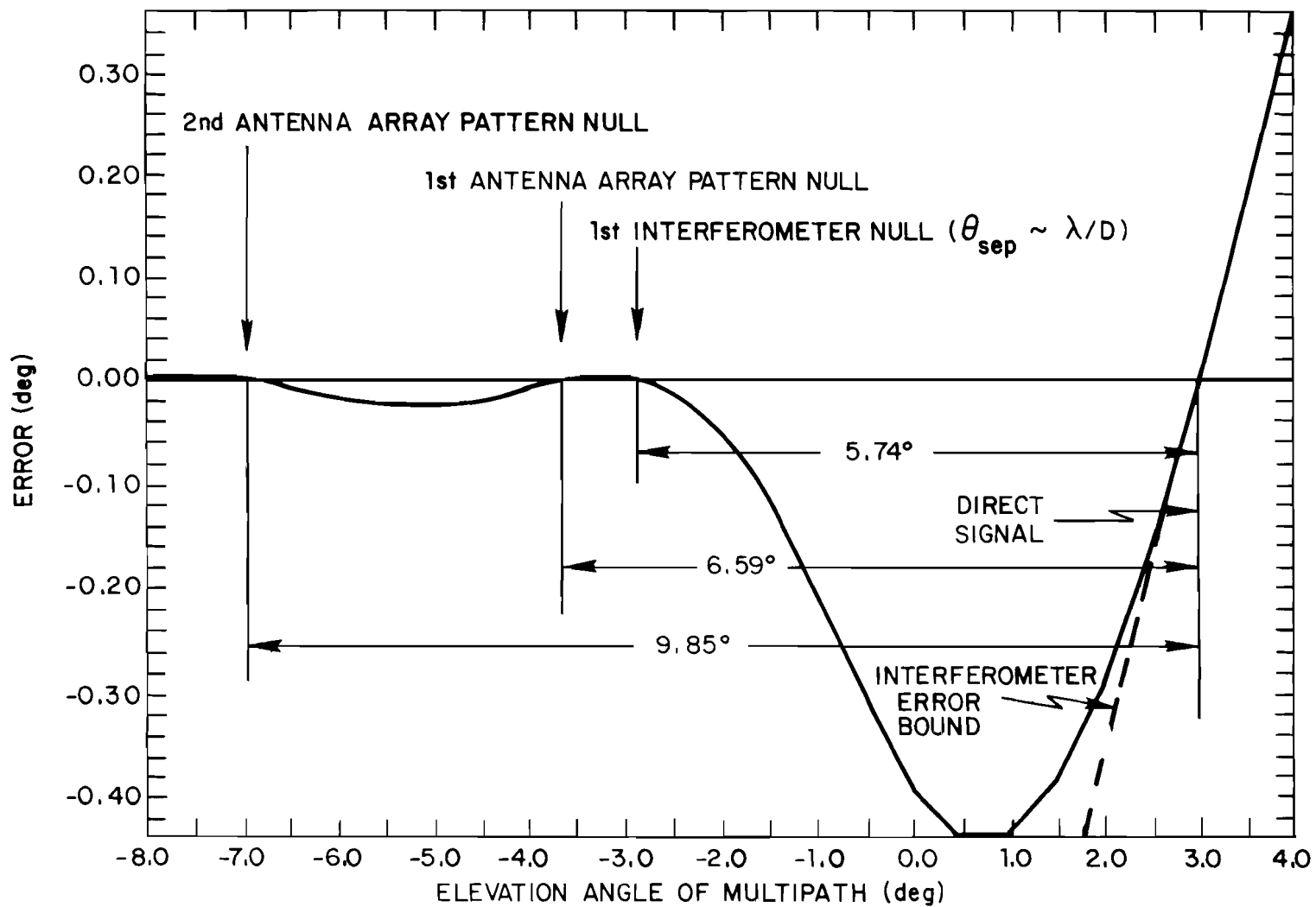
Fig. 6-1   DLS elevation array angle error.
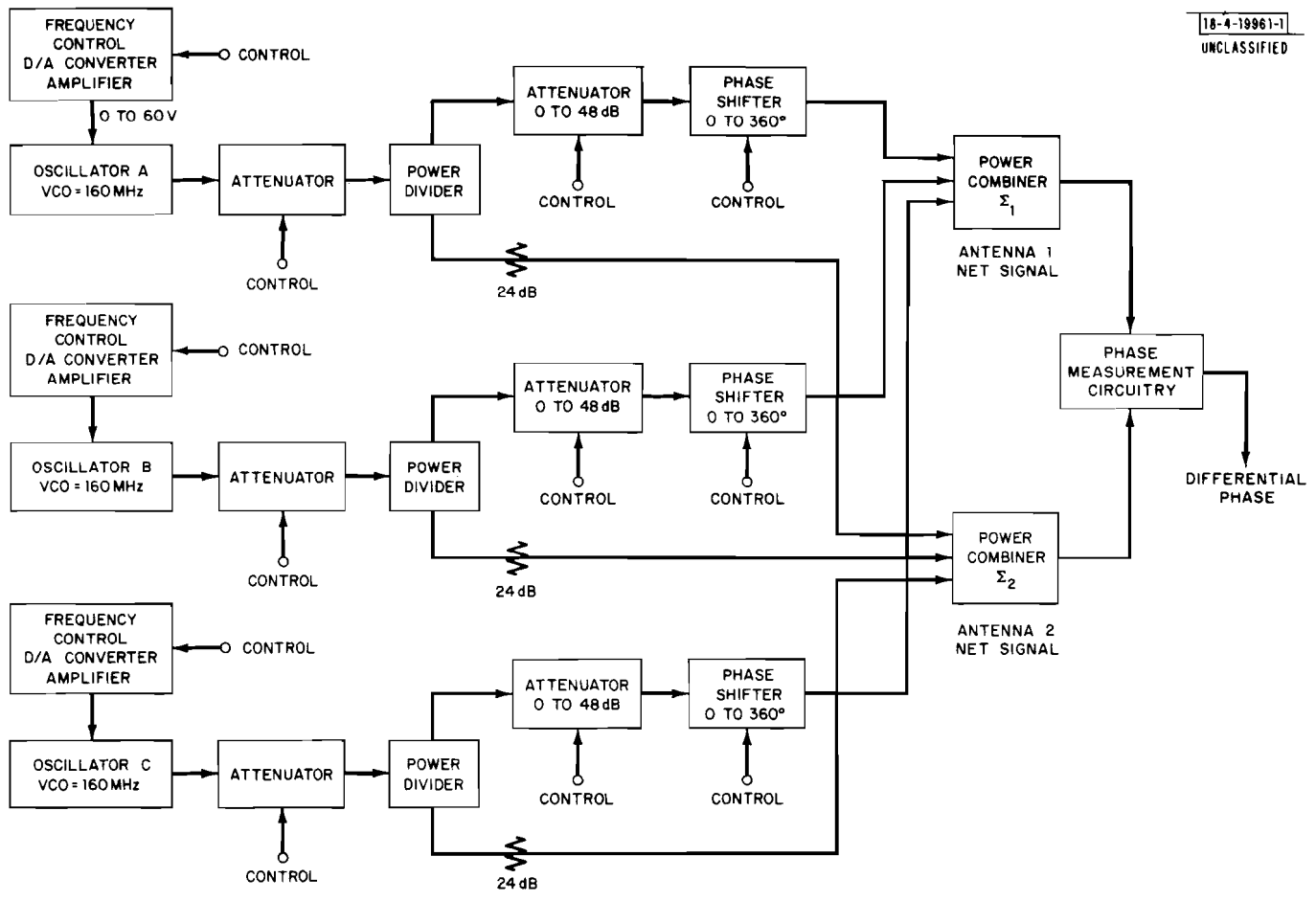
Fig. 6-2 Functional block diagram of interferometric
bench test of signal generating equipment.
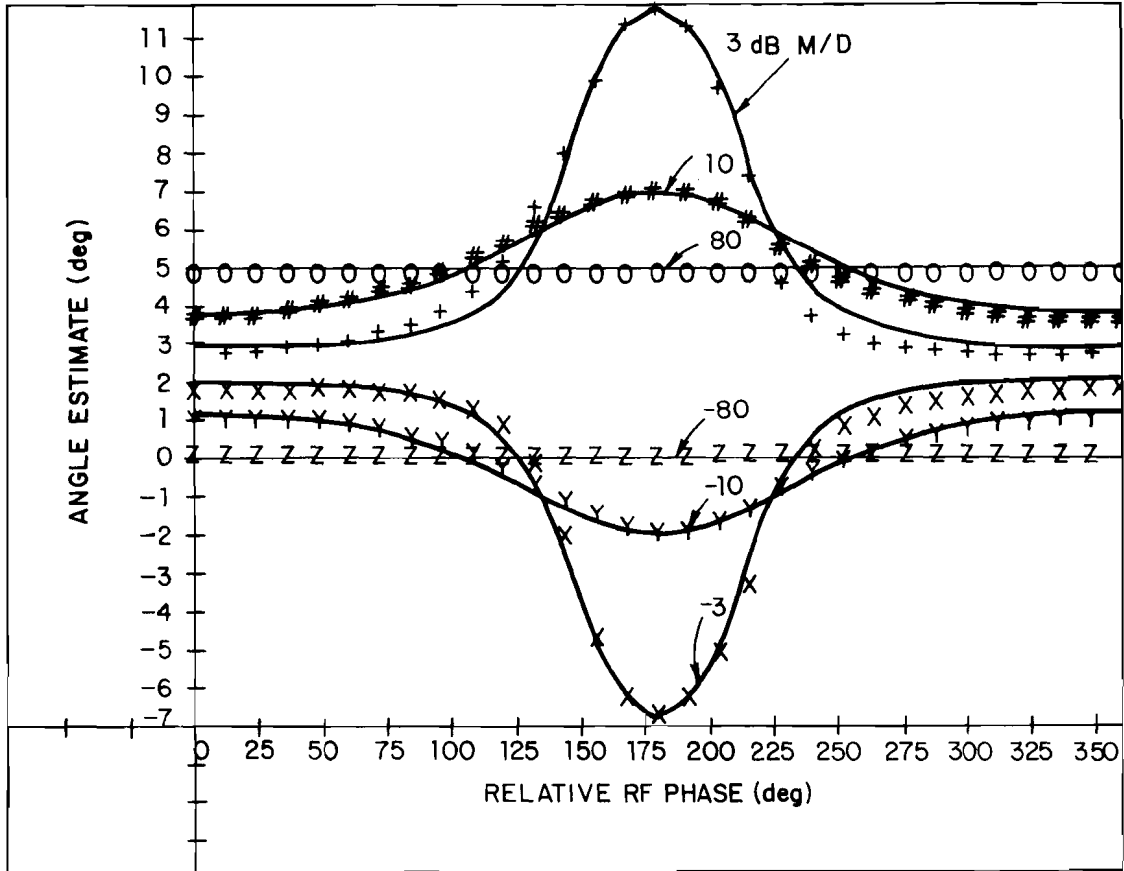
Fig. 6-3 Comparison of measured angles to model generated angles.

characters are the actual measured angles which result as the relative rf phase between the two wavefronts at the reference point varies from 0 to 360 degrees. The agreement is considered excellent, and provides a strong validation for the processor phase error models.

C.   End-to-End Validation

To provide validation of the received signal model for the DLS antenna and the DLS circular azimuth array processing, field measurement were conducted by the FRG using simultaneous DME transmissions from two antennas (at different azimuths) to emulate a direct signal and a multipath signal [108]. A digital phase shifter in one path permitted varying the phase of the smaller signal over the full range of possible values. Figure 6-4 compares the FRG field data with the computer model results. The excellent agreement provides strong confirmation for the validity of the received signal model and circular azimuth array model.

D.   Tolerancing of DLS Simulation Model

As noted at the outset, DLS model validation by comparison with measurements on actual hardware was not possible for many of the angle guidance subsystems due to the lack of actual hardware (e.g., lateral diversity elevation array[*]) and/or controlled field data. However, the experiments using a Lincoln Laboratory phase measurement receiver and bench simulator have demonstrated that it is possible to build a receiver whose multipath response is essentially identical to that of the simulation model. Confirmation of the applicability of the phase measurement error model to the FRG DLS hardware is indicated by the good agreement with the FRG field measurements.

There are a few features of the DLS model which would merit field measurement confirmation, especially:

(1)   the impact of element coupling on the lateral diversity
        elevation array algorithms

---

[*]An interferometric linear elevation array constructed at Lincoln (under FAA sponsorship) showed ground reflection errors which were quite similar to those predicted by simulation [39].
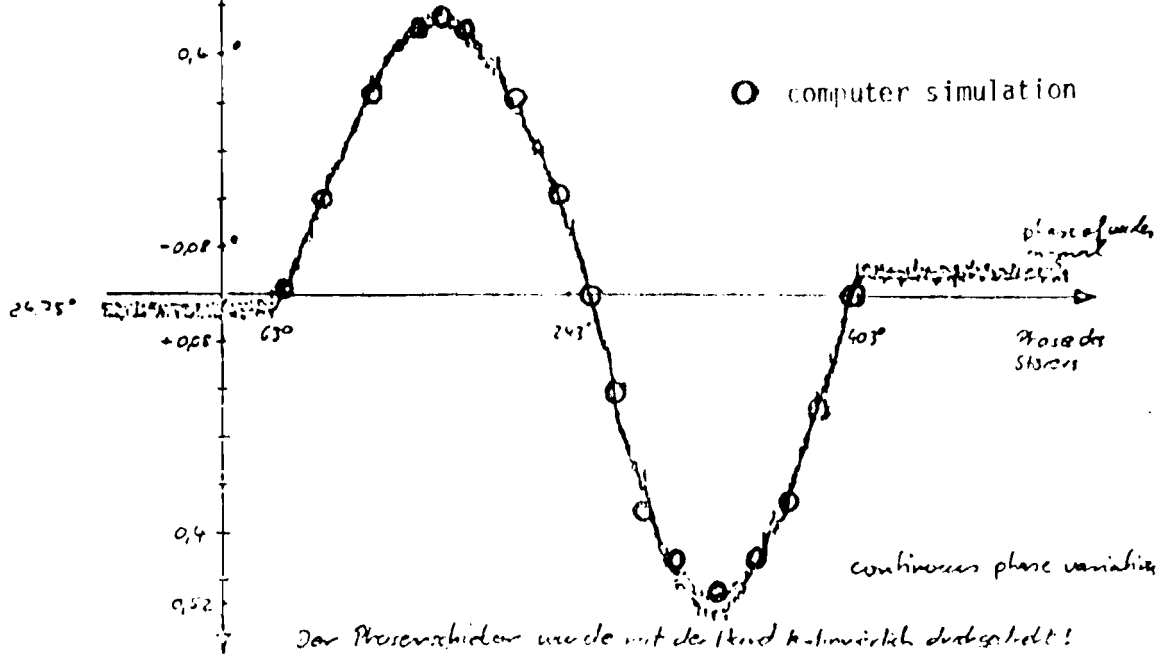
Fig. 6-4 Comparison of DLS model with FRG field measurements.

(2) low signal-to-noise effects when the receiver is at very low
altitudes (e.g., flare) and/or in high multipath level
(e.g., 0 dB) environments

and (3) the effects of near field terrain inhomogenities on the
azimuth array near the centerline region

Nevertheless, given the good agreement with the (limited) available measurement
data, the overall DLS simulation is considered to generally have a tolerance
of ±0.5 dB which is similar to that of the C band systems.

APPENDIX A

COMPUTATION OF OUT-OF-BEAM ENVELOPE PEAKS

In Chapter I, we described an out-of-beam multipath test which is used to increment/decrement the TRSB confidence counter. The details of the algorithm by which the peak locations and values are found are given here, along with the results of some experiments which establish the accuracy of the approximations involved.

The algorithm for finding out-of-beam envelope peaks is as follows:

(i) The envelope is evaluated at the time corresponding to each component coding angle. The envelope value so computed is stored and taken to represent the local envelope maximum.

(ii) The largest envelope value computed is taken to be the scan maximum.

The approximation procedure was checked out numerically by evaluating the function

$$F(\theta) = \left| e^{-k\theta^2} + \rho e^{j\phi} e^{-k(\theta-\theta_m)^2} \right| \quad : \quad k = 2 \ln 2 \qquad \text{(A-1)}$$

representing coherent superposition of two Gaussian beams separated by θ_m BW, at $\theta=0°$, $\theta=\theta_m$, and at the angle of the true peak (found by search). The results were plotted as a function of θ_m up to 2 BW for various multipath levels (-3, -6, -10 dB) and phases (0°, 90°, 180°). Figure A-1 is an example of the results. In this case we have $\rho = -3$ dB, $\phi = 0°$; the largest discrepancy between the peak value and F(0) is 0.6 dB, which occurs at $\theta_m = 0.68$ BW. The worst discrepancy overall occurs for destructive interference, i.e., $\theta = 180°$, in which case as much as 1.7 dB difference occurs at 0.45 BW. However, in such cases the total amplitude is decreased and the combination is less apt to be an overall peak. Fortunately, the approximation is at its best where it is needed, i.e., constructive interference. For the smaller values of ρ, the accuracy is much improved.
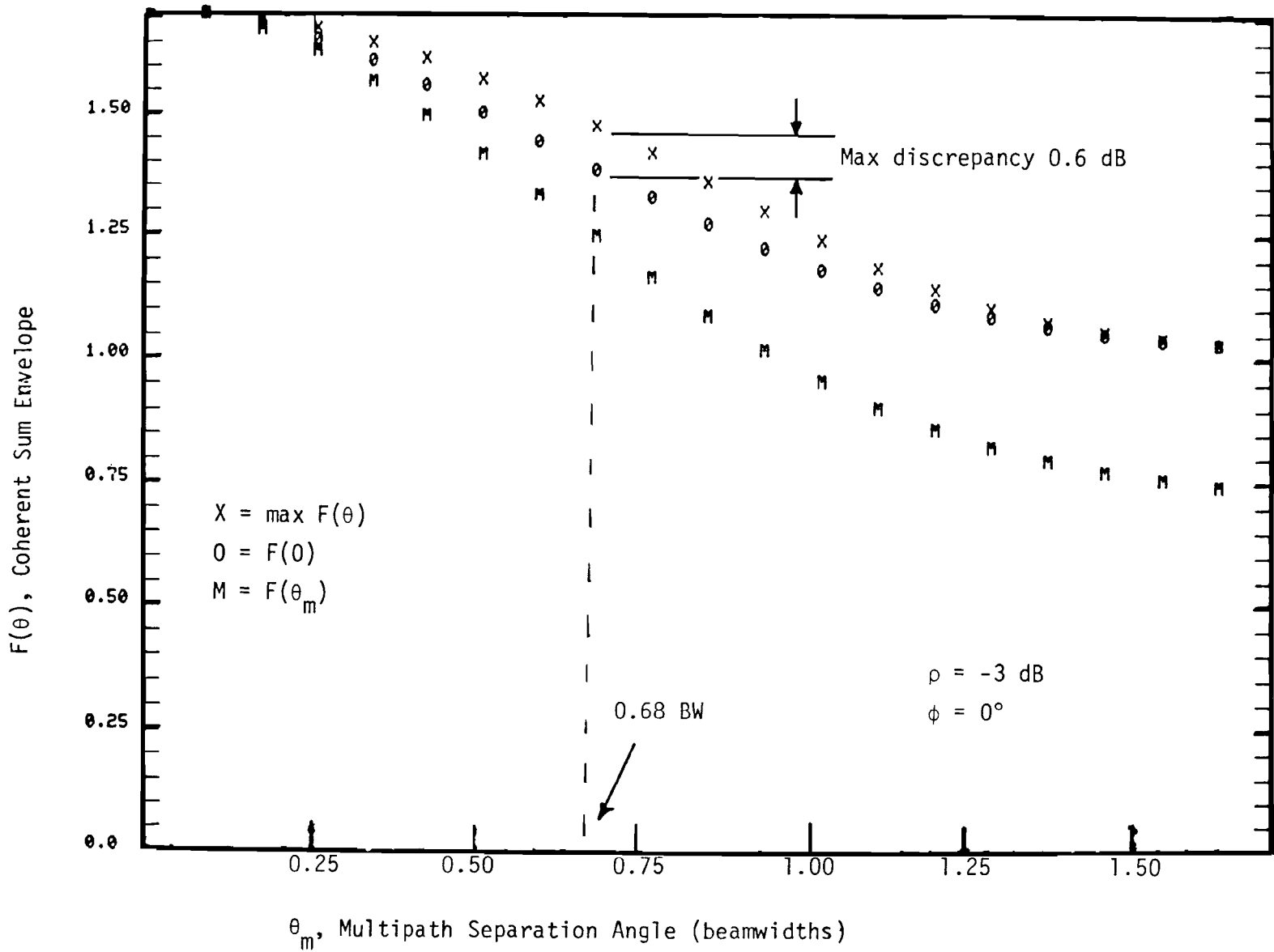
Fig. A-1 Comparison of coherently summed Gaussian envelope values at the peak, direct, and multipath locations.

APPENDIX B

DETAILS OF DWELL GATE DETERMINATION IN TRSB SIMULATION

Within the tracking gate, 25 envelope samples are taken over a coarse grid (0.08 dwell gate width apart). These are used to initiate the search for the peak and the threshold crossings. The first step is that the samples are searched and the largest is found. A fine grid is set up between the peak sample and the two adjacent ones (unless the peak lies at one end of the tracking gate) and envelope samples are taken over the grid. The largest one of those is the in-beam peak.

The threshold level is set some number of dB below the peak. For the Phase III TRSB, the value is 3 dB. A search for threshold crossings is initiated at the leading edge of the tracking gate. Adjacent values of the original coarse grid samples are inspected until a pair which straddle the threshold is found. If the crossing is negative-going it is ignored, but if it is positive-going, then it is remembered as a potential leading edge crossing. When a subsequent negative-going crossing is found, the pair are subjected to the pulse width test.

Let t_1, t_1', t_2, and t_2' be the times at which the four straddling samples occur (see Fig. B-1), and let
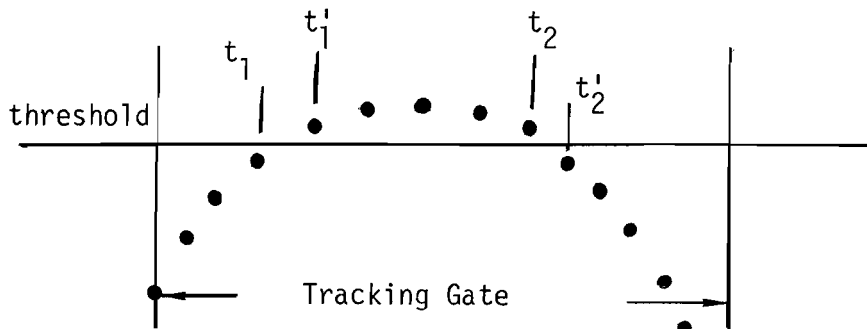
Fig. B-1 Coarse grid points straddling the threshold.

T_{min} and T_{max} be the lower and upper limits, respectively, on dwell gate width. The gate is rejected if either (i) or (ii) below fails:

(i) $t_2 - t_1' > T_{max}$ (B-1)

(ii) $t_2' - t_1 < T_{min}$ (B-2)

since the two left-hand side expressions are an underbound and an overbound respectively, on the dwell gate width.

If the gate succeeds on (i) and (ii), it is accepted as a valid gate.

APPENDIX C

DETERMINATION OF TRSB SCAN TIMING USING JITTERED SIGNAL FORMAT

To determine the scan delay on a particular scan, first an array of the cumulative scan delays is set up over at least two complete jitter sequences. A pointer to this array is initialized to zero, and is incremented each time the receiver routine is invoked. The number of scans required for one cycle of the jitter sequence is also entered. The delay for a particular scan is determined by subtracting the accumulated scan delay at the beginning of the frame from the accumulated scan delay time on the particular scan, which is pointed to by the incremented pointer. Thus, at the beginning of each frame, there is no offset in delay, that is, the first scan of each frame begins at the frame initiation time. At the end of a data frame, the pointer is reset to point to the corresponding location within the first of the two full jitter sequences. This permits the pointer location to increment linearly during the subsequent frame, rather than having to go "around the corner" when it hits a boundary.

APPENDIX D

RATIONALE FOR AND IMPLEMENTATION OF TRSB ANGLE RATE OF CHANGE CORRECTION

The TRSB phase III receiver uses a predictive second order (α,β) filter to combine angle measurements for SNR and motion averaging enhancements. The angle estimate output by the receiver for a given scan is the predicted value for that scan (i.e., the "raw" angle measurement for the current scan does not affect the filtered angle output for this scan). The structure of the MLS multipath simulation is such that if multipath is computed every 0.2 seconds along the flight path, the computed direct signal angle appears to make staircase changes every 0.2 seconds rather than the smooth sequence of changes that occur in the real world (see Fig. D-1)

Consequently, if no correction factor is applied, two problems will arise:

(1) the predictive filter will have unwarranted difficulties in estimating the aircraft angle velocity

(2) the predictive filter could not hope to yield zero error at the times where the direct signal angle has been changed.

The second effect was observed in early TRSB simulations.

Two approaches to reducing this simulation artifact were considered:

(1) modify the multipath and receiver programs to compute multipath at the scan times

(2) yield a "smoother" sequence of angle inputs to the predictive filter and take account of the smoothing in determining the errors.

The first approach would have substantially increased the computation times (e.g., 3-8 fold for the multipath), necessitated substantial program revisions and created a situation where the TRSB multipath was being computed on a space grid different from that for DLS and DMLS. Thus, it was decided to utilize alternative (2).

The idea in alternative (2) was to assume that the errors were a very weak position of direct signal angle over the time period of concern, so that the
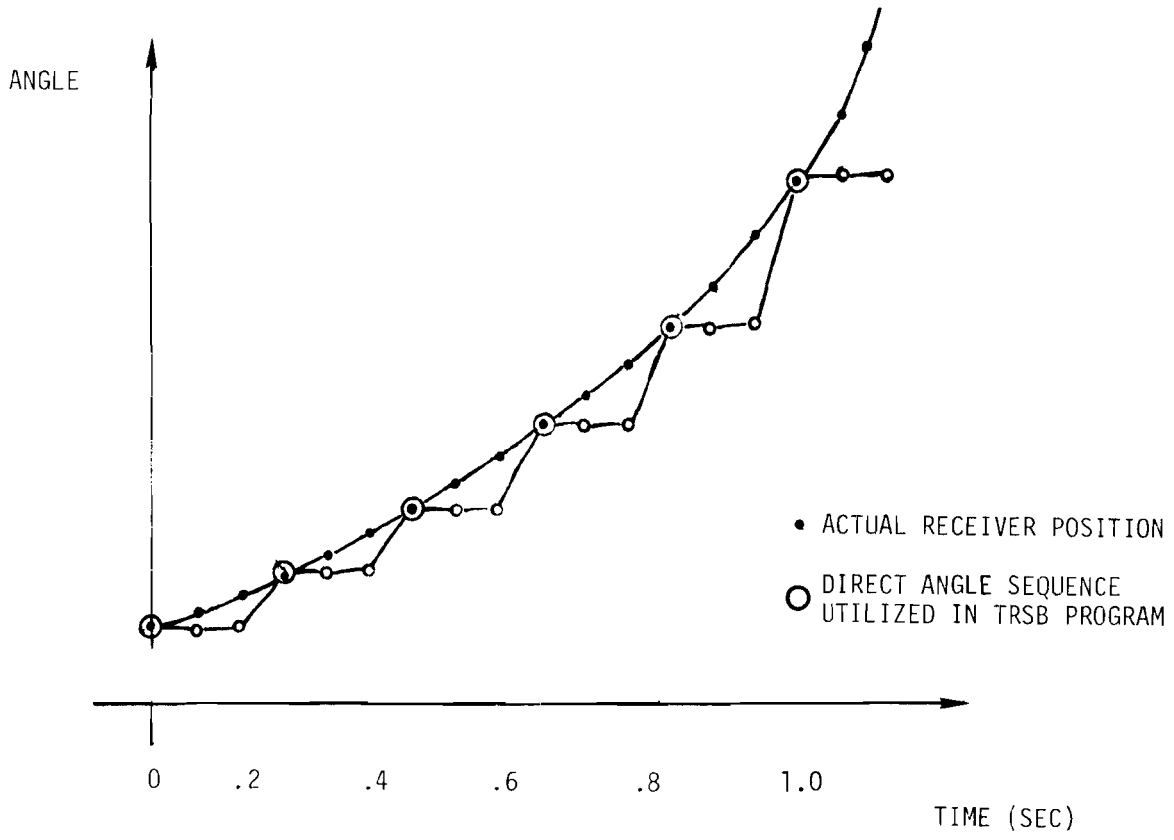
Fig. D-1 Comparison of actual and assumed direct signal angles in TRSB azimuth simulation.

angle estimate input to the predictive filter could be written as:

Angle estimate = "smoothed" direct signal angle +
angle error at the multipath point

To give some perspective on the magnitude of the direct signal angle change over 0.2 seconds, the angle rate of change in the AWOP WG-A scenario 5 which involved a Canarisie type curved approach was 0.6°/second, which corresponds to a variation of $\pm$ .06° about the midframe angle. For the elevation scenarios, the angle rate of change was very low in the inbeam multipath regions (e.g., < 0.05°/sec, corresponding to variations of $\pm$ .005° about the nominal point).

The receiver program has no knowledge of the future direct signal angle values as these may not yet have been read from the tape. Thus, it seemed most appropriate to regard the current direct signal angle as the angle the receiver will be at by the <u>end</u> of the current 0.2 second frame. Moreover, it was found that some STOL scenarios can yield substantial angular accelerations once over threshold. Thus, it was felt advisable to use a second order polynominal fit to the raw angle values.

The specific algorithm fits a second order polynominal to the current direct signal angle and the two preceding direct signal angles for that function, such that the "smoothed" angle on the last scan is equal to the current direct signal angle. If we define the current direct signal angle as $\theta_d(n)$, we can then write the "smoothed" angle as

$$\theta(k) = \theta_d(n-1) + \frac{k}{N} \dot{\theta}_d + \frac{1}{2} \left(\frac{k}{N}\right)^2 \ddot{\theta}_d \qquad \text{(D-1)}$$

where

$$\dot{\theta}_d = \left[\frac{1}{2} \Delta\theta(n) + \Delta\theta(n-1)\right] \qquad \text{(D-2)}$$

$$\ddot{\theta}_d = \Delta\theta(n) - \Delta\theta(n-1) \qquad \text{(D-3)}$$

$$\Delta\theta(n) = \theta_d(n) - \theta_d(n-1) \qquad \text{(D-4)}$$

N = number of scans in 0.2 seconds

k = scan index (= 1, 2, ... N)

$\frac{k}{N}$ = normalized time variable

n = frame index

There is an unfortunate interaction between the angle correction and the TRSB angle estimation by virture of the dwell gate being centered on the angle estimate. Consequently, when the angle correction is used, the dwell gates will be misaligned by the correction amount. Since the correction should always be less than 0.2°, this misalignment should not effect the results (by generating dwell gate check) unless very large errors were occuring.

APPENDIX E

DERIVATION OF SECOND-ORDER TRSB ERROR FORMULA

1. Problem Formulation

A second-order approximation is derived for the TRSB static error in the presence of a single small-amplitude multipath component. Relative to the direct component, the amplitude ratio, angular separation, and phase difference of the multipath components are denoted by ρ, θ, and ϕ, respectively. Since only inbeam effects are of interest here, the assumed antenna pattern is Gaussian,

$$A(x) = 2^{-2x^2} = e^{-kx^2} \qquad k \equiv 2 \ln 2 \qquad \text{(E-1)}$$

where x is angle in BW's. With multipath present, the squared envelope as a function of scan angle is

$$|A(x) + \rho A(x-\theta)e^{j\phi}|^2 = A^2(x)[1 + 2\eta \cos \phi \, e^{2kx\theta} + \eta^2 e^{4kx\theta}] \quad \text{(E-2)}$$

where

$$\eta \equiv \rho \, e^{-k\theta^2} \qquad \text{(E-3)}$$

because the Gaussian pattern factors as follows:

$$\frac{A(x-\theta)}{A(x)} = e^{-k\theta^2} \, e^{2kx\theta} \qquad \text{(E-4)}$$

Define

$$f(x) \equiv \ln |A(x) + \rho A(x-\theta) \, e^{j\phi}|^2$$

$$= -2kx^2 + \ln [1 + 2\eta \cos \phi \, e^{2kx\theta} + \eta^2 \, e^{4kx\theta}] \qquad \text{(E-5)}$$

The objective is to find the leading and trailing edge threshold crossings x_-, x_+. The squared threshold level is assumed to be $e^{-2kv^2} e^{f(x_0)}$, where x_0 is the location of the envelope peak,

$$f(x_0) \geq f(x) \text{ for all } x \qquad \text{(E-6)}$$

and $\pm v$ are the nominal threshold crossing locations (in the absence of multi-path). Therefore, the threshold crossings x_+ in the presence of multipath are solutions of

$$f(x_0) - f(x_+) = 2kv^2 \qquad (E\text{-}7)$$

Approximate solutions to (E-7) are evaluated by using an expansion of $f(\cdot)$ in powers of η and ignoring terms of higher order than η^2. This procedure leads to the results presented in the following section (E.2). The detailed derivations are found in the final section (E.3).

2.   Summary of Results

The threshold crossing locations are expanded as

$$x_+ = \pm v \pm \varepsilon_+ \pm \delta_+ + 0(\eta^3)^* \qquad (E\text{-}8)$$

where $\varepsilon_+ = 0(\eta)$ and $\delta_+ = 0(\eta^2)$. The first-order error ε_+ is already known[†]

$$4kv\varepsilon_+ = 2\eta\,(e^{\pm 2kv\theta} - 1)\cos\phi \qquad (E\text{-}9)$$

The second-order correction δ_+ is found to be

$$4kv\varepsilon_+ = \pm\frac{2\eta^2}{v}\cos^2\phi\;\theta(e^{\pm 2kv\theta} - 1)e^{\pm 2kv\theta} - \frac{\eta^2}{2kv^2}(e^{\pm 2kv\theta} - 1)^2\cos^2\phi$$

$$- \eta^2(e^{\pm 4kv\theta} - 1)\cos 2\phi - 2k\,\eta^2\theta^2\cos^2\phi \qquad (E\text{-}10)$$

The error made by a dwell gate processor is the average of the leading and trailing edge errors, i.e.,

$$e(\rho,\theta,\phi) \triangleq \frac{1}{2}(x_+ + x_-) = \frac{1}{2}(\varepsilon_+ - \varepsilon_-) + \frac{1}{2}(\delta_+ - \delta_-) + 0(\eta^3) \qquad (E\text{-}11)$$

---

[*]The symbol $0(\cdot)$ is used to denote a function for which $\lim 0(\alpha)/\alpha$ is finite.

[†]See [28]. The result in (E-9) corresponds to a minor modification of the threshold criterion assumed there.

which leads to the approximation

$$e(\rho,\theta,\phi) \cong \rho\theta\,e^{-k\theta^2}\left(\frac{\sinh 2kv\theta}{2kv\theta}\right)\cos\phi - \rho^2\,\theta e^{-2k\theta^2}\left(\frac{\sinh 4kv\theta}{4kv\theta}\right)\cos 2\phi$$

$$+ k\,\rho^2\theta^3 e^{-2k\theta^2}\left(\frac{\sinh kv\theta}{kv\theta}\right)^2\left(2\cosh 2kv\theta + 1 - \frac{\sinh 2kv\theta}{2kv\theta}\right)\cos^2\phi$$

$$(E-12)$$

A number of results of interest follow directly from Eq. (E.12); the following results are summarized below: (i) mean, (ii), rms, (iii) peak excursions $e(0°)$ and $e(180°)$, [*](iv) peak-to-peak, (v) slew rate equilibrium error $e(90°)$, and (vi) phase angle at which error crosses a specific level. For the statistical results a uniform phase distribution is assumed.

(i) Mean Error

$$\bar{e} = \frac{1}{2}\,k\rho^2\theta^3 e^{-2k\theta^2}\left(\frac{\sinh kv\theta}{kv\theta}\right)^2\left(2\cosh 2kv\theta + 1 - \frac{\sinh 2kv\theta}{2kv\theta}\right) \quad (E-13)$$

(ii) Standard Deviation

$$\sigma_e = \frac{1}{\sqrt{2}}\,\rho|\theta|e^{-k\theta^2}\left(\frac{\sinh 2kv\theta}{2kv\theta}\right) \quad (E-14)$$

(iii) Peak Excursions

$$e(0°) = \rho\,\theta\,e^{-k\theta^2}\left(\frac{\sinh 2kv\theta}{2kv\theta}\right) - \rho^2\,\theta e^{-2k\theta^2}\left(\frac{\sinh 4kv\theta}{4kv\theta}\right) \quad (E-15)$$

$$+ k\rho^2\theta^3 e^{-2k\theta^2}\left(\frac{\sinh kv\theta}{kv\theta}\right)^2\left(2\cosh 2kv\theta + 1 - \frac{\sinh 2kv\theta}{2kv\theta}\right)$$

$$e(180°) = -\rho\,\theta\,e^{-k\theta^2}\left(\frac{\sinh 2kv\theta}{2kv\theta}\right) - \rho^2\,\theta e^{-2k\theta^2}\left(\frac{\sinh 4kv\theta}{4kv\theta}\right) \quad (E-16)$$

$$+ k\rho^2\theta^3 e^{-2k\theta^2}\left(\frac{\sinh kv\theta}{kv\theta}\right)^2\left(2\cosh 2kv\theta + 1 - \frac{\sinh 2kv\theta}{2kv\theta}\right)$$

---

[*]The peak errors as given by (E-12) do not occur at $\phi = 0°$ and $180°$ for all values of ρ and θ, e.g., $\rho > 0.5$ and small θ, but this is a peculiarity of the second order model; in both the actual and simulated dwell gate processors the extremal errors are at $0°$ and $180°$.

(iv) Peak-to-Peak Error

$$e_{pp} = |e(0°) - e(180°)|$$

$$= 2\rho|\theta| e^{-k\theta^2} \frac{\sinh 2kv\theta}{2kv\theta}. \tag{E-17}$$

(v) Slew Equilibrium Level (e(90°)):

$$e(90°) = \rho^2 \theta e^{-2k\theta^2} \left(\frac{\sinh 4kv\theta}{4kv\theta}\right) \tag{E-18}$$

(vi) Level Crossing Angle

Define ϕ_{E1} and ϕ_{E2} as the solutions of

$$e(\rho,\theta,\phi_E) = E \tag{E-19}$$

Then

$$\phi_{E1} = \frac{\pi}{2} + \sin^{-1} \left[\frac{\rho^2 \theta e^{-2k\theta^2} \frac{\sinh 4kv\theta}{4kv\theta} - E}{\rho\theta e^{-k\theta^2} \left(\frac{\sinh 2kv\theta}{2kv\theta}\right)} \right] \tag{E-20}$$

and

$$\theta_{E2} = 2\pi - \phi_{E1} \tag{E-21}$$

3. Derivations

Derivation of $e(\rho,\theta,\phi)$ is carried out in full, after which the means of obtaining each of the subsidiary results is indicated.

We wish to find $x_\pm$ such that

$$f(0) - f(x_\pm) = 2kv^2 - [f(x_0) - f(0)] \tag{E-22}$$

By expanding the logarithm in Eq. (E-5) in powers of η, we obtain the following $O(\eta^3)$ approximation to $f(0) - f(x_\pm)$:

E-4

$$f(0) - f(x_+) = 2kx_+^2 - 2\eta(e^{2kx_+\theta} - 1)\cos\phi + \eta^2(e^{4kx_+\theta} - 1)\cos 2\phi + O(\eta^3)$$

$$(E\text{-}23)$$

where we have used the identity $\cos 2\phi = 2\cos^2\phi - 1$. Substituting the expansion (E-8) for x_+ into the right side of (E-23) leads to

$$f(0) - f(x_+) = 2k(v^2 + \varepsilon_+^2 + 2v\varepsilon_+ + 2v\delta_+)$$

$$- 2\eta\left[e^{\pm 2kv\theta}(1 \pm 2k\varepsilon_+\theta) - 1\right]\cos\phi$$

$$+ \eta^2(e^{\pm 4kv\theta} - 1)\cos 2\phi + O(\eta^3)$$

$$= 2k(v^2 + \varepsilon_+^2 + 2v\delta_+) \pm 4\eta\theta \, k\varepsilon_+ e^{\pm 2kv\theta}\cos\phi$$

$$+ \eta^2(e^{\pm 4kv\theta} - 1)\cos 2\phi + O(\eta^3) \qquad (E\text{-}24)$$

where the second equality follows from the known expression (E-9) for the first-order error ε_+. Note that all remaining terms in (E-24) are $O(\eta^2)$. By equating the right sides of (E-24) and (E-22) we can solve for the second-order error correction δ_+,

$$4kv\delta_+ = \pm 4\eta\theta \, k\varepsilon_+ \, e^{\pm 2kv\theta}\cos\phi - \eta^2(e^{\pm 4kv\theta} - 1)\cos 2\phi \qquad (E\text{-}25)$$

$$- 2k\varepsilon_+^2 - [f(x_0) - f(0)]$$

By substituting (E-9) for ε_+ and $f(x_0) - f(0) = 2k(\eta\theta\cos\phi)^2 + O(\eta^3)$ (see below) we obtain (E-10).

The expression (E-12) is derived from (E-10) with the help of the identities

$$\cosh 4kv\theta - \cosh 2kv\theta = (2\sinh^2 kv\theta)(2\cosh 2kv\theta + 1)$$

$$\sinh 4kv\theta - 2\sinh 2kv\theta = (4\sinh^2 kv\theta)\sinh 2kv\theta$$

$$(E\text{-}26)$$

The expression $f(x_0) = f(0) + 2k(\eta\theta\cos\phi)^2 + O(\eta^3)$ is obtained as follows. Assuming x_0 is near zero, specifically $x_0 = O(\eta)$,

$$f(x) = -2kx^2 + 2\eta(1 + 2kx\theta)\cos\phi - \eta^2\cos 2\phi + O(\eta^3) \qquad (E\text{-}27)$$

for x near x_0. The quadratic function of x is maximized at

$$x_0 = \eta\theta \cos \phi \qquad (E-28)$$

resulting in

$$f(x_0) = f(0) + 2k (\eta\theta \cos \phi)^2 + 0(\eta^3) \qquad (E-29)$$

Terms proportional to η^2 are not necessary in the evaluation of x_0 because they contribute $0(\eta^3)$ to $f(x_0)$.

(i) Mean

The average error in (E-13) is derived from (E-12) by noting that $\overline{\cos \phi} = \overline{\cos 2\phi} = 0$ and $\overline{\cos^2\phi} = 1/2$ for uniform phase.

(ii) Standard Deviation

The standard deviation calculation follows from the above facts and the additional relations $\overline{\cos^2 2\phi} = 1/2$, $\overline{\cos \phi \cos 2\phi} = 0$.

(iii) Peak Excursions

These results are simply the evaluation of (E-12) at $\phi = 0°$ and 180°, respectively.

(iv) Peak-to-Peak

The difference $|e(0°) - e(180°)|$ is the peak-to-peak error. We note that it is the same as what would be computed from the first order version of $e(\rho,\theta,\phi)$; i.e., the second order correction terms in $e(0°)$ and $e(180°)$ cancel in the difference.

(v) Slew Equilibrium Level

The text contains the argument as to why this level is given by $e(90°)$. The derivation is merely an evaluation of (E-12) at $\phi = 90°$.

(vi) Level Crossing Angle

This result is obtained by approximating the solution of

$$e(\rho,\theta,\phi_E) = E \qquad (E-30)$$

as follows. If the error (E-12) is rewritten replacing $\cos 2\phi$ by $(2\cos^2\phi - 1)$, then (E-30) becomes a quadratic equation in $\cos \phi$, which we write as

$$a \cos^2 \phi_E + b \cos \phi_E + c = E \tag{E-31}$$

we solve this equation under the assumption that the quadratic term is small, more specifically that $4ac/b^2 \ll 1$:*

$$\cos \phi_E = \frac{b}{2a} \left[-1 \pm \sqrt{1 - \frac{4ac}{b^2}} \right]$$

$$\approx - \frac{c-E}{b} ; \quad \frac{4ac}{b^2} \ll 1 \tag{E-32}$$

From (E-12) we have that

$$b \approx \rho \, \theta \, e^{-k\theta^2} \left(\frac{\sinh 2kv\theta}{2kv\theta} \right) \tag{E-33}$$

$$c \approx \rho^2 \, \theta \, e^{-2k\theta^2} \left(\frac{\sinh 4kv\theta}{4kv\theta} \right)$$

As $\rho \to 0$ we know that the solution for $E=0$ approaches $\phi_E = 90°$, thus the general solution is given in terms of the (nominally small) deviation from $90°$;

$$\phi_E = \frac{\pi}{2} + \delta_E \tag{E-34}$$

$$\Rightarrow \cos \phi_E = -\sin \delta_E \tag{E-35}$$

$$\phi_{E1} = \frac{\pi}{2} + \sin^{-1} \frac{\rho^2 \theta e^{-2k\theta^2} \left(\frac{\sinh 4kv\theta}{4kv\theta} \right) - E}{\rho\theta e^{-k\theta^2} \left(\frac{\sinh 2kv\theta}{2kv\theta} \right)} \tag{E-36}$$

The other solution ϕ_{E2} is found by the symmetry of $e(\phi)$ about $\phi = 180°$.

_____

*This approximation ignores a term in $\rho^2(E/e_p)^2$ while retaining one in $\rho^2(E/e_p)$. This will not be accurate for all E (especially values near $\pm e_p$), in which case the exact solution should be used.

The time exceedance characteristics, or probability p_+ of exceeding E, can be found by normalizing (E-27) to π. The quantity P_- is simply $(1 - P_+)$. (These statements assume positive separation angle.)

APPENDIX F

EFFECTS OF SIDELOBE TIME VARIATION ON TRSB EFFECTIVE SIDELOBE LEVELS

An important issue in the modeling of TRSB antenna sidelobes is the temporal variation in the sidelobes as the antenna is electronically scanned. This nature of this time variation is important because

(1) reflected sidelobes cause errors only if they cause an asymmetrical distortion of the received mainlobe shape near the thresholding points.[*]

(2) the received mainlobe signal has its energy concentrated at low frequencies (typically < 21 kHz).

and

(3) the net received envelope is filtered by a low pass filter before any thresholding is applied (see figure F-1).

Consequently, the spatial variation in sidelobes can be as important as the level in determining the net error due to out of beam multipath.

The "worst case" error condition arises when the sidelobe is a sineusoid whose spatial period is approximately $2\lambda/L$ since in that case

(1) peak destructive interference can occur at one threshold crossing when peak constructive interference occurs at the other threshold crossing (see figure F-2).

and

(2) the spatial frequency of the resulting envelope is still within the passband of the envelope filter.

For this particular choice of spatial frequency (which is used in Lincoln antenna models), the "worst case" sidelobe error is approximately

$$\varepsilon = \rho \cdot BW \cdot SL \tag{F-1}$$

---

[*] The discussion here is geared to dwell gate trackers; the effects on split gate trackers will be discussed at the end of this appendix.
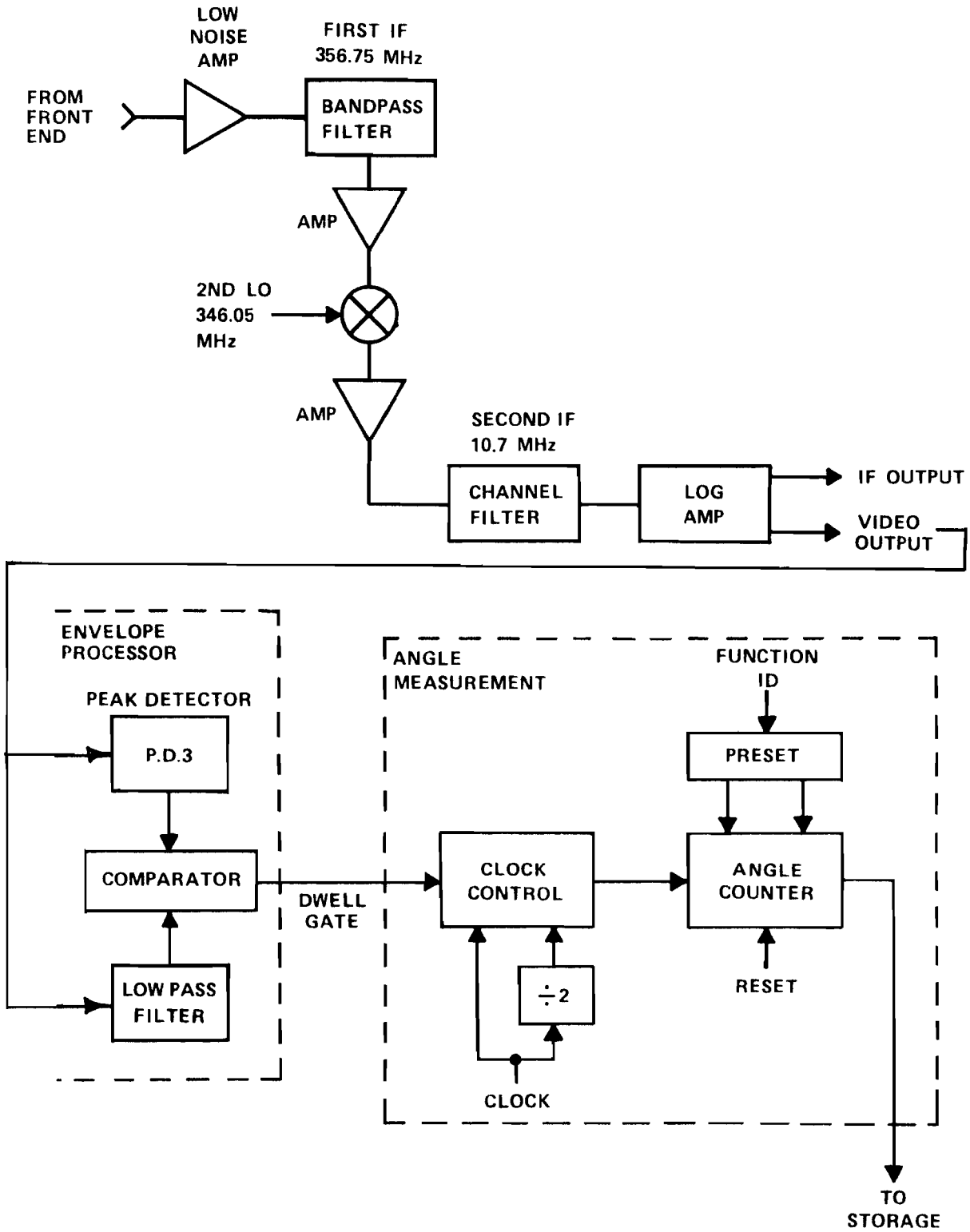
Fig. F-1   TRSB angle measurement circuit.

PATTERN (VOLTAGE)

1.0
0.9
0.8
0.7
0.6
0.5
0.4
0.3
0.2
0.1
0.0
-0.1
-0.2

mainlobe

reflected
sidelobe

-2.00   -1.50   -1.00   -0.50   0.00   0.50   1.00   1.50   2.00
TIME IN BEAMWIDTHS

RAW NET ENVELOPE (DB)

-0.0
-2.5
-5.0
-7.5
-10.0
-12.5

mainlobe

ε

normal
centroid

centroid with
reflected sidelobe

$\varepsilon \approx \rho$ SL

mainlobe +
reflected sidelobe

-0.80   -0.60   -0.40   -0.20   0.00   0.20   0.40   0.60
TIME IN BEAMWIDTHS
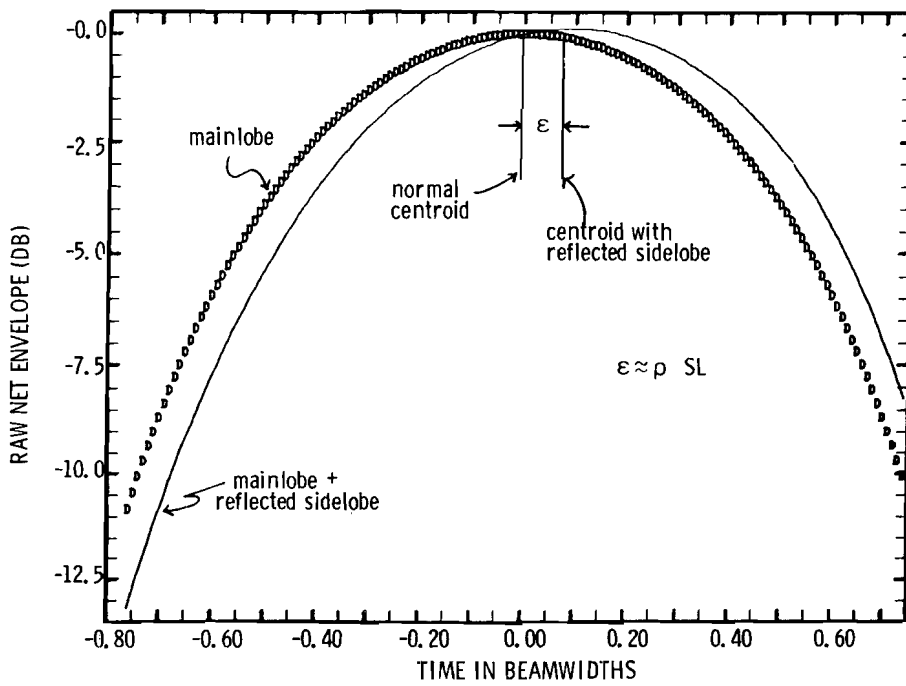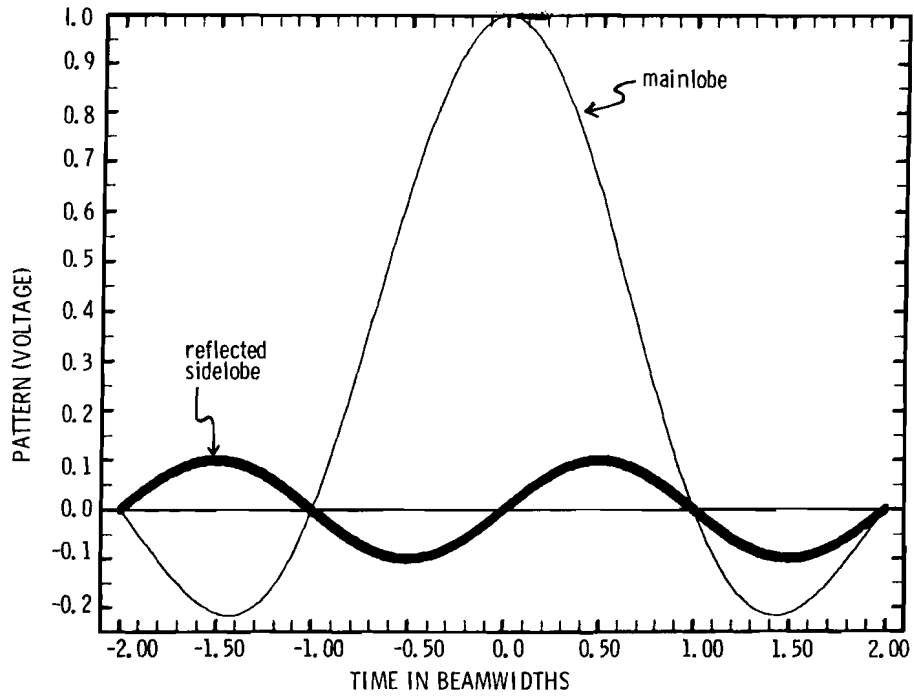
Fig. F-2   TRSB error with "worst case"
sidelobe spatial variation.

F-3

where

BW = antenna beamwidth

ρ = M/D ratio

SL = effective sidelobe level

One situation which could yield the "worst case" spatial frequency is that of high array factor sidelobe antenna such as the "density tapered" array discussed in chapter 1. A nice feature of this case is that the effective sidelobe level SL can be approximately determined from the filtered envelope output of the TRSB receiver as the beam scans by various points.

In many cases, the dynamic sidelobe spatial variation may be such that equation (F-1) is not valid. The simplest such case is one of a constant sidelobe model whereby the antenna pattern is a fixed constant for all angles outside the mainlobe region[*], e.g.,

$$P\ (\theta) = \begin{cases} \sin x / x & |x| \leq \pi \\ K & |x| > \pi \end{cases} \qquad (F-2)$$

where

$$x = \pi \frac{L}{\lambda} \sin \theta$$

This model yields <u>symmetrical</u> displacement of the received envelope at the threshold crossings and hence zero error. It is doubtful that any actual antenna has dynamic sidelobes with this particular character.

However, a much more common situation where equation (F-1) is <u>not</u> valid arises when there is a very rapid spatial variation in the sidelobes such as illustrated in figure F-3. Here, even though the sidelobe as observed by itself at the output of a 26 kHz filter may appear to be worst case (see figure F-4), the filtered <u>sum</u> envelope of the mainlobe and sidelobe is hardly different from the mainlobe envelope along (figure F-5). Figures F-3 and F-4

---

[*] Such a model was utilized in the ELAB studies of MLS multipath for the NATO NIAG group [75].
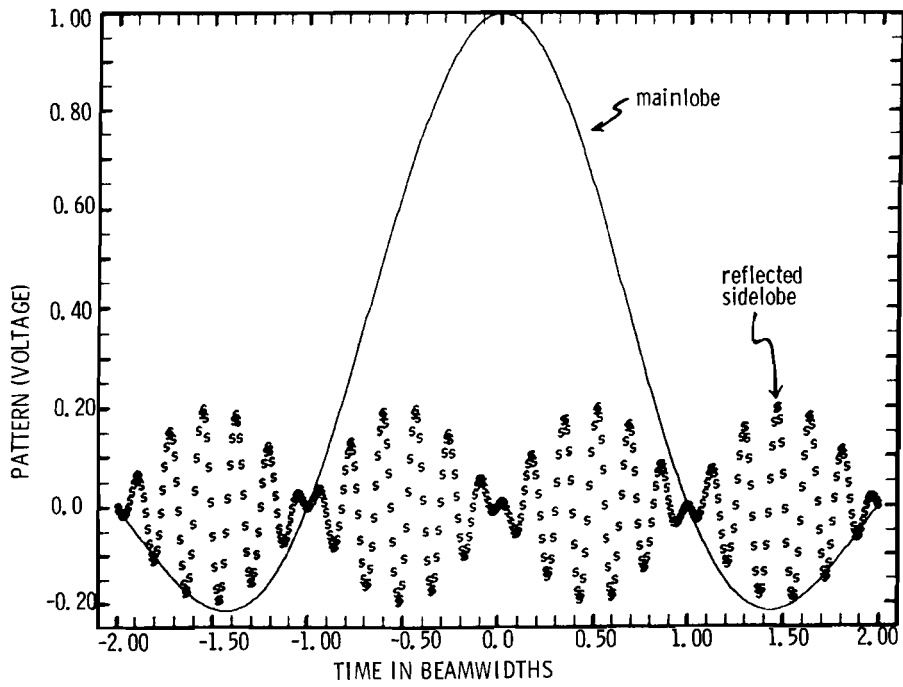
Fig. F-3 TRSB high spatial frequency
dynamic sidelobe.
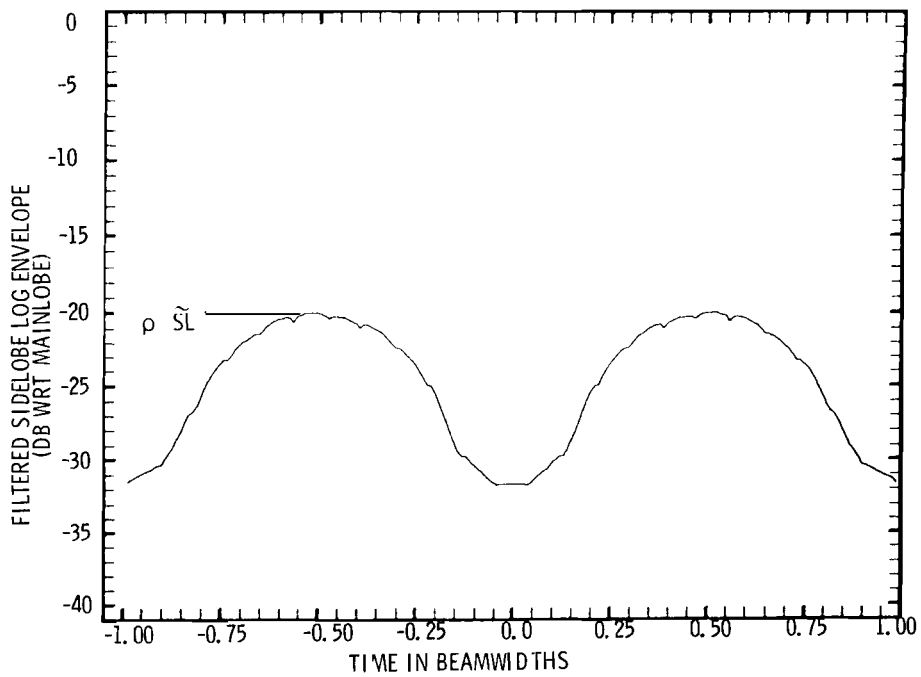
Fig. F-4 Filtered log envelope of high spatial
frequency dynamic sidelobe.
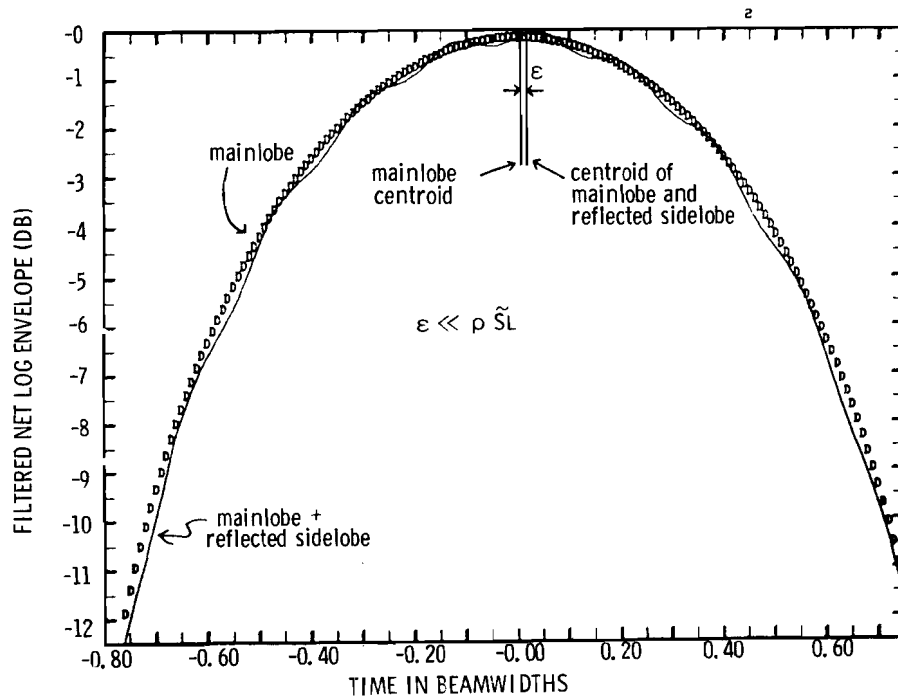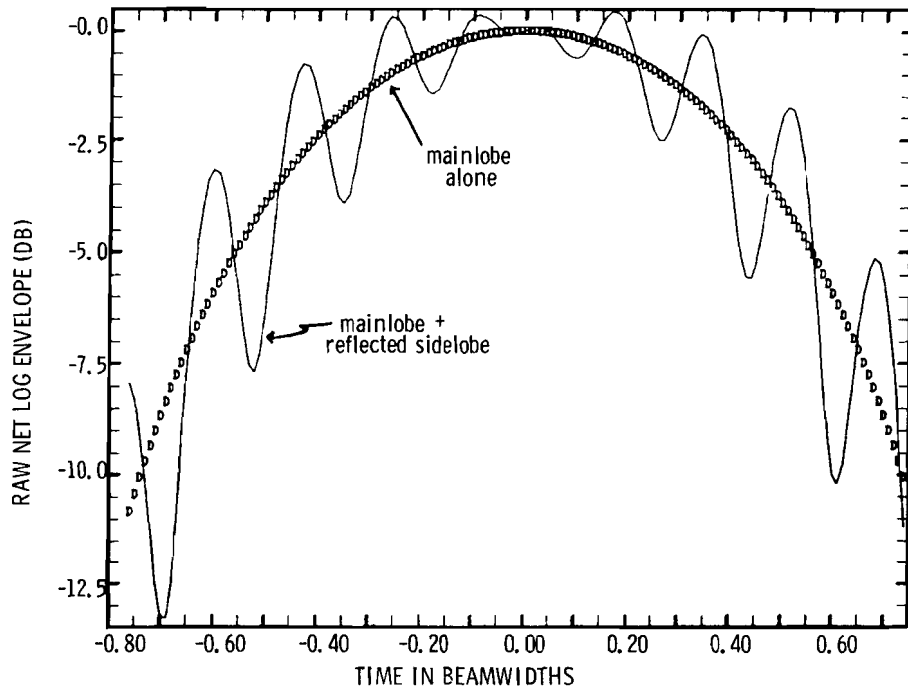
Fig. F-5 Raw and filtered log envelopes of mainlobe and high spatial frequency sidelobe.

were generated for the case where the sidelobe spatial pattern varies at a single high frequency within an overall envelope which varies at a frequency of L/2λ. A similar result would be obtained for any sidelobe variation model which has its energy concentrated above 26 kHz.

A more realistic model for the Bendix testbed phased array dynamic sidelobes probably consists of a wideband noise waveform whose spectrum is flat at frequencies up to 40 kHz. For such a waveform,

(1) only the spatial variation at frequencies below 26 kHz should be significant.

and

(2) the rms sidelobe error for a multipath signal of level ρ would be approximately

$$\varepsilon = \frac{1}{2}\ \rho \cdot BW \cdot \tilde{SL} \qquad\qquad (F\text{-}3)$$

where $\tilde{SL}$ = sidelobe power at frequencies below 26 kHz (note: this is _not_ necessarily equal to the filtered log envelope sidelobe level, as was illustrated in Figs. F-3 and F-4).

Equation (F-3) is obtained by assuming that the envelope distortion at the two threshold crossings are independent random variables whose rms level is $\rho \cdot \tilde{SL}/\sqrt{2}$ where the $\sqrt{2}$ factor arises from considering $\frac{1}{2}$ the sidelobe power to be at 90° relative phase relative to the mainlobe. The other $\sqrt{2}$ needed to arrive at the factor of $\frac{1}{2}$ in (F-3) arises from averaging the errors at the two threshold crossing points.

The rather considerable difference between equations (F-1) and (F-3) shows the difficulty in establishing an effective sidelobe model (and, TRSB antenna specifications). To date, the only suitable means identified for readily determining the spatial nature of the dynamic sidelobes vis a vis the mainlobe has been to coherently combine the two signals as is accomplished with a repeater or multipath screen. It is suggested that such tests be performed

at several of the significant dynamic sidelobes[*] for all antenna technologies under consideration for procurement to ascertain the effective sidelobe level.

For detailed antenna simulation studies, it is suggested that the computed (complex) scanning beam dynamic sidelobe be combined coherently with the computed scanning beam mainlobe (as in the top of Fig. F-5) and then filtered to yield the net received envelope (as in the bottom of Fig. F-5). The resulting angle error can then be computed for any desidred angle processing technique. This calculation should be repeated for several different rf phase relations between the sidelobe and mainlobe signals as well as several different reflector angle locations to arrive at a suitable level for SL.

The discussion above has focused on the dwell gate centroid processing technique since that has been used in the receivers used for the bulk of the U.S. testing. However, the comments above and basic results apply as well to the split gate trackers used in Australia [16] and by CALSPAN [92], except that the error expression (F-3) tends to overestimate the error since (roughly speaking) a split gate tracker matches the effective envelope filter bandwidth to the ground antenna beamwidth. The differences are not very large for a 1° beamwidth antenna, but can amount to several dB for a 3° beamwidth array.

_____
[*] e.g., filtered envelopes for which equation (F-1) would yield unacceptable errors at representative M/D ratios.

APPENDIX G
AMBIGUITY RESOLUTION IN DLS ARRAYS

Ambiguity resolution is a standard feature of interferometric systems with large baselines [87]. The basic method of ambiguity resolution is the same for all three DLS antenna systems; the circular azimuth, the linear azimuth, and the linear elevation. An initial estimate is made with a base-line small enough to avoid an ambiguity problem. Other antenna elements (or combinations of elements) are used with an increased baseline, increased normally by about a factor of two. Using the previous estimate, the expected phase measurement is determined. This is done for the linear systems simply by taking the previously resolved measurement and multiplying it by the in-creased baseline factor. The measurement data corresponding to this antenna element (or combination of elements) are now resolved to within $\pm\pi$ radians ($\pm$ 180°) of the expected phase values. The data resolved in this manner is used for a new estimate. The process is repeated until the final baseline is achieved and this estimate is the accepted value.

The details of this process are described now for each azimuth antenna system. The elevation system was described in the text.

1.   The Circular Azimuth System

The circular azimuth array (Fig. 5-4) has 19 elements on its perimeter and 19 phase measurements are made all relative to a reference element at its center. These measurements are denoted by γ_k, k = 1, 2, ..., 19. There are seven steps in the resolution process which are denoted by i = 1, 2, ..., 7. At each step 19 combinations of the γ_k are made which denote for the ith step by $\delta_{k,i}$. These combinations are best represented by through the use of eight vectors V1 through V8, each of dimension seven, one for each step, where the first four are used for odd k and the second for even k. The quantities $\delta_{k,i}$ can be represented as

$$\gamma \frac{k-1}{2} + V1(i)$$

$$\delta_{k,i} = \begin{cases} \frac{\gamma_{k-1}}{2} + V1(i) \quad -\frac{\gamma_{k-1}}{2} + V2(i) \quad -\frac{\gamma_{k-1}}{2} + V3(i) \quad +\frac{\gamma_{k-1}}{2} + V4(i) \\ \qquad\qquad\qquad\qquad \text{for } k = 1, 3, \ldots, 19 \qquad (G\text{-}1) \\ \\ \frac{\gamma_k}{2} + V5(i) \quad -\frac{\gamma_k}{2} + V6(i) \quad -\frac{\gamma_k}{2} + V7(i) \quad +\frac{\gamma_k}{2} + V8(i) \\ \qquad\qquad\qquad\qquad \text{for } k = 2, 4, \ldots, 18 \qquad (G\text{-}2) \end{cases}$$

where

$\underline{V1} = (5, 4, 3, 6, 4, 4, 5)$

$\underline{V2} = (14, 15, 16, 13, 15, 15, 14)$

$\underline{V3} = (4, 6, 7, 7, 2, 1, 1)$

$\underline{V4} = (15, 13, 12, 12, 17, 18, 1)$

and

$\underline{V5} = (4, 5, 6, 3, 5, 5, 4)$

$\underline{V6} = (14, 13, 12, 15, 13, 13, 14)$

$\underline{V7} = (5, 3, 2, 2, 7, 8, 0)$

$\underline{V8} = (13, 15, 16, 16, 11, 10, 0)$

For steps 1 through 6, the quantities $\delta_{k,i}$ are combined in two ways C_i and S_i,

$$C_i = \frac{\pi}{4} \frac{2}{19} \sum_{k=2}^{19} \delta_{k,i} \qquad\qquad (G\text{-}3)$$

and

$$S_i = \frac{\pi}{4} \frac{2}{19} \left[\sum_{k=1}^{19} \delta_{k,i} - \sum_{k=11}^{19} \delta_{k,i} \right] \qquad\qquad (G\text{-}4)$$

The purpose of this can best be understood by going through the quantities which make up S and C. Since $\gamma_k = 7\pi \cos(\theta_0 + k\frac{2\pi}{19})$ then, for k odd, we have

$$\delta_{k,1} = 7\pi \cos \phi_0 \left[\cos \ \theta_0 + \left(\frac{k-1}{2} + 5 \right) \frac{2\pi}{19} \right]$$

$$-7\pi \cos \phi_0 \left[\cos \ \theta_0 + \left(\frac{k-1}{2} + 14 \right) \ \frac{2\pi}{19} \right]$$

$$-7\pi \cos \phi_0 \cos \left[\theta_0 + \left(\frac{k-1}{2} + 4 \right) \frac{2\pi}{19} \right]$$

$$+7\pi \cos \phi_0 \cos \left[\theta_0 + \left(\frac{k-1}{2} + 15 \right) \ \frac{2\pi}{19} \right]$$

$$= 14\pi \cos \left[\phi_0 \ \sin \left(\theta_0 + \frac{k-1}{19}\pi + \frac{9\pi}{19} \right) \sin \frac{\pi}{19} \right.$$

$$\left. + \sin \left(\theta_0 + \frac{k-1}{19} \pi + \frac{29\pi}{19} \right) \ \sin \ \frac{\pi}{19} \right]$$

$$= 28\pi \cos \phi_0 \ \sin \frac{\pi}{19} \cos \frac{10\pi}{19} \ \sin \left(\theta_0 + \frac{k-1}{19}\pi \right)$$

$$k = 1,3,\ldots,19$$

$$= A \ \cos \phi_0 \ \sin \left(\theta_0 + \frac{k-1}{19} \pi \right)$$

where

$$A = 28\pi \sin \frac{\pi}{19} \ \cos \frac{10\pi}{19} = 1.1956248$$

and, for k even, we have

$$\delta_{k,1} = 7\pi \cos \phi_0 \left\{ \cos \left(\theta_0 + \left(\frac{k}{2} + 4 \right) \frac{2\pi}{19} \right) - \cos \left[\theta_0 + \left(\frac{k}{2} + 14 \right) \frac{2\pi}{19} \right] \right.$$

$$\left. - \cos \left[\theta_0 + \left(\frac{k}{2} + 5 \right) \frac{2\pi}{19} \right] + \cos \left[\theta_0 + \left(\frac{k}{2} + 13 \right) \frac{2\pi}{19} \right] \right\}$$

$$= 28\pi \cos \phi_c \sin \frac{\pi}{19} \cos \frac{9\pi}{19} \left[\sin \theta_0 + (k-1) \frac{\pi}{19} \right]$$

$$k = 2, 4, \ldots, 18$$

$$= A \cos \phi_0 \sin \left[\theta_0 + (k-1) \frac{\pi}{19} \right]$$

where, in the last equality, we have used the fact that

$$\cos \frac{10\pi}{19} = \cos \frac{9\pi}{19}$$

Substituting this result into the expressions for C_1 and S_1, we obtain

$$C_1 = \frac{\pi}{4} \frac{2}{19} A \cos \phi_0 \sum_{k=2}^{19} \sin \left[\theta_0 + (k-1) \frac{\pi}{15} \right]$$

$$= \frac{\pi}{38} A \cos \theta_0 \left[\sin \theta_0 \frac{18}{2} \cos \left(k \frac{\pi}{19} \right) - \cos \theta_0 \frac{18}{2} \sin \frac{k\pi}{19} \right]$$

and

$$S_1 = \frac{\pi}{38} A \cos \phi_0 \left[\sum_{k=1}^{10} \sin \left[\theta + (k-1) \frac{\pi}{19} \right] - \sum_{k=11}^{19} \sin \left[\theta_0 + (k-1) \frac{\pi}{19} \right] \right]$$

$$= \frac{\pi}{38} A \cos \phi_0 \left[\sin \theta_0 \sum_{k=0}^{9} \cos k \frac{\pi}{19} - \cos \theta_0 \sum_{k=0}^{9} \sin k \frac{\pi}{19} \right.$$

$$\left. - \sin \theta_0 \sum_{k=10}^{18} \cos k \frac{\pi}{19} + \cos \theta_0 \sum_{k=10}^{18} \sin k \frac{\pi}{19} \right]$$

$$= \frac{\pi}{38} A \cos \phi_0 \sin \theta_0 \left[1 + 2 \sum_{k=1}^{9} \cos k \frac{\pi}{19} \right]$$

The two identities

$$\sum_{k=1}^{n} \sin k\theta = \frac{\sin\left[\frac{1}{2}(n+1)\theta\right] \sin \frac{n\theta}{2}}{\sin \theta/2}$$

and

$$\sum_{k=1}^{n} \cos k\theta = \frac{\sin\left[\frac{1}{2}(n+1)\theta\right] \sin \frac{n\theta}{2}}{\sin \theta/2}$$

are used to obtain

$$C_1 = \frac{\pi}{38} A \frac{\sin \frac{9\pi}{19}}{\sin \frac{\pi}{38}} \cos \phi_0 \cos \theta_0 \qquad (G-5)$$

and

$$S_1 = \frac{\pi}{38} A \left[1 + 2 \frac{\cos \frac{5\pi}{19} \sin \frac{9\pi}{38}}{\sin \pi/38} \right] \cos \phi_0 \sin \theta_0 \qquad (G-6)$$

so that

$$C_1 = 0.99772066 \; A \cos \phi, \cos \theta_0 \approx A \cos \phi_0 \cos \theta_0$$

and

$$S_1 = 1.00114006 \; A \cos \phi_0, \sin \theta_0 \approx A \cos \phi_0 \sin \theta_0$$

Next, C_1 and S_1 can be used to estimate the $\delta_{k,i}$'s expected at the next step. This is done by forming

$$\Delta_{k,i} = B(i) \left[S_i \cos \frac{k\pi}{19} + C_i \sin \frac{k\pi}{19} \right] \qquad \text{for } i = 1, 2, \ldots, 6 \qquad (G-7)$$

where the vector $\underline{B}$ is

$$\underline{B} = (1.9727, \; 1.8916, \; 1.7749, \; 1.9727, \; 1.8151, \; 1.5458)$$

whose ith element corresponds to the factor by which the baseline increases in going from step i to step i+1. The $\delta_{k,i+1}$ are resolved by the requirement that

$$|\delta_{k,i+1} - \Delta_{k,i}| < \pi \quad \text{for } k - 1, 2, \ldots, 19 \text{ and } i = 1, 2, \ldots, 6 \qquad (G-8)$$

For i = 7 the $\delta_{k,7}$ are identical to the $\Delta\gamma_k$ of section D of the text so that

$$\Delta\gamma_k = -14\pi \sin \frac{9\pi}{19} \cos \phi_0 \sin (\theta_0 + \frac{k-1}{19} \pi).$$

Forming the quantities,

$$S = -\sum_{k=1}^{19} \Delta\gamma_k \sin(k-1) \frac{\pi}{19}$$

$$= 14\pi \sin \frac{9\pi}{19} \cos \phi_0 \frac{19}{2} \cos \theta_0$$

and

$$C = \sum_{k=1}^{19} \Delta\gamma_k \cos (k-1) \frac{\pi}{19}$$

$$= 14\pi \sin \frac{9\pi}{19} \cos \phi_0 \sum_{k-1}^{19} \frac{1}{2} \left\{ \sin \theta_0 + \sin \left[\theta_0 + 2\pi \frac{k-1}{19} \right] \right\}$$

$$= 14\pi \sin \frac{9\pi}{19} \cos \phi_0 \frac{19}{2} \sin \theta_0$$

then we have

$$\theta_{op} = \tan^{-1} (\frac{C}{S}) \tag{G-9}$$

If this value is not accepted as the final estimate it is converted to a conical estimate by use of

$$\ell = \sqrt{S^2 + C^2} = 14\pi \frac{19}{2} \sin \frac{9\pi}{19} \cos \phi_0$$

$$\tag{G-10}$$

$$= \ell_{max} \cos \phi_0$$

where

$$\ell_{max} = 133\pi \sin \frac{9\pi}{19}$$

and

$$\cos \phi_0 = \left(\frac{\ell}{\ell_{max}} \right)$$

With this, we convert to the conical estimate for θ_0

$$\theta_{oc} = \sin^{-1} \left(\cos \phi_0 \sin \theta_{op} \right) \tag{G-11}$$

and the process continues with the linear azimuth array. Note that this last estimate corresponds to approximately a 7 foot baseline.

2. The Linear Azimuth System

The linear azimuth array is formed by using elements 6 and 15 of the circular array together with the dipole elements and the arrays at the extremities. The various spacings are used to increase the baseline from just under seven feet to 63 feet in five steps and a final estimate is made using the pair of six element arrays with a 96.45 foot baseline. In steps 1 to 5 there are symmetric pairs of elements and the phases of both are resolved, averaged and multiplied by the baseline increase for use in resolving the next step. We describe only one side in the table where E1 is the innermost element of the six element array.

TABLE OF RESOLUTION STEPS

Step	Element Pair	Baseline (ft)
1	#6 and the near dipole	14
2	#6 and the far dipole	21
3	The right dipole and the near E1	28
4	#6 and the near E1	42
5	The left dipole and the far E1	63
6	The pair of 6 element arrays	96.45

3. Resolution Errors Due to Multipath

At each step in the resolution process there is a single segment which corresponds to the correct resolution of the angle being estimated. The angle of this segment or wedge grows smaller with each increase in baseline. The angle of each wedge is

$$2 \sin^{-1}\left(\frac{1}{2d/\lambda}\right) \qquad\qquad (G-12)$$

The error from the previous stage must be less than half this value if the resolution is to be done correctly. The error due to a single interfering multipath signal on the precedicng stage with baseline d' is bounded by

$$\sin^{-1}\left[\frac{1}{\pi d'/\lambda} \sin^{-1}\rho\right] .$$

Thus, if

$$\rho > \sin \frac{\pi}{2} \frac{d'}{d} \qquad\qquad (G-13)$$

a single interferer can cause a resolution problem. The ratio d'/d is the factor for the increase in the baseline, which is usually about 2. There-fore, a single interfering signal at -3 dB can cause an error depending on the relative direction of it and the desired signal. In simulations with high multipath environments resolution problems did occur. The most fre-quent place for the problem to occur was in the transfer from the azimuth circular array to the linear array. This was probably due to the fact that the #6 (and #15) antenna element of the circular array has a different phase characteristic than the dipole with which it is coupled at that step.

APPENDIX H
ABBREVIATIONS AND ACRONYMS

A/C	aircraft
AWOP	All Weather Operations Panel (of ICAO)
AZ	azimuth
BN	basic narrow (TRSB ground system)
BSU	beam steering unit
BW	beamwidth
CC	clearance counter
CL	centerline (of runway)
COMPACT	Cost Optimized Phased Array Circuit Technique
DLS	DME Based Landing System
DME	distance measuring equipment
DMLS	Doppler MLS
DPSK	differential phase shift keying
EL	elevation
ELAB	Electronics Research Laboratory (of University of Trondheim, Norway)
FRG	Federal Republic of Germany
FRSB	frequency reference scanning beam
ICAO	International Civil Aviation Organization
ID	identification
IF	intermediate frequency
JFK	John F. Kennedy International Airport (NY)
LOS	line of sight
MLS	microwave landing system

M/D	ratio of multipath signal level to direct signal level
NAFEC	National Aviation Facilities Experimental Center
NIAG	NATO Industrial Advisory Group
OCI	out of coverage indication
PWD	pulse width detector
RAP	receiver, antenna array, and processor
RF	radio frequency
SC	small community (TRSB ground station)
SEP	single edge processor
SL	sidelobe
SLS	sidelobe suppression signal
TDM	time division multiplexed
TRSB	time reference scanning beam
UK	United Kingdom
WG-A	Working Group A (of AWOP)

REFERENCES

1. RTCA SC-117 Final Report,"A New Guidance System for Approach and Landing," RTCA Document DO-148 (Dec. 1970).

2. "National plan for the Development of the Microwave Landing System," DOT/ NASA/DOD Planning Group (July 1971) AD-733268.

3. R. A. Rondini and R. H. McFarland, "Experimental Validation of Boeing 747 ILS Signal Scattering Calculations for Critical Area Determination," FAA SRDS (Jan. 1974) FAA-RD-74-57.

4. "Report of the Seventh Air Navigation Conference," ICAO Doc. 900 4-AN-CONF/7 (April 1972).

5. "Operational Requirements for an Advanced Approach and Landing Guidance System for the Post-1975 Period Prepared by the NATO Industrial Advisory Group (NIAG)," NATO NIAG document NIAG (71) D/1 (March 1971).

6. "The DME-Based-Landing System, DLS," as proposed by the Federal Republic of Germany developed by Standard Elektrik Lorenz AG. and Siemens, AG. (Sept. 1975).

7. "Doppler Microwave Landing Guidance System," proposal submitted by United Kingdom to the International Civil Aviation Organization (Nov. 1975).

8. "Recommendations for Selection of Scanning Beam Technique Using a Time Reference Signal Format for the U.S. Microwave Landing System - Issue Papers and Backup Documentation," Federal Aviation Administration ARD-700 (Jan. 1975).

9. S. Grashoff (chairman) "Report of the Sixth Meeting of the ICAO All-Weather Operations Panel," ICAO Doc. 9200, AWOP/6, (March 1977).

10. T. Breien, "Computer Analysis of MLS in Multipath Environment," IEE Conf. on the Future of All Weather Operations, (Nov. 1976).

11. H. A. Wheeler, "Multipath Effects in Doppler MLS," contained in Hazeltine Corp. Report "Microwave Landing System (MLS) Development Plan as proposed by Hazeltine Corp. During the Technique Analysis and Contract Definition Phase of the National MLS Development Program," FAA-RD-73-185 (Sept. 1972).

12. "Microwave Landing System (MLS) Development Plan as Proposed by Texas Instruments, Inc., During the Technique Analysis and Contract Definition Phase of the National MLS Development Program," FAA-RD-74-170, (1 Sept. 1972).

13. ITT/Gilfillan, "Microwave Landing System (MLS) Development Plan as Proposed by ITT/Gilfillan During the Technique Analysis and Contract Definition Phase," FAA-RD-74-118 (Sept. 1972).

14. P. Fombonne, "Position Errors in Microwave Landing Systems," Electronics and Civil Aviation Int. Conf., Paris, France (June 1972).

15. J. Benjamin and G. E. J. Peake, "Contributions to the UK Microwave Landing System Study (Phase 1)," Royal Aircraft Establishment, Tech. Memo RAD 1021 (May 1973).

16. "Interscan," proposal submitted by Australia to International Civil Aviation Organization (December 1975).

17. R. Giles "Study and Test Report on MLS Performance in Shadowing Conditions," ICAO AWOP Paper AWOP/6-BIP.45 (March 1977).

18. B. F. Oreb and J. G. Lucas, "A 1/20th Scale Millimetric Model of the Microwave Landing System," IEE Conf: Future of All Weather Operations (Nov. 1976).

19. L. N. Spinner and V. L. Bencivenga, "Advanced Scanning Beam Guidance System for All Weather Landing," FAA Syst. Res. Dev. Serv., Washington, D.C., RD 68-2 (Feb. 1968) AD 664 973.

20. V. L. Bencivenga, "Test and Evaluation of a Portable Scanning Beam Guidance System," (March 1972), FAA-RD-72-16.

21. F. X. Kelly, "Tests of Scanning-Beam Microwave Landing Systems at Difficult Sites," presented at technical seminar "Aviation - A Tool for Economic Development," First International Aerospace Show, Sao Paulo, Brazil (Sept. 1973).

22. Bendix Corp. "Refined Microwave Landing System (MLS) Program Development Plan (Phase III)," (Oct. 1974).

23. Texas Instruments, Inc., "Refined Microwave Landing System (MLS) Development Program Plan," DM74-03-04 (1 Oct. 1974).

24. ITT/Gilfillan, "Five Year MLS Development Program Plan (updated) Microwave Landing System," MLS-0420 (1 Oct. 1974).

25. Hazeltine Corp., "Refined Microwave Landing System (MLS) Development Program Feasibility Demonstration, Phase II," Report 11009 (1 Oct. 1974).

26. D. A. Shnidman, "The Logan MLS Multipath Experiment," Project Report ATC-55, Lincoln Laboratory, M.I.T. (23 Sept. 1975), DDC AD-A017083, FAA-RD-75-130.

27. D. A. Shnidman, "Airport Survey for MLS Multipath Issues," Project Report ATC-58, Lincoln Laboratory, M.I.T. DDC AD-A022937/7 (15 Dec. 1975), FAA-RD-75-195.

28. J. E. Evans, R. Burchsted, J. Capon, R. S. Orr, D. A. Shnidman, and S. M. Sussman, "MLS Multipath Studies, Volume I: Mathematical Models and Validation; Volume II: Application of Multipath Model to Key MLS Performance Issues," Project Report ATC-63, Lincoln Laboratory, M.I.T. (25 Feb. 1976), FAA-RD-76-3, DDC AD-A023040/9 and DDC AD-A025108/2.

29. J. Capon, "Multipath Parameter Computations for the MLS Simulation Computer Program," Project Report ATC-68, Lincoln Laboratory, M.I.T. (8 April 1976), FAA-RD-76-55, DDC AD-A024350/1.

30. A. Spiridon, "Impact of Obstacle Shadows in Monopulse Azimuth Estimate," Project Report ATC-50, Lincoln Laboratory, M.I.T. (17 July 1975), FAA-RD-75-91, DDC AD-A015139/9.

31. F. L. Frisbie, "Studies of Comparative Shadowing Behavior for DMLS and TRSB," ICAO AWOP Paper AWOP/6-BIP/50 (Feb. 1977).

32. P. S. Demko, "Polarization/Multipath Study," U.S. Army Electrom. Command Rep. VL-5-72 (Aug. 1971/June 1972).

33. A. E. Brindly, L. C. Calhoun, and T. N. Patton, (IITRI) "Multipath Environment Evaluation," Air Force Flight Dynamics Laboratory (Nov. 1974). AFFDL-TR-74-150.

34. IIT Research Institute "A Joint Army/Air Force Investigation of Reflection Coefficient at C and Ku Bands for Vertical, Horizontal, and Circular System Polarizations," (July 1976), AFFDL-TR-76-67.

35. A. E. Brindley, L. E. Calhoun, T. N. Patton, and L. Valcik, "Analysis, Test and Evaluation Support to the USAF Advanced Landing System Program," USAF Flight Dynamics Lab. (Aug. 1974), AFFDL-TR-74-62.

36. E. Bramley and S. Cherry, "Investigation of Microwave Scattering by Tall Buildings," Proc. IEEE, (Aug. 1973).

37. J. G. Lucas and B. F. Oreb, "MLS Modeling Work," Report from Air Navigation Group, School of Electrical Engineering, Univ. of Sydney, Australia, to Australian Dept. of Civil Aviation (1976).

38. B. F. Oreb and J. G. Lucas, "Blocking and Diffraction Due to an ICAO Sheet," personal communication to J. Evans (May 1977).

39. J. E. Evans, D. Karp, R. R. LaFrey, R. J. McAulay, and I. G. Stiglitz, "Experimental Validation of PALM - A System for Precise Aircraft Location," Technical Note 1975-29, Lincoln Laboratory, M.I.T. (29 April 1975), DDC AD-A010112/1.

40. J. E. Evans, "Aperture Sampling Techniques for Precision Direction Finding," paper presented at IEEE Electro 78, Boston, Massachusetts (May 1978)

41. J. E. Evans and S. M. Sussman, "Doppler Azimuth Reference Errors with Out-of-Beam Multipath," ICAO AWOP Working Group A Paper TH.BIP.3 (30 June 1976).

42. T. E. Bernard, "Analytical Studies of Techniques for the Computation of High-Resolution Wavenumber Spectra," Special Report No. 9, Texas Instruments Incorporated, Dallas, Texas (14 May 1969), Project No. VELAT/7701.

43. J. Capon, "High-Resolution Frequency-Wave Number Spectrum Analysis," Proc. of IEEE, 57, 1408 (1969).

44. N. O. Anderson, "On the Calculation of Filter Coefficients for Maximum Entropy Spectral Analysis," Geophysics, 39, 69 (1974).

45. J. P. Burg, "Maximum Entropy Spectral Analysis," Paper presented at the 37th meeting of the Society of Exploration Geophysicists, Oklahoma City, Oklahoma (31 October 1967).

46. R. T. Lacoss, "Data Adaptive Spectral Analysis Methods," Geophysics, 56, 661 (1971).

47. R. N. McDonough, "Maximum-Entropy Spatial Processing of Array Data," Geophysics, 39, 843 (Dec. 1974).

48. H. R. Radoski, P. F. Fouger, E. J. Zanalick, "A Comparison of Power Spectral Estimates and Applications of the Maximum Entropy Method," J. Geophy. Res., 80, No. 4, 619 (Feb. 1975)

49. T. E. Bernard, "The Maximum Entropy Spectrum and the Burg Technique," Advanced Signal Processing Technical Report No. 1, Texas Instruments Incorporated, Dallas, Texas (25 June 1975), ALEX(03)-TR-75-01.

50. J. Makhoul, "Linear Prediction; A Tutorial Review," Proc. IEEE, 63, 561 (1975).

51. T. P. McGarty, "Models of Multipath Propagation Effects in a Ground-to-Air Surveillance System," Technical Note 1974-7, Lincoln Laboratory, M.I.T. (25 February 1974), DDC AD-777241/1.

52. A. Spiridon, "Effects of Local Terrain and Obstacles Upon Near Horizon Gain of L-Band Beacon Antennas," Technical Note 1975-6, Lincoln Laboratory, M.I.T. (17 July 1975), DDC AD-A013732/3.

53. H. Berger and J. E. Evans, "Diversity Techniques for Airborne Communications in the Presence of Ground Reflection Multipath," Technical Note 1972-27, Lincoln Laboratory, M.I.T. (8 September 1972), DDC AD-752249.

54. F. Harris, "On the Use of Windows for Harmonic Analysis with the Discrete Fourier Transform," Proc. IEEE, 66, 51 (1978).

55. A. Oppenheim and R. Schafer, Digital Signal Processing, (Prentice Hall, 1975).

56. A. Brindley, L. Calhoun, T. Patton, and L. Valcik, "Analysis, Test and Evaluation Support to the USAF Advanced Landing System Program Vol. III Part 1 Doppler MLS Guidance Error Data (DOTS Tracking System)," AFFDL-TR-74-62, Vol. III, Part 1 (August 1974).

57. P. Demko,"Propagation Integrity for Microwave Landing Systems," In AGARD Conference Proceedings No. 240 Guidance and Control Design Considerations for Low-Altitude and Terminal-Area Flight (October 1977).

58. "Flight Trials of TRSB/Interscan Equipment at Sydney International Airport, Australia," Paper AWO/78-WP/88 presented by Australia at ICAO AWO Division Meeting, (April 1978).

59. "Tracked Flight Trials of Doppler MLS at Manchester Airport," Paper AWO/78-WP/123 presented by United Kingdom at ICAO AWO division meeting (April 1978).

60. "Tracked Flight Trials of Doppler MLS Azimuth System at Brussels National Airport," Paper AWO/78-WP/12 presented by the United Kingdom at ICAO AWO Division Meeting (Janauary 1977).

61. "Test Results for a Time Reference Scanning Beam (TRSB) 'Basic Narrow' MLS," Paper AWO/78-WO/119, presented by United States at ICAO AWO Division Meeting (April 1978).

62. "DMLS/TRSB Comparative Demonstration Test Results at Brussels National Airport, Brussels, Belgium," Paper AWO/78-WO/141, presented by United States at ICAO AWO Division Meeting (April 1978).

63. DMLS/TRSB Comparative Demonstration Test Results," Paper AWO/78-WP/153 presented by United States at ICAO AWO Division Meeting (April 1978).

64. J. E. Evans and D. A. Shnidman, "Multipath Characteristics of AWOP WG-A Multipath Scenarios," AWOP WG-A Paper TH.BIP/9 also Revision 1 (4 January 1977).

65. "Time Reference Scanning Beam Microwave Landing System," proposal submitted by the United States to the International Civil Aviation Organization (December 1975).

66. R. Butler (Rappoteur), "Report of the Multipath Subgroup of WG-A Held near Boston, Mass., 11-15 October 1976 ," L.WP/3 in the report of ICAO AWOP Working Group A, Seventh Meeting, London (Nov. 1-12, 1976).

67. M. Whitney, "UK Presentations and Demonstrations of Doppler MLS in Multipath Environments," given at Royal Aircraft Establishment, Bedford, (1 Nov. 1976), CAA Paper 77003 (Feb. 1977).

68. M. Whitney, "DMLS Signal Processing," L.BIP/38 in Report of the Seventh Meeting of ICAO AWOP Working Group A, held in London, U.K. (2-12 Nov. 1976).

69. F. Frisbie, "TRSB Phase III Receiver Functional Description," Paper L.BIP/19 in the report of ICAO AWOP Working Group A, Seventh Meeting, London (Nov. 1976).

70. T. Bohr, "The Proposed DLS Airborne Equipment and DLS System Configuration," L.BIP/42 and L.BIP/43 in Report of ICAO AWOP Working Group A, Seventh Meeting, London (1-12 Nov. 1976).

71. J. Beneke, C. Wightman et. al., "Multipath and Performance Tests of TRSB Receivers," FAA-RD-77-66 (March 1977).

72. ICAO All Weather Operations Panel Working Group A, "Report of the Third Meeting Held in Melbourne During the Period 24-28 February 1975" (Feb. 1975).

73. "Validation of Computer Simulation by Comparison with Tests at Operational Airports," Paper AWO/78-WP/135 presented by the United States at ICOA AWO Division meeting (April 1978).

74. "Application and Validation of Computer Simulation to MLS Multipath Performance Assessment," Paper AWO/78-WP/138 presented by the United States at ICAO AWO Division meeting (Jan. 1978).

75. "Performance of Advanced Approach and Landing Systems (AALS)," Electronics Research Laboratory, Univ. of Trondheim, Norwegian Inst. of Tech. (March 1973).

76. "Study of the Radar Reflectivity Characteristics at SSR Frequency of Pilkington 'Insulight' Metallized Glass," Cosser Electronics Limited Report EF/S/055 (Sept. 1973).

77. A. Von Hippel, Dielectric Materials and Applications, (Chapman & Hall, Ltd., London 1954).

78. G. Bailey, Personal Communication (Feb. 1977).

79. F. L. Frisbie, "Comparison of DMLS and TRSB Acquisition/Validation in an Azimuth Multipath Environment," ICAO All Weather Operations Panel Working Paper AWOP-WP/322 (March 1977).

80. B. L. Oreb, "Modeling of the Microwave Landing System (MLS) at 104 GHz," PhD Thesis, Univ. of Sydney, Australia (1978).

81. G. T. Ruck, D. E. Barrick, W. D. Stuart and C. Krichbaum, Radar Cross Section Handbook, Volume 1 (Plenum, New York, 1970).

82. H. Neugebauer and M. Bachynski, "Diffraction by Smooth Cylindrical Mountains," Proc. of IRE, 41, 1619 (Sept. 1958).

83. I. M. Hunter, "Some Properties of Air-Derived and Ground-Derived Aircraft Landing Guidance Concepts," J. of British Institute of Navigation (1973).

84. K. D. Eckert, "DME Based System for Enroute/Terminal Navigation, All Weather Landing and Air Traffic Control," in AGARD Conference Proc., No. 240 Guidance and Control Design Considerations for Low-Altitude and Terminal Area Flight (Oct. 1977).

85. L. Armijo, K. Daniel, and W. Labuda, "Application of the FFT to Antenna Array Beamforming," EASCON '74 Conference Proceedings, Washington, D.C. (1974).

86. K. Kohler, "Synthetic Radio Direction Finding with Virtual Antenna Patterns," Electric Comm., 48, 299 (1973).

87. W. B. Kendall, "Unambiguous Accuracy of an Interferometric Angle-Measuring System," IEEE Trans. Space Electronics and Telemetry, 11, 67, (June 1965).

88. J. Duncan, "The Effect of Ground Reflections on an Interferometric Direction Finder," IEEE Trans. Aerospace Electron. Systems, AES-3, 927 (1967).

89. D. K. Barton, "Multipath Error in a Vertical Interferometer," Proc. of IEEE, 53, 543 (1965).

90. A. Papoulis, The Fourier Integral and Its Applications, (McGraw-Hill, New York, 1962).

91. M. F. Whitney, "Simulation of Phased Array Antenna Systems," Working Paper TH.WP-3 presented at the Hague Meeting of AWOP WG-A (July 1976).

92. J. Beneke et. al., "TRSB Multimode Digital Processor," Final Report, Calspan Corporation, Report No. FAA-RD-77 (April 1978).

93. Bendix Corp., "Microwave Landing System, Phase III (Basic Narrow and Small Community Configurations) Final Report, Volume 1," Report No. MLS-BCD-R-2801-1 (June 1978).

94. "Report of the All Weather Operations Division Meeting, 1978," International Civil Aviation Organization, Doc. 9242, AWO/78 (April 1978).

95. F. Frisbie, "Out of Coverage Indication (OCI) and Left/Right Guidance," ICAO AWOP Working Group A Background Information Paper L.BIP/20 (Nov. 1976).

96. Hazeltine Corp., "Cost Minimized Phased Array Circuit Technique (COMPACT)," (1976).

97. J. Sebring and J. Ruth, "MLS Scanning-Beam Antenna Implementation," Microwave J., 41 (Jan. 1974)

98. F. Pogust, "Microwave Landing Systems," IEEE Spectrum, 15, 30 (1978).

99. R. Kelly, H. Redlein and J. Shagena, "Landing Aircraft Under Poor Conditions," IEEE Spectrum, 15, 52 (1978).

100. A. Lopez, "Scanning-Beam Microwave Landing System - Multipath Errors and Antenna Design Philosophy," IEEE Trans on Ant. and Prop., AP-3, 290 (May 1977).

101. J. Kuznetsov,"Some Questions Concerning Reduction of Multipath Effect on Microwave Landing System Accuracy," ICAO AWOP 6 Paper WP/305 (1977).

102. F. L. Frisbie, "(Latest) Comparison of DMLS Computer Model with January 1977 DMLS Hybrid Simulator Azimuth Multipath Data," ICAO AWOP 6 Paper BIP/62 (1977).

103. H. L. Van Trees, Detection, Estimation and Modulation Theory Part I (John Wiley & Sons, New York, 1968).

104. M. Skolnik, Introduction to Radar Systems, (McGraw-Hill Book Company, New York, 1962).

105. D. K. Barton and H. R. Ward, Handbook of Radar Measurement (Prentice-Hall, New Jersey, 1969).

106. L. Jolley, Summation of Series (Dover, New York, 1961).

107. R. J. McAulay, "The Effects of Interference on Monopulse Performance," Technical Note 1973-30, Lincoln Laboratory, M.I.T. (1 August 1973), DDC AD-769336/9.

108. Appendix E in "Report of the Seventh Meeting of ICAO AWOP WG-A held in London, UK, Nov. 1-12, 1976" (Dec. 1976).

109. R. Loh, "Preliminary Crows Landing Acceptance Test Data Analysis," MITRE Technical Report MTR-7617 (March 1978).